The Septin Circus: An Unforgettable Show of Cellular Choreography

Castro Linares, G.

DOI
10.4233/uuid:d641823e-eaab-4fca-b856-fe3b0a500f88

Publication date
2023

Document Version
Final published version

Citation (APA)
Castro Linares, G. (2023). *The Septin Circus: An Unforgettable Show of Cellular Choreography*. [Dissertation (TU Delft), Delft University of Technology]. https://doi.org/10.4233/uuid:d641823e-eaab-4fca-b856-fe3b0a500f88

The Septin Circus: An Unforgettable Show of Cellular Choreography

The Septin Circus: An Unforgettable Show of Cellular Choreography

Dissertation

for the purpose of obtaining the degree of doctor
at the Delft University of Technology,
by the authority of the Rector Magnificus, Prof.dr.ir. T.H.J.J. van der Hagen,
chair of the Board of Doctorates
to be defended publicly on
Thursday 30 November 2023 at 12:30 o'clock

by

Gerard CASTRO-LINARES

Master of Science in Molecular Life Sciences,
Radboud University, The Netherlands,
born in Vilanova i la Geltrú, Spain

This dissertation has been approved by the promotors

Composition of the doctoral committee:

Rector Magnificus,	chairperson
Prof.dr. G.H. Koenderink,	Delft University of Technology, promotor
Dr. A. Jakobi,	Delft University of Technology, copromotor
Independent members:	
Prof.dr. S. Mostowy	London School of Hygiene & Tropical Medicine, United Kingdom
Dr. A. Baillet	Université Paris-Saclay, France
Prof.dr.ir. S.J.J. Brouns	Delft University of Technology
Dr. K.A. Ganzinger	AMOLF
Dr.ir L. Laan	Delft University of Technology
Prof.dr. C. Joo	Delft University of Technology, reserve member

The work in the thesis was performed at AMOLF and TU Delft. It is part of the research programme *BaSyC - Building A Synthetic Cell* of the Netherlands Organization for Scientific Research (NWO) .

Printed by: Gildeprint

Cover design: Hilman Assiddiq and Gerard Castro-Linares

Style: TU Delft House Style, with modifications by Moritz Beller
`https://github.com/Inventitech/phd-thesis-template`

ISBN: 978-94-6384-491-8

When you think about rules, you have to realize that they are closely entangled with the intentions of whoever set them.

Xenoblade Chronicles 3, Ninentendo Switch, 2022

Summary

The world we inhabit has long been home to an immense multitude of living beings: small bacteria and other microscopic organisms that elude our vision, as well as plants, fungi, and animals. Despite these vast differences in size and appearance, we classify all of these entities as living. Scientists, including the author of this thesis, have been captivated by the mechanisms that sustain the diversity of life, all while maintaining fundamental characteristics that define all this diversity of organisms as alive. At the basis of this remarkable diversity and functionality of life are cells. From single cells existing as unicellular organisms to multiple cells interacting to form multicellular organisms, cells are the minimum living building block of life. Cells between and even within single organisms are very diverse in shape, components, functionalities, and organization. Even with these differences, they all share common traits: cells have a cell membrane that separates their interior from their exterior, possess genetic material that contains all the information needed for the cell to function, they use components from their environment to fuel and renew themselves, and they are able to divide to reproduce. In order to carry out these functions: cells generate a multitude of components, proteins, nucleic acids, lipids, sugars, and other small metabolites, that are stored inside the cell, making it a complex self-sustaining chemical reactor with tens of thousands of interconnected and sometimes redundant reactions. Understanding how the basic commonalities between cells emerge from the intricate interaction of those reactions is the key to understand what is life and how it works.

With this aim, scientists are investigating these reactions within and outside cells using many different approaches. An interesting approach that emerged in the early 2000s is synthetic biology, a discipline that aims to use engineering principles to build biological systems. Of special interest to identify the properties that define living organisms and to understand how cells work is bottom-up synthetic biology, which aims to build a synthetic cell from its purified components while investigating how these components interact with each other and work together to make a cell alive. This minimalist approach uses *in vitro* reconstitution, which is, in other words, putting purified components together outside of a living cell to simplify interesting cellular subsystems, allowing for a more profound understanding of their workings and helping to identify the minimal required components and functions.

With this aim, the Dutch "BaSyC - Building a Synthetic Cell" consortium aims to build a synthetic cell from the bottom-up. The work presented in this dissertation is part of this BaSyC project and has the objective to work towards designing a mechanism that controls the shape of the synthetic cell, with a special emphasis on a synthetic cell division mechanism. We work towards this goal by getting inspiration from animals cells for two main reasons: (1) to simplify the cell shape control mechanism by avoiding the need to construct a cell wall and (2) to learn more how animal cells control their shape since it is more relevant for human physiology and disease.

It is know that behind animal cell shape control there is the interaction of the membrane with the cytoskeleton, a network of filament-forming proteins composed of actin filaments, microtubules, intermediate filaments, and septins. Septins, proteins that form filaments from smaller complexes made of six (hexameric) or eight (octameric) septins, are a less widely studied component of the cytoskeleton that participates in many important processes, such as cell migration. Especially important for septin functions are its interaction with microtubules, the cell membrane, and actin filaments. Interestingly, these three components are all key players during cell division and cell shape control. Therefore, we think that septins are a good candidate to orchestrate the choreography between them to lead to cell shape control and division. Unfortunately, the scientific community does not know enough about how septins interact with these cellular components. So, we cannot use engineering principles to design this synthetic cell shape control mechanism. Consequently, the aim of this thesis is to investigate the basic (or BaSyC) properties of the septins' interactions with microtubules, lipid membrane, and actin filaments using *in vitro* reconstitution.

In this thesis, we first delve into bottom-up synthetic biology and the role of the cell membrane and the cytoskeleton in animal cell shape control in **Chapter 1**. We do so with a focus on what is the importance of septins' interactions for cell shape control and how to use them for building a synthetic cell.

In order to use septins for *in vitro* reconstitution, we first need to purify them. In **Chapter 2** we detail the protocol that we use to purify septin complexes from the bacterium *Escherichia coli* by using a double-affinity chromatography approach. Protein purification procedures can vary a lot in yield and in correct functionality of the protein, therefore we use a set of techniques to determine the quality of the purified septins in terms of integrity and functionality, which is also detailed in Chapter 2.

In **Chapter 3** we investigate the interactions between septins and microtubules. We use a combination of bioinformatics, experiments in cells, and *in vitro* reconstitution to find and validate the region of septins that binds microtubules. We find that this domain is only present in the very start of a specific septin, SEPT9. Knowing this, we then examine how hexameric septin complexes, that do not have SEPT9, and octameric septin complexes with either the full SEPT9 or shorter or mutated versions of it interact with microtubules. We find that SEPT9 has two domains that regulate the interaction with microtubules, namely the domain that we found with bioinformatics that allows binding and affects microtubule polymerization dynamics, and another region deeper in SEPT9 that tunes this interaction by lowering the binding affinity.

In **Chapters 4 and 5** we focus on the interactions of septins with lipid membranes. In **Chapter 4** we look into the interaction of septins with a specific model of lipid membranes, supported lipid layers, in which the lipid membranes is bound and supported by a solid surface. We use a multi-technique approach to investigate what governs septin-membrane binding. We find that septins require the lipid phosphatidylinositol 4,5-bisphosphate (PIP2) to bind membranes, while the lipid phosphatidylserine (PS) has a synergistic effect on membrane binding, likely due to its negative charge. We also find that septins form either a stiffer bundle-based networks or a softer filament-based networks depending on the length of the septin complex, and on environmental conditions, in particular, the presence of the small molecule GTP and the properties of the lipid membrane. We finally use computer simulations to more deeply understand this process and identify that the formation of the stiffer network is likely based on filament growth, pairing, and alignment. In **Chapter 5** we move to a more cell-like membrane by using cell-sized vesicles, which are spherical. In these conditions and putting the septins inside the vesicle, we replicate and validate our conclusions that septin-membrane binding requires PIP2 lipids and is synergistically enhanced by PS lipids. In this condition, the membrane of the vesicle is left smooth and spherical. In contrast, when the septins are added to the outside of the vesicles, they deform the membranes forming a golf ball-like structure with bumps evenly spaced on the vesicle surface, suggesting that septins detect membrane curvature and are able to deform the membranes if they do not find their preferred curvature.

In **Chapter 6** we investigate the interactions of septin with actin filaments. We find that septin complexes are able to bring actin filaments together forming tight bundles at high concentrations while simply making connections at lower concentrations. Interestingly, octameric septin complexes could do this at much lower concentrations than hexameric septin complexes. We then add to the system the motor protein muscle myosin-2, which is able to form bipolar filaments that can bind actin filaments, and pull them to reorganize them, being therefore important for cell shape control. Interestingly, at high septin concentrations myosin activity was stopped, while at low septin concentrations it was enhanced allowing for long-range actin network deformations, showing that septins can have different effects on the reorganization of actin networks.

In cells, the cell cortex is a critical structure made of actin that is the main reinforcer of the cell membrane. Additionally, its reshaping is also one of the main forces that generate cell shape changes, including cell division. In **Chapter 7** we follow a synthetic biology approach and use the knowledge acquired from chapters 4-6 to design a septin-anchored actin cortex. We combine the ability of septins to bind actin and lipid membranes containing PIP2 and PS to successfully make septin anchor actin filaments to flat supported lipid layers and to the inside of cell-sized vesicles. With the aim of tuning the shape of this septin-anchored cortex-like structure, we include another protein, Arp2/3, that interacts with actin forming branched actin filaments. We find that in the presence of this additional protein, septins anchor radial arrays called asters of actin to membranes.

Despite the advancements in understanding how septins interact with important structures that modulate cell shape, we are still far from being able to use them for controlling the shape of synthetic cells. In **Chapter 8** we discuss further research lines to increase our knowledge of the interactions of septins with the ultimate goal of using these proteins to build a synthetic cell.

Finally, I include a gallery of microscopic images and photographs to illustrate how science is a beautiful discipline that can not only contribute to deepening our knowledge but also to art.

Samenvatting

De wereld waarin wij leven is al meer dan 350 miljoen jaar een thuisbasis van een enorme diversiteit aan levende wezens: kleine bacteriën en andere microscopisch kleine organismen die met het blote oog niet waarneembaar zijn, als ook planten, schimmels en dieren. Ondanks de grote verschillen in grootte en uiterlijk van deze levensvormen classificeren we ze allen als levend. Wetenschappers, waaronder ook de auteur van dit proefschrift, zijn gefascineerd door de mechanismen die enerzijds voor deze diversiteit zorgen en anderzijds zorgen voor de fundamentele karakteristieken die al deze organismen als levend definiëren. Aan de basis van deze opmerkelijke diversiteit en functionaliteit van het leven staan cellen. Cellen zijn de kleinste levende bouwstenen van het leven: van individuele cellen die bestaan als eencellige organismen tot meerdere cellen die samenwerken om meercellige organismen te vormen. Cellen van verschillende organismen en zelfs binnen eenzelfde organisme zijn zeer divers en hebben uiteenlopende vormen, componenten, functionaliteiten en organisaties. Ondanks deze verschillen hebben ze gemeenschappelijke kenmerken: cellen hebben een celmembraan dat hun binnenkant van hun buitenkant scheidt, bezitten genetisch materiaal dat alle informatie bevat om de cel te laten functioneren, ze gebruiken componenten uit hun omgeving als brandstof en voor zelfvernieuwing, en kunnen zich delen om zich voort te planten. Om deze functies uit te voeren kunnen cellen meerdere componenten zoals eiwitten, nucleïnezuren, lipiden, suikers en andere kleine metabolieten aanmaken die binnen de cel worden opgeslagen. Zodoende is de cel een complexe en zelfvoorzienende chemische reactor met tienduizenden verbonden, en soms overbodige, reacties. Inzicht krijgen in hoe deze fundamentele overeenkomsten tussen cellen voortkomen uit de ingewikkelde interactie tussen deze reacties is de sleutel tot het begrijpen wat leven is en hoe het werkt.

Met dit doel onderzoeken wetenschappers deze reacties binnen en buiten cellen met behulp van verschillende benaderingen. Een interessante benadering die in het begin van de jaren 2000 opkwam is synthetische biologie, een discipline die als doel heeft technische principes te gebruiken voor het bouwen van biologische systemen. Van bijzonder belang om eigenschappen te identificeren die levende organismen definiëren en om te begrijpen hoe cellen werken is “bottom-up” synthetische biologie, dat als doel heeft om een synthetische cel te bouwen vanuit zijn componenten en hiermee te onderzoeken hoe deze componenten met elkaar interageren en samenwerken om een cel te laten leven. Deze minimalistische benadering maakt gebruik van *in vitro* reconstitutie, hetgeen betekent dat gezuiverde componenten buiten de levende cel worden samengevoegd met als doel om versimpelde modellen voor cellen te bouwen. Dit maakt het mogelijk een beter begrip te krijgen van de werkingsprincipes van de cel en om de minimaal vereiste componenten en functies te identificeren.

Met dit doel wil het Nederlandse consortium “BaSyC – Building a Synthetic Cell” een synthetische cel opbouwen vanuit de basis. Het werk dat in dit proefschrift wordt ge-

presenteerd is onderdeel van dit BaSyC project en heeft als doel het ontwerpen van een mechanisme dat de vorm van een synthetische cel reguleert, met een speciale nadruk op het mechanisme van synthetisch celdeling. We werken naar dit doel door inspiratie te krijgen van dierlijke cellen om twee belangrijke redenen: (1) dierlijke cellen hebben in tegenstelling tot bacterieën, gisten en planten geen celwand, hetgeen het makkelijker maakt om de cel te delen, en (2) om meer te leren over hoe dierlijke cellen hun vorm reguleren aangezien dit relevanter is voor menselijke fysiologie en ziekte.

Het is bekend dat achter de regulatie van dierlijke celvorm een interactie schuilgaat tussen het membraan en het cytoskelet, een netwerk van filamentvormende eiwitten dat bestaat uit actine filamenten, microtubuli, intermediaire filamenten en septins. Septins zijn eiwitten die filamenten vormen uit kleinere complexen gemaakt van zes (hexamere) of acht (octamere) septins. Ze vormen een onderbestudeerd onderdeel van het cytoskelet, ondanks het feit dat ze deelnemen aan veel belangrijke cellulaire processen, zoals cel migratie. Voor de functionaliteit van septin zijn hun interacties met microtubuli, het celmembraan en actine filamenten van groot belang. Interessant is dat deze drie componenten allemaal belangrijke rollen vervullen tijdens celdeling en celvorm regulatie. Daarom verwachten we dat septins een goede kandidaat zijn om de choreografie tussen deze componenten te leiden tijdens celvorm regulatie en celdeling. Helaas weet de wetenschappelijke gemeenschap niet genoeg over hoe septins interageren met deze cellulaire componenten. Hierdoor kunnen we niet de technische principes toepassen om de synthetische celvorm controlemechanismen te ontwerpen. Derhalve is het doel van dit proefschrift om de basis (of BaSyC) eigenschappen van de interacties van septins met microtubuli, lipide membranen en actine filamenten te onderzoeken met gebruik van de *in vitro* reconstitutie.

In dit proefschrift duiken we eerst in de zogeheten bottom-up synthetische biologie en de rol van het celmembraan en het cytoskelet in de celvorm regulatie van dierlijke cellen in **Hoofstuk 1**. Hierin leggen we de nadruk op het belang van de interacties van septins voor de celvorm regulatie en hoe we deze eiwitten kunnen gebruiken voor het bouwen van een synthetische cel. Om septins te kunnen gebruiken voor *in vitro* reconstitutie, moeten we de septins eerst zuiveren. In **Hoofdstuk 2** beschrijven we het protocol dat we gebruiken om septin complexen uit de *Escerichia coli* bacterie te zuiveren met het gebruik van een dubbele affiniteits chromatografie. Omdat eiwitzuiveringen sterk kunnen variëren in opbrengst en functionaliteit van het eiwit, gebruiken we een reeks technieken om de kwaliteit van de gezuiverde septins te bepalen in termen van integriteit en functionaliteit, die ook in Hoofdstuk 2 worden beschreven.

In **Hoofdstuk 3** onderzoeken we de interacties van septin en microtubuli. We gebruiken een combinatie van bioinformatica, experimenten in cellen, en *in vitro* reconstitutie om het precieze onderdeel van septin eiwitten dat bindt aan microtubuli te vinden en te valideren. We ontdekten dat dit domein alleen aanwezig is aan het begin van een specifiek septineiwit, SEPT9. Aan de hand van deze bevinding onderzoeken we vervolgens hoe hexamere septin complexen, die geen SEPT9 hebben, en octamere septin complexen met de volledige of korte gemuteerde versies van SEPT9 interageren met microtubuli. We tonen aan dat SEPT9 twee domeinen heeft die de interactie met microtubuli reguleren, namelijk het domein dat we vonden met bio-informatica, dat de binding mogelijk maakt en de dynamiek van microtubuli-polymerisatie beïnvloedt, en een ander domein dieper in

SEPT9 dat deze interactie afstemt door de bindingsaffiniteit te verlagen.

In **Hoofdstukken 4 en 5** richten we ons op de interacties ven septins met lipide membranen. In **Hoofdstuk 4** onderzoeken we de interactie van septins met een specifiek model van lipide membranen, gedrapeerd over een vlak substraat dat het membraan ondersteunt. We gebruiken een combinatie van verschillende meettechnieken om te onderzoeken welke factoren de interactie tussen septin eiwitten en het membraan reguleren. We tonen aan dat septins het lipide molecuul phosphatidylinositol 4,5-bisphosphate (PIP2) nodig hebben om membranen te binden, terwijl het lipide molecuul phosphatidylserine (PS) een synergetisch effect heeft op de membraanbinding, waarschijnlijk vanwege diens negatieve lading. Daarnaast vinden we dat septins twee soorten netwerken, ofwel stijvere bundel-gebaseerde netwerken ofwel zachtere filament-gebaseerde netwerken, vormen, afhankelijk van de lengte van het septin complex en condities uit de omgeving, in het bijzonder de aanwezigheid van het kleine GTP molecuul en de eigenschappen van het lipide membraan. Tenslotte gebruiken we computersimulaties om de vorming van de netwerken beter te begrijpen en te identificeren dat vorming van het stijvere netwerk waarschijnlijk is gebaseerd op filamentgroei, paring en uitlijning. In **Hoofdstuk 5** gaan we richting een meer celachtig membraan waarbij we bolvormige vesikels gebruiken ter grootte van een cel. Door de septins in de vesikels te encapsuleren repliceren en valideren we onze eerdere conclusies dat de septin-membraan binding afhankelijk is van PIP2 lipiden en synergetisch wordt versterkt door PS lipiden. Met de septins binnenin blijft het membraan van het vesikel glad en bolvormig. Wanneer de septins daarentegen worden toegevoegd aan de buitenkant van de vesikels, vervormen de membranen tot een golfbalachtige structuur met hobbels die gelijkmatig verdeeld zijn over het oppervlak, hetgeen suggereert dat septins de krommingen in het membraan kunnen detecteren en de membranen kunnen vervormen als ze niet de gewenste kromming kunnen vinden.

In **Hoofdstuk 6** onderzoeken we de interacties van septins met actine filamenten. We ontdekken dat septin complexen in staat zijn om actinefilamenten samen te brengen tot bundels bij hoge concentraties, terwijl ze vooral kruisverbindingen maken bij lagere concentraties. Interessant is dat octamere septin complexen dit kunnen doen bij veel lagere concentraties dan hexamere septin complexen. Vervolgens voegen we het motoreiwit myosine-2 opgezuiverd uit spierweefsel toe aan het systeem, dat in staat is om bipolaire filamenten te vormen die de celvorm reguleren door aan actine filamenten te binden en eraan te trekken. Interessant is dat bij hoge septin concentraties de myosine activiteit wordt gestopt, terwijl deze bij lagere concentraties juist wordt versterkt, waardoor actinenetwerk vervormingen over lange afstanden mogelijk worden. Ons werk laat dus zien dat septins verschillende effecten kunnen hebben op de reorganisatie van actinenetwerken.

In cellen geeft vooral de cortex, die bestaat uit actine, stevigheid aan het celmembraan. Bovendien is de aktieve vervorming van de cortex een van de belangrijkste krachten die celvorm veranderingen genereren, inclusief celdeling. In **Hoofdstuk 7** volgen we een synthetische biologie benadering en gebruiken we de kennis uit de hoofdstukken 4-6 om een actine cortex te ontwerpen die via septins is verankert aan het lipide membraan. We combineren het vermogen van septins om aan actine en lipide membranen die PIP2 en PS bevatten te binden, om met succes septin actine filamenten te verankeren aan vlakke ondersteunde lipide lagen en aan de binnenkant van vesikels ter grootte van een cel. Met het doel de vorm van deze septin-verankerde cortexachtige structuren te controleren en meer op de structuur in de cel te laten lijken, gebruiken we een ander eiwit, Arp2/3, dat interageert met actine en vertakte actine filamenten vormt. We tonen aan dat met de aanwezigheid van dit extra eiwit, septins stervormige structuren van actine filamenten verankeren aan membranen.

Ondanks de vooruitgang in het begrijpen hoe septins interageren met belangrijke structuren die de vorm van de cel reguleren, zijn we nog lang niet in staat om ze te gebruiken voor het gecontroleerd reguleren van de vorm van synthetische cellen. In **Hoofdstuk 8** bespreken we verdere onderzoekslijnen om onze kennis van septin interacties vergroten met als uiteindelijk doel deze eiwitten te gebruiken om een synthetische cel te bouwen.

Ten slotte voeg ik een galerij toe met microscopische afbeeldingen en foto's om te illustreren dat wetenschap een prachtige discipline is, die niet alleen kan bijdragen aan verdieping van onze kennis, maar ook aan kunst.

Resumen

El mundo en el que vivimos ha sido durante mucho tiempo, y aún es, el hogar de una inmensa multitud de seres vivos: desde pequeñas bacterias y otros organismos microscópicos que escapan a nuestra visión, hasta otros más grandes como plantas, hongos y animales. A pesar de estas grandes diferencias en tamaño y apariencia, clasificamos a todas estos seres como vivos. Los científicos, incluido el autor de esta tesis, estamos cautivados por los mecanismos que sustentan la diversidad de los seres vivos, a la vez que se mantienen las características básicas que definen a estos seres como vivos. Fundamentando esta diversidad se encuentran las células. Desde células individuales que existen como organismos unicelulares hasta múltiples células que interactúan para formar organismos multicelulares, las células son la mínima unidad de vida. Las células son muy diversas, tanto dentro de un mismo organismo como entre organismos, en forma, componentes, funcionalidades y organización. A pesar de estas diferencias, todas comparten rasgos comunes: las células tienen una membrana celular que separa su interior de su exterior, poseen material genético que contiene toda la información necesaria para que la célula funcione, utilizan componentes de su entorno para alimentarse y renovarse, y son capaces de dividirse para reproducirse. Para llevar a cabo todas estas funciones, las células generan multitud de componentes: proteínas, ácidos nucleicos, lípidos, carbohidratos y otros pequeños metabolitos. Estos componentes se almacenan en el interior de la célula, convirtiéndola en un complejo reactor químico que se autosustenta con decenas de miles de reacciones interconectadas. Comprender cómo surgen los elementos comunes básicos entre las células a partir de esta compleja interacción de reacciones es la clave para entender qué es y cómo funciona la vida.

Para averiguar esto, los científicos están investigando estas reacciones dentro y fuera de las células utilizando muchos enfoques diferentes. Un enfoque interesante que surgió a principios de la década de los 2000 es la biología sintética, una disciplina que tiene como objetivo utilizar principios de ingeniería para construir sistemas biológicos. Dentro de la biología sintética, para identificar las propiedades que definen a los organismos vivos y comprender cómo funcionan las células es de especial interés la biología sintética *bottom-up*. Esta tiene como objetivo construir una célula sintética a partir de sus componentes purificados mientras investiga cómo estos componentes interactúan entre sí para mantener viva a la célula. Este enfoque minimalista utiliza la reconstitución *in vitro*, que es, en otras palabras, juntar componentes purificados fuera de una célula viva para simplificar sistemas celulares de interés, lo que permite una comprensión más profunda de su funcionamiento y ayuda a identificar los componentes y funciones necesarios.

Con este objetivo, el consorcio neerlandés "BaSyC - Building a Synthetic Cell" pretende construir una célula sintética con una estrategia *bottom-up*. El trabajo presentado en esta tesis forma parte de este proyecto y tiene como objetivo trabajar en el diseño de un mecanismo que controle la forma de la célula sintética, con especial énfasis en un mecanismo de

división celular sintética. Para lograr este objetivo nos inspiramos en células animales por dos razones principales: (1) para simplificar el mecanismo de control de la forma celular al evitar la necesidad de construir una pared celular y (2) para aprender más sobre cómo las células animales controlan su forma, ya que esto es más relevante para la fisiología y patología humana.

Se sabe que detrás del control de la forma de la célula animal está la interacción de la membrana con el citoesqueleto, una red de proteínas que forman filamentos compuesta por filamentos de actina, microtúbulos, filamentos intermedios y septinas. Las septinas, uno de los componentes menos estudiado del citoesqueleto y que participa en migración y división celular, son proteínas que forman filamentos a partir de complejos más pequeños compuestos por seis (complejos hexaméricos) u ocho (complejos octaméricos) septinas. Para que las septinas lleven a cabo sus funciones, sus interacciones con microtúbulos, la membrana celular y filamentos de actina son de vital importancia. Curiosamente, estos tres componentes son elementos clave para la división y el control de la forma celular. Por esta razón, creemos que las septinas son un buen candidato para orquestar la coreografía entre esos componentes durante el control de la forma y la división de una célula sintética. Desafortunadamente, la comunidad científica no sabe lo suficiente sobre cómo interactúan las septinas con estos componentes celulares, por lo que no podemos utilizar principios de ingeniería para diseñar este mecanismo de control de la forma celular. En consecuencia, el objetivo de esta tesis es investigar las propiedades básicas (o BaSyCas) de las interacciones de las septinas con los microtúbulos, la membrana lipídica y los filamentos de actina utilizando reconstitución *in vitro*.

En el **Capítulo 1** de esta tesis, profundizamos en la biología sintética *bottom-up* y el papel de la membrana celular y el citoesqueleto en el control de la forma de las células animales. Esto lo hacemos centrándonos en la importancia de las interacciones de las septinas en el control de la forma celular y en cómo utilizarlas para construir la célula sintética.

Para utilizar las septinas para reconstitución *in vitro*, primero debemos purificarlas. En el **Capítulo 2** detallamos el protocolo que usamos para purificar los complejos de septinas expresados en la bacteria *Escherichia coli* utilizando una estrategia de cromatografía de afinidad de dos pasos. Los protocolos de purificación de proteínas pueden variar mucho en el rendimiento y en la correcta funcionalidad de la proteína, por lo que utilizamos un conjunto de técnicas para determinar la integridad y la calidad de las septinas purificadas, que también se detalla en el mismo capítulo.

En el **Capítulo 3** investigamos las interacciones de las septinas y los microtúbulos usando una combinación de bioinformática, experimentos en células y reconstitución *in vitro* para encontrar y validar la región de las septinas que se une a los microtúbulos. Tras los análisis vimos que este dominio solo está presente en el principio de una septina específica, la SEPT9. Sabiendo esto, examinamos cómo los complejos de septina hexamérica, que no tienen SEPT9, y los complejos de septina octamérica con la SEPT9 completa, más corta o mutada interactúan con los microtúbulos. Gracias a esto vimos que la SEPT9 tiene dos dominios que regulan la interacción con los microtúbulos, el dominio que encontramos con bioinformática que permite la unión y afecta la dinámica de polimerización de los microtúbulos, y otra región en el interior de SEPT9 que modula esta interacción al reducir la afinidad de unión.

En los **Capítulos 4 y 5** nos enfocamos en las interacciones de las septinas con las membranas lipídicas. En el **Capítulo 4** analizamos la interacción de las septinas con un modelo específico de membranas lipídicas, bicapas lipídicas sostenidas, en las que las membranas lipídicas están unidas y apoyadas por una superficie sólida. Utilizamos un enfoque multitécnico para investigar qué controla la unión de la septina a la membrana y vimos que las septinas requieren el lípido fosfatidilinositol 4,5-bifosfato (PIP2) para unirse a las membranas, mientras que el lípido fosfatidilserina (PS) tiene un efecto sinérgico en la unión a la membrana, probablemente debido a su carga negativa. También encontramos que las septinas se unen a la membrana formando redes en manojos o redes en filamentos dependiendo de la longitud del complejo de septinas y de otras condiciones ambientales, en particular, la presencia de la molécula GTP y las propiedades de la membrana lipídica. Finalmente, usamos simulaciones computacionales para comprender mejor este proceso e identificar que la formación de la red de septinas se basa en el crecimiento, el emparejamiento y la alineación de filamentos. En el **Capítulo 5** utilizamos una membrana lipídica más parecida a la de una célula usando vesículas esféricas del tamaño de una célula. Poniendo las septinas dentro de la vesícula, replicamos y validamos nuestras conclusiones de que la unión de la septina a la membrana requiere lípidos PIP2 y se potencia sinérgicamente con lípidos PS. En estas condiciones, la membrana de la vesícula queda lisa y esférica. Por el contrario, cuando las septinas se encuentran en el exterior de las vesículas, deforman las membranas formando protuberancias uniformemente esparcidas en la superficie de la vesícula, similar a una pelota de golf. Esto sugiere que las septinas detectan la curvatura de la membrana y pueden deformar las membranas si no encuentran su curvatura preferida.

En el **Capítulo 6** investigamos las interacciones de la septina con los filamentos de actina y vimos que los complejos de septina son capaces de juntar los filamentos de actina formando manojos apretados de filamentos de actina en altas concentraciones mientras que simplemente hacen conexiones entre los filamentos en concentraciones más bajas. Curiosamente, los complejos de septina octamérica hacen esto en concentraciones mucho más bajas que los complejos de septina hexámera. Después agregamos al sistema la proteína motora miosina muscular de tipo 2, que es capaz de formar filamentos bipolares que pueden unirse a los filamentos de actina y tirar de ellos para reorganizarlos, por lo que son importantes para el control de la forma celular. Curiosamente, a altas concentraciones de septina, la actividad de la miosina se detuvo, mientras que a bajas concentraciones, las septinas favorecieron la reorganizacion de la red de actina a largo alcance, lo que demuestra que las septinas pueden tener diferentes efectos en la reorganización de las redes de actina.

En las células, el córtex celular es una importante estructura hecha de filamentos de actina que se considera el principal reforzador de la membrana celular. Además, su remodelación es una de las principales fuerzas que generan cambios en la forma de las células, incluida la división celular. En el **Capítulo 7** utilizamos un enfoque de biología sintética y usamos el conocimiento adquirido en los capítulos del 4 al 6 para diseñar un córtex de actina anclado a la membrane simplemente por septinas. Para ello, combinamos la capacidad de las septinas para unirse a actina y membranas lipídicas que contienen PIP2 y PS para hacer que la septina ancle los filamentos de actina a capas lipídicas sostenidas y al interior de vesículas del tamaño de una célula. Con el objetivo de ajustar la forma del córtex anclado por septina, incluimos otra proteína, Arp2/3, que interactúa con la actina formando filamentos de actina ramificados. En la presencia de esta proteína, las septinas anclan matrices radiales de actina, o ásteres, a las membranas.

A pesar de los avances en la comprensión de cómo interactúan las septinas con estructuras importantes que modulan la forma celular, todavía estamos lejos de poder utilizarlas para controlar la forma de células sintéticas. En el **Capítulo 8** exploramos otras líneas de investigación para aumentar nuestro conocimiento de las interacciones de las septinas con el objetivo final de utilizar estas proteínas para crear una célula sintética.

Finalmente, incluyo una galería de imágenes microscópicas y otras fotografías para ilustrar cómo la ciencia es una hermosa disciplina que no solo puede contribuir a profundizar nuestro conocimiento sino también al arte.

Resum

El món on vivim ha estat durant molt de temps, i encara és, la llar d'una immensa multitud d'éssers vius: des de petits bacteris i altres organismes microscòpics que escapen a la nostra visió, fins a d'altres de més grans com plantes, fongs i animals. Tot i aquestes grans diferències en grandària i aparença, classifiquem tots aquests éssers com a vius. Els científics, inclòs l'autor d'aquesta tesi, estem captivats pels mecanismes que sustenten la diversitat dels éssers vius, mentres es mantenen les característiques bàsiques que defineixen aquests éssers com a vius. Fonamentant aquesta diversitat es troben les cèl·lules. Des de cèl·lules individuals que existeixen com a organismes unicel·lulars fins a múltiples cèl·lules que interactuen per formar organismes multicel·lulars, les cèl·lules són la mínima unitat de vida. Les cèl·lules són molt diverses, tant dins un mateix organisme com entre organismes, en forma, components, funcionalitats i organització. Tot i aquestes diferències, totes comparteixen característiques comuns: les cèl·lules tenen una membrana cel·lular que separa el seu interior del seu exterior, tenen un material genètic que conté tota la informació necessària per a que la cèl·lula funcioni, utilitzen components del seu entorn per alimentar-se i renovar-se, i són capaçes de dividir-se per reproduir-se. Per dur a terme totes aquestes funcions, les cèl·lules generen una gran multitud de components: proteïnes, àcids nucleics, lípids, glúcids i altres petits metabòlits. Aquests components s'emmagatzemen a l'interior de la cèl·lula, i la converteixen en un complex reactor químic que s'autosustenta amb desenes de milers de reaccions interconnectades. Comprendre com sorgeixen els elements comuns entre les cèl·lules a partir d'aquesta interacció complexa de reaccions és la clau per entendre què és i com funciona la vida.

Per entendre-ho, els científics estan investigant aquestes reaccions dins i fora de les cèl·lules utilitzant molts punts de vista diferents. Un enfocament interessant que va sorgir a principis de la dècada dels 2000 és la biologia sintètica, una disciplina que té com a objectiu utilitzar principis d'enginyeria per construir sistemes biològics. Dins de la biologia sintètica, per identificar les propietats que defineixen els organismes vius i comprendre com funcionen les cèl·lules, és especialment interessant la biologia sintètica *bottom-up*. Aquesta té com a objectiu construir una cèl·lula sintètica a partir dels seus components purificats mentre investiga com aquests components interactuen entre si per mantenir viva la cèl·lula. Aquesta estratègia minimalista utilitza la reconstitució *in vitro*, que és, en altres paraules, combinar components purificats fora d'una cèl·lula viva per simplificar sistemes cel·lulars d'interès, cosa que permet una comprensió més profunda del seu funcionament i ajuda a identificar els components i funcions necessaris.

Amb aquest objectiu, el consorci neerlandès "BaSyC - Building a Synthetic Cell" pretén construir una cèl·lula sintètica amb una estratègia *bottom-up*. L'estudi presentat en aquesta tesi forma part d'aquest projecte i té com a objectiu treballar en el disseny d'un mecanisme que controli la forma de la cèl·lula sintètica, amb un èmfasi especial en un mecanisme de divisió cel·lular sintètica. Per assolir aquest objectiu ens inspirem en cèl·lules animals per

dues raons principals: (1) per simplificar el mecanisme de control de la forma cel·lular ja que evitariem la necessitat de construir una paret cel·lular i (2) per aprendre més sobre com les cèl·lules animals controlen la seva forma, ja que això és rellevant per a la fisiologia i patologia humana.

Sabem que darrere del control de la forma de la cèl·lula animal trobem la interacció de la membrana amb el citoesquelet, una xarxa de proteïnes que formen filaments composta per filaments d'actina, microtúbuls, filaments intermedis i septines. Les septines, un dels components menys estudiat del citosquelet i que participa en migració i divisió cel·lular, són proteïnes que formen filaments a partir de complexos més petits compostos per sis (complexos hexamèrics) o vuit (complexos octamèrics) septines. Per a que les septines duguin a terme les seves funcions, les interaccions amb microtúbuls, la membrana cel·lular i filaments d'actina són de vital importància. Curiosament, aquests tres components són elements clau per a la divisió i el control de la forma cel·lular. Per això creiem que les septines són un bon candidat per orquestrar la coreografia entre aquests components durant el control de la forma i la divisió d'una cèl·lula sintètica. Malauradament, la comunitat científica no sap suficient sobre com interactuen les septines amb aquests components cel·lulars, per tant, no podem utilitzar principis d'enginyeria per dissenyar aquest mecanisme de control de la forma cel·lular. En conseqüència, l'objectiu d'aquesta tesi és investigar les propietats bàsiques (o BaSyCas) de les interaccions de les septines amb els microtúbuls, la membrana lipídica i els filaments d'actina utilitzant reconstitució *in vitro*.

Al **Capítol 1** d'aquesta tesi, aprofundim en la biologia sintètica *bottom-up* i el paper de la membrana cel·lular i el citoesquelet en el control de la forma de les cèl·lules animals. Això ho fem centrant-nos en la importància de les interaccions de les septines en aquest control i en com utilitzar-les per construir la cèl·lula sintètica.

Per utilitzar les septines per a reconstitució *in vitro*, primer les hem de purificar. Al **Capítol 2** detallem el protocol que utilitzem per purificar els complexos de septines expressats al bacteri *Escherichia coli* utilitzant una estratègia de cromatografia d'afinitat de dos passos. Els protocols de purificació de proteïnes poden variar molt en rendiment i correcta funcionalitat de la proteïna, per la qual cosa utilitzem un conjunt de tècniques per determinar la integritat i la qualitat de les septines purificades, que també es detalla en el mateix capítol.

Al **Capítol 3** investiguem les interaccions de les septines i els microtúbuls utilitzant una combinació de bioinformàtica, experiments en cèl·lules i reconstitució *in vitro* per trobar i validar la regió de les septines que s'uneix als microtúbuls. Amb aquest anàlisis vam veure que aquest domini només és present al principi d'una septina específica, la SEPT9. Sabent això, examinem com els complexos de septina hexamèrica, que no tenen SEPT9, i els complexos de septina octamèrica amb la SEPT9 completa, més curta o mutada interactuen amb els microtúbuls. Gràcies a això vam veure que la SEPT9 té dos dominis que regulen la interacció amb els microtúbuls, el domini trobat amb bioinformàtica que permet la unió i afecta la dinàmica de polimerització dels microtúbuls, i una altra regió a l'interior de la SEPT9 que modula aquesta interacció reduir l'afinitat d'unió.

Als **Capítols 4 i 5** ens enfoquem en les interaccions de les septines amb les membranes lipídiques. Al **Capítol 4** analitzem la interacció de les septines amb un model específic de membranes lipídiques, bicapes lipídiques sostingudes, en què les membranes lipídiques unides i sostingudes per una superfície sòlida. Vam utilitzar un enfocament multitècnic per investigar què controla la unió de la septina a la membrana i vam veure que requereixen el lípid fosfatidilinositol 4,5-bifosfat (PIP2) per unir-se a les membranes, mentre que el lípid fosfatidilserina (PS) té un efecte sinèrgic en la unió a la membrana, probablement a causa de la seva càrrega negativa. També trobem que les septines s'uneixen a la membrana formant xarxes en feixos o xarxes en filaments depenent de la longitud del complex de septines i altres condicions ambientals, en particular, la presència de la molècula GTP i les propietats de la membrana lipídica. Finalment, fem servir simulacions computacionals per comprendre millor aquest procés i identificar que la formació de la xarxa de septines es basa en el creixement, l'aparellament i l'alineació de filaments. Al **Capítol 5** utilitzem una membrana lipídica més semblant a la d'una cèl·lula utilitzant vesícules esfèriques de la mida d'una cèl·lula. Posant les septines dins de la vesícula, repliquem i validem les nostres conclusions que la unió de la septina a la membrana requereix lípids PIP2 i es potencia sinèrgicament amb lípids PS. En aquestes condicions, la membrana de la vesícula queda llisa i esfèrica. Per contra, quan les septines es troben a l'exterior de les vesícules, deformen les membranes formant protuberàncies uniformement distribuïdes a la superfície de la vesícula, com en una pilota de golf. Això suggereix que les septines detecten la curvatura de la membrana i poden deformar les membranes si no troben la seva curvatura preferida.

Al **Capítol 6** investiguem les interaccions de la septina amb els filaments d'actina i veiem que els complexos de septina són capaços d'reunir els filaments d'actina formant feixos compactes de filaments d'actina en altes concentracions mentre que simplement fan connexions entre els filaments en concentracions més baixes. Curiosament, els complexos de septina octamèrica fan això en concentracions molt més baixes que els complexos de septina hexamèrica. Al afegir la proteïna motora miosina muscular 2, que és capaç de formar filaments bipolars que poden unir-se als filaments d'actina i estirar-los per reorganitzar-los, per la qual cosa són importants per al control de la forma cel·lular. Curiosament, a altes concentracions de septina, l'activitat de la miosina s'aturar, mentre que a baixes concentracions, les septines favoreixen la reorganització de la xarxa d'actina a llarga distància, cosa que demostra que les septines poden tenir diferents efectes en la reorganització de xarxes d'actina.

A les cèl·lules, el còrtex cel·lular és una important estructura feta de filaments d'actina que es considera el principal reforçador de la membrana cel·lular. A més, la seva remodelació és una de les principals forces que generen canvis en la forma de les cèl·lules, inclosa la divisió cel·lular. Al **Capítol 7** utilitzem un enfocament de biologia sintètica i fem servir el coneixement adquirit als capítols del 4 al 6 per dissenyar un còrtex d'actina ancorat a la membrane simplement per septines. Per això, combinem la capacitat de les septines per unir-se a actina i membranes lipídiques que contenen PIP2 i PS per fer que la septina ancli els filaments d'actina a capes lipídiques sostingudes i a l'interior de vesícules de la mida d'una cèl·lula. Amb l'objectiu d'ajustar la forma d'aquest còrtex ancorat per septina, incloem una altra proteïna, Arp2/3, que interactua amb l'actina formant filaments d'actina ramificats. Amb la presència d'aquesta proteïna, les septines ancoren matrius radials d'actina, o àsters, a les membranes.

Tot i els avenços en la comprensió de com interactuen les septines amb estructures importants que modulen la forma cel·lular, encara estem lluny de poder utilitzar-les per controlar la forma de cèl·lules sintètiques. Al **Capítol 8** explorem altres línies d'investigació per augmentar el nostre coneixement de les interaccions de les septines amb l'objectiu final d'utilitzar aquestes proteïnes per crear una cèl·lula sintètica.

Finalment, incloc una galeria d'imatges microscòpiques i altres fotografies per il·lustrar com la ciència és una bonica disciplina que no només pot contribuir a aprofundir el nostre coneixement sinó també a l'art.

Contents

Chapter 1
Introduction

The cell is the minimal living building block of life, and it forms from the simplest bacteria to the most complex multicellular organisms. Cells are complex and diverse, but all fulfill, in one way or another, specific basic functions like growing and dividing. Although cells have been researched since their first observation four centuries ago, we still do not understand how they work. With the aim of understanding cellular functions, scientists aim to build a synthetic cell from their purified components. In this thesis, we explore the possibility of designing a mechanism that supports and controls the shape of such synthetic cells, leading ultimately to a synthetic cell division, taking the mechanism used by animal cells as inspiration. The coordination between crucial cell components such as the cell membrane, the actin cortex, and microtubules, is a challenge that we must tackle to design an animal cell-inspired cell shape control mechanism. This chapter serves as an introduction to synthetic biology and to the components that control cell shape in animal cells. Then we detail our motivation of why septins, the fourth component of the cytoskeleton, are a good candidate to mediate the crosstalk between the cell membrane, actin, and microtubules. Finally, we explain the strategy used in the rest of this thesis to learn more about these interactions, with the ultimate goal of building a synthetic cell.

1

1.1. The complexity of the cell

Throughout history, humans have been captivated by the complexity and diversity of life, inspiring countless attempts to understand and classify the natural world. From the early taxonomic systems of Aristotle to the modern molecular methods of genomics, the study of life has evolved and expanded to encompass a vast array of disciplines and subfields. The discovery of the cell was a pivotal moment in the history of biology [1]. Being considered the basic building block of life, this discovery forever changed the way we view and understand living organisms. The first observations of cells were made possible by the invention of the microscope in the 17th century [1]. They revealed a remarkable diversity in size, shape, structure, and organization: from tiny round, elongated or even spiraling bacteria to giant and complex multicellular organisms made of a huge diversity of cell types. Despite this diversity, all cells share common features, such as a plasma membrane that encloses the cell and regulates the passage of molecules in and out of the cell, a set of genetic material that contains the instructions for the cell's functions, the presence of a crowded cytoplasm where most chemical reactions that maintain the cell alive occur, and their ability to divide in order to reproduce [2].

It is currently clear that in order to understand life, it is essential to understand the workings of its minimal expression, the cell. Simple observation of the cell and its inner workings using microscopes was the earliest method used (such as the first description of mitosis by Walther Flemming [3]). Developments in microscopy and biochemistry have made it possible to even observe single molecules at work within the cell, which is a useful way to study how certain components of the cell work together [2, 4, 5]. Cells can also be studied by altering their functions, either via mutagenesis or by the use of drugs, to reveal the roles of specific components in the cell [2]. The advent of systems biology allowed scientists to model the complex interactions and emergent properties of biological systems at different levels of organization, from molecules to organisms, using computational and mathematical tools [6]. An alternative approach consists of getting rid of the cell itself and use purified components to create simplified versions of specific cellular processes in order to study them in isolation [7, 8]. These approaches have all contributed to our current understanding of the complexity of life at the cellular level.

1.2. Synthetic biology

1.2.1. Bottom-up synthetic biology

Despite the progress made in the study of cells, understanding the basic properties of life remains a significant challenge due to the complexity and diversity of cells. To address this challenge, a growing community of scientists are attempting to create a minimal cell that can exhibit the essential characteristics of life, in what is known as a new discipline in biology: synthetic biology. This can be achieved through two different approaches: **top-down**, which involves removing non-essential components from a cell to determine the minimum set of genes required for life, and **bottom-up**, which involves building a cell from scratch using individual components [9–12].

The bottom-up approach is proving to be a powerful tool in understanding the basic principles of life and the workings of cells. Based on *in vitro* reconstitution, the bottom-up approach consists of building minimal systems by combining purified components to investigate which components and interactions are essential for life. By carefully controlling the composition of these minimal systems, and investigating how these components interact to produce life-defining properties, scientists can gain insights into how complex cellular behaviors emerge from simple molecular interactions. Through this bottom-up approach, researchers are able to investigate the fundamental properties of life and identify the core mechanisms that underlie cellular function [7, 10, 13].

An additional advantage of synthetic cells is their potential to be designed to carry out specific functions with greater efficiency than natural organisms. While it is possible to modify natural organisms to perform desired functions [14], this can be a challenging and inefficient process due to the complexity of biological systems. Synthetic cells, on the other hand, can be designed from the bottom-up to precisely incorporate the components necessary for a given function. This level of control over the design of biological systems holds great promise for fields such as biotechnology, where engineered cells can be used to produce valuable products or perform specific tasks [15, 16].

1.2.2. Modules of a synthetic cell

One bottom-up effort to build a synthetic cell is being pursued in The Netherlands by the "BaSyC - Building a Synthetic Cell" consortium (basyc.nl [17]), in which the work of this thesis is embedded. BaSyC is a research program led by more than 17 scientists from six Dutch universities and research institutes that aims to build an autonomous and self-reproducing synthetic cell using bottom-up reconstitution. BaSyC aims to build a synthetic cell by first studying in isolation the different systems, or modules, that a cell needs. These modules are divided in 3 groups (Fig. 1.1):

1. **Cell fueling:** the cell fueling module aims to understand how cells obtain and utilize energy to carry out their essential functions. This involves studying the various metabolic pathways involved in energy production and consumption within cells. The goal is to identify and reconstitute key regulatory mechanisms such as energy regeneration, metabolite synthesis, volume and pH homeostasis, and lipid synthesis for cell growth.

2. **DNA processing:** the DNA processing module is focused on studying the fundamental processes of DNA replication, transcription, and translation to understand the mechanisms by which genetic information is transferred from DNA to RNA to proteins. Additionally, the goal is to understand how to assemble genetic networks to regulate gene expression in the synthetic cell.

3. **Cell division:** The cell division module focuses on understanding the principles of cell division and how they can be implemented in synthetic cells. This includes the study of the molecular machinery involved in cell division, the regulation of the process, and the spatiotemporal organization of the cell during division.

While the mentioned modules focus on studying the design and engineering of the basic functionalities of the synthetic cell, BaSyC also includes two additional research-focused

1

modules aimed at achieving integration and autonomy (Fig. 1.1, right). The **spatio-temporal integration** module aims to integrate the core modules and develop strategies for spatio-temporal control. The **autonomy** module tries to tackle the synthetic cell autonomy by synthesizing the synthetic cell genome encoding all the information necessary to put together the other modules. Following this strategy, the ultimate goal is to synthesize a chromosome that encodes all the necessary molecules to perform the described functions and to encapsulate it inside a cell-sized vesicle together with an *in vitro* transcription/translation machinery to create the synthetic cell.

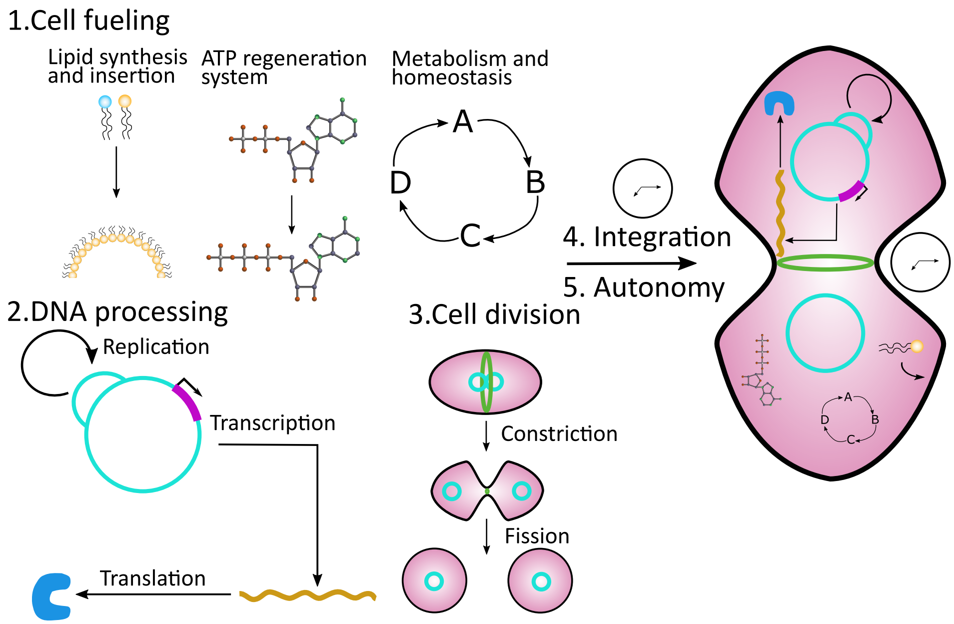

Figure 1.1. Strategy of the BaSyC consortium to build a synthetic cell. Schematic representation of the strategy of the research-based part of the BaSyC consortium. Basically, the research work is divided in 5 modules: cell fueling, to reconstitute the metabolism of the cell, DNA processing, to reconstitute genetic expression, cell division, to reproduce the cell, integration, to combine and give spatio-temporal control, and autonomy, to encode all the necessary information in a single genome that the synthetic cell can use.

1.3. Shaping and dividing cells

One important aspect to consider in the design of the synthetic cell, which is directly related to the cell division module, is the maintenance and control of changes of the cell's shape. Many cells, such as bacteria, archaea, fungi, and plants, maintain their shape and even regulate specific cell changes, such as cell division, through the cell wall, a rigid layer of polysaccharides and/or proteins that surrounds the cell membrane [18–20]. The cell wall can be difficult to reconstitute in a synthetic cell because it requires specific enzymes and substrates. For instance, the bacterial cell wall requires peptidoglycan synthases, which are enzymes that link sugar and amino acid units to form the peptidoglycan polymer, as well as membrane-bound glycosidases, which are enzymes that cleave the peptidoglycan to allow for its insertion and remodeling [21]. Therefore, the most common strategies to maintain and reshape the synthetic cell try to do it cell wall-free.

As animal cells lack a cell wall [22, 23], they are an interesting model to inspire a cell-wall-free mechanism to mechanically support and reshape synthetic cells. The research outlined in this thesis aims to investigate how the cytoskeleton of animal cells, especially the septin cytoskeleton, can be utilized to provide mechanical support and actively shape synthetic cells, with a particular emphasis on developing an animal cell-inspired cell division mechanism.

1.3.1. The cell membrane

The cell membrane is a vital structure that encloses the contents of a cell, separating the interior from the external environment. The cell membrane is selectively permeable, meaning that it allows certain molecules to pass through while preventing others from crossing the membrane. Therefore, it plays a crucial role in maintaining the integrity of the cell, controlling the exchange of materials between the cell and its surroundings, and enabling communication with other cells [2].

The plasma membrane is primarily composed of phospholipids, which consist of a hydrophilic polar headgroup and two hydrophobic hydrocarbon chains, or tails. Their amphiphilic nature causes them to spontaneously self-assemble in aqueous solutions to minimize the hydrophobic surface area exposed to water. In the cell membrane, the phospholipids are arranged tail-to-tail, forming a bilayer (Fig. 1.2). Cell membranes contain a vast array of phospholipid species that vary in both their polar headgroups and the length and saturation of their tails. The composition of these phospholipid species and their prevalence in the plasma membrane differ among cell types and also between the inner and outer leaflets of the lipid bilayer [24, 25]. For instance, among the most abundant phospholipids in the cell membrane, phosphatidylcholine (PC), phosphatidylethanolamine (PE), phosphatidylserine (PS), and sphingomyelin (SM), PC and SM are mainly found in the outer leaflet, facing the extracellular environment, while PE and PS are mainly found in the inner leaflet, facing the cytoplasm [25–28]. The cell membrane also has signaling lipids, such as phosphoinositides (PI), which recruit or activate proteins, eicosanoids, which regulate ion channels and other proteins, and sphingolipids, which act as signals to regulate different cell process [29].

In addition to phospholipids, the cell membrane also contains other types of lipids, such as cholesterol, which helps to stabilize the membrane, and glycolipids, which are important for cell recognition and signaling. Proteins are also embedded in the lipid bilayer, serving a variety of functions such as transport of molecules across the membrane, cell signaling, and structural support. The organization of lipids and proteins within the membrane is not uniform, but rather arranged in functional domains or patches that contribute to membrane function [30, 31].

The cell membrane, being only about ~6nm thick, is highly deformable and mechanically fragile, yet it plays a crucial role in maintaining cellular integrity and shape during vital functions such as cell division, migration, and morphogenesis [32]. To balance the requirements of mechanical protection and deformability, cells need to maintain a delicate

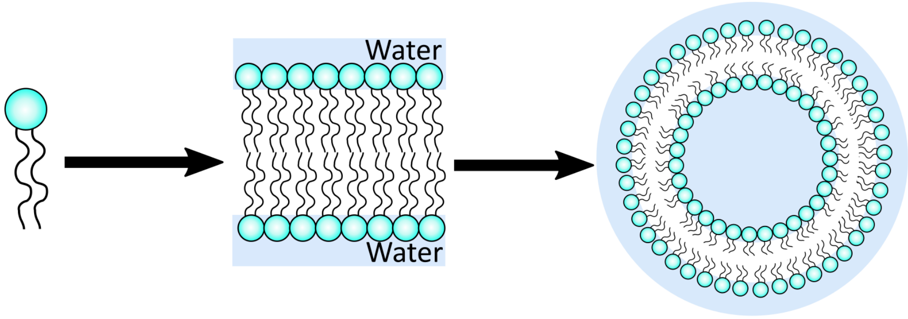

Figure 1.2. Formation of lipid bilayers from phospholipids. Phospholipids (left) arrange in two layers, leaving the heads in contact with the aqueous solution and the tails towards each other (centre). When this lipid bilayer arranges into a sphere, it forms a vesicle (right), the basic container of a synthetic cell. Aside from this lipid bilayer, the plasma membrane of a cell also contains proteins, other classes of lipids, and carbohydrate chains.

balance between rigidity and deformability [33]. Overly rigid cells are brittle and susceptible to fracture under stress, while overly flexible cells cannot generate the forces necessary to maintain or alter their shape [34]. To achieve the necessary balance, cells contain a supportive network to regulate their shape and reinforce membrane mechanics, allowing for controlled and precise changes to the membrane topography, which in animal cells is the cytoskeleton.

1.3.2. The cytoskeleton

The mechanical support of animal cells is provided by the cytoskeleton, a network of protein filaments that runs throughout the cell's cytoplasm with connections to the plasma membrane. The cytoskeleton provides mechanical resistance to deformation, while also allowing for cell shape changes to drive cell movement and division. There are four main types of cytoskeletal filaments: actin filaments, microtubules, intermediate filaments, and septins, each with its unique properties and functions in maintaining cell shape and mechanics. Below follows a brief descriptions of each filament type.

Actin filaments

Actin filaments (F-actin) are thin, semiflexible protein fibers that are part of the cytoskeleton of animal (and other *Eukaryotic*) cells. They are composed of actin protein monomers (G-actin) that polymerize to form long, double-helical filaments that are typically 7-9 nanometers in diameter [35, 36]. Actin filaments are involved in a variety of cellular processes, including cell division, cell movement, and maintenance of cell shape. They are also involved in intracellular transport, cell signaling, and the formation of specialized cell surface structures such as microvilli and stereocilia.

The polymerization process [37] follows a nucleation-and-growth pathway in which four monomers must form a stable seed complex before filament growth can begin [38] (Fig 1.3). Since the formation of seeds is energetically unfavorable compared to staying in the form of G-actin, nucleation serves as the rate-limiting step in actin polymerization, allowing cells to control when and where actin assembles via regulatory proteins. Once a seed/filament is formed, it has a pointed end (minus-end) and a barbed end (plus-end). While new monomers can in principle be added to both ends, the two ends have different affinities. In the presence of adenosine triphosphate (ATP), the concentration at which actin monomers can bind to a filament is lower for the barbed end than the pointed end. Therefore, as the seeds grow into filaments, the pointed end eventually stops growing and starts to depolymerize, while the barbed end continues to grow. When the speed of pointed-end depolymerization matches the speed of barbed-end polymerization, net actin polymerization is zero, and filaments are said to "treadmill". *In vitro*, the process of

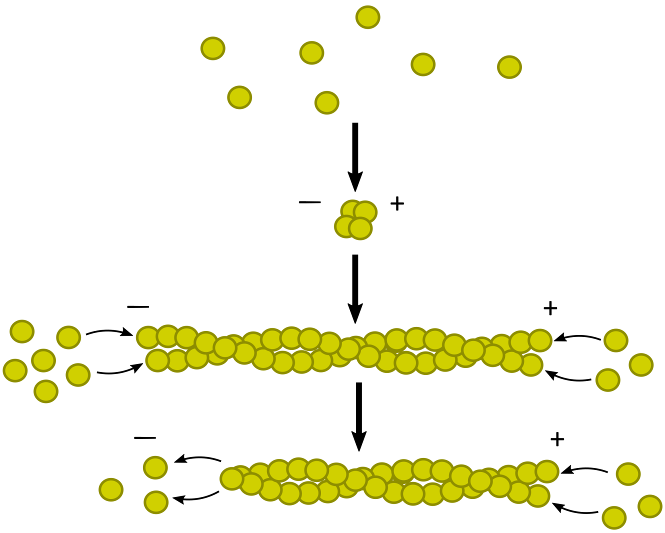

Figure 1.3. Polymerization of actin filaments. Single actin monomers (G-actin) first form a seed in the rate limiting-step of the polymerization process. After the seed is formed, monomers can be added to the both plus- and minus-end, as indicated by the + and - signs in the schematic. In longer filaments, the minus-end starts to depolymerize while the plus-end keeps polymerizing, leading to treadmilling.

actin polymerization can be induced by manipulating the environment around monomeric actin [39]. Specifically, when globular actin (G-actin) is dissolved in a buffer with low ionic strength, it is stabilized in solution by a charged hydration layer. However, when salt is added to the solution, the resulting buffer, which has a higher ionic strength, disrupts the hydration layer, allowing the monomers to approach each other closely enough to form stable seeds. These seeds then trigger filament formation.

In cells, however, this process need to be precisely controlled, to trigger actin polymerization where and whenever needed. This is done using actin binding proteins (ABPs). Specifically, proteins such as profilin sequester the actin monomers to inhibit their polymerization and avoid spontaneous polymerization [40]. When actin needs to be polymerized, specific actin nucleators, mainly formin, which nucleates long and linear actin filaments, and Arp2/3, which nucleates short and branched actin filaments, produce the actin filaments [41].

Other ABPs control the higher-order structures that actin filaments form, including disordered networks (with α-actinin [42]), parallel or antiparallel filament bundles (with fascin, filamin, or fimbrin [42, 43]), and even curved bundles and rings (with IQGAP or anillin [44, 45]). The lengths of actin filaments are regulated by a multitude of other ABPs such as capping protein, tropomyosin, and severing proteins like cofilin and gelsolin. The resulting actin networks can be remodeled by the motor protein myosin-2, a protein which forms bipolar filaments that can move along single actin filaments and slide actin filaments past each other [43].

Using these ABPs, the actin cytoskeleton forms various types of structures within the cell, such as stress fibers, the cell cortex, and filopodia and lamellipodia, to perform a diverse array of functions. Stress fibers are contractile bundles of actin filaments that generate mechanical tension, which are important for cell adhesion, migration, and differentiation [46]. The cell cortex, a thin and dense actin-based network found underneath the plasma membrane, is involved in cell shape maintenance, cell division, and membrane trafficking [47]. Filopodia and lamellipodia are finger-like and sheet-like protrusions, respectively, that are involved in cell motility and sensing the extracellular environment [48].

Of special interest for the maintenance and reshaping of the cell and the cell membrane is the actin cortex. This is a highly organized network of actin filaments located underneath the plasma membrane and anchored to it, creating a shell-like structure. The cortical actin network is highly dynamic and is continuously remodeled to adapt to the cell's changing needs. The network can be remodeled through various mechanisms, such as nucleation and branching of new actin filaments, severing of existing filaments, crosslinking of filaments with different orientations, and active remodeling through myosin motors. The cortical actin network also interacts with other cellular components, such as membrane-bound proteins and organelles, to regulate their localization and function. For instance, the cortex plays a crucial role in cell division by organizing the mitotic spindle and forming the contractile ring that drives cytokinesis [47, 49].

Microtubules

Microtubules, essential components of the eukaryotic cytoskeleton, are dynamic and tubular structures formed by the polymerization of α- and β-tubulin subunits. These cylindrical filaments have an approximate diameter of 25nm and extend throughout the cell, providing structural support and participating in various cellular functions [50]. Microtubules are crucial for cell division, and play important roles in cell motility, cell shape maintenance, intracellular signaling, and the formation of specialized structures like cilia and flagella [51, 52].

Microtubules polymerize through nucleation and elongation processes (Fig. 1.4). Polymerization starts with the formation of a stable seed structure that serves as a template for the addition of α- and β-tubulin dimers that arrange into protofilaments. Typically 13 of these protofilaments assemble side-by-side to create a hollow tubular structure. Further addition of tubulin subunits allows the microtubule to elongate [53, 54]. Similarly as actin filaments, microtubules are structurally polar, with the plus end growing faster than the minus end [55]. Microtubule polymerization is facilitated by the hydrolysis of guanosine triphosphate (GTP), which is bound to the β-tubulin subunits. GTP-bound tubulin dimers are more likely to incorporate into the growing microtubule, while GDP-bound tubulin dimers are more likely to dissociate. As the microtubule elongates, GTP molecules bound to the tubulin dimers are gradually hydrolyzed to GDP. Once the concentration of GDP-bound tubulin reaches a critical threshold, a catastrophe event occurs, resulting in rapid disassembly or shrinkage of the microtubule. Following catastrophe, there can be a rescue event where new GTP-bound tubulin subunits are incorporated, allowing the microtubule to regrow. This stochastic alternation between growing and shrinking phases is what characterizes microtubules, and is termed dynamic instability [56–58].

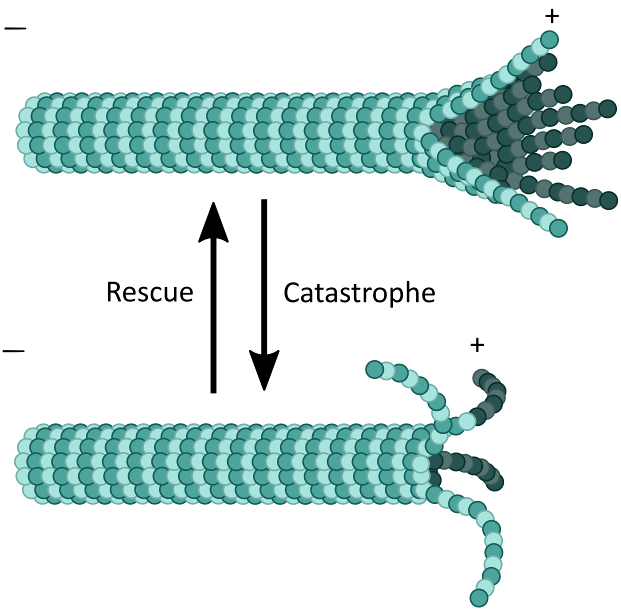

Figure 1.4. Dynamic instability of microtubules. α- and β-tubulin dimers can be added to the protofilaments of both plus- and minus-ends of microtubules with different rates, as indicated by the + and - signs in the schematic. When a catastrophe occurs, the microtubules starts to depolymerize or shrink. Tubulin dimers can be added to the protofilaments again, in a process called rescue, leading to polymerization or growth.

In vitro, microtubule dynamics are governed not only by the GTP/GDP ratio in the solution, but also by temperature and pH. Temperature influences microtubule dynamics by affecting the rate of microtubule assembly and disassembly [59]. This temperature sensitivity is primarily due to the temperature dependence of tubulin conformational changes and the strength of noncovalent interactions between tubulin subunits [60, 61]. Generally, low temperatures lead to microtubule depolymerization, intermediate temperatures lead to slow polymerization/depolymerization rates and favor microtubule stability, while higher temperatures lead to faster polymerization/depolymerization rates [59]. In general, microtubule dynamic assays in vitro are done at temperatures between 25℃ and 37℃ [62]. pH affects microtubule dynamics by affecting the ionization states of specific amino acids of the tubulin dimers, which affect tubulin-tubulin interactions [52, 63]. In general, in slightly acidic pH, microtubules exhibit increased stability and polymerization rates, while basic pH can lead to microtubule depolymerization. In general, microtubule dynamic assays *in vitro* are done at a pH around 6.9 [62]. However, other factors such as presence of small molecules and salt concentration can also affect the dynamics of microtubules *in vitro* [64].

In cells, the dynamics of microtubules are tightly regulated by centrosomes, microtubule associated proteins (MAPs) and post-translational modifications (PTMs). Centrosomes serve as the primary microtubule-organizing centers in many cells and contribute to microtubule nucleation, organization, and anchoring. They contain γ-tubulin ring complexes that initiate microtubule assembly and recruit other proteins involved in microtubule regulation [52, 65]. MAPs, such as Tau and MAP2, interact with microtubules and modulate their stability, bundling, and spacing. They can promote microtubule polymerization and cross-link microtubules to form networks [54]. PTMs, such as acetylation and detyrosination of tubulin, can also influence microtubule behavior by affecting protein-protein interactions, motor protein binding, and stability [66].

Microtubules are vital to mechanically support cells and participate in cell reshaping. Microtubules are remarkably stiff and can withstand large forces without buckling or breaking. This allows them to maintain the cell shape and integrity against external or internal stresses [67, 68]. Additionally, microtubule dynamics can create forces that push or pull on other structures, such as the plasma membrane, the nucleus, or organelles. They also interact with actin structures that form protrusive structures such as filopodia or lamellipodia, which are involved in cell migration and adhesion [69]. Finally, there are also microtubule-associated motor proteins that can generate forces that rearrange the cytoskeleton or transport cargo within the cell, which are essential for the correct formation of cilia and flagella [70, 71].

Intermediate filaments

Intermediate filaments are a type of cytoskeletal protein filament found in animal cells. They are composed of a diverse family of proteins called intermediate filament proteins (IFPs), which include keratins, vimentin, desmin, lamin, and neurofilaments, among others. The specific type of intermediate filament protein expressed in a cell depends on its tissue type and function. These proteins can form filaments with a diameter of about 10nm. Intermediate filaments are known for their high mechanical strength and provide structural support and stability to cells [72, 73].

The polymerization of intermediate filaments follows a stepwise assembly process. IFP monomers consist of a central α-helical rod domain, which provides the structural backbone, and globular head and tail domains. The monomers dimerize by aligning their rod domains in antiparellel orientations. This dimerization is facilitated by specific interactions between the head and tail domains of the monomers. The dimers then associate longitudinally to form short oligomers. These oligomers continue to assemble end-to-end through interactions between their rod domains. The polymerization process is regulated by various factors, including phosphorylation of the IFPs and the presence of chaperones and other accessory proteins [73].

Unlike actin filaments and microtubules, intermediate filaments do not have a dynamic or polarized structure. Instead, they form a stable, flexible network throughout the cell, extending from the nucleus to the cell periphery. Intermediate filaments are responsible for maintaining cell shape, resisting mechanical stress and deformation, and providing structural support to cells and tissues. They are particularly abundant in cells that experience mechanical strain, such as epithelial cells, muscle cells, and neurons. Intermediate filaments also play a role in organizing and anchoring other cellular structures, such as the nucleus and organelles [74].

Septins

Septins are a group of GTP-binding proteins that are expressed in all eukaryotic cells except higher plants [75]. About 10 years ago, they were acknowledged as the fourth component of the cytoskeleton because of their ability to assemble into 4nm thick filaments that in turn form various structures such as paired filaments, rings and gauzes [76]. Septins have various functions in cells, such as providing a scaffold for protein recruitment, forming a barrier for subcellular compartmentalization, regulating cell division, and participating in cell migration. They are also involved in host-microbe [77] interactions and in various human diseases including cancer and neurodegenerative disorders.

The septin family of proteins is divided in different subfamilies based on sequence similarity [75, 76] (Table 1.1). In animals, there are four groups, SEPT2, SEPT3, SEPT6, and SEPT7. All the septins have a GTP-binding domain that is highly conserved. On the carboxy-terminal side, there is a domain known as the septin unique element (SUE) whose function remains unknown. The N and C termini are the most variable domains in the septin sequence, and distinguish the four subfamilies. The N-terminus contains in most of the septins a proline-rich domain. However, SEPT9, a member of the SEPT3 subfamily with widespread expression, has a longer disordered N-terminus. Alternative splicing of the SEPT9 RNA generates five isoforms (SEPT9_i1 - SEPT9_i5) that exhibit differences in the translation start site [78], leading to proteins with varying lengths and N-terminal sequences. The longer isoforms of SEPT9 (i1, i2, and i3) share an extended disordered N-terminus with slight variations in length and amino acid composition. The C-terminus of all septins except the SEPT3 subfamily septins contains an extended coiled-coil (CC) domain. The SEPT2' CC is shorter than that of the SEPT6 and SEPT7 subfamily members. Finally, the SEPT7 and SEPT6 subfamilies differ in their ability to hydrolyze GTP. While all septins are able to, hydrolyze GTP into GDP albeit slowly, SEPT6 is unable to do so [79].

Table 1.1. Septin subfamilies. Overview of the septins in each subfamily and their main characteristics. From left to right: subfamily name, members of the subfamily, canonical septin of the subfamily, characteristic domain at the N-terminus, ability to hydrolyze GTP, and characteristic domain at the C-terminus.

Subfamily	Members	Canonical	N-terminus	GTP hydrolysis	C-terminus
SEPT2	SEPT1, SEPT2, SEPT4, SEPT5	SEPT2	Pro-rich	Yes	Short CC
SEPT3	SEPT3, SEPT9, SEPT12	SEPT9	Pro-rich; SEPT9 has disordered domain	Yes	No CC
SEPT6	SEPT6, SEPT8, SEPT10, SEPT11, SEPT14	SEPT6	Pro-rich	No	Long CC
SEPT7	SEPT7	SEPT7	Pro-rich	Yes	Long CC

Septin monomers longitudinally associate by interactions between two types of interfaces: the G interface, which contains the GTP-binding domain, and the NC interface, which contains the N and C termini. By interactions of interfaces of the same type, septins can form rod-shaped palindromic hetero-oligomers. The length and composition of these hetero-oligomers is species dependent, with *Caenorhabditis elegans* septins forming tetramers [80], *Drosophila melanogaster* septins forming hexamers [81], *Saccharomyces cerevisiae* septins forming octamers [82], and human septins forming both hexamers and octamers [83–85]. Septins from a specific subfamily can be substituted or replaced by another protein from the same subfamily, as suggested by the Kinoshita rule [86]. In the case of human septins, the ones studied in this thesis, the order of the septins in the hetero-oligomer, using the canonical septins from each subfamily, is SEPT2-SEPT6-SEPT7-SEPT7-SEPT6-SEPT2 for septin hexamers and SEPT2-SEPT6-SEPT7-SEPT9-SEPT9-SEPT7-SEPT6-SEPT2, for septin octamers [87, 88]. These hetero-oligomers can further longitudinally associate through the NC interfaces of the terminal SEPT2 subunits to form apolar filaments, which can, in turn, interact to form paired filaments, meshes, rings, and gauzes [76]. However, it remains poorly understood what interactions drive this self-assembly into higher order structures.

In vitro, polymerization of septin oligomers into filaments is controlled by the ionic strength of the solution [83]. The salt concentration modulates the electrostatic interactions among septin subunits, which play a crucial role in their stability and assembly processes. Under low salt conditions (<150mM KCl), septin complexes remain stable and can efficiently bind to each other, whereas under high salt conditions (>150mM KCl), the equilibrium shifts towards the oligomeric side, preventing filament formation at low septin concentrations [89].

In cells, septin polymerization regulation is poorly understood. It is known that the binding of septin to GTP or GDP is crucial for its polymerization [90]. However, the role of the nucleotide remains poorly understood. Additionally, septin PTMs can also regulate septin assembly [91]. For instance, in yeast, septin phosphorylation plays a critical role in determining the arrangement of septins at the bud neck [92, 93], and sumoylation has been identified as a regulatory mechanism that triggers the disassembly of septin rings at the bud neck [94]. In mammalian cells, sumoylation appears to prevent the formation of septin bundles that could potentially interfere with proper cell division [94]. Additionally, the interaction of septin with various cellular constituents also regulates septin polymerization. For instance, purified septin can directly bind model lipid membranes containing phosphatidylinositols (PI) and/or phosphatidylserine (PS) [82, 95, 96] and form a mesh of single and paired filaments [82, 96, 97] or small bundles [96]. Septins also bind differently to membranes with different curvatures [95, 97, 98], and even reshape vesicles [97, 99, 100], suggesting that membrane curvature is also important for septin binding. Septins can also bind actin filaments and microtubules, which in turn affects the organization and dynamics of septin filaments [101–103]. Finally, the binding of the Borg family members to the SEPT6-SEPT7 interface can stabilize the coiled-coil structure of the NC interface and promote septin polymerization [89, 104].

Septins play crucial roles in many cellular processes such as cell division, cell polarity, and various membrane remodeling processes. Their distribution in animal cells varies depending on factors such as the organism, cell type, and developmental stage [105, 106]. The

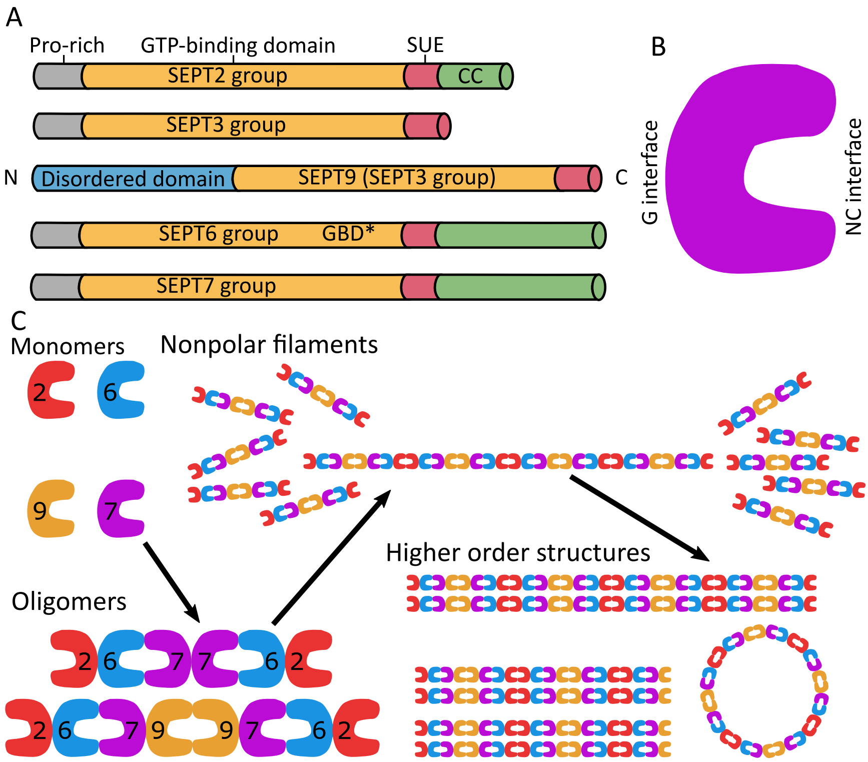

Figure 1.5. Septin polymerization from septin subunits. A. Schematic representation of the different septin subfamilies. From N to C terminus: proline-rich domain, GTP-binding domain, septin unique element, coiled-coil. SEPT6 has a GTP-binding domain incapable of GTP hydrolysis, as represented with "GBD*". SEPT9 is part of the SEPT3 subfamily, but since it is the canonical SEPT3 group septin and has an additional long disordered N-terminal domain, an additional schematic has been added. B. Schematic representation of a folded septin subunit showing the G and NC interfaces. C. Schematic representation of the self-assembly process of septin: monomers form stable hetero-oligomers, which in turn polymerize into nonpolar filaments that can self-assemble into higher-order structures.

high stability of septin filaments suggests that septins serve as a scaffold, regulating the composition of lipids and cytoskeletal proteins at the interface of the actin cortex and the plasma membrane. Additionally, septins act as scaffolds for specialized cellular machineries, such as the cytokinetic ring [107], and have been observed to form a cage around pathogenic bacteria within infected human cells, aiding in their elimination through autophagy [77]. Notably, they often localize in regions of high curvature, forming diffusion barriers. Examples include their presence at the cytokinetic ring, the base of the cilium, the annulus of sperm cells, dendritic spines, and the phagocytic cup [76, 108]. Dysregulation of septin expression levels and the occurrence of mutations have been associated with various neurological disorders like Alzheimer's and Parkinson's diseases [109], as well as conditions such as male infertility, bleeding disorders, and a wide range of cancers [76, 110, 111].

Roles of septins' interactions in cell shape stability and cell shape changes

It is interesting to note that most of septin's functions are based on their interaction with other cellular components. Of special interest for cell shape maintenance and change, and especially cell division, is the interaction of septins with the cell membrane, the actin cytoskeleton, and microtubules.

Septins are found to localize to the membrane of cells, especially to curved regions [95]. It is still unclear whether this cortical localization comes from septins binding to the cell membrane, to the actin cortex, or to both simultaneously. However, this localization is important for maintaining specialized cell shapes. For instance, septins form a ring-like annulus in spermatozoa, and its absence makes the tail bend or break [112]. Septins also seem to compartmentalize the primary cilium, by localizing on their base, as found for IMCD3 cells [113]. Septins are also important for membrane fusion during exocytosis by interaction with the exocyst and the syntaxin complexes [114]. Additionally, septins are essential for the migration of a multitude of cell types, such as epithelia, fibroblasts, lymphocytes, neurons, and stem cells [115]. They do so by reinforcing the cortical actin by crosslinking it, readying the cell for the mechanical stresses coming from migration, and by regulating the formation of membrane protrusions [115]. In the context of cell migration, septins have been found to enhance migratory and invasive phenotypes of cancer cells.

One special form of cell shape change is cell division, in which the genetic material is separated during karyokinesis, and the daughter cells are divided during cytokinesis. During karyokinesis, septins play a role in a variety of processes via their interaction with microtubules [115]. First, SEPT7 is important for centrosome replication, since its knock-down leads to the formation of multipolar spindles [116]. Septins also seem to bind the kinetochores of chromosomes, assisting microtubule-chromosome anchorage and chromosomal alignment in the metaphasic plate [117]. Finally, septins also seem to play a role in spindle positioning via microtubule-plus end interactions [116, 118]. In the context of cytokinesis, septins play important roles during cell rounding [119, 120], constriction of the actomyosin ring [121–124], and midbody abscission [125, 126]. SEPT9 knockout in HeLa cells showed clear rounding defects, leading to cell shape defects during cell division [120]. Septins are also important for the correct constriction of the cytokinetic ring since they are recruited early to the ring [124], locally activate myosin motors [121], and in the absence of septins, the contractile ring is not anchored and retracts after constriction is completed [121, 122]. Finally, septins form a double ring at the midbody that regulates abscission by regulating the ESCRT machinery [125, 126].

1.4. Using septins for bottom-up synthetic biology

As explained above, septins are a component of the cytoskeleton with the ability to bind lipid bilayers, actin, and microtubule. Therefore, they can potentially be used to mediate several important animal cell-inspired processes in synthetic cells.

First, septins could participate in the mechanical reinforcement of the cell. Since septins bind PI and PS-containing lipid bilayers and form a mesh of filaments/bundles [82, 96, 97] they could potentially reinforce the membrane of a liposome-based synthetic cell. Furthermore, if they can bind simultaneously to the membrane and to actin and crosslink the actin, they could further mechanically reinforce the synthetic cell by the formation of a membrane-anchored synthetic actin cortex. Together with its putative ability to interact with myosin [121], this could also make septin a regulator of actin-mediated synthetic cell-shape changes.

Evidence from *in vitro* reconstitution and experiments in cells also suggest that septins could be useful for synthetic cytokinesis. First, septins bind preferentially to curved regions of the plasma membrane such as the cytokinetic furrow [95, 127, 128] and they prefer negative curvature *in vitro* [97, 98]. These observations suggest that septins could be used to initiate or maintain initial curvature to start cytokinesis. Additionally, the fact that septins are important for the constriction of the contractile ring and the activation of myosin in dividing cells [121], together with *in vitro* evidence showing that septins can crosslink and bundle actin, suggests that septins could participate in contractile ring formation, stabilization, and membrane anchorage in synthetic cells.

Finally, the interaction of septins with microtubules, by stabilizing them and anchoring them to the chromosomes, could make septin an important regulator of karyokinesis. Septin could not only mediate microtubule-chromosomal binding, but also help orientating the microtubule spindle by mediating crosstalk between actin and microtubules.

1.5. Outline of this thesis

Despite the big potential of septins to mediate several processes in animal-inspired synthetic cell modules, we currently lack *in vitro* knowledge of how these processes can be controlled. It is still unclear how septins bind actin, microtubules, and lipid membranes, whether septin hexamers and octamers would interact differently, and how the binding of septin to other structures affects their polymerization. Additionally, although we know that under *in vitro* conditions septins can bind to the three components, it is still unclear how the crosstalk between the three is mediated by septins. Finally, there is also not sufficient evidence to understand how septins contribute to processes such as division in actual cells. Using *in vitro* reconstitution is a very useful tool to understand the basic properties and interactions of septins and how they are involved in morphogenesis.

Therefore, in this thesis, we use *in vitro* reconstitution to study how septins interact with microtubules, model lipid membranes, and actin with a focus on understanding how to use them for bottom-up synthetic biology and to understand their roles in cellular processes. We do so in the context of human septins for several reasons. First, they contain a wider variety of septin subunits as compared to septins from other model organisms such as yeast or fly septins and can form simultaneously septin hexamers and octamers. This diversity could help regulate their roles in the synthetic cells. And second, exploring the functions of human septins is more relevant from the perspective of understanding the potentially differential roles of different septin oligomers in human development and diseases.

In **Chapter 2** we describe a generalized protocol to purify high quality septin hetero-oligomers and to assess their quality. We use a two-step affinity chromatography approach to purify *Escherichia coli*-expressed recombinant septins of varied subunit composition by selectively tagging two of the subunits. Then we describe a set of techniques consisting of gel electrophoresis, transmission electron microscopy, and interferometric scattering microscopy to check the quality of the purified septin oligomers. Finally, we detail the imaging assays that we use to check whether the purified septins are able to polymerize.

It is known that the isoform 1 of SEPT9 (SEPT9_i1) is responsible for mediating the binding of septin octamers to microtubules in cells. In **Chapter 3** we use a combination of bioinformatics, experiments in cells, and *in vitro* reconstitution to deepen our knowledge of this interaction. First, we use bioinformatics to find a 25-amino acid long sequence unique to SEPT9_i1 resembling the microtubule binding domains of other MAPs, suggesting that this unique N-terminus could potentially mediate septin-microtubule interactions. Then we use experiments in cells and *in vitro* assays comparing the binding of septin hexamers containing no SEPT9 and septin octamers bearing different isoforms or mutants of SEPT9 to validate this binding. Finally, we explore the effect of septins on the dynamic behavior of microtubules in our *in vitro* assays and show that septins stabilize microtubules.

In **Chapter 4 and 5** we study the interactions of human septin complexes with model lipid membranes. In **Chapter 4**, we first use an array of techniques to investigate the interaction of septin complexes with flat supported lipid layers. In that context, we use quartz crystal microbalance with dissipation monitoring to investigate the lipid specificity of human septin oligomers and the effect of GTP on their binding. We show that human septin oligomers need the presence of both DOPS and PIP2 lipids to efficiently bind to supported lipid bilayers in the conditions used, and that the presence of excess GTP slightly increases membrane binding. Finally, by analyzing the dissipation changes upon septin binding, we obtain evidence that in the presence of excess GTP, human septin hexamers form networks that are stiffer than those formed by octamers. Then we use transmission electron microscopy and atomic force microscopy to image the membrane-bound septin networks at high resolution. We find that on PIP2-containing lipid monolayers, both septin hexamers and octamers form a cross-hatched network composed of single and paired filaments. On supported lipid bilayers, octamers formed a similar meshwork, but, surprisingly, hexamers form a network based on curved bundles. Finally, we use computer simulations to understand the formation of the bundle-based network.

In **Chapter 5**, we move closer to synthetic cell-like systems by studying the interactions of septin complexes with free-standing curved membranes in the form of giant unilamellar vesicles (GUVs). We encapsulate septins inside GUVs for the first time and found that they bind the inner bilayer leaflet provided that DOPS or PIP2 are present, with binding being enhanced when lipids both were present simultaneously. Membrane binding is not affected by the curvature of the GUVs when binding from the inside of the vesicle and septins did not deform the membrane. In contrast, when binding from the outside, septin complexes strongly deformed the membrane forming small bumps or spikes separated by 1µm, suggesting that the preference for negative curvature of septins [97, 98] can lead to membrane reshaping.

Previous research has shown that septins are able to interact with actin, bundling it in reconstitution experiments [101, 102], and that septins might interact with myosin [121]. To further investigate these two observations, in **Chapter 6** we use *in vitro* reconstitution to examine the actin-binding and bundling ability of septin complexes and their effect on myosin activity. We found that both septin hexamers and octamers are able to crosslink the actin network at low concentrations and bundle actin filaments at high concentrations. However, hexamers require higher concentrations, suggesting that the SEPT9 subunits present in octamers reinforce binding. When adding muscle myosin-2 thick filaments, septin octamers have a non-monotonic effect on myosin-driven network contraction. At low concentrations, they crosslink the network, promoting force transmission and allowing long-range myosin-driven contraction. At high concentrations, septin-mediated bundling protect the actin from contraction by shielding the actin filaments from direct myosin interactions. This finding indicates that simply modulating the septin concentration could help tune the effect of myosin on actin filaments in synthetic cells.

In **chapter 7**, we bring together the knowledge acquired in **Chapters 4-6** and explore the possibility of using septin to anchor actin to lipid membranes. We found that septins alone are able to anchor a network of actin bundles to model membranes containing PIP2 and DOPS lipids, forming a cortex-like structure. When adding the actin nucleator Arp2/3, the architecture of these networks changes, and septins anchor aster-like structures to the model membranes.

Finally, in **Chapter 8**, we conclude with a view into the future, and delve into how we can learn more about the interaction of septins with each of the described components, explore how septins might mediate crosstalk between them, and describe their potential for synthetic cells.

The chapters described above are the bulk of this dissertation and make up its scientific part. During my studies and PhD, I have always found that the work we scientists do could easily be translated into art: complex and impressive setups to do very specific experiments, visual representations of the systems we study, amazing movies showing weird yet beautiful results, and astonishing images from both telescopes and microscopes are clear examples of how the scientific world can contribute art. Having this in mind, I wanted to reserve a small part of my thesis to exemplify this. Considering that this dissertation I wrote is simply a book and movies cannot be included, I decided to include a **Gallery** of different images (microscopic or not) that either one of the students I have supervised or myself have collected during my PhD.


Exploring the human septins
interactions in vitro
Gerard Castro-Linares
27/09/2021

Chapter 2
Septin purification and quality control

Septins are a family of conserved eukaryotic GTP-binding proteins that can form cytoskeletal filaments and higher-order structures from oligomeric complexes. They interact with other cytoskeletal components and the cell membrane to participate in important cellular functions such as cell migration and division. Due to the complexity of septins' many interactions, a large number of septin genes (13 in humans), and the ability of septins to form oligomeric complexes with different subunit compositions, cell-free reconstitution is a vital strategy to understand the basics of septin biology. Here, we first describe our method to purify recombinant septins in their oligomeric form using a two-step affinity chromatography approach. Then the process of quality control used to check for purity and integrity of the septin complexes is detailed. This process combines native and denaturing gel electrophoresis, negative stain electron microscopy, and interferometric scattering microscopy. Finally, we describe our routine to check the polymerization ability of the septin complexes using negative stain electron microscopy and fluorescent microscopy. Our findings demonstrate that it is possible to produce high-quality human septin hexamers and octamers containing different isoforms of SEPT_9, as well as Drosophila septin hexamers.

This chapter is partly based on:
F. Iv et al. Insights into animal septins using recombinant human septin octamers with 2 distinct SEPT9 isoforms, JCS, 134(15), 2021 [102]
and *G. Castro-Linares et al. Purification and quality control of recombinant septin complexes for cell-free reconstitution, JoVE, 2022* [129].

The work described in this chapter is a collaborative effort between the groups of Gijsje Koenderink, Manos Mavrakis, and Aurelie Bertin. Specifically, purification, denaturing electrophoresis, and fluorescence microscopy were performed at both the Koenderink and Mavrakis labs. iSCAT and native electrophoresis experiments were performed at the Koenderink lab. Transmission electron microscopy was performed at the Koenderink and Bertin labs, while the class averaging was done by the Bertin Lab. A video showing all steps can be found on `https://www.jove.com/v/63871/purification-quality-control-recombinant-septin-complexes-for-cell`

2.1. Introduction

The cytoskeleton has been classically described as a three-component system consisting of actin filaments, microtubules, and intermediate filaments [76]. Septins have been acknowledged as a fourth component of the cytoskeleton [76]. Septins are a family of GTP-binding proteins that are conserved in eukaryotes [75] and are involved in many cellular functions such as cell division [106], cell-cell adhesion [130], cell motility [119], morphogenesis [131], cellular infection [77], and the establishment and maintenance of cell polarity [132]. Despite their important functions, how septins are involved in such processes is poorly understood.

The septin family of proteins is subdivided into several subgroups (four or seven, depending on the classification) based on protein sequence similarity [75]. Members of different subfamilies can form palindromic hetero-oligomeric complexes that are the building blocks of filaments, which in turn assemble into higher-order structures such as bundles, rings, and meshworks [76, 86, 96, 102, 133, 134]. Further molecular complexity arises from the presence of different splice variants, an important example being human SEPT9, where there is evidence for specific functions of different splice variants ([103, 135–137], and see Chapter 3). Additionally, the length of the oligomers depends on species and cell type. For instance, *Caenorhabditis elegans* septins form tetramers [80], *Drosophila melanogaster* septins form hexamers [81] (Fig. 2.1A), *Saccharomyces cerevisiae* septins form octamers [82], and human septins form both hexamers and octamers [85] (Fig. 2.1A). The (co-)existence of differently sized oligomers and the ability of septin isoforms and splice variants from the same subfamily to substitute each other in the complex [86] have made it difficult to delineate the cellular functions of different oligomeric complexes.

Another interesting feature of septins is their ability to interact with many binding partners in the cell. Septins bind the plasma membrane and membranous organelles during interphase and cell division [99, 138, 139]. In dividing cells, septins cooperate with anillin [122, 124, 140] and actin and myosin during cytokinesis [101, 123]. At the late stages of cytokinesis, septins regulate the endosomal sorting complexes required for transport (ESCRT) system for midbody abscission [125, 141]. Additionally, there is also evidence of septin located on the actin cortex and on actin stress fibers of cells in interphase cells [142–144]. In specific cell types such as neurons, septins also bind and regulate the microtubule cytoskeleton [103, 145].

All of these features make septins a very interesting protein system to study, but also a challenging one. The combination of the large number of septin subunits (13 genes in human without counting splice variants [75]) together with the potential of septin subunits from the same subfamily to substitute each other and form differently sized oligomers makes it difficult to draw conclusions on the cellular function of a specific septin by genetic manipulation. Furthermore, the multiple interactions of septins make interpreting the effects of common research tools such as drugs [146] directed at cytoskeletal or membrane components a hard task.

A way to overcome this situation is to complement research in cells with *in vitro* (cell-free) reconstitution of septins. *In vitro* reconstitution allows for the isolation of a single type of septin oligomer with a specific subunit composition and length [82, 147–149]. This complex can then be studied in a controlled environment, either alone, to discover the basic structural and physicochemical properties of septins [150–152], or in combination with desired partners such as model biomembranes ([95, 96, 98], and Chapters 4, 5, and 7), actin filaments ([101, 102] and Chapters 6 and 7), or microtubules ([103, 148] and Chapter 3), to decipher the nature of their interactions.

Therefore, a reliable method to purify different septin complexes efficiently is vital for septin research. However, even using the same protocol, different purifications can give proteins with different activity/functionality or even integrity. For commercially available proteins such as enzymes, the functionality and enzymatic activity are carefully validated [153]. Implementing careful quality control for cytoskeletal or structural proteins such as septins can be challenging, but it is essential to make experiments across labs comparable.

In this chapter, we describe a robust method to purify high quality recombinant septins in their oligomeric form based on the simultaneous expression of two vectors containing mono- or bi-cistronic constructs (Table 2.1) in *Escherichia coli* cells. The method consists of a two-step affinity chromatography approach to capture septin oligomers containing both a his_6-tagged septin and a Strep-II-tagged septin (either hexamers or octamers, see Fig. 2.1B and C, respectively). This protocol, first described in Iv et al. [102], has been used to purify *Drosophila* septin hexamers [96, 101, 147], human septin hexamers [102, 103], and several human septin octamers containing different native isoforms (SEPT9_ 1, 3, and 5 SEPT9) [102, 103] or mutated SEPT9 variants [103]. Furthermore, we describe a set of techniques to assess the quality of the purified septins. First, we check the integrity and correct stoichiometry of the septin subunits using denaturing electrophoresis and transmission electron microscopy (TEM). Then, we validate the correct molecular mass of the purified oligomers and test for the presence of monomers or smaller oligomers indicative of complex instability using native electrophoresis and mass photometry via interferometric scattering microscopy (iSCAT). Finally, we assess the polymerizing activity of the septins by the formation of septin bundles and their observation using fluorescence microscopy and transmission electron microscopy (TEM).

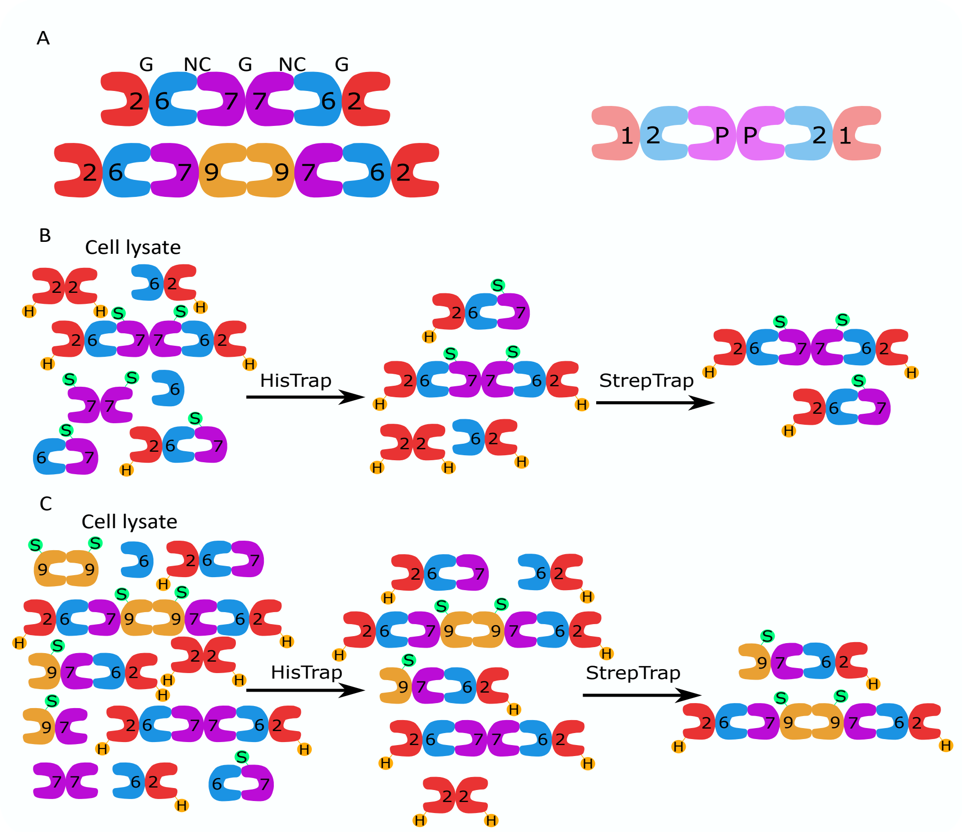

Figure 2.1. Purification strategy. A) Schematics of the septin oligomers that exist in human (left) and *Drosophila* (right) cells. Numbers denote septin subunits from the indicated groups, P denotes Peanut. Note that human SEPTIN9 can be any of its isoforms. The septin subunits have an asymmetric shape and longitudinally associate with two distinct interfaces, the NC:NC and the G:G interface, as shown by the labels NC and G, respectively, on top of the human hexamer. (B and C) Schematic illustration of the rationale of the two-step affinity chromatography strategy, here shown for human septin hexamers (B) and octamers (C). S denotes Strep-tag-II and H denotes His-tag. These tags bind StepTrap and HisTrap columns, respectively.

2.2. Materials and methods

All chemicals were obtained from Sigma Aldrich unless specified otherwise.

2.2.1. Purification protocol

1. Transformation of bacterial cells with the expression vectors:

   1.1 Select a combination of one pnEA and one pnCS plasmid that will be used for expression. Choose the combination depending on the desired septin oligomer and whether or not fluorescent tagging is required.

   Note: C-terminally tagged msfGFP-SEPT2 (for human septins) or msfGFP- or mEGFP-DSep2 (for *Drosophila* septins) is used. (Table 2.1).

   1.2 Pipette 1µL of each plasmid (~1 ng/µL) in 100 µL BL21 *Escherichia coli* cells and incubate on ice for 20min.

   1.3 Place the cells in a water bath at 42℃ for 40s and immediately after incubate them 3 minutes on ice.

   1.4 Add 0.9 mL Lysogeny broth (LB) medium to the cell suspension and let the cells grow for 1h at 37℃.

   1.5 Plate the 100 µL cells on warm LB-agar plates containing 100 µg/ml of ampicillin and 100 µg/ml spectinomycin and incubate overnight at 37℃.

2. Grow pre-culture

   2.1 Fill a 250mL Erlenmeyer flask with 100mL Terrific broth (TB) or LB medium containing 100 µg/mL of ampicillin and 100 µg/ml spectinomycin.

   2.2 Pick out a single colony from the LB-agar plate with a sterile inoculation loop and transfer it to fresh media from the previous step.

   2.3 Incubate at 37℃ in a rotatory shaker incubator, either o/n or for at least 6 hrs.

   Note: From this culture, a glycerol stock can be prepared by mixing the bacterial suspension 1:1 with glycerol and storing it at -80℃. This stock can be then be used in step 2.2. instead of a freshly transformed colony.

3. Bacterial culture and protein expression induction

   3.1 Transfer the 100mL volume of bacteria into 5L of TB or LB containing 50µg/ml of ampicillin and 50µg/ml spectinomycin.

   3.2 Grow this culture at 37℃ in a shaker incubator until it reaches an optical density (OD) measured at a wavelength of 600nm in the range of 2-3 for unlabeled septins or 0.6-0.8 for msfGFP/mEGFP-labeled septins and induce protein expression by adding 0.5 mM IPTG. The lower OD for the labeled septins is to avoid reaching the death phase in their longer expression time, as detailed in the next step.

   3.3 Incubate the cells expressing unlabeled septin oligomers for 3h at 37℃ or the cells expressing msfGFP-labelled oligomers overnight at 17℃.

Note: The short protein expression time for unlabeled complexes, facilitated by the use of the richer TB medium, is chosen to avoid protein degradation. The longer expression time combined with lower temperature for labelled complexes is chosen to allow for correct folding of the msfGFP tag.

4. Bacterial lysis and lysate clarification

Note: from this point onward in the purification procedure, keep the protein-containing solution on ice or at 4℃ at all times, to prevent proteolytic protein degradation or loss of protein activity.

4.1 Collect the cultured cells by centrifuging at 4000x g for 20min at 4℃. Discard the supernatant.

Optional: The pellet can be snap frozen in this step and stored at -80℃ for up to 6 months. If this option is chosen, the pellet should be thawed on ice before continuing.

4.2 Dissolve the pellet in 100mL lysis buffer (20mM Tris-HCl pH 7.4, 300mM KCl, 2mM $MgCl_2$, 20mM $MgSO_4$, 1mM PMSF, and freshly dissolved 0.25mg/mL lysozyme, 10mg/L DNAse, and 1tablet/50mL of EDTA-free protease inhibitor cocktail from Roche (Cat. # 481761) and lyse the cells. Choose one of the two options:

- Sonicate in 7 cycles of 30s ON and 59s OFF with a tip sonicator using 30% amplitude (Q500 Sonicator, Qsonica).
- Break down the cells in the French press by passing them at least 3 times.

4.3 Clarify the cell lysate by centrifuging at 20.000x g for 30min at 4℃ and keep the supernatant.

Note: We recommend to start with step 5.1 during this centrifugal step.

Optional: Take a sample for denaturing electrophoresis.

5. Affinity chromatography for His-tagged proteins to yield complexes containing human SEPT2 or *Drosophila* Sep1 using a Nickel column.

Note: The septin complexes purification was performed in an Äkta system (AKTA pure 25 M1, GE healthcare)

5.1 Equilibrate a HisTrap HP column (GE healthcare, product number: 29-0588-3) with septin buffer (20mM Tris-HCl pH 7.4, 300mM KCl, 2mM $MgCl_2$).

5.2 Load the clarified supernatant onto the column at 1 mL/min and wash the bound protein with at least three column volumes of septin buffer.

5.3 Elute the septin complexes with 50% HisTrap elution buffer (20mM Tris-HCl pH 7.4, 300mM KCl, 2mM $MgCl_2$, and 500mM imidazole, diluted in septin buffer to give a final of 250mM imidazole) at 1mL/min while collecting 0.5 mL fractions.

5.4 Pick the fractions containing septin complexes as indicated by the optical absorbance of the eluate monitored online at 280 nm with the Äkta system or after the purification with a Nanodrop spectrophotometer.

Note: Imidazole absorbs light at 280 nm. This probably explains why the protein peak does not go back to zero absorbance after the septin elution (Fig. 2.1A).

6. Affinity chromatography for Strep-II-tagged proteins.

Note: This step yields complexes containing either human SEPT7 (hexamers), human SEPT9 (octamers), or *Drosophila* hexamers Peanut using a Strep-Tactin column (Fig. 2.1B and C). The chromatography column is based on a modified biotin-streptavidin system. The tagged septin is modified biotin (Strep-II-tag) and the column contains an engineered streptavidin (Strep-Tactin). Despite being modified from the biotin-streptavidin system, there is no interference between the Strep-Tactin-Strep-II-tag system and the biotin-streptavidin system. The described system is used to avoid interference with reconstitution assays using biotin and streptavidin.

6.1 Equilibrate a 1mL StrepTrap HP (GE healthcare, product number: 28-9075-46) column with septin buffer.

6.2 Load the septin-containing fractions recovered from the HisTrap column at 1mL/min and wash the bound protein with at least three column volumes of septin buffer.

6.3 Elute the septin complexes with 100% StrepTrap elution buffer (20mM Tris-HCl pH 7.4, 300mM KCl, 2mM $MgCl_2$, and freshly dissolved 2.5mM Desthiobiotin) at 1mL/min while collecting 0.5 mL fractions.

Note: The desthiobiotin in the StrepTrap elution buffer must be dissolved fresh for stability of the compound.

6.4 Pick the fractions containing septin complexes as indicated by the optical absorbance of the eluate monitored online at 280 nm with the Äkta system or after the purification with a Nanodrop spectrophotometer.

Note: The denaturing electrophoresis is usually done at this point with samples of the column washings and septin fractions. The order of columns can be inverted with indistinguishable results, i.e. the clarified lysate can be subjected to Strep-Tactin affinity chromatography followed by nickel affinity chromatography [102].

7. 7. Dialysis and storage

7.1 Dialyze the septin complexes in a ~1:300 sample-to-buffer volume ratio against septin buffer supplemented with 1mM DTT overnight, or for at least 4h, at 4℃ using a 30 kDa MWCO dialysis membrane (Thermo Fisher scientific, product number: 66381).

Optional: Concentrate the septins using a 30kDa MWCO centrifugal concentration column (Sartorius, product number: VS0622) up to the desired concentration. We aim for a final concentration of 5-7 µM, as measured via the solution optical absorbance at 280nm and using a theoretical extinction coefficient calculated via ProtParam (Table 2.2).

7.2 Aliquot the protein complexes into the desired aliquot size, snap-freeze and store it at -80℃.

Table 2.1. List of plasmids. Plasmids to purify septin oligomers following this protocol. All plasmids have been deposited in Addgene (first column). Fluorescently tagged septins are C-terminally labeled with monomeric superfolder GFP (msfGFP) or monomeric enhanced GFP (mEGFP) on SEPT2, for human complexes, or Dsep2, for *Drosophila* complexes.

Addgene ID	Plasmid	Inserts	Used for
174491	pnEA-vH_His-TEV-SEPT2	SEPTIN2 (Human)	Unlabelled human hexamers
174492	pnEA-vH_His-TEV-SEPT2-msfGFP	SEPTIN2-msfGFP (Human)	msfGFP-human hexamers
174497	pnEA-vH_His-TEV-SEPT2_SEPT6	SEPTIN2 (Human) and SEPTIN6 (Human)	Unlabelled human octamers
174498	pnEA-vH_His-TEV-SEPT2-msfGFP_SEPT6	SEPTIN2-msfGFP (Human) and SEPTIN6 (Human)	msfGFP-human octamers
174493	pnEA-vH_His-TEV-DSep1	Sep1 (*Drosophila*)	Unlabelled and mEGFP-*Drosophila* hexamers
174494	pnEA-vH_His-TEV-DSep1-msfGFP	Sep1-msfGFP (*Drosophila*)	msfGFP-*Drosophila* hexamers
174499	pnCS_SEPT6_SEPT7-TEV-Strep	SEPTIN6 (Human) and SEPTIN7 (Human)	Human hexamers
174500	pnCS_SEPT7_SEPT9_i1-TEV-Strep	SEPTIN7 (Human) and SEPTIN9 (Human)	Human octamers with Septin 9_i1
174501	pnCS_SEPT7_SEPT9_i3-TEV-Strep	SEPTIN7 (Human) and SEPTIN9_i3 (Human)	Human octamers with Septin 9_i3
174502	pnCS_SEPT7_SEPT9_i5-TEV-Strep	SEPTIN7 (Human) and SEPTIN9_i5 (Human)	Human octamers with Septin 9_i5
174495	pnCS_DSep2_Peanut-TEV-Strep	Sep2 (*Drosophila*) and peanut (*Drosophila*)	Unlabelled and msfGFP-*Drosophila* hexamers
174496	pnCS_mEGFP-DSep2_Peanut-Strep	mEGFP-Sep2 (*Drosophila*) and peanut (*Drosophila*)	mEGFP-*Drosophila* hexamers

Note: We recommend to not store the protein more than six months. In addition, we recommend to perform regular quality control experiments, especially if the protein is stored longer than the recommended time.

2.2.2. Denaturing electrophoresis

We use denaturing electrophoresis to measure the stoichiometric ratio of septin subunits and thereby check for presence of the correct septins in the septin oligomers.

1. Mix 10 µL of the selected fractions with 10 µL Laemmli 2x concentrate SDS sample buffer, load them onto a precast 4-15% TGX gel (BIORAD, product number: 4561086), and fill the system with 1x running buffer (BIORAD, product number: 1610772).

2. Run the electrophoresis for 35min at 200V and stain the gel with your preferred method to visualize the results. We use InstantBlue Protein Gel Stain (Westburg Life Sciences, product number: EP ab119211). Molecular weights of the individual septin proteins and septin oligomeric complexes can be found in table 2.2 and table 2.3, respectively.

Table 2.2. Molecular weights of septin subunits. List of molecular weights (MW) calculated from the amino acid sequence of the different septin subunits that can be purified with the plasmids listed in Table 2.1 using ProtParam [155].

Name	MW (kDa)
Human septins	
His-TEV-Sept2	44.2
His-TEV-Sept2-msfGFP	70.9
Sept6	48.9
Sept7-TEV-Strep (hexamers)	52.9
Sept7 (octamers)	50.7
Sept9_i1-TEV-Strep	67.5
Sept9_i3-TEV-Strep	65.8
Sept9_i5-TEV-Strep	40.7
***Drosophila* septins**	
His-TEV-DSep1	43.8
His-TEV-DSep1-msfGFP	70.5
DSep2	48.5
mEGFP-DSep2	75.8
Peanut-Strep	61.2
Peanut-TEV-Strep	62.3

3. Measure the relative intensity of each band inside each lane containing purified septins in a contrast inverted image. Do this in FIJI[154] by calculating the mean intensity of equally sized rectangles around each band and of an equally sized rectangle on a region without any band in the same lane. Then, normalize the values by dividing the intensity of each band by the intensity of the region without bands.

Note: If the intensity is saturated (for example, values of 255 for an 8-bit image on a contrast inverted image), skip the lane.

2.2.3. Native electrophoresis

We use native electrophoresis to measure the ensemble-averaged size distribution of the purified septin oligomers.

1. Prepare 800mL of anode buffer and 200mL of light blue cathode buffer the day before and store them in the fridge. To prepare the anode buffer dilute 40mL of 20x running buffer with 760mL of MilliQ water. To prepare the light blue cathode buffer dilute 10mL of 20x running and 1mL of 20x cathode additive with 189mL of MilliQ water.

2. Prepare 10µL of sample by mixing ~500ng of septin with with 2.5 µL of 4x sample buffer (Thermo Fisher scientific, product number: BN2003), and enough MilliQ water to reach the 10µL.

3. Load the samples and 5µL NativeMArk unstained protein standard (invitrogen, product number: LC0725) onto the gel and fill the system with the ice-cold anode and light cathode buffers.

4. Run the electrophoresis for around 115min at 150V with a power supply that does not stop at low currents and stain InstantBlue Protein Gel Stain. Molecular weights of the septin complexes calculated based on the sequence using ProtParam [155] can be found in table 2.3.

2.2.4. Interpherometric scattering microscopy

We use iSCAT to measure the mass distribution of the purified septin oligomers via mass photometry. Our mass photometry experiments were done using the OneMP (Refeyn) iSCAT microscope following the manufacturer's indications.

1. Wash # 1.5 glass slides by sonicating them in a bath sonicator for 5 min in MilliQ water, then 5 min in isopropanol, and finally 5 min in MilliQ water.

2. Dry two glass slides with a gentle stream of nitrogen gas and place a 7µL drop of 0.01% Poly-lysine (PLL) solution on the center of one of the slides. Then place the center of the other slide on top of the PLL drop, orientating it orthogonally for easy separation. Incubate 30 seconds.

3. Wash by immersing in a beaker with MilliQ water once, and by directly applying a stream of MilliQ water twice. Then dry the two slides with a flow of nitrogen gas. These slides can be stored afterwards for around 6 weeks at room temperature in dry conditions.

Note: Label the side of the slide that is treated with the PLL-PEG to correctly run the experiment. We do this by drawing a dot on the top left corner of the glass slide.

4. Just before the experiment, cut a piece of 2x2, 3x2, or 3x3 silicone gasket and stick it on the PLL-PEG treated part of a glass slide while avoiding the glass slide and the gaskets to contact any dirty surface. We place the slide on a light-duty wiper tissue and press on the gaskets with a pipette tip to stick them while there is still the protecting plastic on the gaskets.

5. Warm up septin buffer to room temperature and thaw the proteins in your hand (keep them in ice afterwards).

Note: iSCAT shows signal of some detergents and small molecules that resemble protein signals[156]. DTT is one of those small molecules, which is why leave it out for this experiment. There is only a trace of DTT coming from the stored septin.

6. Place the slide with gaskets on the iSCAT microscope containing 19µL of septin buffer and focus the microscope using the autofocus option. Follow the manufacturer's instructions to check if the found focus is correct.

7. Pipette 1µL of sample on the buffer drop and mix, while minimizing the movement of the slide by not touching anything while doing so. Then record a 6000 frame video. If the slide has moved, refocus again. Samples:

   7.1 Septin buffer.

Table 2.3. Molecular weights and extinction coefficients of septin complexes. List of molecular weights (MW) and optical extinction coefficients (EC) at a wavelength of 280 nm calculated with ProtParam [155] based on the sequences of the complex assuming a linear fusion of the septin subunits, for the different septin complexes that can be purified with the plasmids listed in Table 2.1.

Name	MW (kDa)	EC ($\mu M^{-1}cm^{-1}$)
Human septin complexes		
dark human septin hexamers	291.9	0.164
SEPT2-msfGFP human septin hexamers	345.3	0.202
dark human septin octamers_9i1	422.6	0.213
SEPT2-msfGFP human septin octamers_9i1	476.0	0.251
dark human septin octamers_9i3	419.1	0.210
SEPT2-msfGFP human septin octamers_9i3	472.5	0.248
dark human septin octamers_9i5	368.8	0.212
SEPT2-msfGFP human septin octamers_9i5	422.2	0.248
***Drosophila* septin complexes**		
dark *Drosophila* septin hexamers	309.2	0.170
DSep1-msfGFP *Drosophila* septin hexamers	362.6	0.208
mEGFP-DSep2 *Drosophila* septin hexamers	361.6	0.211

7.2 Protein mass standard (Invitrogen, product number: LC0725) for the calibration of the signal to mass ratio. If a recent calibration is available and the environmental conditions have not changed, this sample can be skipped.

7.3 250nM of septin complexes diluted in septin buffer without DTT. This gives a final concentration of 12.5 nM.

8. Analyze the videos using the manufacturer's software to obtain the protein mass distribution. Check for good quality data:

   - If peaks of different septin oligomers sizes overlap too much or too many events are detected (>3500 events for a 6000 frames video with the regular field of view of 128x34 px spanning 10.8 x 2.9 µm), decrease the final septin concentration and measure again.
   - If there are not enough counts of single molecules measured (at least 2500-3500 for a 6000 frame video with the regular field of view), increase the concentration and measure again.

2.2.5. TEM of septin oligomers and class averaging

We use class averaging of single septin complexes seen in TEM images to check for the integrity of the septin complexes and to find the mass distribution of complexes present in the prep.

1. Dilute samples to a concentration of about 50 nM in septin buffer and prepare the staining solution: use either 2% uranyl formate or uranyl acetate in MilliQ water.

Note: Uranyl formate has to be prepared fresh.

2. Pipette 4µL of diluted septins onto a glow discharged electron microscopy grid and incubate for 30s.

3. Remove most of the protein solution using a filter paper and wash the grid twice with septin buffer and once with MilliQ water to remove loosely adsorbed septins.

4. Stain with staining solution for 1 min, absorb the staining solution with a filter paper, and air dry the grid for a few minutes.

5. Screen the grid using a properly aligned electron microscope (we used a Tecnai Spirit microscope from Thermo Scientific FEI, equipped with a Quemesa camera from Olympus) to search for regions of enhanced stain and collect about 100 images at a magnification of at least 50.000x to obtain a pixel size of about 2Å. Use an acceleration voltage of 200kV.

6. Perform 2D image processing using a dedicated software:

   6.1 Box out at least 2000 particles using a dedicated software such us EMAN [157].

   6.2 Perform two-dimensional alignment and classification iteratively, until classes are obtained without further improvement. The first alignment and classification step should be reference-free to avoid any bias in the classification. Each class should be based on 50 to 100 picked particles. Individual subunits should be clearly visible. Different software tools can be used [157–159], here we used EMAN.

2.2.6. Fluorescence microscopy of septin bundles

We use both fluorescence microscopy and transmission electron microscopy as a functional quality control to check whether the septin oligomers are able to polymerize into bundles.

Note: Below, we refer to unlabelled septins as "dark" septins and to the buffer used for polymerizing unlabelled septins as "dark" septin polymerization buffer (SPB).

1. Prepare the 5x fluoSPB (83.3mM Tris-HCl pH 7.4, 8.3mM $MgCl_2$, 5mM DTT, 0.75% w/v Methylcellulose, 5mM Protocatechuic acid (PCA), 5mM 6-hydroxy-2,5,7,8-tetramethylchroman-2-carboxylic acid (TROLOX)) and a septin mix consisting of 90% Dark septin and 10% msfGFP-septin at six times higher concentration than the desired final concentration in septin buffer + 1mM DTT. We usually use a final concentration of 300nM, giving a concentration of 1800 nM for this mix.

2. Polymerize the septin by mixing, in this specific order, MilliQ water (enough to top up to the final desired volume), 20% 5xfluoSPB (1:5 dilution), 0.05µM Protocatechuate 3,4-Dioxygenase (PDC, Cat. # P8279), and 16.67% Septin mix (1:6 dilution). We usually prepare 10µL, corresponding to 6.23µL MilliQ water, 2µL 5xfluoSPB, 0.1µL Protocatechuate 3,4-dioxygenase (PCD) (with a stock of 5µM), and 1.67µL septin mix. This gives a final buffer condition of fluoSPB (20mM Tris-HCl pH 7.4, 50mM KCl, 2mM $MgCl_2$, 1mM DTT, 0.15% w/v Methylcellulose, 1mM PCA, 0.1µM and 1mM

TROLOX). In this mix, methylcellulose is used as a crowding agent, PCA and PCD as an oxygen scavenger system [160], and TROLOX as a photoblinking suppressor. Incubate this mix for at least 30 min at room temperature.

3. Add the samples to your preferred imaging chamber washed with fluoSPB and image the septin bundles. We typically use PLL-PEG passivated flow channels as described in ([96, 102, 103], and Chapters 3 and 6). To image, we have used either a TIRF microscope or a confocal microscope. The TIRF microscope was composed of a Nikon Ti2-E (Nikon instruments) microscope with an iLAS2 azimuthal TIRF illumination system (Gataca), and equipped with a iXon Ultra 897 EM-CCD camera (Andor) and a 488nm laser combiner iLAS2 (Gataca). The confocal microscope was based on an Eclipse Ti2-E microscope (Nikon instruments) with a CSU-X1-M1 confocal unit (Yokogawa),an iXon Ultra 888 EMCCD camera (Andor) and a 488nm Sapphire laser line (Coherent).

2.2.7. TEM of septin bundles

TEM gives a much higher resolution as compared to TIRF, which can be used to differentiate bundles and to observe the individual filaments that form each bundle.

1. Prepare the 5x darkSPB (83.3mM Tris-HCl pH 7.4, 8.3mM $MgCl_2$, 5mM DTT) and a septin mix consisting of 100% Dark septin at six times higher concentration than the desired final concentration in septin buffer + 1mM DTT. We usually use a final concentration of 300nM, giving a concentration of 1800nM for this mix.
2. Polymerize the septin by mixing, in this specific order 3.16µL MilliQ-water, 1µL 5xfluoSPB, and 0.83µL septin mix. This gives the following final composition of darkSPB buffer: 20mM Tris-HCl pH 7.4, 50mM KCl, 2mM $MgCl_2$, and 1mM DTT. Incubate this mix for at least 30 minutes at room temperature.
3. Add 3-5µL of sample to a glow discharged electron microscopy grid and incubate for one minute. Then wash the grid twice with darkSPB by absorbing the liquid with a filter paper and adding a drop of buffer, wash once with MilliQ water, incubate for ~30s with 2% uranyl acetate, blot the stain and air dry the sample for a few minutes.
4. Image the septin bundles. We used two electron microscopes. Either the one described in section 2.2.5 or a JEM-1400plus microscope (JOEL) equiped with a 4k X 4k F416 CMOS camera (TVIPS).

2.3. Results

2.3.1. Purification of septin oligomers

We purified recombinant septins in their oligomeric form using a two-step affinity chromatography approach. We first applied the complexes onto a HisTrap column (Fig. 2.2A), and next pooled the septin-containing fractions and applied them onto a StrepTrap column (Fig. 2.2B). This two-step chromatography procedure typically yields around 3-5mL of ~1 µM of septin complex from 5L of *E. Coli* cells grown to an optical density of 2.5 at 600nm. Before pooling the septin containing fractions, we usually run a denaturing gel to check for the integrity of the septin subunits and a 1:1:1:1 stoichiometric ratio of the four subunits (Fig. 2.3A). If the gel shows similarly intense bands corresponding to the molecular weights (table 2.2) of the septin subunits, we proceed with the protocol. In the example shown for human septin octamers with SEPTIN9_i1 in Figure 2.3A, we can clearly observe bands of similar intensity; the 99% confidence interval of the normalized intensity over the average was 1.128±0.048 for SEPT2, 1.092±0.034 for SEPT6, 1.108±0.040 for SEPT7, and 1.067±0.029 for SEPT9. If SEPT2 is tagged with msfGFP, its band will shift up, very closely below the SEPT9_i1 band. Depending on the electrophoresis system used and the presence of the C-terminal TEV-Strep tag for SEPT7 (which makes it migrate more slowly than untagged SEPT7), the SEPT7 and SEPT6 bands sometimes merge due to their comparable molecular weights.

Next, we pool the fractions and dialyze them against septin buffer with 1mM DTT. If, after the dialysis, the concentration is too low (<2 µM) or we need a higher concentration for specific experiments, a concentration step can be included as described in the protocol. Concentrations below 1 µM usually indicate bad functional quality of the septins. We aim for a final septin complex concentration between 3.5 and 7 µM, that typically works well for most *in vitro* assays. These concentrations are usually obtained when the volume after concentration reaches 0.5-1 mL.

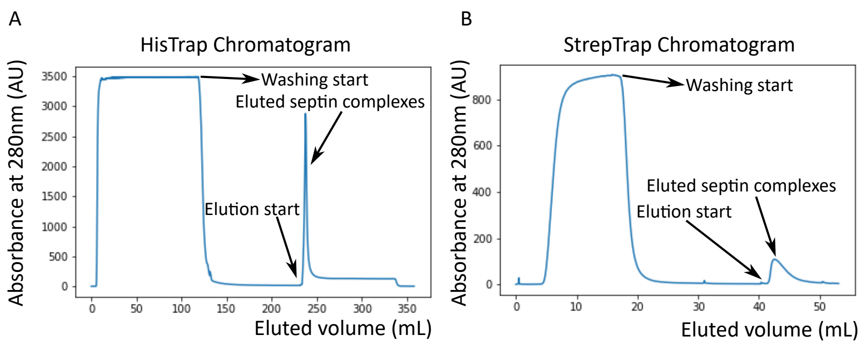

Figure 2.2. Example chromatograms corresponding to a purification of dark human septin octamers_9i1. A) HisTrap column chromatogram. After the septin elution peak, the absorbance does not go back to zero, likely due to the presence of imidazole in the buffer [161]. B) StrepTrap column chromatogram.

2.3.2. Quality control of septin oligomer integrity

To continue with the quality control, we perform a native electrophoresis as described in the protocol (Fig. 2.3B). On the gels, we can see a major band corresponding to the intact oligomers and usually a minor band corresponding to dimers. Human hexamers can be a little bit above the 242kDa marker band, while octamers are found above the 480kDa band. The location of these bands was checked by Western blot analysis of eukaryotic cell extracts [103]. Tagging of the two SEPT2 subunits of the oligomer with msfGFP causes an increase of the molecular weight of septin complexes of 52.4 kDa. Nevertheless, on the native electrophoresis gel, the apparent molecular weight of the msfGFP-tagged complexes is indistinguishable from that of the untagged complexes.

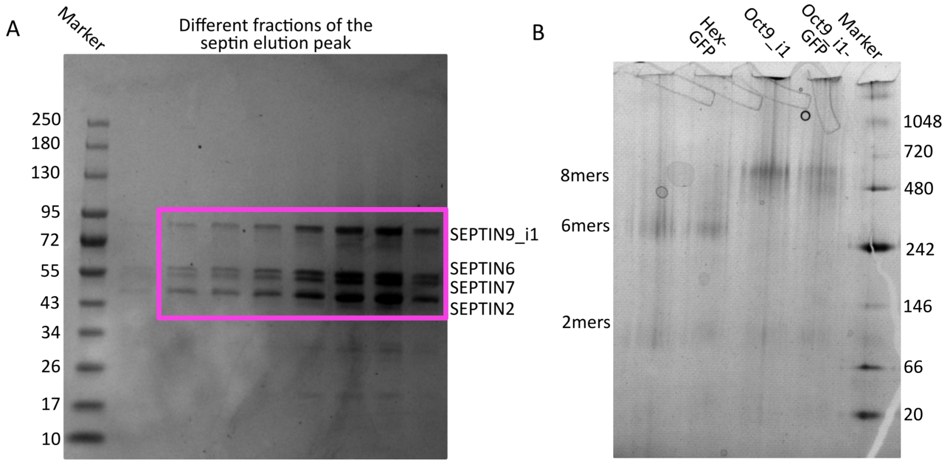

Figure 2.3. Examples of denaturing and native electrophoresis gels for oligomer quality control. A) Denaturing gel of different fractions of the elution peak of a purification of dark human septin octamers_9i1. Magenta box indicates the fractions that were picked and pooled for the next steps. B) Native electrophoresis gel of different septin complexes.

A complementary technique to native electrophoresis is mass photometry by iSCAT microscopy (Fig. 2.4). With iSCAT, we monitor light scattering of molecules landing on a glass slide amplified by interference with reference light, typically the reflection of the laser on the bottom of the glass slide. Then, a background subtraction approach is used to give contrast to the particles. Due to this correction, the signal shows positive and negative values depending on whether the particles land on the glass or move away from it [162]. The detected signal is directly proportional to the molecular weight of proteins [163]. Therefore, a calibration of the signal with a mass standard can determine the mass of sample proteins. Our example result with human septin octamers containing SEPTIN9_i1 (Fig. 2.4A) shows that about half of the detected single particles are of a molecular weight expected for complete octamers containing SEPTIN9_i1 (423 kDa). There are also particles with masses between 150 and 300 kDa, but no clear peak is observed, indicating the possible presence of different species in low abundance. Similarly, half of the detected single particles for mEGFP-tagged *Drosophila* hexamers (Fig. 2.4B) are of a molecular weight expected for intact hexamers (361 kDa). An additional clear peak at 241 kDa indicates the presence of stable tetramers containing two Peanut proteins, one DSep1, and one mEGFP-DSep2. Finally, both the human and the fly septin complexes show a peak around 80kDa, that could be a mix of monomers and dimers, possibly amplified by a trace of DTT or any other small molecule that aggregates showing a peak in the positive side of the plot [156].

Given that both native gels and iSCAT provide ensemble-averaged information only, we also use class averaging of transmission electron microscopy images of single septin oligomers to check the integrity and purity of individual complexes by direct visualization. In TEM images of septin complexes in septin buffer, rods of 24 (hexamers [82]) or 32nm

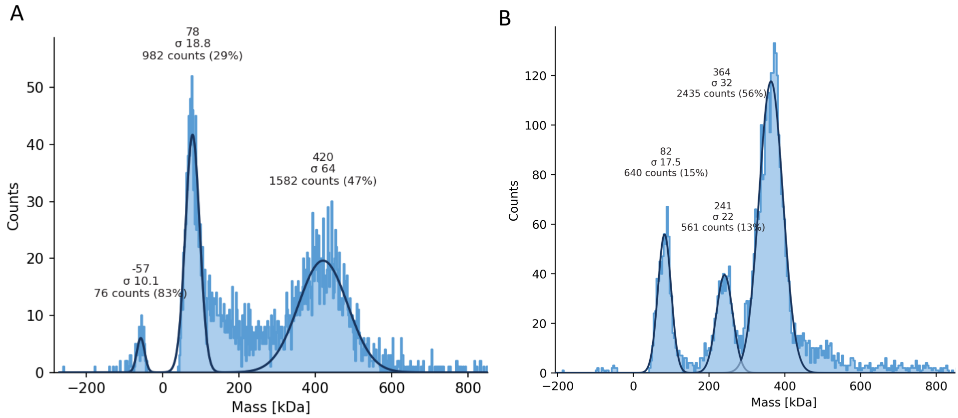

Figure 2.4. Typical mass photometry results for the oligomer quality control. A) Dark human septin octamers_9i1. B) DSep1-msfGFP *Drosophila* septin hexamers. Both complexes were measured at a concentration of 12nM. Lines are Gaussian fits.

(octamers [149]) in length can be observed. An example of a human septin octamer containing SEPTIN9_i1 can be seen in figure (Fig. 2.5A). When class averaging them, we can observe and count each of the subunits, as seen for the msfGFP-tagged human octamer with SEPTIN9_i1 in Figure 2.5B. In case the oligomer is fluorescently labelled, we can also observe extra densities at the ends of the rods, corresponding to the msfGFP (Fig. 2.5B). The combination of the above techniques proves that we purify octamers (or hexamers) with the correct stoichiometric ratio of the septin subunits and with high purity.

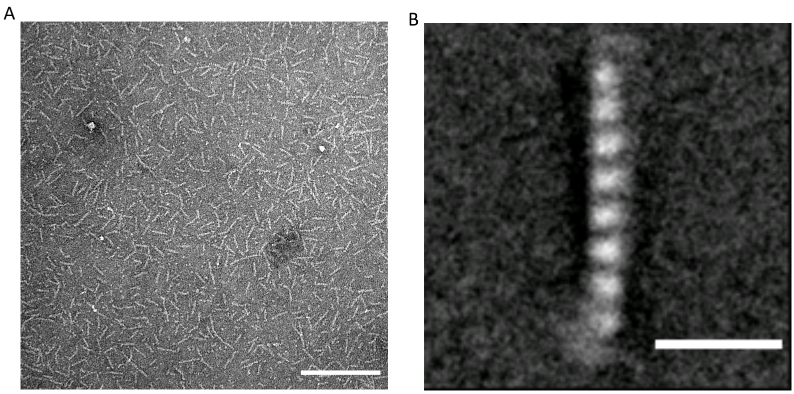

Figure 2.5. Typical results of TEM data for the oligomer quality control. A) TEM image of 25nM dark human septin octamers_9i1 in septin buffer. Scale bar of 200 nm. B) Class average image of SEPT2-msfGFP human septin octamers_9i1. The msfGFP tags are visible as fuzzy densities on the two ends. Scale bar of 10 nm.

2.3.3. Quality control of septin oligomer functionality

Finally, we also check for the functionality of the septin complexes in terms of their polymerization ability. In the presence of low salt concentration (<150mM KCl with our buffer [133]), in the absence of other proteins or negatively charged lipid membranes, the septin complexes self-assemble into bundles [133]. We rapidly dilute the septin complexes, which are prevented from polymerization in the storage buffer by maintaining a high (300 mM) KCl concentration, in a 1:6 volume ratio in a buffer of the same composition but without KCl, to a final KCl concentration of 50mM. When we do fluorescence imaging, we complement this buffer with an oxygen scavenging system, to protect from photobleaching (see methods section), and with a blinking suppressor. In TIRF microscopy, we observe small clusters of protein within the shallow TIRF field (~100nm) for both human septin hexamers (Fig. 2.6A) and octamers (Fig. 2.6B). On a confocal microscope, we can observe large clusters of filamentous structures floating higher up in solution (Fig. 2.6C). Finally, with TEM we can observe small septin bundles (Fig. 2.6D), likely corresponding to the clusters observed by TIRF, as well as large bundles (Fig. 2.6E), likely corresponding to the structures observed by confocal microscopy. The insets of figure 2.6D and E show that both the small and the large bundles consist of long and thin filaments that run in parallel, forming bundles with tapered ends. Together, the fluorescence and TEM images prove that the purified septin complexes can polymerize into filaments, which in turn self-assemble into bundles.

2.4. Discussion

The method described here allows for the robust purification and quality control of preformed septin oligomers. We want to stress some things of vital importance for the correct application of the method. First, during the elution steps in the chromatographic separations, it is important to use the recommended (or lower) flow rate to minimize dilution of the septin complexes. Additionally, to maximize the recovery of protein during the final concentration step, we orient the concentrator column in such a way that the solution is not pushed against the filter (when there is only a filter on one side). In our experience, if the solution goes directly to the filter, the protein sticks more to it, substantially decreasing the final yield. It is also important to consider that the concentration step is not always necessary. Picking fractions only from a narrow range around the peak in the chromatogram usually gives a high enough stock concentration (>3000 nM) for many reconstitution applications (which usually operate between 10 and 300 nM). Finally, for the quality control of the functionality of the septin complexes by fluorescence microscopy, it is important to correctly passivate the surface of the microscopy slides, since septin complexes avidly stick to glass. We perform passivation either via PLL-PEG functionalization or by the formation of neutral (100% DOPC) supported lipid bilayers [96, 103].

Compared to the original purification and assembly protocols first described in Iv et al. [102], we note that there is a change in the buffer compositions: the concentration of $MgCl_2$ has been reduced from 5mM to 2mM and the concentration and pH of Tris-HCl have been reduced from 50mM to 20mM and from 8 to 7.4, respectively. These changes were made to make the buffer conditions compatible with our studies of the interactions of human septins with lipid bilayers, actin filaments, and microtubules as described in the following chapters. We form supported lipid bilayers and polymerize actin in F-buffer (see Chapter 4), whose composition is identical to that of darkSPB, apart from the presence of ATP in F-buffer. The buffer change has not produced any noticeable changes in the quality

2

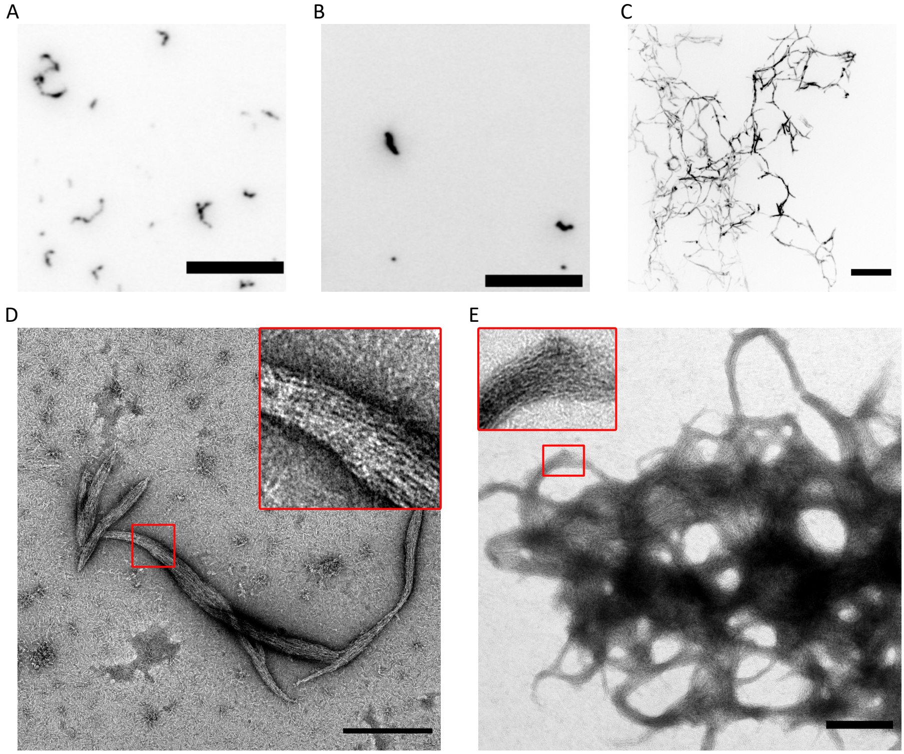

Figure 2.6. Example fluorescence and electron microscopy data for quality control of septin functionality. A) TIRF image of 300nM human septin hexamers (10% msfGFP-labelled hexamers) in fluoSPB. B) TIRF image of 300nM human septin octamers containing SEPTIN9_i1 (10% msfGFP-labelled octamers9_i1) in fluoSPB. C) Confocal maximum-intensity projections of Z-stacks across a depth of ~30µm with 0.5 µm spacing of 300nM human septin octamers_9i3 in fluoSPB. A-C) Scale bar of 10 µm and inverted grayscale. D and E) Example TEM images of small (D) and large (E) bundles of human septin octamers_9i1 in darkSPB. Insets show regions where we clearly observe filaments running parallel within the bundle. Scale bars are 500 nm.

or lifetime of the purified septins compared to the original buffers.

This method of purification still has several limitations. First, different purification attempts can vary in yield (0.5-1mL of 2-5 µM of septin complexes) and in functional quality, as evident from variations in the bundle formation ability of the purified septin complexes. It is therefore important to consistently perform the quality checks described in this chapter. Careful control of the duration of protein of expression and the optical density of the bacterial culture can help mitigate the differences in yield. Second, this purification pipeline cannot distinguish between trimers and hexamers, or between tetramers and octamers (Fig. 2.1B). However the quality control experiments can be used to prove that the majority of septin complexes are in their long oligomer form. In case an even narrow oligomer size distribution is required, a size exclusion chromatography can be inserted after the second chromatographic column. This optional step, however, in our hands dramatically decreases the yield and it is not recommended unless it is strictly needed. Finally, a more fundamental limitation comes from the use of *E.coli* as an expression system for recombinant septin complexes. Naturally, this system does not allow for post-translational modifications (PTMs) which have been reported in animal cells, such as phosphorylation, acetylation, and sumoylation [91, 93, 94, 131]. These posttranslational modifications could be added by implementing a similar purification strategy in insect or human cells. Furthermore, we only discussed reconstitution of septins by themselves, but studies in cells indicate that regulatory proteins such as proteins from the Borg family [104, 141, 164] and anillin [122, 140, 165] can have substantial, as yet poorly understood, effects on the assembly and functions of septins and should thus also be eventually incorporated in *in vitro* studies. Protocols for the purification of Borg proteins and anillin have been reported [45, 104].

The septin purification protocol we report here offers a standardized way to purify septins in their oligomer form with the correct subunit stoichiometry, offering an important advance over many earlier *in vitro* studies relying on single septin subunits. Even though some septins in specific contexts can act as a single subunit [75], the current body of literature strongly suggests that, in animal cells, septins mostly function in complexes [133, 144, 166]. Therefore, the use of pre-formed oligomers, such as the ones described in this paper and in others [82, 96, 102, 103, 147–149, 167], is of great importance to study the structural and biophysical properties of septins via *in vitro* reconstitution in order to dissect their functions in the cell.

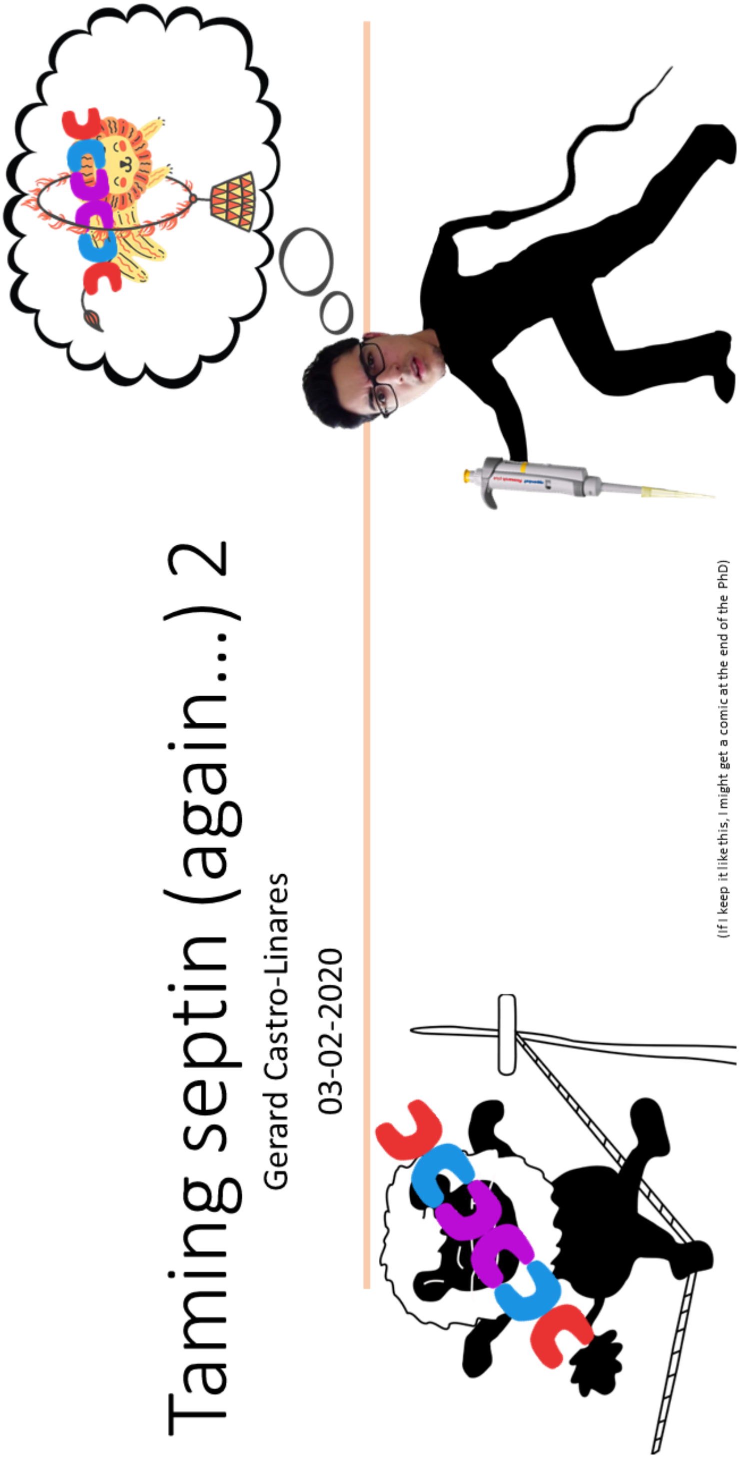
Taming septin (again…) 2
Gerard Castro-Linares
03-02-2020
(If I keep it like this, I might get a comic at the end of the PhD)

Chapter 3

Human septin octamers containing SEPT9_i1 bind and stabilize microtubules

Tight regulation of microtubule dynamics is crucial for many important cellular processes in animal cells. Cytoskeletal septins are important microtubule-binding proteins but the molecular basis of their interactions with microtubules remains poorly understood. Based on prior studies in cells showing that only septin octamers containing SEPT9 isoform 1 interact with microtubules, we identified the unique first 25 amino acids of SEPT9_i1 as a possible microtubule-binding domain via bioinformatics analysis. We validated this prediction using mutagenesis and localization studies in cells. To learn more about the interaction of septins with microtubules and their effect on microtubule dynamics, we used a cell-free dynamic microtubule assay in the presence of recombinant human septin complexes. Only septin octamers containing SEPT9_i1 were able to interact with microtubules and affect their dynamics, whereas octamers containing SEPT9_i3 did not exhibit any significant binding nor effect on microtubules. Septin hexamers, which lack the SEPT9 subunit, did interact and stopped microtubule growth at high concentrations. Finally, we used septin octamers containing a mutant SEPT9 consisting of SEPT9_i5 fused to the predicted microtubule binding domain of SEPT9_i1. This septin complex behaved similarly to octamers with SEPT9_i1 at low concentration, and similarly to hexamers at high concentrations. This evidence, together with the localization experiments in cells, proves that the unique N-terminus of SEPT9_i1 is a microtubule binding domain mediating septin octamer-microtubule interactions, whereas the common N-terminus shared by SEPT9_i1 and SEPT9_i3 regulates this interaction by stopping unspecific interactions.

This chapter is partly based on *M. Kuzmić et al. Septin-microtubule association via a motif unique to isoform 1 of septin 9 tunes stress fibers, JCS, 2022 [103].* Manos Mavrakis and Pascal Verdier-Pinard did the bioinformatics analysis, Mira Kuzmić and Pascal Verdier-Pinard performed the experiments in cells and wrote the paper, and Gerard Castro-Linares designed and performed all the *in vitro* experiments and adapted the paper for this thesis chapter.

3.1. Introduction

After their discovery six decades ago [168], microtubules have been established as an essential machinery for *eukaryotic* cells [169] that participate in vital cell processes such as cell motility, cell division, and vesicle trafficking [54, 170]. As explained in Chapter 1, microtubules are composed of multiple (usually 13) protofilaments of tubulin dimers [171] that form a hollow polar tube that stochastically switches between phases of growth and shrinkage [172]. This growth dynamics is different at each end of the microtubule, with the so-called plus end being the fast-growing end. In cells, microtubules form highly organized arrays, often radiating out from a centrosome where the minus ends are anchored. This organization is important for guiding intracellular transport by motor proteins and for organizing cell polarity. It requires accessory proteins that maintain or reorganize the microtubules depending on the cell's needs. This group of accessory proteins, also known as microtubule associated proteins (MAPs), encompass nucleators, stabilizing proteins, bundlers, severing proteins, and minus- or plus-tip binding proteins [54, 173]. Additionally, interactions of microtubules with other cytoskeletal systems have recently been gaining attention for their relevance in important cellular functions [69, 115, 174, 175].

Recent evidence shows that septins form a new class of microtubule-binding proteins. Septins have been found to colocalize with subsets of microtubules in a cell type specific manner [176–183]. They participate in tuning the dynamics, organization, and post-translational modifications of microtubules [116, 148, 177, 184, 185]. These abilities make septins important for epithelial [186] and neuronal [187] cell morphogenesis, microtubule-dependent transport, karyokinesis, and cytokinesis [115].

Similarly to tubulins, septins are a family of cytoskeletal GTP-binding proteins. They are divided in four subfamilies based on sequence similarity. The different septin subfamilies share a conserved domain structure with N- and C-terminal domains varying in length, a septin unique element, and a GTP-binding domain that varies in GTPase activity. Members of different subfamilies interact, forming linear palindromic hetero-oligomers that are the building blocks of apolar filaments [76]. Specifically, human cells form hetero-hexamers, composed of septins from the SEPT2, SEPT6 and SEPT7 subfamilies, and hetero-octamers that additionally include a member from the SEPT3 family [85].

Within the SEPT3 subfamily, SEPT9 is especially interesting because it is the most ubiquitously expressed, is over-expressed in some tumors [135, 136], and mutated in hereditary neuralgic amyotrophy (HNA) [188, 189]. Additionally, previous studies in cultured cells showed that SEPT9 mediates binding of septins to microtubules [190–192]. Alternative splicing of the SEPT9 RNA gives rise to five isoforms (SEPT9_i1 - SEPT9_i5) that differ in their translation start site [78], giving proteins with different length and sequence of the N-terminus (Fig. 3.1A). The longer SEPT9 isoforms (i1, i2, and i3) share a long disordered N-terminus with slightly different lengths and variations in the sequence of amino acids (Fig. 3.1B).

Bai et al. [193] found in *in vitro* studies a motif that drives septin-mediated bundling of microtubules within the shared region of the SEPT9 long N-terminus. Based on co-sedimentation assays of stable microtubules with wild type and mutated fragments of SEPT9, they reported that the N-terminus of the long SEPT9 isoforms (i1-i3) contains

(K/R-R/x-x-D/E) motifs that interact with the carboxy-terminal tails of βII-tubulin. Despite this interesting evidence, their own experiments in cells could only prove that the motif is important for microtubule bundling during neuronal morphogenesis, and not that it mediates septin-microtubule bunding. Additionally, several other studies in cells found that only SEPT9_i1 mediates septin-microtubule interactions [190–192]. This findings indicate that the (K/R-R/x-x-D/E) motifs that are shared between the isoforms 1, 2 and 3 of SEPT9 in the context of septin octamers only participate in microtubule bundling but do not mediate binding.

Further *in vitro* studies showed that both isolated SEPT9_i1 protein and human septin hexamers bundle microtubules and have a stabilizing effect by pausing microtubule dynamics in a concentration-dependent manner [148, 184]. However, we think that conclusions derived from these experiments cannot be directly extrapolated to how septins interact with microtubules in cells without further research. First, hexamers lack SEPT9, the septin subunit that drives the interaction with microtubules [190–192]. Second, isolated SEPT9_i1 proteins, despite the evidence that in some specific cases septins might function outside their normal hetero-oligomeric context [75], are unlikely to be relevant in the cellular context, where SEPT9_i1 interacts with microtubules in their octameric context [144].

Considering all of the available data, it is clear that the SEPT9_i1 subunit specifically drives the interaction of septin octamers with microtubules in cells. However, what makes this interaction specific and what is the role of the common N-terminal region between the long SEPT9 isoforms is still poorly understood. Answering these questions is difficult using only experiments in cells, because septins can form octamers composed of different septin subunits and they interact with many other partners such as actin [101, 102], cellular membranes [95, 96, 98], anillin [122, 140, 165], and the Borg proteins [104, 141, 164]. Using *in vitro* reconstitution permits the study of the interactions of septin complexes of a specific subunit composition with microtubules in well-controlled conditions. Therefore, in this chapter we used a combination of bioinformatics, *in vivo* experiments, and *in vitro* experiments to (1) identify the SEPT9_i1 microtubule binding domain (MBD), (2) study the regulatory effect of the common N-terminal region shared by the long SEP9 isoforms, (3) find whether septin octamers need to polymerize to bind microtubules, and (4) investigate the effect of septin on microtubule dynamics.

3.2. Results

3.2.1. Determination of the human septin microtubule binding domain

As mentioned above, there is evidence that only SEPT9_i1 is able to mediate binding of septin octamers to microtubules in cells [190–192]. The difference between the i1, i2, and i3 isoforms is in the length and amino acid sequence of the very beginning of the N-terminus (Fig. 3.1B). SEPT9_i1 has a unique 25 amino acid long sequence at its N-terminus which is followed by a long N-terminal region common between SEPT9_ i1-3. We therefore hypothesized that the unique sequence is responsible for binding. To test this idea, we performed a bioinformatic analysis to find if this SEPT9_i1 unique N-terminus shares any

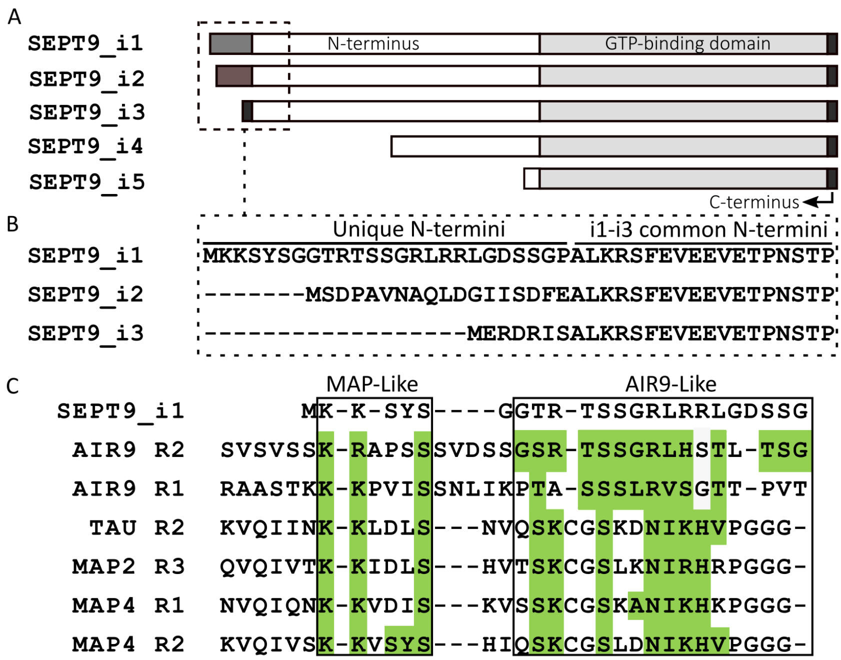

Figure 3.1. The unique N-terminus of SEPT9_i1 is a putative MBD. A. Graphic representation of the SEPT9 splice isoforms. B. Unique N-termini and part of the common N-termini of the long isoforms of SEPT9. C. Alignment of the unique N-terminus of SEPT9_i1 with AIR9 and repeats of Tau, MAP2 and MAP4. Green highlights amino acids in the MAPs that have similar properties to amino acids in the unique N-terminus of SEPT9_i1. R means "region" for AIR9 and "repeat" for the MAPs. Sequences were obtained from UniProt

sequence similarity to the microtubule binding domains of other MAPs. We found a high similarity within two regions (region 1: 46-78 and region 2: 173-205) of the MBD of AIR9, a microtubule binding protein involved in cell division of *Arabidopsis thaliana* [194] (Fig. 3.1C). We furthermore found similarity with the microtubule binding repeats of tau, MAP4 and MAP3, especially to the repeat 2 of MAP4 (Fig. 3.1C). Thus, the unique N-terminal 25-residues region in SEPT9_i1 presents a putative MBD consisting of a MAP-like and an AIR9-like domain.

3.2.2. Only septin octamers containing the putative MBD from SEPT9_i1 are able to interact with microtubules in human cells

To test whether the identified region is indeed a MBD, we examined the localization of GFP-tagged SEPT9_i1, SEPT9_i1 mutants presenting deletions or point mutations, SEPT9_i3, SEPT9_i5, and SEPT9_i5 fused to the putative SEPT9_i1 MBD on its N-terminus in siRNA SEPT9-knocked down U2OS cells (Fig. 3.2A). We chose U2OS cells because they have a high expression of SEPT_i3 and a low expression of SEPT9_i1, so they normally lack of septin-microtubule colocalization [103].

The expression of exogenous SEPT9_i1-GFP in the SEPT9-knocked down U2OS cells showed localization of SEPT9_i1-GFP on actin stress fibers in 100% of the cells and on

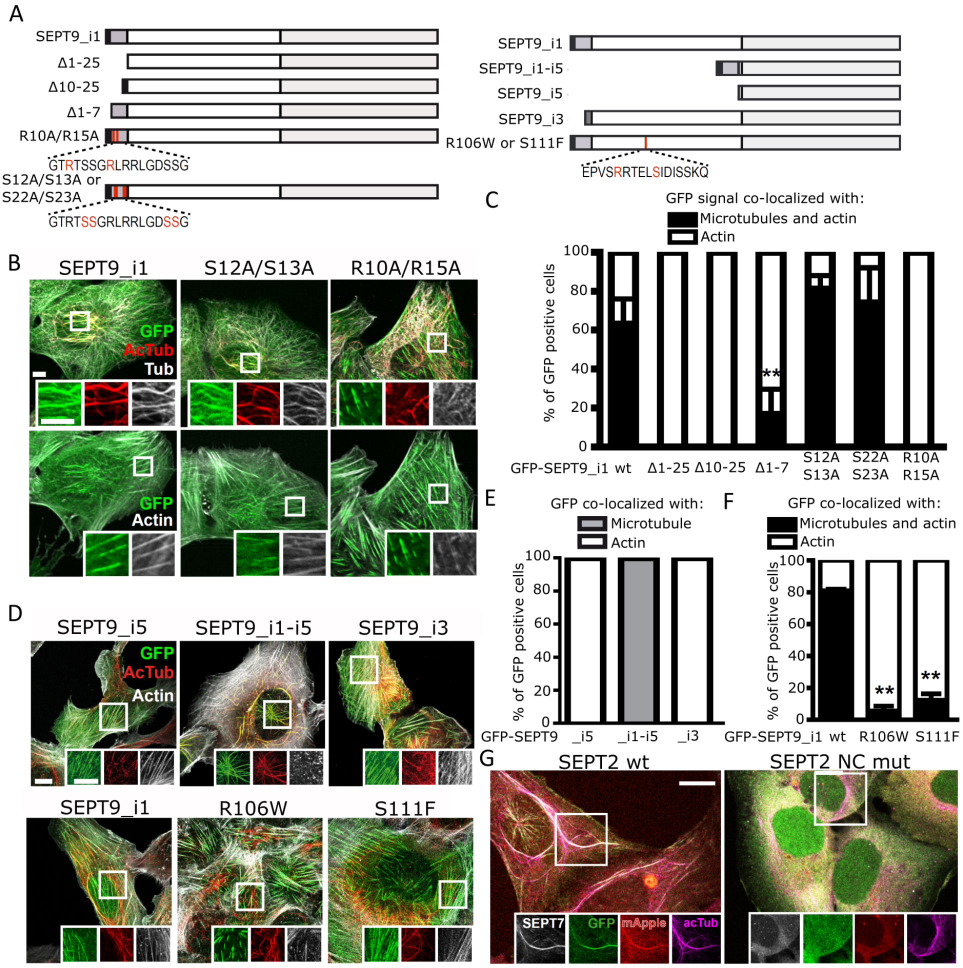

Figure 3.2. The unique N-terminus of SEPT9_i1 mediates microtubule localization of polymerizable septin octamers in cells. A. Schematic of the SEPT9 variants and mutants used for the localization experiments in cells. Left panel shows the unique N-terminus mutants. Right panel shows the different SEPT9 isoforms and the common N-terminus mutants. B. Representative results of the localization experiments of GFP-SEPT9_i1 unique N-terminus mutants. C. Percentage of cells that showed colocalization of the GFP-SEPT9_i1 unique N-terminus mutants with actin fibers alone or with actin fibers and microtubules simultaneously. D. Representative results of the localization experiments for GFP-SEPT9_ i1, i3 and i5, and the common N-terminus mutants. E and F. Percentage of cells that showed colocalization of GFP-SEPT9 variants (i1, i3 and i5) and the common N-terminus mutants with actin fibers alone, microtubules alone, or actin and microtubules simultaneously. C, E, and F. Data are shown as mean ± s.e.m. **P<0.01 (unpaired two-tailed t-test with Welch's correction). G. Representative results of the localization experiments of polymerizable septin octamers containing mApple- SEPT2 wt versus nonpolymerizable octamers containing SEPT2_NCmut and GFP-SEPT9_i1. Scale bars = 10μm.

microtubules in 60% of the cells (Fig. 3.2B and C). In contrast, SEPT9_i3 and _i5-GFP localized only to actin fibers (Fig. 3.2D and E). Several SEPT9_i1 mutants were then used to identify important regions within the MBD of SEPT9_i1. Deletion of the 25 first amino acids (the whole putative MBD) or the amino acids from 10-25 (the AIR9-like region) led to a complete loss of septin-microtubule colocalization (Fig. 3.2C). In contrast, the deletion of the first 7 amino acids (the MAP-like region) decreased the percentage of cells that showed microtubule localization (to~20%), but did not completely inhibit the colocalization (Fig. 3.2C). Finally, to identify important residues for the MBD of SEPT9_i1, we did the same experiments with SEPT9 with different point mutations (Fig. 3.2A). Specifically, we mutated R10A/R15A because they are also present in AIR9 and substituted both residues by a similar amino acid (K for R10 or N for R15) in found in other MAPs (Fig. 3.1C). We also mutated two sets of contiguous serine residues conserved in AIR9, S11A/S11A and S21A/S22A (Fig. 3.2A). We found that R10A/R15A mutants could not bind to microtubules, while S12A/S13A mutants showed enhanced colocalization (Fig. 3.2B and C). This data confirms that the unique N-terminus of SEPT9_i1 is indeed likely a MBD analogous to the repeats in MAP2, MAP4, tau and AIR9.

Prompted by the suggestion from Bai et al. [193] that the common N-terminus of the long SEPT9 isoforms can mediate microtubule binding, we did more experiments to check the effect of the (K/R-R/x-x-D/E) motif on septin-microtubule colocalization. Specifically, we compared the localization of SEPT9_i1, SEPT9_i3, and SEPT9_i5 with the localization of specific mutants. The first variant we tested, named SEPT9_i1-i5, was a SEPT_9i5 with the MBD of SEPT9_i1 directly fused to its N-terminus. In this SEPT9i1-i5 variant, we effectively delete the common N-terminus shared between the long SEPT9 isoforms. This led to the complete loss of SEPT9 from actin fibers and transferred to microtubules (Fig. 3.2D and E). Then, we introduced either the R106W or the S111F, common SEPT9_i1 mutations in HNA patients [188]. In cells containing either HNA-like mutated SEPT9_i1, SEPT9_i1 colocalization with microtubules was impaired (Fig. 3.2D and F). This finding suggests that, despite not being needed for microtubule colocalization, the common N-terminus of the SEPT9 long isoforms is an important regulatory sequence with both positive and negative effects on microtubule binding.

3.2.3. Septin octamers need to polymerize to bind microtubules in human cells

Septin is considered the fourth cytoskeleton component thanks to its ability to polymerize [76]. We therefore wondered whether this polymerization ability is needed for the septin octamers containing SEPT9_i1 to interact with microtubules. To test this hypothesis, we tested the localization of septin octamers in which the terminal SEPT2 subunits contained two point mutations (F20D and V27D, named SEPT2_NCmut) in the NC interface that inhibit polymerization [83, 195]. To do that, we knocked down the endogenous SEPT9 and SEPT2 and exogenously expressed SEPT9_i1-GFP and SEPT2_NCmut-mApple. In these conditions, septin octamers did not colocalize with either microtubules or actin stress fibers (Fig. 3.2G), indicating that septin polymerization is needed for septin-microtubule interactions, as also shown by using tripartite split-GFP assays [144].

3.2.4. Microtubule reconstitution assay with the septin-microtubule hybrid buffer

To test whether septins are able to directly bind microtubules, we moved to *in vitro* reconstitution experiments. As mentioned previously, microtubules grow and shrink in a process called dynamic instability [56, 196]. To reconstitute this process, short GMPCPP-stabilized microtubules, also called seeds, were bound to a glass surface. When GTP is present and the environmental temperature is between 30-37℃, free tubulin dimers can use the seed as a nucleation site to grow a microtubule. This microtubule will grow at a certain velocity until it undergoes a sudden catastrophe, where it starts to depolymerize or shrink. The shrinkage is usually complete, leaving only the seed. The shrinkage can also be incomplete and end by a so-called rescue, when the microtubule starts to grow again before it has reached the microtubule seed.

Since our experiments in cells showed that septin octamers need to be able to polymerize to interact with microtubules (Fig. 3.2G and [144]), we performed the *in vitro* experiments in low-salt conditions, where septins are able to polymerize. As shown in Chapter 2, septins are stored in oligomeric form in a high-salt septin buffer and are polymerized by rapidly diluting them 1:6 into a buffer such that the salt concentration falls below the threshold for polymerization. Since the kinetics of microtubule dynamic instability *in vitro* can vary depending on the environmental conditions [64], we first tested the effect on the microtubules of adding 1:6 Septin buffer into the standard microtubule dynamic assay buffer MRB80 (see section 3.4).

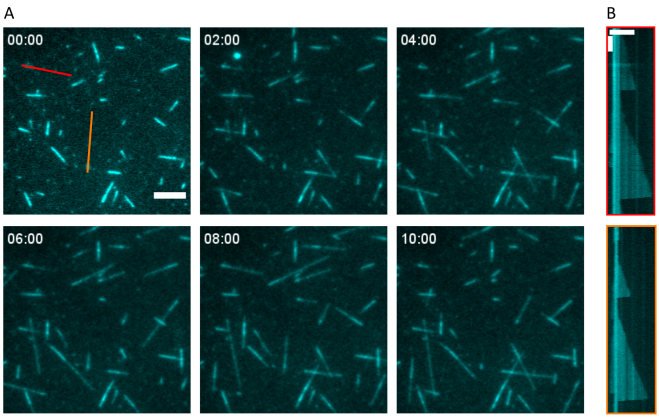

Figure 3.3. MT dynamic assay in the microtubule-septin hybrid buffer. A. Example of time-lapse experiment of microtubules growing and shrinking in microtubule-septin hybrid buffer. Time stamp in the upper-left corner shows time in units of min:sec. B. Kymographs showing the dynamics of the two microtubules indicated by the red and orange lines in A. Horizontal scale bars are 5µm. Vertical bar is 50 seconds.

As shown in Figure 3.3, microtubules started to grow from the GMPCPP-seeds around 1 minute after addition of the tubulin mix to the seeds. The microtubules behaved as expected, presenting a stochastic switching between growth phases, catastrophes, and shrinkage phases, with no rescues, as seen in the kymographs in Figure 3.3B. In this specific condition, consisting of a 5:1 mixture of MRB80 buffer and septin buffer, 30℃, and 20μM tubulin, microtubules grew with a speed of 0.9±0.3 μm/min (180 events measured from 3 independent experiments), a shrinking velocity of 51.3±30 μm/min (150 events measured), and a catastrophe rate of 0.4±0.2 min^{-1} (114 events counted).

3.2.5. Effect of human septin hexamers on microtubule dynamics

Having established that microtubules behave normally in the microtubule-septin hybrid buffer, the next step was to add septins. We started the series of experiments with human septin hexamers, which do not interact with microtubules in cells [103, 192].

At 50nM, septin hexamers bound very weakly to microtubules (Fig. 3.4A). Microtubules remained dynamic and septins did not accumulate over time, as revealed by kymographs (Fig. 3.4B). As the septin hexamer concentration was raised to 100nM or 200nM, the septins were initially bound only to the microtubule seeds (Fig. 3.4A). During the first 10 minutes, the septin signal started to extend onto the lattice of the dynamic microtubules, as revealed by kymographs (Fig. 3.4B). When visualized again between 1 and 2 hours later, the septin signal completely decorated the microtubules and was higher than in the first 10 minutes of the assay (Fig. 3.4C). At the same time, the dynamics of the microtubules had completely stopped and their tips were curved, forming a sort of loop (Fig. 3.4C, green arrowheads). Finally, when the septin hexamer concentration was raised to 300nM, microtubule dynamics were stopped from the start (Fig. 3.4A); however, microtubules did not curve the tip of microtubules 1-2h after the start of the experiment (Fig. 3.4C). These finding indicate that the accumulation of septin hexamers on microtubules is able to halt microtubule dynamics, consistent with previous work [148].

3.2.6. Human septin octamers with SEPT9_i3 have low binding affinity to microtubules and minimal impact on microtubule dynamics

From our results in U2OS cells, we did not expect human septin octamers containing SEPT9_i3 (in short oct_9i3) to have any effect on the microtubules due to the lack of the microtubule binding domain that is unique to the N terminus of SEPT9_i1. Indeed, at low concentration (10nM), oct_9i3 did not bind microtubules at all (Fig. 3.5A). With increasing concentration (50, 100, and 300 nM), septins started to display spotty binding to seeds and lattices of microtubules. These spots of oct_9i3 were present only transiently on the lattices, disappearing upon shrinkage of the microtubule. Oct_9i3 did remain on the seeds, likely because the seeds are stable (Fig. 3.5B).

The microtubules in the presence of oct_9i3 behaved normally. They grew and shrunk at similar rates as the control samples where septins were absent (Fig. 3.7B, C and D). All microtubules dynamic parameters exhibited small variations, but these did not follow any obvious trend.

3.2.7. Effect of human septin octamers_9i1 on microtubule dynamics

Human septin octamers containing SEPT9_i1 (oct_9i1) do contain the MBD identified by the bioinformatics analysis. So, we expected to observe consistent binding of the septin to both microtubule seeds and lattices. At concentrations as low as 10nM, the oct_9i1 indeed

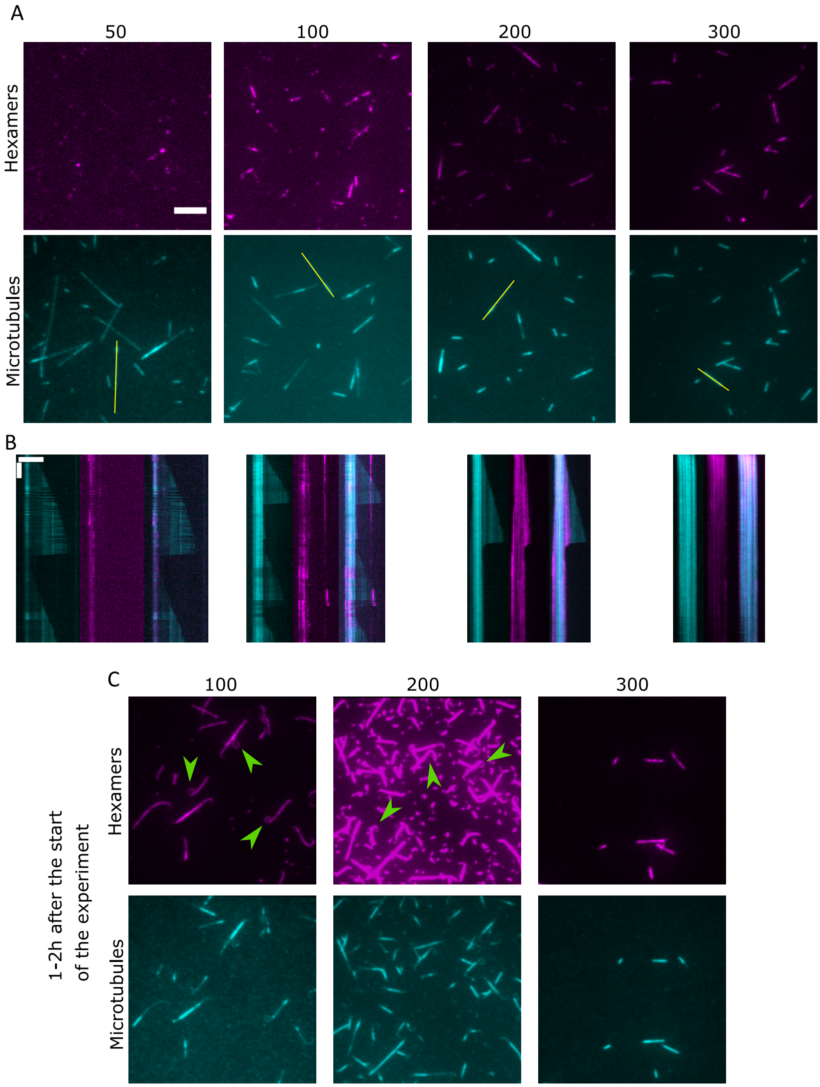

Figure 3.4. Microtubule association of septin hexamers. A. Representative still images taken during time lapse imaging of the microtubule (cyan) dynamic assay in the presence of different concentrations (50, 100, 200, and 300nM) of septin hexamers (magenta). B. Representative kymographs showing the dynamics of the microtubules and hexamers indicated by the yellow lines in A. In kymographs (left to right): microtubules, septins, overlay. C. Representative image of the state of the microtubules and their associated septins at a time point in the range of 1-2h after tubulin and septin hexamers were initially mixed, for different septin concentrations marked on top of the images. Green arrowheads point to loops on the septin-microtubule structures. For all panels, horizontal scale bars are 5µm, and vertical bars are 50 seconds.

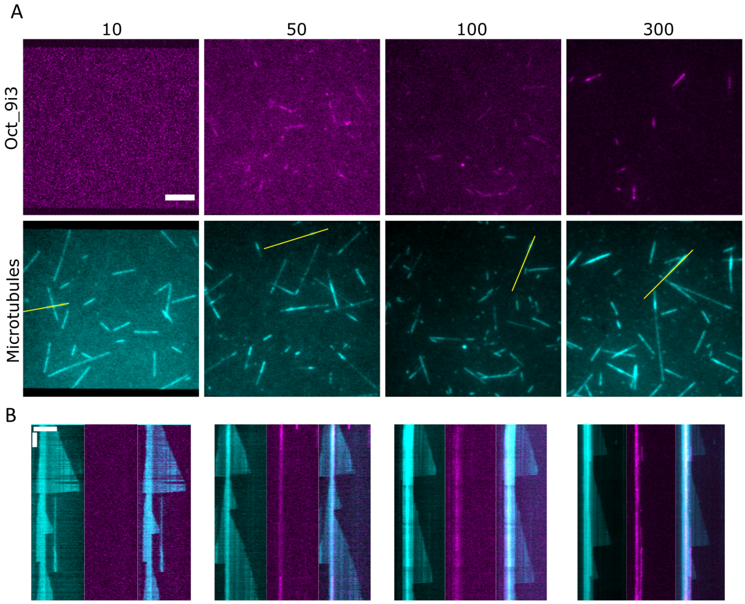

Figure 3.5. Microtubule association of septin octamers with SEPT9_i3. A. Representative still images taken during time-lapse imaging of microtubules (cyan) in the presence of different concentrations (10, 50, 100, and 300nM) of Oct_9i3 (magenta). B. Representative kymographs showing the dynamics of the microtubules and Oct_9i3 indicated by the yellow lines in A. In kymographs (left to right): microtubules, septins, overlay. For all panels, horizontal scale bars are 5μm, and vertical bars are 50 seconds.

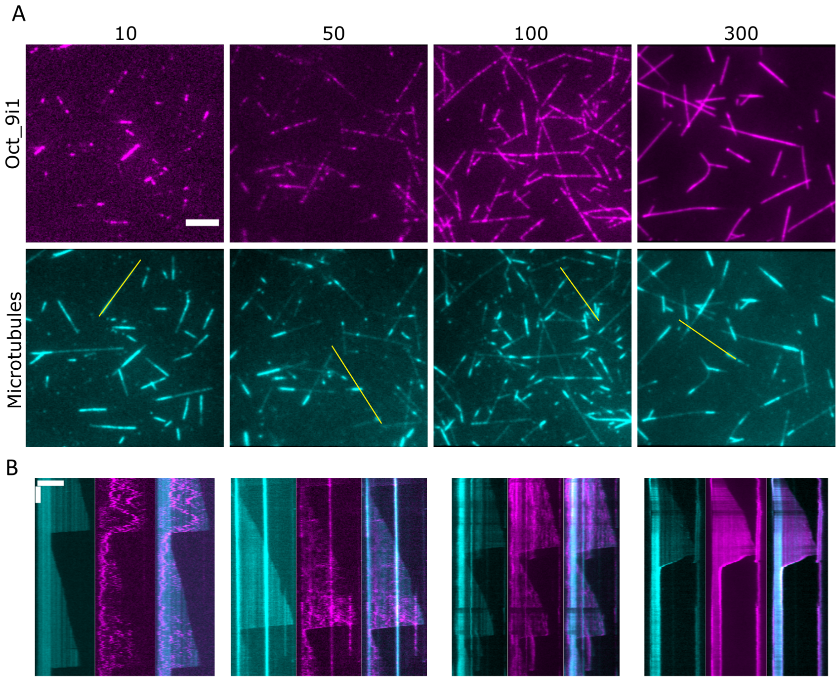

Figure 3.6. Microtubule association of septin octamers containing SEPT9_i1. A. Representative still images taken during time-lapse imaging of microtubules (cyan) in the presence of different concentrations (10, 50, 100, and 300nM) of Oct_9i1 (magenta). B. Representative kymographs showing the dynamics of the microtubules and Oct_9i3 indicated by the yellow lines in A. In kymographs (left to right): microtubules, septins, overlay. For all panels, horizontal scale bars are 5µm, and vertical bars are 50 seconds.

already bound the microtubules, evident from the spotty signal of septin colocalized with microtubules (Fig. 3.6A). These clusters were able to randomly diffuse along the microtubule, as seen on kymographs (Fig. 3.6B). At increasing concentration (50, 100, and 300 nM), the signal of the septin became homogeneous along the whole microtubule (Fig. 3.6A). From the septin signal alone, we could not distinguish between the microtubule seed and the lattice, indicating an homogeneous coverage of the microtubule by the oct_9i1. This is in contrast with the microtubule itself, which shows a higher signal on the seed due to an increased percentage of labeled tubulin used to identify microtubule seeds. The septin signal also perfectly followed the dynamics of the microtubules, as seen in kymographs (Fig. 3.6B).

We analyzed the shrinking velocities, growing velocities, and catastrophe rates of microtubules in the presence of different septin octamers from kymographs like the ones shown in Figure 3.7A. Oct_9i1 showed, similarly to Oct_9i3, only small, likely-non meaningful, variations in the growing speeds and catastrophe rates (Fig 3.7 C and D, respectively). Interestingly, oct_9i1 had a strong impact on the shrinking velocities above a threshold concentration (Fig. 3.7B). At 10 and 50nM of oct9_i1, the shrinking velocity was the same as for the control, around 50µm/min. At 75nM, the shrinking velocity decreased to around 35.3 ±18.1µm/min. This trend was maintained and at 100 and 200nM, the microtubules shrunk at a speed of 24.1 ±22.6 and 16.8 ±15.3μm/min, respectively. The decrease seemed to saturate, since at 300nM the shrinking velocity was 12.5 ±5.4μm/min (Fig. 3.7B).

We observed another interesting behavior of the microtubules in the presence of oct_9i1. Starting at around 200nM, about 10% of the microtubules showed curving of the tips when shrinking (Fig. 3.7 E). A few moments after the catastrophe, the tip of the microtubule was observed to curve, forming a loop that eventually disappeared upon microtubule shrinkage. This effect has previously been proposed to be indicative of protofilament stabilization [197]. The septin signal co-localized with the curved depolymerizing end throughout the shrinkage events (Fig. 3.7E).

Finally, at high enough surface densities of microtubules, we could see septin mediating microtubule interactions. We could observe microtubules pushing (Fig. S3.1A) and pulling from each other (Fig. S3.1B). We even observed microtubule seeds coming together and binding (Fig. S3.1C) and several microtubules growing and shrinking from the same seed (Fig. S3.1D). This indicates that oct_9i1 bound to a microtubule can still interact with other partners (either other oct_9i1 or microtubules).

3.2.8. Effect of human septin octamers bearing mutations that inhibit polymerization in cells on microtubule dynamics

Experiments with non-polymerizable septin mutants (bearing SEPT9_2NCmut) in cells showed that polymerization is needed for oct_9i1 to localize to microtubules (Fig. 3.2G). In order to check if this phenotype is also present in the *in vitro* experiments, we purified human septin octamers containing SEPT2_NCmut tagged with monomeric superfolder GFP (msfGFP) at the C-terminus (Oct_9i1_2NCmut), also used in [144]. As detailed in section 3.4, most experiments in this chapter were done with a mix of 90% unlabeled septin complexes and 10% labeled septin complexes. Due to the lack of an unlabeled Oct_9i1_2NCmut, we performed microtubule dynamics assays with 10, 50, 100 and 300nM of both Oct_9i1 and Oct_9i1_2NCmut with 100% msfGFP tagged octamers. We checked that Oct_9i1 with 100% msfGFP labeling gave similar results as Oct_9i with 10% msfGFP.

We observed no striking difference between Oct_9i1_2NCmut and wild type Oct_9i1 on microtubule binding. At 10nM of Oct_9i1_2NCmut, the coverage of the microtubule was punctate (Fig. 3.8A). At concentrations of 50nM and above, the mutant hetero-octamer fully covered the microtubules (Fig. 3.8A). When analyzing the dynamics, we found that Oct_9i1_2NCmut also had a similar, though not identical, effect on the microtubule dynamics as Oct_9i1. At 10 and 50nM, there was no effect on any of the analyzed parameters for both septin complexes (Fig. 3.8B-D). The Oct_9i1_2NCmut increased the growing speed while Oct_9i1 did not (Fig. 3.8C). At 300nM, both types of complexes slowed down the microtubule shrinking speed to a similar extent (Fig. 3.8B). Interestingly, at 100nM, Oct_9i1_2NCmut slowed down the microtubule shrinking significantly less than the Oct_9i1 (Fig. 3.8B). We conclude that while non-polymerizable Oct9_i1 does not bind microtubules in cells, they do bind and affect microtubule dynamics *in vitro*, though at a somewhat higher concentration than polymerizable Oct9_i1.

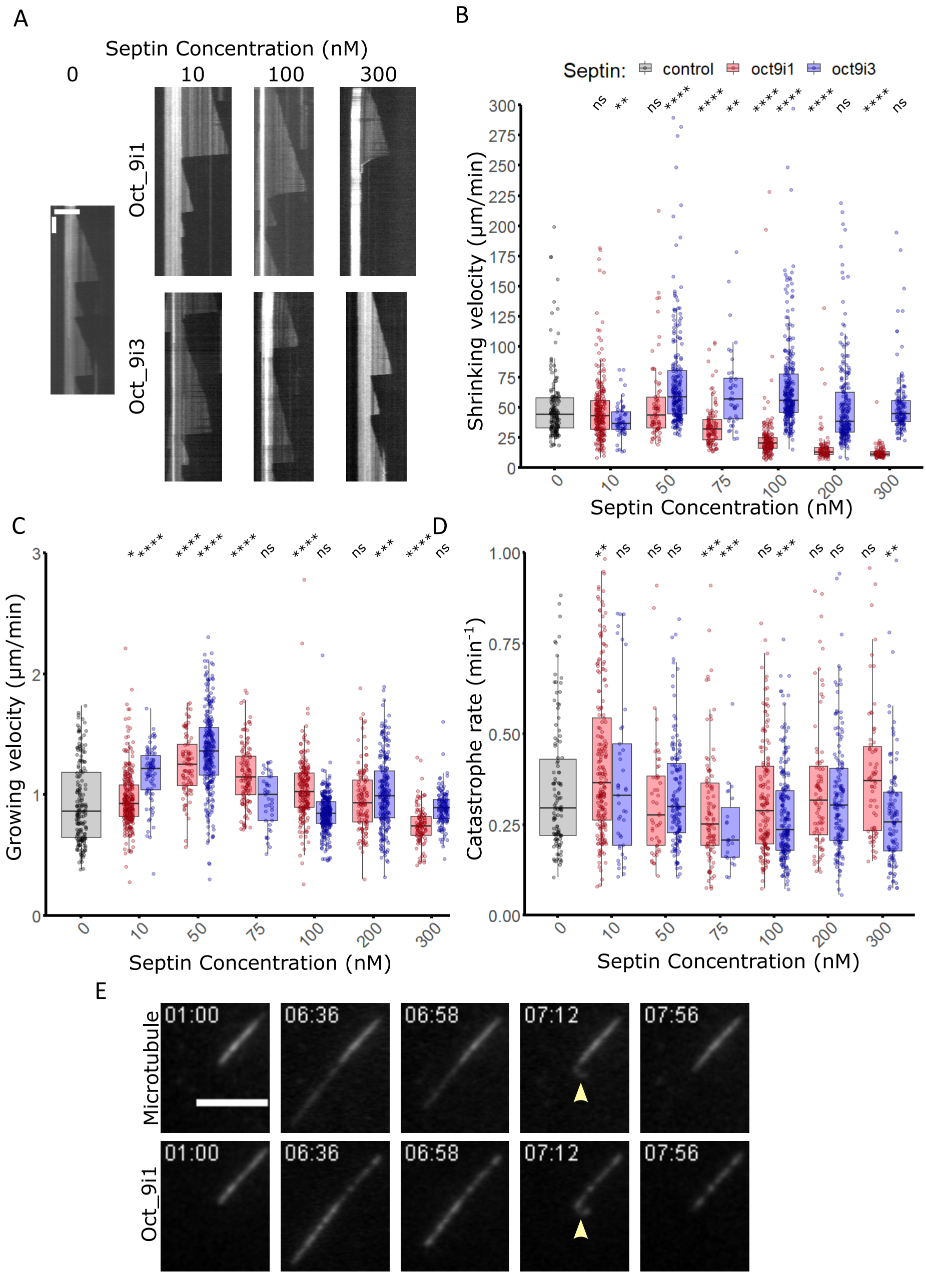

Figure 3.7. Comparison of the effect of septin octamers bearing SEPT9_i1 and i3 on microtubule dynamics. A. Representative kymographs of microtubules illustrating the effect of recombinant septin octamers at different concentrations (see legend) on microtubule dynamics compared to the control case (0 nM septins, left). Horizontal scale bar is 5 µm; vertical white scale bar is 50 sec. B, C, and D. Quantification of microtubule dynamic parameters (shrinking velocity (B), growing velocity (C), and catastrophe rate (D)) as a function of septin octamer concentration. Results are presented as box and whiskers plots superposed with individual data points including outliers (grey: no septin octamers, pink: oct_9i1, light blue: oct_9i3). Two-tailed t-test with Benjamini & Hochberg p-value correction with R, * $p<0.05$, ** $p<0.01$, *** $p<0.001$, **** $p<0.0001$. E. Snapshots at indicated times (min:sec) of a microtubule (top) and associated oct_9i1 at 200nM (bottom). Yellow arrowheads point to the curved tip of the microtubule. Scale bar is 5 µm.

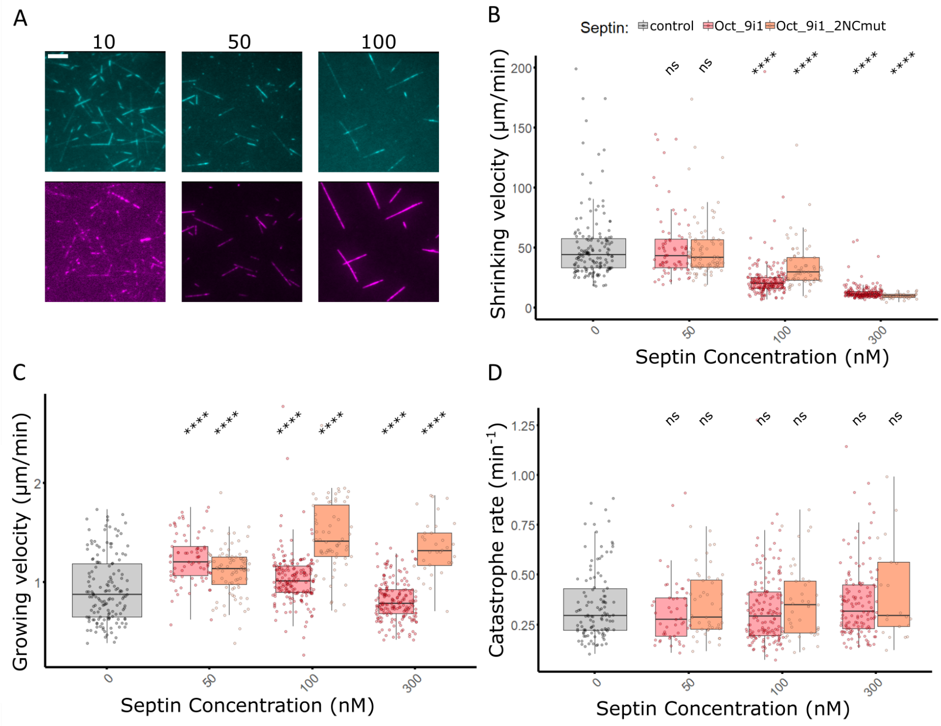

Figure 3.8. Binding and effect of Oct_9i1_2NCmut on microtubules. A. Representative still images taken during time lapse imaging of microtubules (cyan) in the presence of different concentrations (10, 50, 100nM) of Oct_9i1_2NCmut (magenta). Scale bar is 5µm. B, C, and D. Quantification of microtubule dynamic parameters (shrinking velocity (B), growing velocity (C), and catastrophe rate (D)) as a function of septin octamer concentrations. Results are presented as box and whiskers plots superposed with individual data points including outliers (grey: no septin octamers, red: oct_9i1, orange: oct_9i1_2NCmut). Two-tailed t-test with Benjamini & Hochberg p-value correction with R, * $p<0.05$, ** $p<0.01$, *** $p<0.001$, **** $p<0.0001$. p-value 2-tailed t-test = $4.3*10^{-4}$ for the difference between Oct_9i1 and Oct_9i1-i5 at 100nM.

3.2.9. Effect of human septin octamers_9i1_9i5 on microtubule dynamics

In parallel to our experiments in cells, we next studied the effect of the SEPT9_i1-3 common N-terminus in the context of human septin octamers *in vitro*. To do so, we purified recombinant dark and msfGFP-tagged human septin octamers containing SEPT9_i1-i5 (Oct_9i1-i5) (Fig. 3.2A).

In contrast to Oct_9i1 (Fig. 3.6), Oct9_i1-i5 fully covered the microtubules at 10nM (Fig. 3.9A). Interestingly, Oct_9i1-i5 had stronger and also qualitatively different effects on the microtubule dynamics compared to Oct_9i1. At 10nM, Oct_9i1-i5 already reduced the shrinking velocity of the microtubules to the same level that required 75-100nM of Oct_9i1 (Fig. 3.9B). At 50 nM, shrinkage of microtubules was frequently blocked before the shrinking microtubule plus end reached the seed (Fig. 3.9C). This effect was never observed for Oct_9i1 and indicates a much stronger stabilizing effect. At 50nM, the shrinkage velocity was reduced by the same extent by Oct9_i1-i5 as at 10nM (Fig. 3.9B). At 100nM, Oct_9i1-i5 binding blocked microtubule shrinkage even more strongly (Fig. 3.9A and C), with complete blockage of microtubule shrinkage in 50% of cases. For the microtubules that still shortened, the shrinking velocity was unchanged with respect to the control in the absence of septin complexes and there was low fluorescent signal of oct_9i1-i5 on the growing plus end. For the microtubules that did not shrink, we initially observed growth upon incubation with septin complexes, but growth eventually stopped (Fig. 3.9A and C). At 300nM, Oct_9i1-i5 prevented microtubule growth from the start of the experiment. Some of the microtubules showed a very short and curved lattice that had formed during the time that it took to place the sample in position for imaging (inset in Fig. 3.9A).

Since microtubules did not shrink in the presence of Oct_9i1-i5 above 100nM, we did not observe any curving during shrinkage. This effect, in combination with a lower microtubule seed density, also did not allow us to analyze oct_9i1-i5-mediated microtubule-microtubule interactions. At concentrations above 100nM, some microtubules (inset in Fig. 3.9A) grew with a curved plus end that retained it shape, not undergoing catastrophe. This phenotype was similar to what was observed for microtubules in the presence of more than 100nM hexamers after 1-2h (Fig. 3.4C).

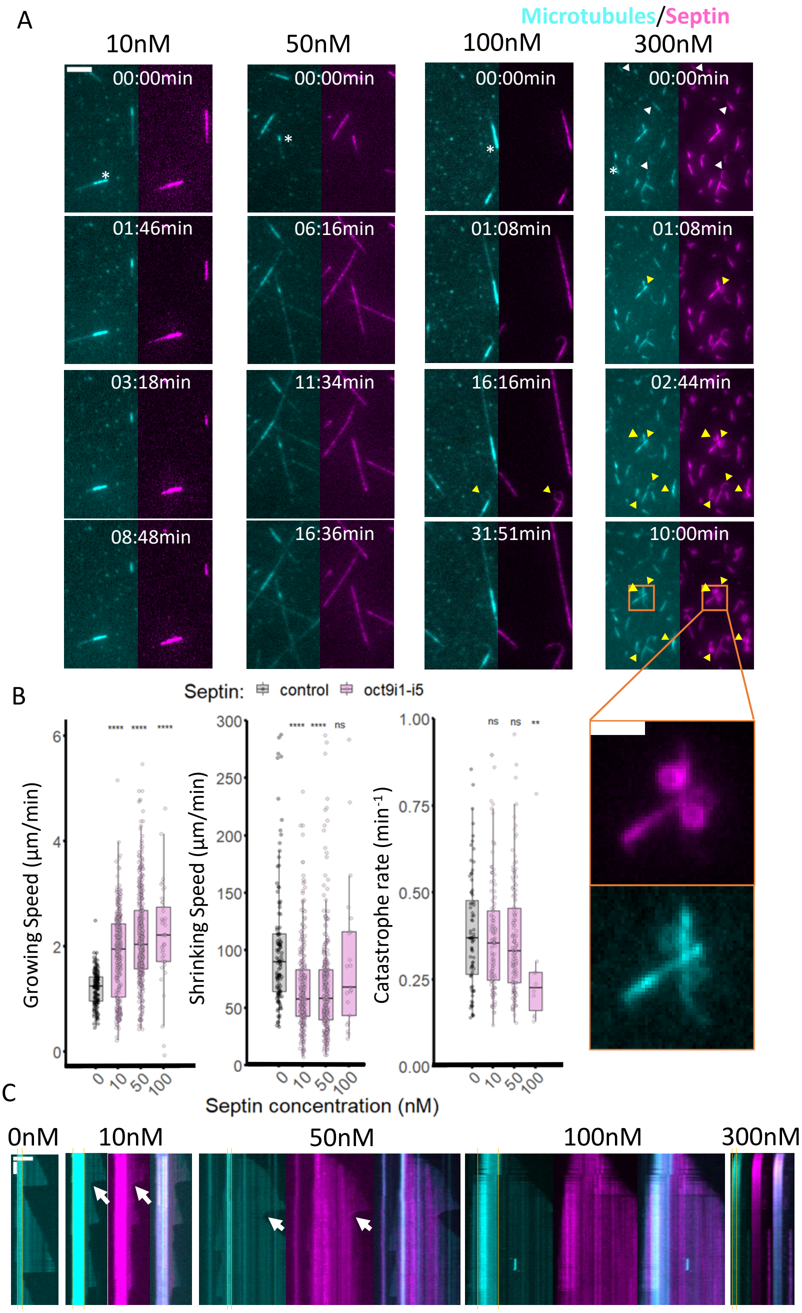

A
Microtubules/Septin
10nM
50nM
100nM
300nM
00:00min
01:46min
03:18min
08:48min
06:16min
11:34min
16:36min
01:08min
16:16min
31:51min
02:44min
10:00min
B
Septin: control oct9i1-i5
Growing Speed (µm/min)
Shrinking Speed (µm/min)
Catastrophe rate (min-1)
Septin concentration (nM)
0 10 50 100
C
0nM
10nM
50nM
100nM
300nM

Figure 3.9 ***(preceding page).*** **Effect of Oct9_i1-i5 octamers on MT dynamics.** A. Time-lapse image series (time stamp in units of min:sec) of oct9_i1-i5 octamers (magenta) interacting with dynamic microtubules (cyan) at different concentrations in the range of 10-300nM. Close up of loops seen at 300nM is shown in the inset. White asterisks indicate the microtubule for which kymographs are shown in B. White arrowheads indicate MTs with a short lattice formed in the presence of 300nM Oct9_i1-i5. Yellow arrowheads indicate curved MT structures formed in the presence of 300 nM Oct9_i1-i5. Scale bar indicates 5µm. Scale bar in close up inset indicates 2µm. B. Quantification of microtubule dynamic parameters (growing velocity, shrinking velocity, and catastrophe rate) as a function of septin octamer concentration. Results are presented as box and whiskers plots superposed with individual data points including outliers (grey: no septin octamers, pink: oct_9i1-i5). Two-tailed t-test with Benjamini & Hochberg p-value correction with R, * $p<0.05$, ** $p<0.01$, *** $p<0.001$, **** $p<0.0001$. C. Representative kymographs. White arrows indicate regions where septin is accumulated, which coincided with regions where microtubule shortening is blocked. In kymographs (left to right): microtubules, septins, overlay. Yellow lines indicate the positions of the GMPCPP-stabilized microtubule seed. In all panels, horizontal scale bar is 5µm, vertical scale bar is 50s.

3.3. Discussion

In this work we found that the unique N-terminus of SEPT9_i1 is a MBD that mediates septin-microtubule binding. A typical MBD of the MAP2/Tau family consists of tandem repeats that mediate binding of the MAP to the interphase between α and β tubulin [198]. SEPT9_i1 lacks these repeats. We hypothesize that this is compensated by the oligomeric and polymerizing nature of septins. First, the NC interface-mediated SEPT9-SEPT9 binding in the center of septin octamers brings together two SEPT9_i1 MBDs. This arrangement may mimic a tandem repeat of other MAPs. However, other MAPs contain more than two repeats and, typically, are smaller proteins [198]. By comparison, oct_9i1 has a lower density of microtubule-binding repeats. This might make the septin octamer-microtubule binding weaker. A way to compensate for this weakening may be septin's ability to polymerize. On oct_9i1 filaments, two MBD repeats would be located along the filament with a repeat distance of 32nm [102], strengthening the binding of a septin filament compared with a single septin octamer. Our experiments in cells showed that, indeed, SEPT9_i1 containing octamers need to polymerize into filaments in order to bind microtubules, as seen by the inability of Oct_9i1_2NCmut to colocalize with microtubules. Other recent work also confirms that microtubule-bound septins in cells are polymeric [144]. However, in our *in vitro* reconstitution experiments, Oct_9i1_2NCmut did bind microtubules and affect their dynamics similarly to Oct_9i1. We think that this discrepancy with the observation in cells is due to the *in vitro* conditions. Obviously, cells have many more proteins, such as the Borg family that may regulate septin-microtubule interactions [141], a different pH, and crowding effects that could affect the septin-microtubule interactions more than in the reconstituted system. We hypothesize that the recruitment of septins to the microtubule interface could rescue the polymerization of the 2NC mutant septin complexes in the *in vitro* conditions, leading to the same microtubule-stabilizing effects as the WT octamers, though at increased concentrations (Fig. 3.8B).

The dynamic microtubule assays showed important evidence to understand how septins interact with microtubules, specifically the role of the N-terminus of SEPT9 in the interaction.

First, recombinant septin octamers containing SEPT9_i1, the septin complex that interacts with microtubules in cells, were able to bind microtubules already at low (10nM) concentrations and stabilize microtubules at higher (>100nM) concentrations. These octamers furthermore mediated microtubule-microtubule interactions and even microtubule seed bundling. All these effects hint to a possible role of septins in microtubule bundling. Septins have been found to colocalize with bundled microtubules in cells, even in the absence of microtubule acetylation [103], a bundling marker. However, it is not known if septins preferentially recognize microtubule bundles or create these bundles, similarly to their ability to bundle actin *in vitro* ([101, 102] and see Chapter 6). Septin-mediated microtubule bundling could further stabilize the septin-microtubule interaction, by increasing the number of binding points of a single septin filament or paired filament. The loss of bundling ability could thus explain the lower colocalization on microtubules of the mutants containing changes in the (K/R-R/x-x-D/E) motifs that we observed in R106W and S111F SEPT9_i1 mutants.

Second, both human septin hexamers and Oct_9i1-i5 showed a high microtubule stabilizing ability. At low concentrations, hexamers only weakly bound microtubules while oct_9i1-i5 bound microtubules more than oct_9i1 and even affected their dynamics. At higher concentrations, both hexamers and oct_9i1-i5 accumulated on microtubules over time - oct_9i1-i5 faster than hexamers likely due to the presence of the MBD - and stopped microtubule dynamics. In contrast, oct_9i3 could not bind microtubules at low concentrations and only partially colocalized with microtubules at higher concentration. Consistent with the strong binding of Oct_9i1-i5 *in vitro*, in cells found that Oct9_i1-i5 completely relocalized septins to microtubules whereas Oct_i1 left part of the septin pool on actin. The only difference shared by hexamers and oct_9i3, and oct_9i1-i5 and oct_9i3, is the absence of the common N-terminus shared by the long isoforms of SEPT9. These observations lead to the conclusion that the common N-terminus of the SEPT9 long isoforms hinders the microtubule association of septins. This hindering effect, together with other modulating proteins such as the Borg family [141], possibly modulates the septin-binding interactions in cells by allowing septin octamers to localize to actin filaments, to microtubules, or to both, depending on the cell's needs. Recent evidence already shows that septins furthermore mediate actin-microtubule crosstalk in neuronal growth cones [199], highlighting the importance of understanding how septin binds to these two types if cytoskeleton filaments and how their interaction is regulated.

Summarizing, we identified the MBD of septin octamers located in the first 25 amino acids of SEPT9_i1 and we studied the effect of septins on microtubules *in vitro*. Our findings revealed the need of septins to polymerize into filaments to bind microtubules, septin-mediated microtubule stabilization, and the regulatory effect of the SEPT9 long isoform common N-terminus. However, we could not establish the spatial arrangement of the septin-microtubule association. Studying this arrangement using other techniques, such as cryoEM, could give insight into how the unique SEPT9_i1 MBD and the common N-terminal region of the long SEPT9 isoforms mediate and modulate septin-microtubule binding. CryoEM experiments could also determine whether septins bind as single or paired filaments to the microtubule lattice. Further research is also required to determine whether septins associate with pre-existing microtubule bundles or mediate microtubule bundling. We have evidence to suggest the latter, but other targeted experiments both *in vitro* and in cells are needed to answer this question. Finally, despite the interesting evidence that we found on the role of the common N-terminus of the SEPT9 long isoforms in microtubule binding, we still do not exactly understand how this region tunes the binding of septin octamers to microtubules. Further studies, for instance with mutant on the (K/R-R/x-x-D/E) motifs, are needed to better understand the interaction of septins with microtubules and as a way to understand how this region affects HNA. Additionally, septin [91, 94] or microtubule [200] post-translational modifications (PTM) and other accessory proteins [141] likely further tune the interaction between septin and microtubules. Using *in vitro* reconstitution of septin complexes and microtubules with controlled PTMs or accessory proteins included can help understanding the precise control of this interaction.

3

3.4. Materials and methods

All chemicals were obtained from Merck Sigma unless specified otherwise.

3.4.1. Human cell lines

U2OS (ATCC) cells were maintained in Dulbecco's modified Eagle's medium (DMEM, Gibco) supplemented with 4 mM GlutaMAX (Gibco), 10% fetal bovine serum (Gibco), and 1% sodium pyruvate (Gibco) (supplemented DMEM). They were maintained in the presence of a 5% CO_2 humidified atmosphere at 37℃.

3.4.2. Plasmids coding for fluorescent septin constructs and transfection

To drive expression of the constructs in the U2OS cells, we used the immediate early enhancer and promoter of human cytomegalovirus (CMV promoter, 508 base pairs). Human SEPT9_i1 cDNA was a gift from C. Montagna (Albert Einstein College of Medicine, NY, USA). Human SEPT9_i3 cDNA was a gift from W. Trimble (University of Toronto, ON, Canada). A synthetic human SEPT2 coding sequence (Eurofins Genomics, Germany) was generated using the codon usage of mouse SEPT2 except for the five codons that differ between the two species, for which we used codons encoding the human residues. C-terminal green and red fluorescent protein fusions were generated using msfGFP (Costantini et al., 2012; Cranfill et al., 2016; Pedelacq et al., 2006; Zacharias et al., 2002) and monomeric Apple (mApple) (Cranfill et al., 2016; Shaner et al., 2008), respectively. All constructs were generated with two-insert seamless cloning (In-Fusion HD Cloning Plus Kit from Takara Bio, 638910) using NheI/BamHI linearized plasmid backbones (Addgene plasmid 54759) and the oligonucleotide primer sequences (listed inTable S3). Cloning oligo (<60 bp) or EXTREmer (>60 bp) primers were synthesised and purified by Eurofins Genomics, Germany. The restriction enzymes used were FastDigest enzymes obtained from Thermo Fisher Scientific. All plasmids were verified by sequencing (Eurofins Genomics, Germany) after each cloning step, including the midipreps used for plasmid production. Constructs (3 μg) were transiently transfected by nucleofection in cells using a Cell line Nucleofector kit V and the Amaxa nucleofector program U2OS X- 001 and T47D X-005, following the manufacturer's instructions (Lonza). Cells were cultured for 72 h after transfection and either fixed or extracted for proteins to perform immunocytochemical or biochemical analyses, respectively.

3.4.3. siRNA and transfection

The following 19-mer duplex siRNAs were purchased from LifeTechnologies: siRNA control (siCtrl) targeting the Escherichia coli β galactosidase (LacZ) (5′-GCGGCUGCCGGAAUUUACC-3′); SEPT9 (5′-GGAUCUGAUU- GAGGAUAAA-3′) targeting the 3′ untranslated region of all human SEPT9 mRNA variants; SEPT7 (5′-CGACUACAUUGAUAGUAAA-3′) targeting the human mRNA coding region; and αTAT1 (5′-CGCACCAA- CUGGCAAUUGA-3′), the design of which was based on validated siRNA αTAT1 #2 from Shida et al. [201]. Transfection of 200 or 134 pmol of siRNA was performed using Lipofectamine RNAiMAX (Invitrogen, 13778075) or an Amaxa cell line nucleofection kit V (Lonza, VCA-1003) following the manufacturer's instructions, respectively. Cells were cultured for 72 h after transfection and were fixed to perform immunostaining.

3.4.4. Antibodies

Labeling of septins on immunocytochemistry coverslips (ICCs) was achieved with the following antibodies: rabbit polyclonals against human SEPT2 (Sigma-Aldrich, HPA018481, WB 1:500); human SEPT9 (Sigma-Aldrich, HPA042564 and HPA050627, WB 1:1000 and ICC 1:1000; Proteintech, 10769-1-AP, WB1:500); SEPT7 (IBL, 18991, WB 1:500 and ICC 1:100); SEPT6 (a kind gift from Makoto Kinoshita, Nagoya University, Japan; WB 1:500); and SEPT10 (Sigma-Aldrich, HPA047860, WB 1:500). Rat monoclonals against human SEPT9_i1 (clone 4D2A5, WB 1:500), human SEPT9_i2 (clone 5A65F, WB 1:500) or human SEPT9_i3 (clone 1A6C2, WB 1:500), and human SEPT7 (clone 10A7, WB 1:250 and ICC 1:50) were also used and produced as described previously (Verdier-Pinard et al., 2017). Antibodies against α-tubulin consisted of: mouse monoclonal (Sigma-Aldrich, DM1A, 05-829,WB1:4000 and ICC:100); rat monoclonal (Invitrogen, YL1/2, MA1-80017, ICC 1:100); mouse monoclonal anti-acetylated K40 (Santa Cruz Biotechnology, 6-11B1, sc- 23950, WB 1:2000 and ICC 1:250). The mouse monoclonal anti-glutamylated tubulin (Adipogen, GT-335, AG-20B-0020-C100, and polyE, AG-25B-0030-C050,WB1:2000) was also used. Labeling of actin was performed using phalloidin-Atto 390 (Sigma-Aldrich, 50556, ICC1:100) or phalloidin-tetramethylrhodamine B isothiocyanate (Sigma-Aldrich, P1951, ICC 1:100). For ICC (1:250) the following fluorophores conjugated to secondary antibodies were used: DYLIGHT405, Alexa Fluor 405, Alexa Fluor 488 and Alexa Fluor 594 (Jackson ImmunoResearch), and Alexa Fluor 647 (Invitrogen).

3.4.5. Immunocytochemistry

Multiplex immunocytochemistry was carried out on cells cultured on collagen-coated coverslips followed by 4% formaldehyde fixation as described previously (Verdier-Pinard et al., 2017). Images were acquired using a Zeiss structured light ApoTome microscope equipped with a 63×/ 1.4 Plan Apochromat objective and an Axiocam MRc5 camera using AxioVision software, or a Zeiss LSM880 META confocal microscope equipped with a 63×/1.46 Plan Apochromat objective and a GaAsP detector using Zen software.

3.4.6. Analysis of the colocalization of septins with microtubules and with actin stress fibers

For the assessment of SEPT9-GFP construct colocalization with microtubules and actin fibers in individual cells, stack of images (z steps of 0.85μm) were acquired using an inverted Zeiss LSM880 META confocal microscope and a Plan Apochromat 63×/1.4NA oil objective. Colocalization evaluation was achieved by image analysis using Fiji Software (Schindelin et al., 2012). z-stacks of individual cells were examined for colocalization of septins with total α-tubulin, acetylated K40 α-tubulin, and F-actin, from top to bottom. Cells were counted as positive for colocalization of septins with microtubules or with F-actin when septin the fluorescence signal was co-aligned with microtubules and/or acetylated microtubules, or with ventral stress fibers, respectively. The percentage of cells positive for both septin-microtubule and septin-stress fiber colocalization, only positive for septin-stress fiber colocalization, and only positive for septin-microtubule colocalization were designated in graphs as ’microtubule and actin’, ’actin’, and ’microtubule’, respectively.

3.4.7. Purification of human septin complexes

All the variants of septin oligomers were purified and their quality was checked as detailed in chapter 2. We used wild type hexamers and Oct_9i1, Oct_9i3, Oct_9i1_2NCmut, and Oct_9i1-i5. In the Oct_9i1_2NCmut oligomers, SEPT2 contained two point mutations, F20D and V27D. These mutants contain two residues of the α 0 helix changed to negatively charged amino acids, which inhibits septin polymerization in cells [83, 195]. In Oct_9i1-i5, SEPT9 is mutated to SEPT9_i1-i5, which consists of a deletion on SEPT9_i1 (Δ26-252). This mutation removes the common N terminus of the long SEPT9 isoforms (i1-i3) by fusing the unique N-terminus of SEPT_9i1 to SEPT9_i5, a short N-terminus SEPT9 isoform. Septin complexes were fluorescent tagged with msfGFP on the C-terminus of SEPT2. For purification, SEPT2 contained a his_6-tag in the N-terminus and SEPT7, for hexamers, or SEPT9, for octamers, contained a Strep-II-tag on the C-terminus.

3.4.8. GMPCPP-stabilized microtubule seeds preparation

GMPCPP-stabilized microtubule seeds serving as a nucleation site for dynamic microtubules were prepared using an established double-cycle method [202]. Briefly, a ~22 µM mixture of tubulin (~11 µM tubulin dimers) in MRB80 (80mM PIPES pH 6.8, 4mM $MgCl_2$, 1mM EGTA), composed of 75% unmodified tubulin dimers (Cytoskeleton, Inc.), 15% rhodamine-labeled tubulin dimers (Cytoskeleton, Inc.) and 10% biotin-modified tubulin dimers (Cytoskeleton, Inc.), was spun down using an Airfuge® Air-driven ultracentrifuge (Beckman Coulter Inc., Brea, California, USA) for 5 minutes at 30psi with a rotor at ~4℃. Then, the mixture was complemented with 1mM guanylyl-(alpha, beta)-methylene-diphosphonate (GMPCPP) from a 10mM stock solution in MRB80, thus diluting the tubulin to 20µM. This mixture was incubated at 37℃ for 30 minutes to polymerize tubulin, and immediately airfuged for 5 minutes at 30psi with the rotor at room temperature to pellet GMPCPP-stabilized microtubules. Afterwards, the supernatant was discarded and the pellet was resuspended in MRB80 at 37℃ to a final tubulin concentration of 20µM, assuming an 80% recovery of the tubulin. The mixture was incubated on ice for 20 minutes to depolymerize the microtubules. Subsequently, it was complemented with 1mM GMPCPP, incubated at 37℃ for 30 minutes to repolymerize the microtubules, and airfuged for 5 minutes at 30psi with a rotor at room temperature. The pellet, containing GMPCPP-stabilized microtubule seeds, was resuspended in MRB80 at 37℃ supplemented with 10% glycerol, snap-frozen, and stored at -80℃ until use.

3.4.9. Microtubule dynamic assay

Nr. 1 Menzel coverslips (Thermo Fisher scientific, Cat. # 11961988) and glass slides (Thermo Fisher scientific, Cat. # 11879022) were cleaned in base piranha solution (5% hydrogen peroxide, 5% ammonium hydroxide, both from Sigma-Aldrich with product numbers 31642 and 221228, respectively) at 70℃ for 10 minutes in a fume hood. Using using safety goggles, gloves, and a plastic apron, the slides and the coverslips were washed extensively by rinsing with Milli-Q water and stored in Milli-Q water for up to 5 days.

Just before use, a coverslip and a glass slide were blow dried with a stream of N_2

gas. Flow channels were prepared by placing parallel 2x20 mm parafilm strips spaced by 2-3mm between the glass slide and the coverslip. The parafilm was melted by placing the chambers on a hotplate at 120℃. After cooling down, the chambers were passivated by subsequent 10 minutes incubations with 0.2mg/mL Poly(L-lysine)-graft-biotinylated Polyethylene glycol (SuSoS, Cat. # CHF560.00) in MRB80, 0.2mg/mL neutravidin (Thermo Fisher Scientific, Cat. # 10675574) in MRB80, 0.5mg/mL κ-casein (Sigma-Aldrich, Cat. # C0406) in MRB80, and 1wt% Pluronic F-127 (Sigma-Aldrich, Cat. # p2443) in MRB80, in that order and without intervening washing steps. The channels were washed with three channel volumes (~30µL) of MRB80 at the end of the passivation process.

Then the channels were incubated for 10 minutes with an aliquot of GMPCPP-stabilized seeds that was quickly thawed at 37℃, allowing the microtubule seeds to bind to the surface via biotin-neutravidin interactions. Microtubule polymerization was induced by immediately flushing into the channel 20 µM tubulin (3% rhodamine-labeled tubulin) in a 5:1 volume ratio of MRB80:septin buffer complemented with 0.5 mg/mL κ-casein to prevent unspecific interactions, 0.1% methylcellulose (Sigma-Aldrich, Cat. # M0512) as a crowding agent, 1 mM ATP (Sigma-Aldrich, Cat. # A9187), 1 mM GTP (Sigma-Aldrich, Cat. # G8877) and an oxygen scavenging system composed of 50 mM glucose(Sigma-Aldrich, Cat. # G8270), 200 µg/ml catalase (Sigma-Aldrich, Cat. # C30), 400 µg/ml glucose-oxidase(Sigma-Aldrich, Cat. # G6125), and 4 mM dithiothreitol (DTT) (Sigma-Aldrich, Cat. # 11583786001). If needed and unless otherwise specified, a mixture of 90% unlabelled and 10% msfGFP-labeled septin hexamers or octamers (containing either SEPT9_i1, SEPT9_i3, or SEPT9_i1-i5) was added to the previous mix at different concentrations in the range of 10 to 300 nM. Oct_9i1_2NCmut was used 100% msfGFP-labelled. Before flushing the solution into the channel, it was airfuged for 5 minutes at 30 psi with a rotor at ~4℃ to remove any protein aggregates.

3.4.10. TIRF microscopy imaging

The samples were immediately imaged after the addition of septin using a Nikon Ti2-E microscope complemented with a Gataca iLAS2 azimuthal TIRF illumination system heated to 30℃ using an Okolab incubator system. The sample was illuminated with 488-nm and 561-nm lasers (Gataca laser combiner iLAS2) to visualize the septin and the tubulin signals, respectively. To allow for fast imaging, the fluorescence signal was split with a Cairn Research Optosplit II ByPass containing a Chroma ZT 543 rdc dichroic mirror and filtered with either a 525/50 or a 600/50 chroma bandpass filter. The images were recorded with a Andor iXon Ultra 897 EM-CCD camera using an exposure time of 75 ms, for 10-20 minutes with a frame rate of 1 frame/second.

3.4.11. Image analysis and statistics

Microtubule dynamics were analysed by kymograph analysis [203]. Kymographs were built with the reslice tool in FIJI [154] by reslicing a manually drawn line that went from the beginning of the microtubule seed to the tip of the microtubule in its maximum length. In the kymographs, we can observe the positions of the microtubule tips over time. Despite septins bound to both ends, the analysis was only done on the plus ends of the microtubules, which can be distinguished from the minus ends via the longer final length and higher growth velocity of the former. Growth and shortening rates were obtained as the slopes of manually fitted straight lines on the growing or shortening phases, determined by manual inspection, of the microtubule plus ends. The catastrophe rate was calculated as the inverse of the time that a microtubule spends growing.

3.5. Supplementary information

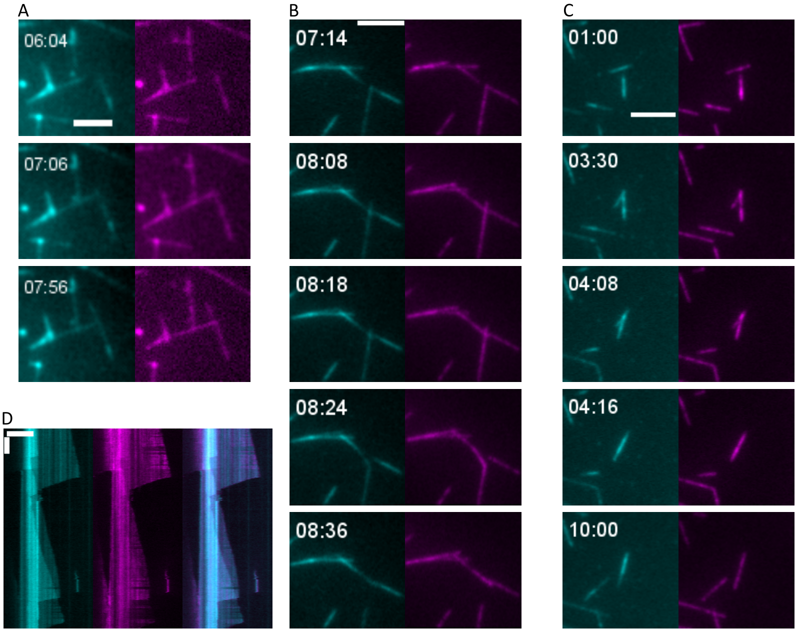

Figure S3.1. Septin octamers with SEPT9_i1 mediate microtubule-microtubule interactions. A. Snapshots at indicated times (min:sec) of a microtubule (cyan) and associated oct_9i1 at 200nM (magenta) showing a microtubule pushing another one. B. Snapshots at indicated times of a microtubule and associated oct_9i1 at 200nM showing a microtubule pulling from another one. C. Snapshots at indicated times of a microtubule and associated oct_9i1 at 200nM showing two microtubule seeds binding to each other. D. Representative kymograph of several microtubules (cyan) and their associated oct_9i1 growing from the same seed. Scale bars are 5 μm. Vertical scale bar are 50s.

Acknowledgements

We thank Jeffrey den Haan for his help with protein purification. We thank Marileen Dogterom, Celina Alkemade, and Ilina Bareja for their advise on the use of tubulin for reconstitution experiments and on the image analysis of the dynamic microtubule assays.

3

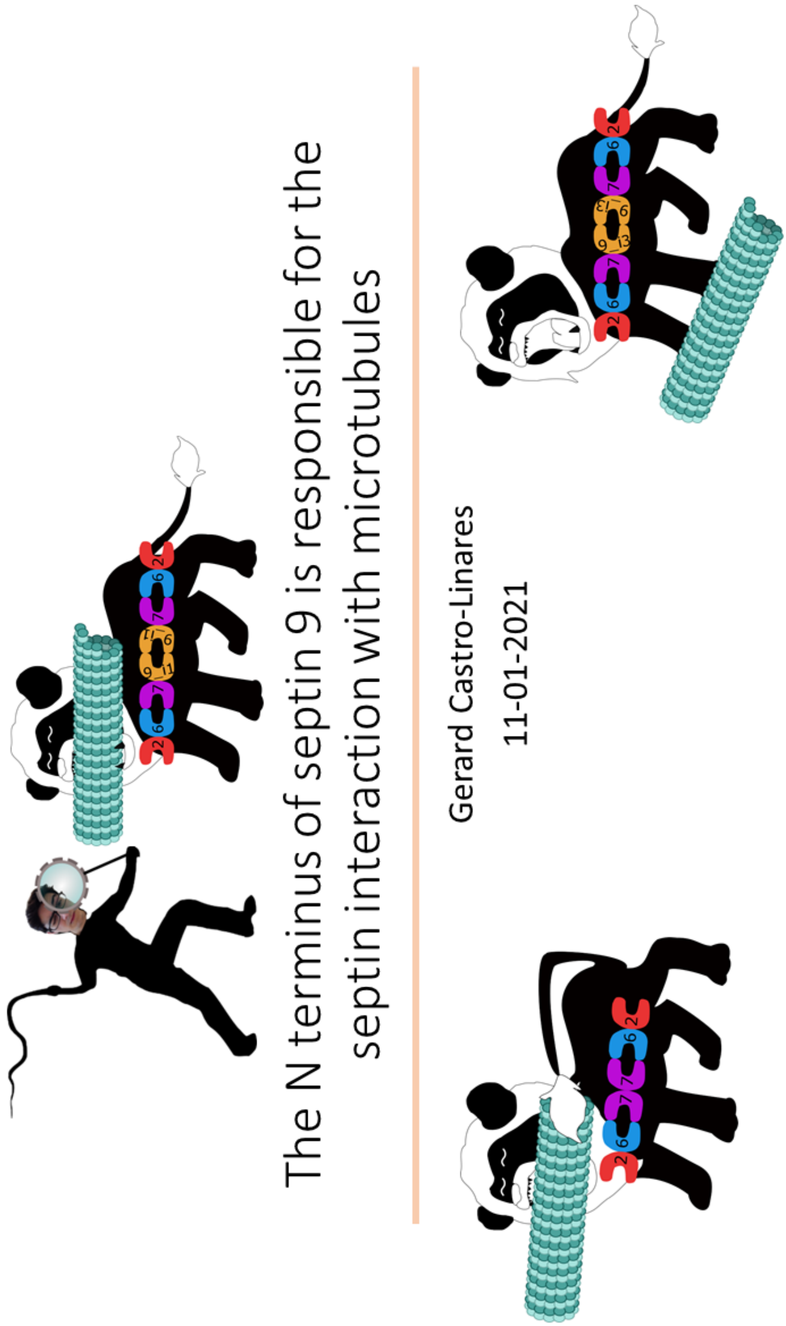
The N terminus of septin 9 is responsible for the septin interaction with microtubules
Gerard Castro-Linares
11-01-2021

Chapter 4

Septin oligomers form morphologically different membrane-bound networks depending on the oligomer species and on the environmental conditions

The cell membrane is a critical but mechanically fragile cellular component whose chemical and physical properties are tightly regulated. Septins' cortical localization and their ability to directly bind lipid membranes in vitro is increasing their interest as a membrane regulator. In this chapter we investigate how septins bind lipid bilayers with a special focus on the question of whether human septin hexamers and octamers differ in their membrane-binding behavior and how environmental conditions control this behavior. We use a multi-modal approach consisting of quartz crystal microbalance with dissipation monitoring, atomic force microscopy and transmission electron microscopy of septins on flat supported lipid layers. We found that PIP2 is critical for septin binding and polymerization on lipid membranes, while DOPS synergistically assists this process. We also show that septin oligomers form two morphologically different types of membrane-bound films, one bundle-based and the other filament-based, depending on the oligomer species, the type of membrane model, and the presence or absence of GTP. Finally, we use computer simulations to find the critical processes governing the formation of the bundle-based networks based on assumptions derived from the experimental observations. We find that filament growth, pairing and alignment can lead to the formation of bundle-based networks resembling the experimental observations.

This chapter is based on a manuscript with the same name by Gerard Castro-Linares*, Djim de Ridder*, Felix Frey*, SaFyre Reese, Manos Mavrakis, Ralf Richter, Timon Idema, and Gijsje H. Koenderink, which is currently in preparation for publication. Gerard Castro-Linares and SaFyre Reese did the QCM-D experiments. Djim de Ridder and Gerard Castro-Linares did the TEM experiments. Djim de Ridder also did AFM experiments under the supervision of Gerard Castro-Linares and Lucia Baldauf. Felix Frey performed the simulations with input

4.1. Introduction

The cell membrane is a key cellular structure composed of a lipid bilayer that separates the cell from its environment. In animal cells, which lack a cell wall to protect the fragile lipid bilayer, the membrane needs to resist external forces while being flexible enough to allow for movements that drive cell migration, cell division, and other important processes [204]. This remarkable mechanical behavior emerges from coupling the cell membrane to the cytoskeleton. The cell cortex, which is thin layer of cytoskeletal proteins anchored to the membrane, is the main cytoskeletal structure that provides rigidity and controls the membrane shape. The filamentous proteins found in the cortex are actin [43, 204, 205], septin [106], and spectrin [206], which together with accessory proteins that mediate membrane-anchoring, nucleation, bundling, and motility [47] form a dynamic cortex. The most widely studied filamentous protein in the cortex is actin. So, the relative contributions and interactions of the different filamentous components are not fully understood.

There is growing evidence that septins in the cell cortex also exert a major influence on membrane shape and rigidity. They are a family of cytoskeletal [76] proteins conserved in all eukaryotes except in higher plants [75]. They are involved in many cellular functions such as cell division [106], cell-cell adhesion [130], cell motility [119], morphogenesis [131], bacterial and viral infection [77], and the establishment and maintenance of cell polarity [132]. In most species, septins form small palindromic rod-shaped hetero-oligomers composed of septins from different subfamilies [76, 86, 96, 102, 133]. The length of the hetero-oligomers depends on the species. For example, *Caenorhabditis elegans* septins form tetramers [80], *Drosophila melanogaster* septins form hexamers [81], *Saccharomyces cerevisiae* septins form octamers [82], and human septins form both hexamers and octamers [85]. These hetero-oligomers are then the building blocks to form apolar filaments [76] that are able to interact, in a species-specific manner, with the cell membrane [96, 98, 207], actin filaments [101, 102, 130, 144], and microtubules [103]. These apolar filaments can, in turn, interact with each other to form paired filaments and bundles [82, 96, 102, 208], which according to *in vitro* studies promotes membrane binding [96]. This pairing interaction is proposed be mediated via the C-terminal coiled-coils (CC) of either SEPT2, which contains a short CC that leads to ~5nm spacing between the filaments, or SEPT6 and SEPT7, which have longer CCs that lead to ~15nm spacing [208]. The interactions of septins are not limited to the plasma membrane [106, 144] but also involve membranous organelles such mitochondria [209], lysosomes [210], macropinosomes [211], and lipid droplets [138]. Through these interactions, septins participate in membrane trafficking processes, such as phagocytosis, clathrin-mediated endocytosis, micropinocytosis, macropinosome fusion, and degradative sorting [212]. At the plasma membrane, septins play a role in bleb retraction in T-cells [119], tension regulation [213], cell division [119, 120, 214], and cell migration [109, 215, 216].

It is still unclear whether septins in cells actually bind the plasma membrane directly. Reconstitution studies have shown that septins can directly bind to lipid membranes. However, it has also been shown that septins can bind and crosslink actin, the main component

from Timon Idema. Gerard Castro-Linares, Djim de Ridder, and Felix Frey wrote the manuscript while all other authors gave feedback.

of the actin cortex (Chapter 6, and [101, 102]). The cortical localization of septin can therefore come from its interaction with actin, the cell membrane, or both. To disentangle this, previous research has looked into the lipid specificity and binding mode between lipid bilayers and septins. Biochemical studies have shown that septins specifically bind phosphatidylinositols (PI) with different phosphorylation status, specifically, PI lipids with no phosphorylation, monophosphorylation (PI(3)P, PI(4)P, PI(5)P) (PIP), di-phosphorylation (PI(4,5P)P_2 (PIP2), PI(3,4)P_2), and tri-phosphorylation (PI(3,4,5)P_3) [82, 95, 99, 100, 217, 218]. The most abundant and well-studied PI lipid is PIP2, which is involved in numerous cellular processes, including cytoskeletal dynamics, membrane trafficking, and ion channel regulation [219–221]. Based on its widespread interaction with septins from multiple species [96, 152, 222], PIP2 has been acknowledged as the canonical septin binding lipid. However, recent studies showed that septins also bind other lipids in a species-specific manner. For instance, fly septin hexamers bind equally well to lipid bilayers with a similar net negative charge containing either PIP2 (-4 net charges at pH 7 [223]) or the negatively charged lipid phosphatidylserine (PS) (-1 net charge [28]), indicating that binding is electrostatically mediated [96]. Yeast septin octamers capped with Shs1 likewise do not seem to specifically recognize PIP2, yet the same octamers but capped with Cdc11 do exhibit specificity for PIP2 [224]. Molecular docking simulations recently provided first insights in the determinants of PIP2 specificity of the GTPase domains of Cdc11 [224]. Septins can additionally bind to other anionic lipids, such as mammalian septins binding to cardiolipin [225] or to LecA-activated Gb3 (globotriaosylceramide)-containing membranes [226], or yeast septins binding to sterol-rich membranes [227].

The precise mechanism of binding of septins to lipid membranes is not understood. There are up to three proposed regions that could mediate septin-membrane binding. The first region described is a polybasic stretch of amino acids located on the N-terminus of the SEPT2, SEPT3, and SEPT7 subfamilies, that mediates binding to PI, PIP, and PIP2 [138, 222, 228]. The second domain is another polybasic region located in the GTP-binding domain and conserved in all subfamilies of septin, which cooperates with the first polybasic domain for membrane binding [139, 229]. Finally, alpha-helical domains located close to the polybasic domains have been suggested to mediate septin binding, since they affect SEPT9 binding to membranes [139] and direct curvature-selective binding of yeast septins [230]. However, the fact that most of this work has been done with monomeric septins or fragments thereof, rather than oligomers, makes it difficult to interpret these findings, since septins need to polymerize [82, 96, 139] and to form paired filaments [96] to bind lipid membranes, and the described regions could also affect these two septin properties. There is also evidence that GTP binding by septin and the GTP/GDP ratio may affect membrane binding. First, tubulation of giant vesicles containing PI, PIP, or PIP2 in the presence of mammalian septins was more robust when supplemented with either GTP or GDP [99]. Additionally, structural studies suggested that the $\alpha0$ helix from SEPT3, one of the alpha-helix domains mentioned above, is hidden when SEPT3 is bound to GDP, and becomes exposed when bound to GTP, which could aid membrane binding [150]. Finally, septin octamers capped by Shs1 displayed different types of structures depending on the presence or absence of excess GTP or GDP on PI-, PIP- or PIP2-containing lipid monolayers [224].

Despite the clear evidence from cell-free studies that septins bind to lipid bilayers, the film structure that they form is not clear. Yeast septin octamers have been reported to form a single-layer network of paired and single filaments stabilized by cross-bridging octamers on lipid membranes containing PIP2 [82, 98]. Fly septins were shown to form a similar single-layer mesh of filaments and paired filaments on lipid monolayers, whereas they formed a double-layered mesh of thin and curved septin bundles on supported lipid bilayers [96]. The membrane interaction of human septins, which form both hexamer and octamer complexes [83–85], has not been explored in detail in an *in vitro* reconstitution setting. There is a single report about the binding of recombinant septin octamers to model membranes by Nakazawa et al. [97]. This work, similarly to their previous research with yeast septins [82, 98], showed that human septin octamers bind to supported lipid bilayers forming a a double-layered network of paired filaments and single filaments. Within these two layers, paired filaments were found to lie parallel to each other in the same layer, but perpendicularly to the filaments in the other layer. It is not clear yet what controls the formation of these different structures. There could be different explanations, related to septins from different species behaving differently when polymerized in bulk solution (yeast [82], fly [96], human [102]), or relating to different behaviors of hexamers and octamers.

To summarize, there is not a clear consensus on what controls septin-membrane interactions or whether the rules governing these interactions are conserved between species. To shed light on this question, in this work we studied membrane-binding of human septins by comparing how human septin hexamers and octamers bind to model lipid membranes under different environmental conditions (i.e. lipid layer type (monolayer or bilayer) and presence of GTP). To do this we used a multi-modal approach. First, we employed quartz crystal microbalance with dissipation monitoring (QCM-D) to investigate the lipid specificity of septin binding to membranes, nucleotide preference, the binding kinetics, and the reversibility of binding. Then, we used transmission electron microscopy (TEM) and atomic force microscopy (AFM) to study the structure of the formed network. Finally, we brought these data together using particle-based simulations to understand the basic mechanism by which septins bind lipid membranes.

4.2. Results

4.2.1. QCM-D experiments to test septin-membrane binding

To probe and quantify the binding of human septin complexes to SLBs, we utilized QCM-D, which allows real-time measurement of both mass and changes in mechanical properties of particles that adsorb to a surface using acoustic waves [231–233]. Changes in mass/thickness are shown as changes in the resonance frequency (Δf) of the QCM-D sensor, while the mechanical properties can be derived from changes in the energy dissipation of the system (ΔD) [231]. To probe septin binding to membranes, we followed the 4 step procedure described in Figure 4.1A, used previously also for fly septins [96]. The first step is the formation of an SLB on the QCM-D sensor by flowing in small unilamellar vesicles (SUVs) [231–234]. Depending on the charge of the SUVs, they can either rupture immediately or accumulate and then rupture, forming the SLB [233]. For both neutral and PS/PIP2-containing lipid mixtures, the frequency shift revealed initial SUV binding (observed as a decrease of Δf and increase in ΔD) followed by SUV rupture (observed as a peak in Δf and ΔD, indicating the release of the SUV contents) (Fig. 4.1A). This behavior is consistent with prior reports [233]. As exemplified in Figure 4.1A, the final net frequency shift (Δf) was around ~-25Hz and the net dissipation change (ΔD) was in the order of ~$0.1*10^{-6}$, which is characteristic of a well-formed SLB [233]. The second step was to flush out remaining SUVs and, simultaneously, change to the buffer in which septins are eventually added (F-buffer, see Section 4.4). Depending on how different the SUV and septin buffers were, this produced larger or smaller changes in Δf and ΔD. In the third step we added 50nM septin complexes in F-buffer, which has the right ionic conditions to promote septin polymerization (see Chapter 2 and [102, 129]). Once the septins reached the sensor, in cases where the lipid membrane triggered septin binding, there was an immediate decrease in Δf and an increase in ΔD, indicating septin adsorption (Fig. 4.1A). These changes leveled off after ~30min, indicating that, even though free septin complexes were still supplied through continuous flow, binding had saturated. We observed similar binding kinetics for human septin hexamers and octamers (Fig. 4.1B for Δf and Fig. 4.1C for ΔD). In the fourth step, to check whether septin binding was reversible, we finally washed the system with septin buffer, a high salt buffer (300mM KCl) that promotes septin depolymerization. This produced an immediate and rapid change of both Δf and ΔD, which returned close to the values they had before septin addition, indicating that septins need to be polymerized for membrane binding (Fig. 4.1A). This was the case for both hexamers and octamers (Fig. 4.1B). In case of neutral SLBs, there was no change in Δf (Fig. 4.1B) nor in ΔD (Fig. 4.1C) after septin addition, indicating that neither septin hexamers nor octamers bind neutral membranes. We observed a small change after the addition of high-salt septin buffer. Since the final values after washing with high-salt septin buffer were comparable for neutral and charged membranes and septins did not bind to neutral membranes, we surmise that the septin buffer completely dissociates the bound septins from charged membranes.

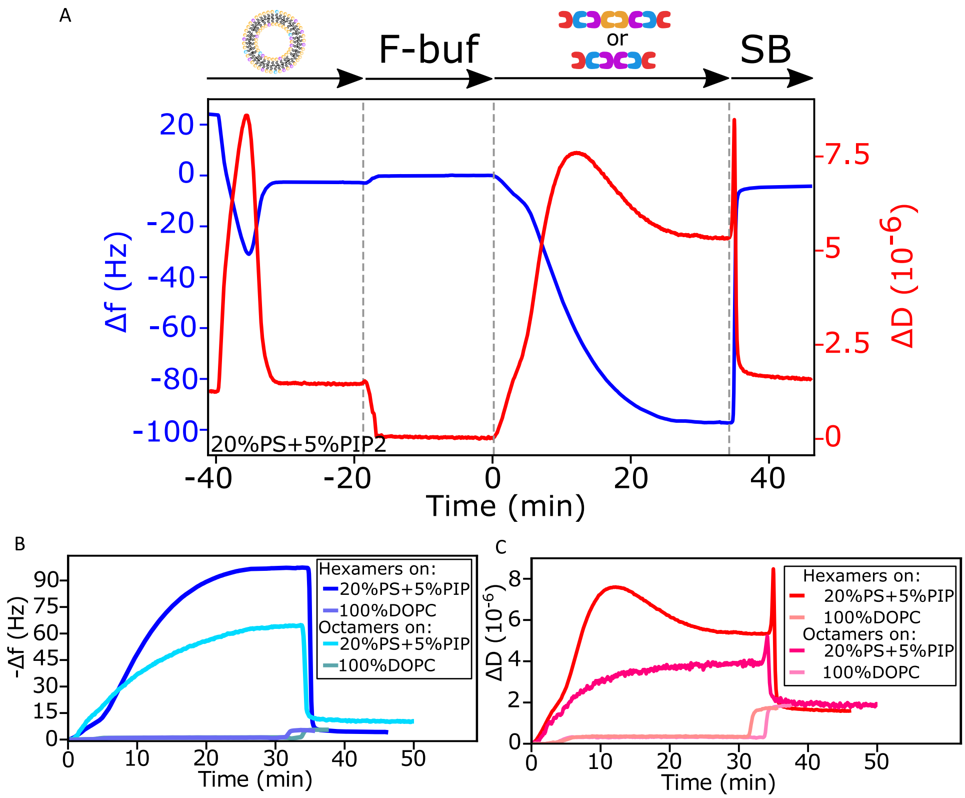

Figure 4.1. QCM-D measurement of septin complexes binding to and unbinding from supported lipid bilayers. A. Time-traces of frequency shift (Δf) and dissipation change (ΔD) of SLB formation, SLB washing, septin adsorption, and desorption. Vertical gray lines indicate at what time each component (as indicated on top: SUVs, F-buffer, septin complexes, and high-salt septin buffer) is flown over the QCM-D sensor. The specific trace shown is of septin hexamers in the presence of excess GTP interacting with a 20%PS+5%PIP2 SLB. We set the zero values for Δf, ΔD, and time as the moment where septin was first supplied to the sensor. B. Time trace of -Δf for septin hexamers and for septin octamers during binding (first 35 min) and subsequent release with high salt septin buffer, on 20%PS+5%PIP2 versus 100%DOPC SLBs. The hexamer trace for 20%PS+5%PIP2 is the same as in A. C. Same as in B, but for ΔD.

4.2.2. Human septin complexes specifically bind PIP2-containing lipid bilayers in a GTP-dependent manner

We previously found that *Drosophila* septin hexamers bind negatively charged lipids such as DOPS and PIP2 [96]. To test whether DOPS alone is enough for human septin binding, or the physiological septin-binding lipid PIP2 is needed, we did QCM-D experiments as described above for SLBs containing 100mol% DOPC (100%PC SLB), 80mol%DOPC and 20mol%DOPS (20%PS SLB), 95mol%DOPC and 5mol%PIP2 (5%PIP2), or 75%DOPC, 20%DOPS, and 5%PIP2 (20%PS+5%PIP2 SLB). We additionally tested the effect of added nucleotides, prompted by previous results suggesting that septin binding to membranes needs a nucleotide [99] and depends on the GTP/GDP status of septins [224], especially for SEPT9 [150]. To probe the nucleotide dependence for human septin complexes in our QCM-D experiments, we tested membrane binding for all lipid compositions in the presence or absence of excess 1mM GTP. The results are summarized in Figure 4.2A. As expected, neither septin hexamers nor octamers bound to 100%PC SLB, as shown by Δf remaining close to 0Hz. The addition of GTP did not change this behavior. Neither of the human septin complexes bound to 20%PS SLBs in the absence or presence of GTP, in contrast to our results with fly septins [96]. Interestingly, we found different results for septin hexamers and octamers on 5%PIP2 bilayers. In the absence of GTP, the binding of septin hexamers was poorly reproducible: sometimes we obtained high -Δf values between 30Hz and 70Hz, while other times the signal stayed close to 0Hz. This variable behavior occurred in sam-

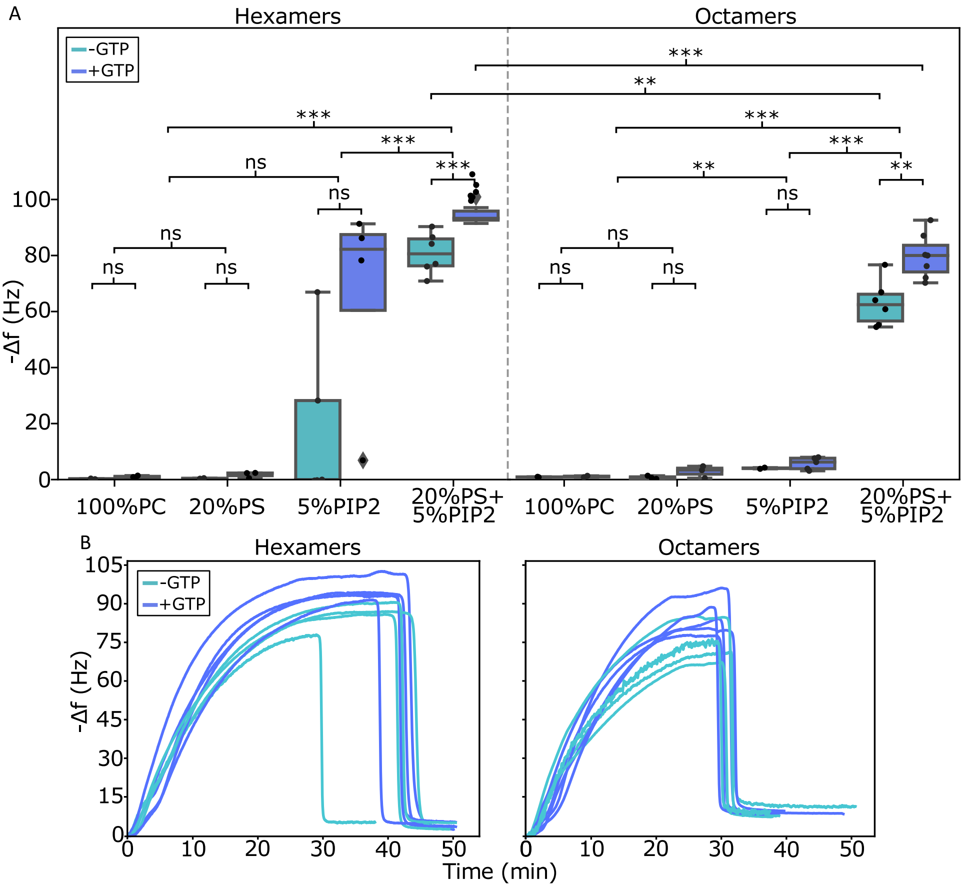

Figure 4.2. Final frequency shift values characterizing the steady-state amount of binding for septin hexamers and octamers on SLBs of different lipid compositions and in the presence or absence of added GTP. A. Left panel shows hexamers for each of the lipid compositions tested, while right panel shows the same for octamers. Darker blue means in the presence of added GTP, while lighter blue means absence of added GTP. Two-tailed t-test (* p<0.05, ** p<0.001, ****p<0.0001, ns=non-significant). B. Time traces of four random examples of -Δf for septin hexamers or octamers binding to a 20%PS+5%PIP2 SLB and subsequent unbinding prompted by flowing in high-salt septin buffer. Dark blue represents the presence of 1mM GTP while light blue represents absence of GTP.

ples done in parallel with the same batch of septins, same batch of SUVs to form the SLBs, and with QCM-D sensors treated equally, therefore, we could not identify any reason for this inconsistency. Surprisingly, adding excess GTP to the system resulted in more consistent behavior, with final -Δf being mostly around ~80Hz. Octamers behaved differently than hexamers, showing a consistently weak tendency to bind the 5% PIP2 SLBs in absence of GTP, with -Δf values between 5Hz and 10Hz, which is slightly but significantly higher than for the 100%PC and 20%PS SLBs. Moreover, addition of GTP in this case did not impact the binding behavior.

Finally, we tested the binding of both complexes on 20%PS+5%PIP2 lipid bilayers. Time traces for four random examples of these experiments can be seen in Figure 4.2B. We found that both complexes bound the SLBs robustly, reaching -Δf values between 70Hz and 80Hz. Interestingly, adding excess GTP significantly increased this binding by ~10-20Hz to values between 80Hz and 100Hz. Final net -Δf values for septin hexamers were higher than for septin octamers regardless of the presence of GTP (Fig. 4.2A), indicating that a larger amount of hexameric complexes bound the lipid bilayer. This data suggests that, while DOPS alone is not enough to trigger septin binding, it has a synergistic effect with PIP2. This effect made membrane binding more reproducible on 20%PS+5%PIP2 bilayers than on 5% PIP bilayers for septin hexamers and was necessary for significant membrane binding for septin octamers. Additionally, our data reveals that, despite not being vital for membrane binding, GTP somewhat promotes binding of septins to PIP2-containing lipid bilayers.

4.2.3. Thickness of the membrane-bound septin film

For sufficiently dense and homogeneous protein films, QCM-D measurements can be used to determine the film thickness. The Sauerbrey equation (Eq. 4.1) can be used to relate the frequency shift to the areal mass density, m, of the adsorbed films [231, 235]. The mass density is equivalent to the product of the film density (ρ) and the film thickness (d):

$$\Delta f = -\frac{n}{C} m = -\frac{n}{C} \rho d \tag{4.1}$$

Here, n is the overtone at which the measurement is done, and C is the mass sensitivity constant, which is 18ng/cm²/Hz for the used QCM-D sensors [231]. Considering that the film contains proteins with a typical density of 1.4g/cm³ together with more than 50% solvent [236], with a density of 1g/cm³, we assumed an average density of ~1.1g/cm³. Since the accuracy of the Sauerbrey equation depends on the uniformity, density, and rigidity of the septin film, we only used it for the films on 20%PS+5%PIP2 SLBs, where binding was highest. We obtained film thickness values between 10nm and 16nm, consistent with film thicknesses observed for fly [96] and human [97] septins, where imaging confirmed the presence of a double film of septins.

4.2.4. Mechanical properties of the membrane-bound septin films

In QCM-D the dissipation change is a proxy for the mechanical properties of the adsorbed film [231, 233]. Upon incubation of 50nM septin complexes with 20%PS+5%PIP2 SLBs, ΔD increased as septin complexes bound the lipid bilayer (Fig. 4.3A). For hexamers (Fig. 4.3A, left), regardless of the presence of GTP, we could observe a quick rise up to ~$7{*}10^{-6}$ and a subsequent decrease that stabilized to a value around $5{*}10^{-6}$, causing a prominent peak in ΔD. These transient dissipation peaks have been observed before for globular proteins [237], being attributed to a weak linkage between the globular particles and the surface or between different domains of the particle. As the density of the particles increases on the surface, the particles on the surface become more highly packed, reducing dissipation. Interestingly, such a transient peak is not observed for octamers (Fig. 4.3A, right), which are stabilized at higher ΔD values between $6*10^{-6}$ and $7.5*10^{-6}$, suggesting that septin hexamers and octamers bind similarly at early stages, but that the mechanics of the film is different in later stages.

To investigate how the mechanical properties of the membrane-bound septins compare with those of other membrane-binding proteins, we calculated the softness parameter that is defined as the ratio of the dissipation change over the frequency shift, ΔD/-Δf. For thin films, such those formed by septins, the softness parameter is a reporter of the deformability of the bound film [231]. Figure 4.3B shows the softness parameter as a function of -Δf. We can see that the ΔD/-Δf ratio linearly decreased as more septins adsorbed to the surface (Fig. 4.3B), consistent with previous studies for other nanosized objects, including colloidal particles, globular proteins, virus particles, and small unilamellar vesicles (SUVs) [237–239]. These studies showed that this linear decrease is typical of globular objects with weak linkage regions, as mentioned above. Computer simulations explained this tendency in terms of mechanical stabilization upon increased coverage [237, 239]. However, as seen in Figure 4.3C, the time trace looks more linear for the hexamers than for the octamers. To check linearity, we calculated the slope of the softness against -Δf traces for two different regimes of binding, at the early stages between -Δf's of 20Hz and 50Hz, and for the later stages for -Δf's above 50Hz (Fig. 4.3D). We can see that the slope is indeed constant for the hexamers, whereas the slope for the octamers increases between early and late stages. Interestingly, the slope for the hexamers and octamers was the same for the early stage, indicating that septin complexes may initially bind in a similar manner, but later assemble in a different manner, leaving the octamer film softer than the hexamer film. This is also indicated by the final value of the softness at the end of the binding process (t=29 minutes), where septin hexamers in the presence of GTP have a consistently lower value of ΔD/-Δf of $0.06*10^{-6}$/Hz, whereas septin hexamers in the absence of GTP and septin octamers in the presence or absence of GTP had a more variable final value between $0.15*10^{-6}$/Hz and $0.06*10^{-6}$/Hz (Fig. 4.3E). To compare with the softness of other proteins, the highest ΔD/-Δf values are close to the softness shown by the PIP2-binding domain of ezrin ($0.125*10^{-6}$/Hz [240]), while the lowest are close to the pentameric B-subunit of cholera toxin ($0.05*10^{-6}$/Hz [241]) and to annexin ($0.01*10^{-6}$/Hz [242]). This suggests that septin hexamers in the presence of GTP may be able to form more rigid films as compared to octamers, when binding SLBs with DOPS and PIP2.

4

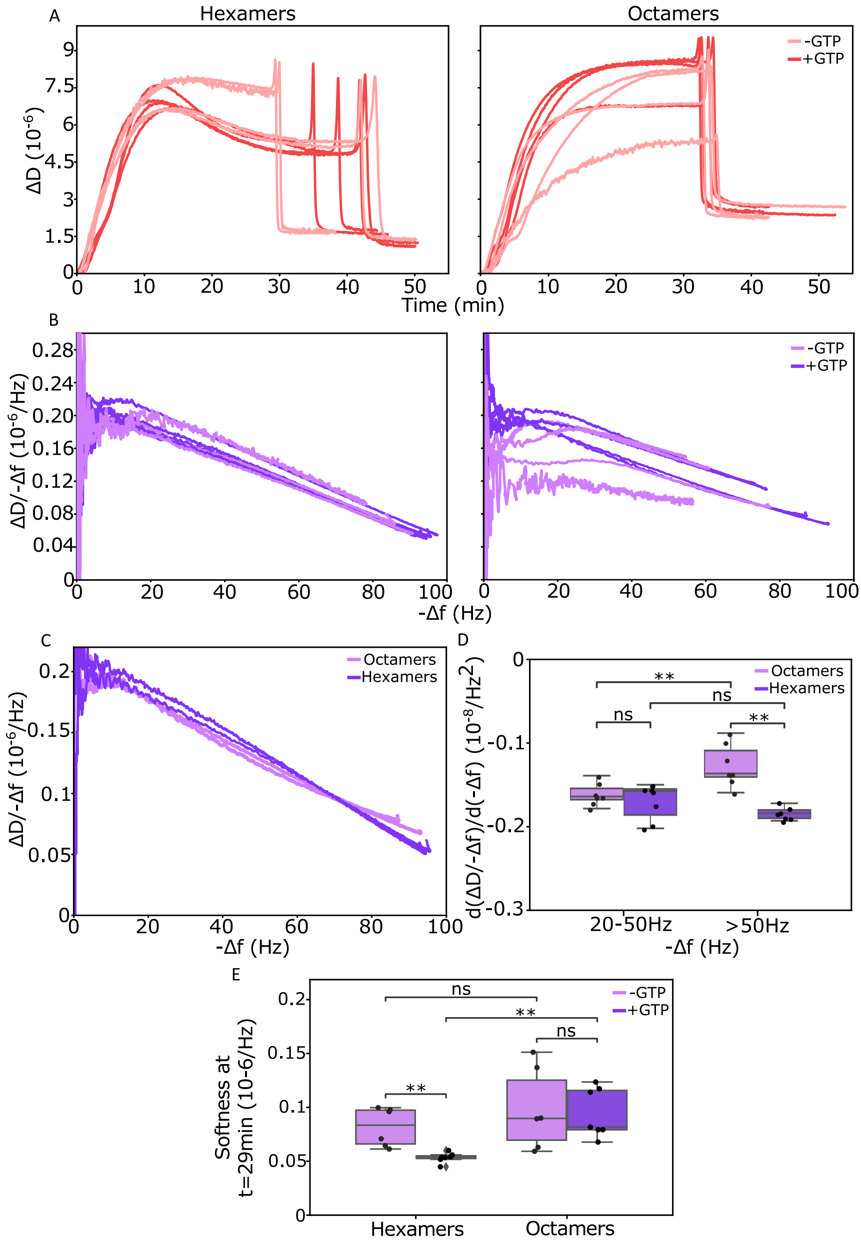

Figure 4.3. Dissipation and softness of septin hexamers and octamers binding 20%PS+5%PIP2 SLBs. A. Time traces of four random examples of ΔD for septin hexamers or octamers binding (and unbinding from) an SLB. Dark red represents the presence of excess GTP while light red represents absence of GTP. B. Plot of four random examples of ΔD/-Δf as a function of the adsorbed amount (expressed as -Δf) of septin. Dark purple represents the presence of excess GTP while light purple represents absence of GTP. C. Two traces from B for hexamers and octamers in the presence of excess GTP in the same plot to compare their shapes. D. Boxplots of the slopes of the ΔD/-Δf as a function of -Δf curves for low surface coverage (-20-50Hz) and for higher surface coverage (<-50Hz) for hexamers and octamers in the presence of excess GTP. E. Boxplots of the softness at the end of the binding process (t=29min) for septin hexamers and octamers in the presence and absence of GTP. Two-tailed Mann–Whitney U test with p-values (ns: p ≤ non-significant, *: $1*10^{-2} < p \leq 5*10^{-2}$, **: $1*10^{-3} < p \leq 1*10^{-2}$, ***: $1*10^{-4} < p \leq 1*10^{-3}$).

4.2.5. Septin complexes form a mesh of single and paired filaments on lipid monolayers containing PIP2

To understand the organization of septin complexes on lipid layers, we previously used transmission electron microscopy on lipid monolayers and atomic force microscopy on lipid bilayers [96]. Here we use the same two approaches. We first performed TEM for septin octamers incubated on 100%PC and 20%PS lipid monolayers and for both septin hexamers and octamers incubated on 5%PIP2 lipid monolayers. The incubation of septin octamers at a concentration of 50nM on both 100%PC and 20%PS monolayers resulted in the appearance of short and scattered filaments on the lipid surface (Fig. S4.1A and D). The PS-containing monolayer showed a higher density of adsorbed septin octamers as compared to the 100%PC monolayer. These data indicate that neither PC or PS monolayer can trigger septin octamer polymerization.

Similarly to the QCM-D experiments, we obtained variable results for both septin hexamers and octamers at a concentration of 50nM on 5%PIP2 monolayers, obtaining three main types of results. On occasions we would observe a pattern similar to that of the 100%PC and 20%PS monolayers of short and scattered filaments (Fig. S4.1B and C), other times only septin bundles would be seen adsorbed on the surface (Fig. S4.1E and F). The third type of pattern observed for both septin hexamers and octamers was a pattern of single (3-6nm width) and paired (8-12nm width) filaments adsorbed to the surface (Fig. 4.4). The meshwork pattern formed by the octamers consisted of paired and single filaments that ran past each other displaying a cross-hatching pattern. In this patters, filaments displayed multiple directions and were poorly organized. In contrast, the hexamers formed a more ordered pattern with filaments following two main directions. A first set, of mostly paired filaments, ran in parallel to each other and perpendicular (85.02° ±13.21°) to the second set of mostly single filaments. We then measured the distance between these paired filaments and observed a wide peak ranging from 14nm to 29nm, with a tail extending up to 60nm (Fig. S4.2). Additionally, a peak appeared at 0nm, which can be attributed to the merging of filaments (Fig. S4.2). The average distance between the parallel paired filaments was 21.4nm ±10.4nm, which is comparable to the length of a single hexamer of 24nm [82, 83]. Similar single-oligomer distances have been observed for fly and yeast septins, which were caused by single septin complexes bridging the filaments [96, 152]. In the case of the human hexamers, these bridges are not observed, but we did observe perpendicular single filaments that might be stabilizing the paired filaments distances in similar ways (Fig. 4.4D). We conclude that both septin hexamers and octamers form filamentous meshwork on lipid monolayers containing PIP2, but these meshworks are more ordered in case of hexamers.

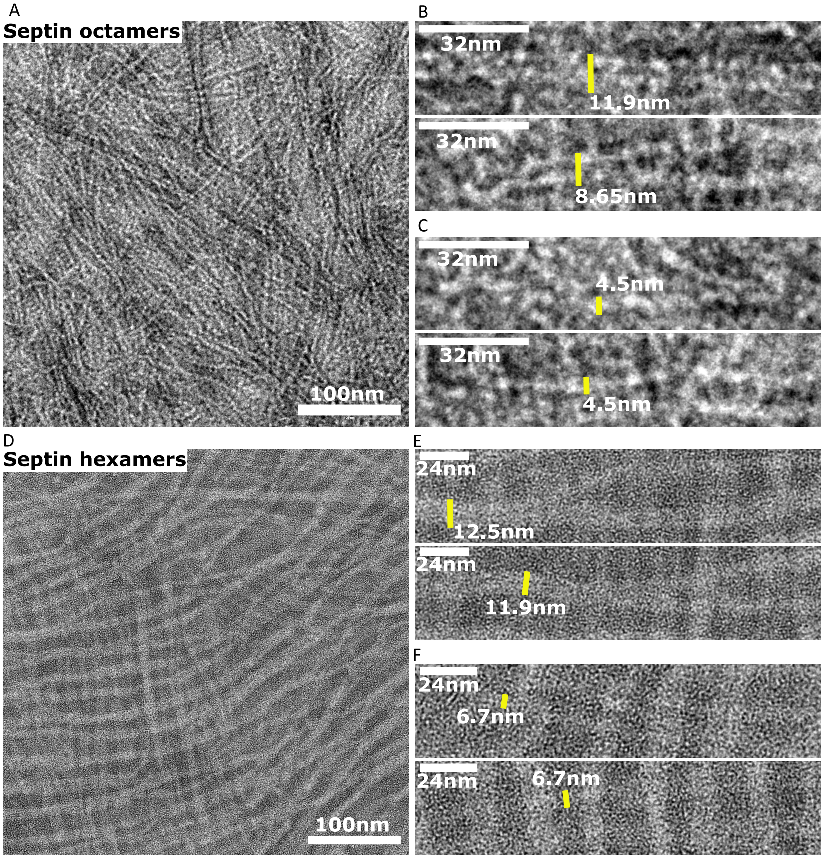

Figure 4.4. Paired and single septin filaments binding lipid monolayers containing 5% PIP2. A. Representative image of the mix of paired and single septin octamer filaments. B. Close up to paired filaments. In the bottom image, the paired filaments split into two thinner filaments. C. Close up to single filaments. D. Representative images of the mix of paired (magenta arrowheads) and single (green arrowheads) septin hexamer filaments. E. Close up to paired filaments. Both images show the paired filaments splitting into thinner filaments. F. Close up to single filaments. Scale bars for the close ups represent the length of single oligomers. Yellow bars show the filament widths measured by manual analysis.

4.2.6. Septin hexamers and octamers assemble into morphologically different networks on lipid bilayers containing PS and PIP2

To gain further insights into the structure of septin networks on lipid layers, we employed atomic force microscopy (AFM) as a complementary high-resolution imaging technique alongside TEM. AFM allowed us to visualize reconstituted septin networks on supported lipid bilayers (SLBs) in an aqueous environment, providing a more physiological environment than the monolayer configuration and drying required for TEM experiments. Following a protocol similar to a previous study on fly septins with AFM [96], we conducted AFM imaging on septin oligomers at a concentration of 60nM or 120nM fixed with 1% glutaraldehyde (GTA) and incubated on silicon-supported lipid bilayers. For our experiments, we used SLBs consisting of 20% PS+5%PIP2, as these lipid conditions consistently promoted septin layer formation as observed in QCM-D (Fig. 4.2A), and always included excess 1mM GTP.

AFM imaging revealed that septin hexamers organized into locally aligned filaments and bundles on the SLB (Fig. 4.5A). The corresponding height histogram revealed that the filaments had an average height of ~5nm above the surface (Fig.4.5A), with occasional measurements of 8nm measured in individual bundles in line profiles drawn across them (Fig.S4.3A), suggesting the formation of two layers of filaments. In contrast, incubating septin hexamers in the absence of an SLB did not lead to clear filament formation (Fig. S4.4), underscoring the influence of the SLB on septin filament organization and alignment. The observed alignment and bundling of filaments are consistent with previous findings for fly septins incubated on DOPS-containing SLBs [96].

Interestingly, when septin octamers were incubated on the SLBs, bundled filament networks did not emerge. Instead, a dense isotropic network of septin filaments with a similar height as the septin hexamer films was observed (Fig.4.5B). While displaying some resemblance to the septin octamer meshworks observed on lipid monolayers in our TEM experiments (Fig.4.4A) on 5%PIP2 lipid monolayers, no clear layering pattern was discernible through AFM imaging. A possible reason for this discrepancy could be that the AFM tip did not reach into the voids left between the filaments in these dense layers. Similarly as for the hexamers, the height histogram revealed an average height of ~5nm (Fig.4.5A), with occasional measurements of 8nm measured in individual filaments in line profiles drawn across them (Fig.S4.3A). These contrasting behaviors exhibited by septin hexamers and octamers under identical environmental conditions emphasize the significance of the septin oligomer length in determining the resulting network architecture.

4.2.7. Computer simulation results suggest that the hexamer films consist of paired filaments that align with each other

In order to understand the mechanism governing the formation of the SLB-bound septin films, we implemented computer simulations allowing us to determine how nucleation, growth and interactions of septin filaments with each other can control the global properties of the emerging network structures such as orientational order. Since the formation of networks of single and paired septin filament networks has been more extensively studied [82, 97, 98, 218, 230], we focused on simulating the formation of the bundle-based networks, which were also observed earlier for fly septin hexamers [96]. By deducing the microscopic simulation assumptions directly from insights of the experiments described in the previous sections, we connect experiments and simulations.

In the model, we represent septin filaments as chains of septin subunits, where a filament is defined as a chain of at least two concatenated subunits (Fig. 4.6A). We consider septin hexamers to have a width of $d = 4\,\mathrm{nm}$ and a length of $l_s = 24\,\mathrm{nm}$ [76]. We simulate the assembly of septin filaments on a 2d surface that is coupled to a finite reservoir of N_s subunits, mimicking the conditions in AFM experiments. In the simulation, we consider a surface of quadratic shape with length $L_x = L_y = 5\,\mu\mathrm{m}$, similar to the typical field of view (FOV) in the AFM experiments. To reflect the experimental observation of filaments growing bound to the surface without intersecting, we prohibit intersecting filaments in

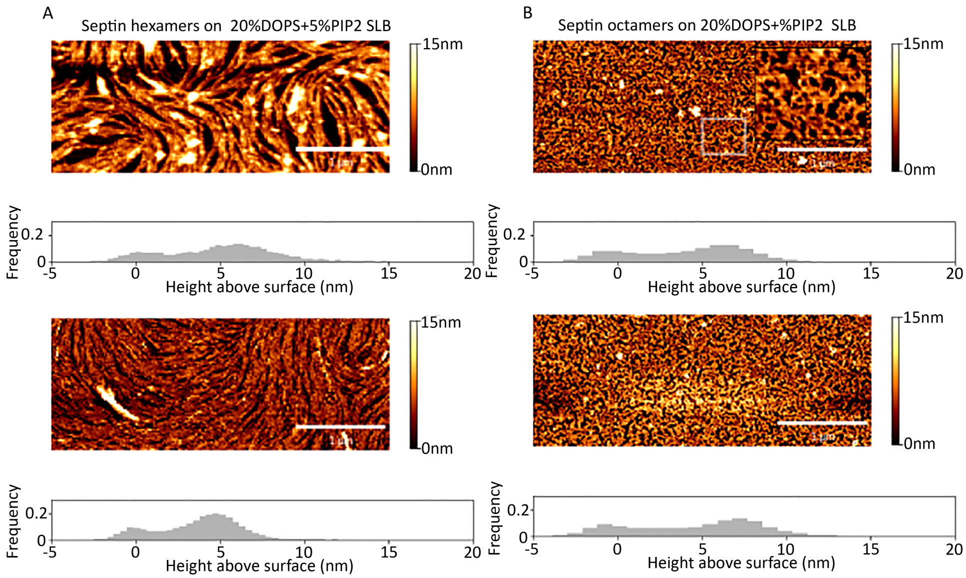

Figure 4.5. Septin network formation on 20%PS+5%PIP2 lipid bilayers. A. Representative atomic force microscopy (AFM) images and corresponding height histograms illustrating the morphologies observed for 120 nM septin hexamers organizing on a 20%PS+5%PIP2 SLB. B. Representative AFM images and corresponding height histograms illustrating the morphologies observed for 60 nM septin octamers organizing on a 20%PS+5%PIP2 SLB. Inset in upper image in B shows zoom-in of the rectangular area in the white box. Color bars on the right denote height. Zero height corresponds to the height at the gaps between filaments. Top and bottom images corresponding to similar-looking regions of independent samples. Scale bars are 1μm.

the simulation. Instead, when filaments meet, they can either align or stop growing. Moreover, given our observation on the TEM experiments that paired filaments are typically formed (Fig. 4.4), we assumed that filaments can pair by nucleating and growing next to an already-grown filament on the surface. The used parameter values are summarized in Table 4.1.

We assume that septin subunits can only assemble into filaments on the SLB, but do not assemble into higher order structures in the bulk. Therefore, in the simulation, we only consider the membrane surface to which the septin subunits can bind to and neglect to simulate the bulk. In addition, we assume that subunits alone can detach from the membrane, while septin filaments remain adhered to the membrane. In general, both subunits and filaments are expected to diffuse on the membrane surface. However, because of their larger size filaments should diffuse much slower compared to subunits. Therefore, we neglect to model filament diffusion. The dynamics of septin filament assembly is driven by septin subunits that frequently bind to, unbind from and diffuse on the membrane. In the model, we hence track the dynamics and structure of septin filaments, but we do not track the much faster dynamics of septin subunits.

In the simulation, septin filaments can undergo different events: nucleation, growth with or without aligning with other filaments, paired growth, and paired nucleation (Fig. 4.6A). In detail: during filament nucleation two septin subunits bind to each other, which generates a membrane-bound filament of two subunits. In a growth step, a subunit

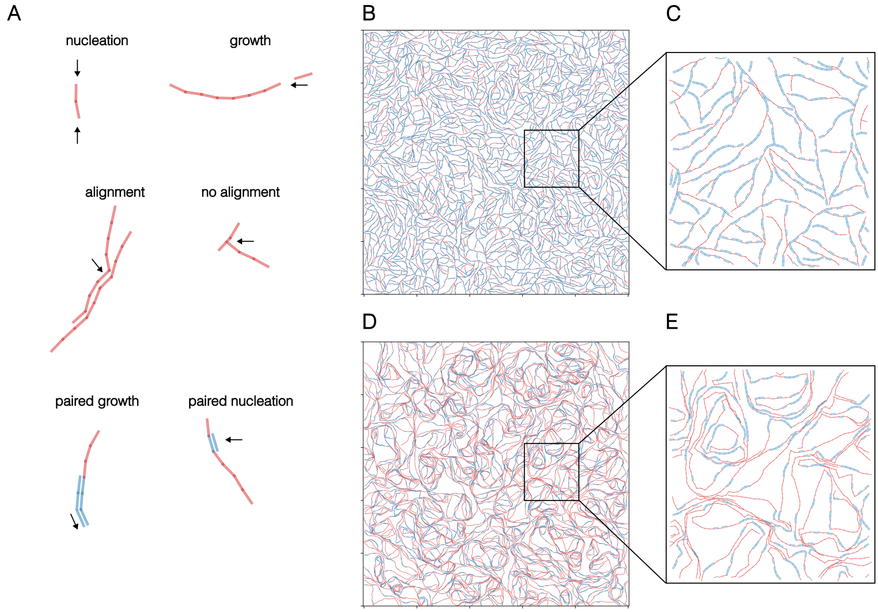

Figure 4.6. Computational model of septin filament assembly on a flat membrane surface. A. Schematics of the different simulation events: septin filament nucleation, growth, growth without alignment, growth with alignment, paired growth, and paired nucleation. B. Example of a simulated filament network with paired (blue) and unpaired (red) septin filaments without filament alignment ($\alpha = 0$) where $N_s = 3 \times 10^4$, $l_s = 24\,\text{nm}$, $k_n = 1\,\text{s}^{-1}$, $k_g = 10^4\,\text{s}^{-1}$ and $k_p = 1\,\text{s}^{-1}$. C. Zoom-in of the example in B. D. Example of a simulated filament network with paired (blue) and unpaired (red) septin filaments with filament alignment ($\alpha = 2\pi$) where $N_s = 3 \times 10^4$, $l_s = 24\,\text{nm}$, $k_n = 1\,\text{s}^{-1}$, $k_g = 10^4\,\text{s}^{-1}$ and $k_p = 1\,\text{s}^{-1}$. E. Zoom-in of the example in D.

binds to an available end of a membrane-bound filament. If a filament grows close to another filament, it can either grow paired, align with it, or stop growing in case a filament intersection occurs. During paired nucleation, a septin subunit is nucleated in parallel to a subunit of a filament that was previously unpaired. All simulation events, whether nucleation, growth, or paired nucleation, can only occur if they do not result in an overlap of septin filaments. Instead, if during growth filaments got too close, growth either stops (Fig. 4.6B and C) or filaments align with each other (Fig. 4.6D and E).

The dynamics of septin filament assembly is governed by kinetic rates for nucleation k_n, growth k_g and paired nucleation k_p. We simulated the dynamics of the model using the Gillespie algorithm. In all simulations, we set the nucleation rate to a fixed value of $k_n = 1\,\text{s}^{-1}$ but varied the growth rate k_g and the paired nucleation rate k_p from $1\,\text{s}^{-1}$ to $10^4\,\text{s}^{-1}$. Moreover, we simulated until the initial septin subunit reservoir of $N_s = 3 \times 10^4$ was completely depleted and all subunits were bound to the membrane. The details of the implementation of the model are given in the Methods section together with the used parameter values in Table 4.1.

By studying the structure of the emerging networks, we aim to understand the importance of the effects of filament nucleation, filament growth, and paired nucleation on the global organization during septin assembly. Therefore, in Fig. 4.7, we set the nucleation rate to the value of $k_n = 1\,s^{-1}$, which is kept constant in all simulations. Then, to investigate what are the effects of different frequencies of filament growth and paired nucleation relative to each other on the network organization, we vary the growth rate k_g on the horizontal axis and the paired nucleation rate k_p on the vertical axis from $1\,s^{-1}$ to $10^4\,s^{-1}$ in steps of two orders of magnitude each. Since the nucleation rate is kept constant in Fig. 4.7, one can also interpret the vertical and horizontal axes as varying k_g and k_p normalized with respect to the nucleation rate. Moreover, since hexamer network in the AFM showed bundles that were clearly thicker than individual filaments (Fig. 4.5), we include that septin filaments are able to align with each other during growth.

When both the growth and paired nucleation rate were identical to the nucleation rate (Fig. 4.7G), septin subunits assembled into short filaments that were only partially paired. The overall network structure showed randomly oriented and homogeneously distributed filaments. As the paired nucleation rate increased at constant nucleation and growth rate to $k_p = 10^2\,s^{-1}$ (Fig. 4.7D) and $k_p = 10^4\,s^{-1}$ (Fig. 4.7A), more and more filaments became paired. However, septin filaments remained short and the overall network structure did not change much. In contrast, as the growth rate increased at constant nucleation and paired nucleation rate to $k_g = 10^2\,s^{-1}$ (Fig. 4.7H) and $k_g = 10^4\,s^{-1}$ (Fig. 4.7I), filaments got longer and less paired. Since the filaments became longer and thus came into contact with each other, they could also align with each other during growth. Importantly, the difference in the single filament properties led to a much more organized global network structure. Finally, as we increased the paired nucleation rate to $k_p = 10^2\,s^{-1}$ (Fig. 4.7F) and $k_p = 10^4\,s^{-1}$ (Fig. 4.7C) at constant nucleation rate and growth rate of $k_g = 10^4\,s^{-1}$, more filaments paired and the network structure became more homogeneous compared to Fig. 4.7I, as we observed less space without any filaments. We concluded that filament networks can get more organized when growth dominates filament nucleation and can keep a homogenous density if paired nucleation occurs with a similar frequency as growth rate. We note that the networks in Fig. 4.7B and Fig. 4.7E represent mixed cases of intermediate growth and paired nucleation rates that confirm the observed trend.

Next, we tested the impact of how individual filaments interact with each other during growth on the global organization of the septin networks. Therefore and in contrast to Fig. 4.7, in Fig. 4.8, we now investigated how emerging septin networks look like when the growing filaments could not align with each other during growth but instead stopped growing before filaments intersect. Again, we investigated the effect of different frequencies of filament growth and paired nucleation relative to each other and relative to the constant nucleation rate of $k_n = 1\,s^{-1}$. When filament nucleation, growth and paired nucleation occured at the same frequency (Fig. 4.8G), as expected, we again saw networks of homogeneously distributed short filaments. The filaments become more and more paired as the paired nucleation rate increased at constant nucleation and growth rate to $k_p = 10^2\,s^{-1}$ (Fig. 4.8D) and $k_p = 10^4\,s^{-1}$ (Fig. 4.8A), but the overall network organization did not change much. The emerging networks became more different as the growth rate increased at constant nucleation and paired nucleation rate to $k_g = 10^2\,s^{-1}$ (Fig. 4.8H) and $k_g = 10^4\,s^{-1}$ (Fig. 4.8I). With increasing growth rate, filaments get longer but the resulting networks were not as ordered as with alignment interactions in (Fig. 4.7I), although more space without filaments was generated. While in Fig. 4.7H and I the filaments were long and entangled, in Fig. 4.8H and I the filaments were considerably shorter and straighter since no alignment occurred. Finally, Figs. 4.8B,C,E and F represent mixed cases where both paired nucleation and filament growth contribute. However, although filaments were relatively long and got paired, we did not observe networks as dense as before (Fig. 4.7). We conclude that entangled filament networks emerge when filaments align during growth.

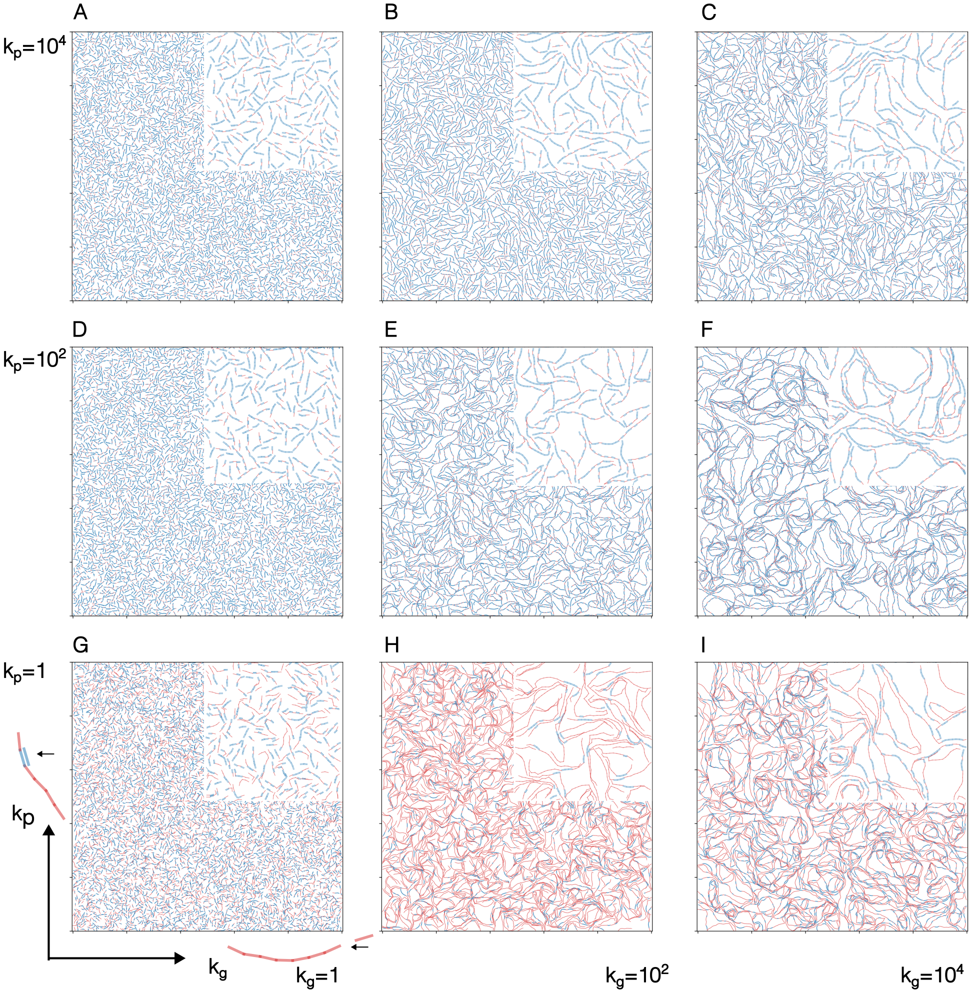

Figure 4.7. State diagram of simulated septin filament networks with filament alignment (α=2π) where N_s = 3×10^4 , l_s = 24nm and k_n = 1s-¹. On the vertical axis, the pairing rate k_p ranged from $1\,s^{-1}$ to $10^4\,s^{-1}$ in steps of two orders of magnitude and on the horizontal axis, the growth rate k_g varies between $1\,s^{-1}$ to $10^4\,s^{-1}$ in steps of two orders of magnitude. Single filaments are shown in red, paired filaments are shown in blue.

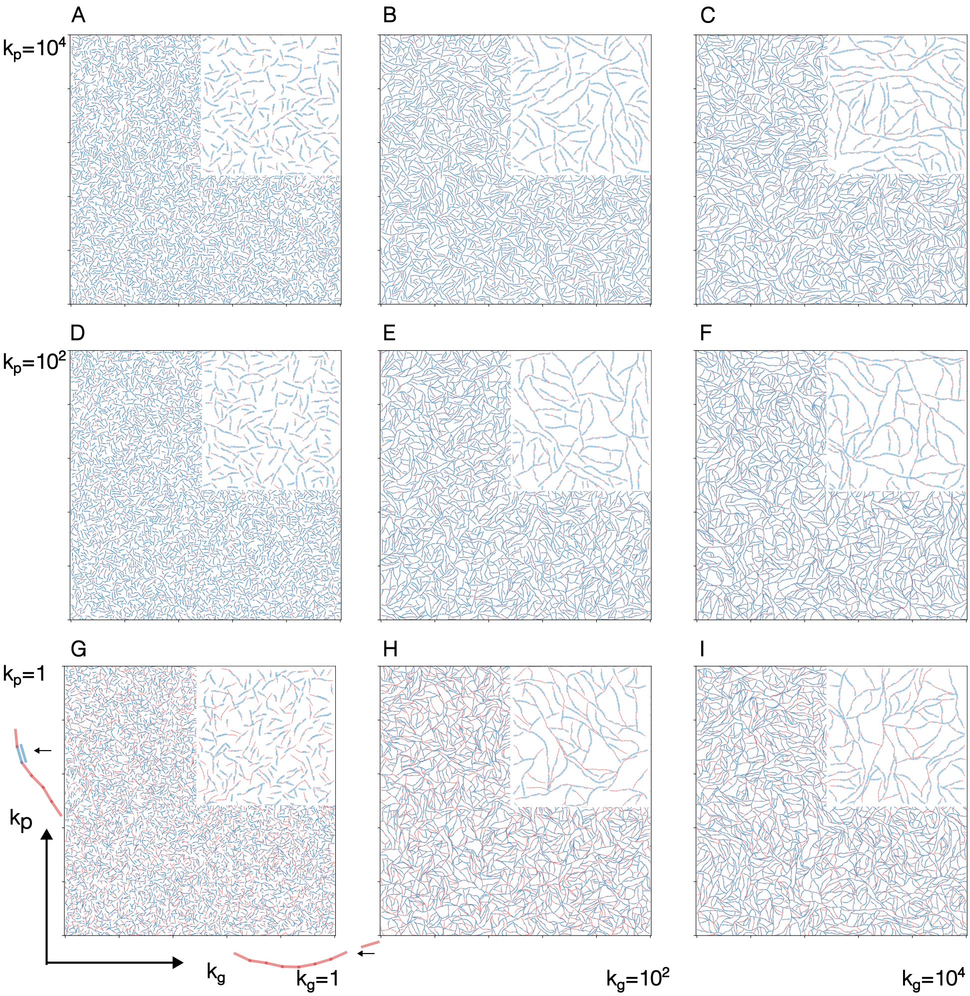

Figure 4.8. State diagram of simulated septin filament networks without filament alignment (α=0) where $N_s = 3 \times 10^4$, l_s = 24 nm and k_n = 1 s^{-1}. On the vertical axis, the pairing rate k_p ranged from 1 s^{-1} to 10^4 s^{-1} varies in steps of two orders of magnitude and on the horizontal axis, the growth rate k_g ranged from 1 s^{-1} to 10^4 s^{-1} varies in steps of two orders of magnitude. Single filaments are shown in red, paired filaments are shown in blue.

4.3. Discussion

In this chapter we investigated how septins interact with flat lipid layer models using a multi-modal approach. First we looked at the lipid specificity of septin binding by QCM-D measurements where septins were flown over lipid bilayers. Previous research found that yeast septin octamers only bind and assemble to PIP2-containing lipid layers [82, 100, 218], while fly hexamers are not selective for PIP2 and also bind PS [96]. This could either be a species-dependent or oligomer size-dependent difference. To distinguish between these options, we tested the binding of human septin hexamers and octamers to 20%PS, 5%PIP, and 20%PS+5%PIP2 SLBs. Interestingly we found that neither of the septin complexes could bind to 20%PS SLBs, indicating that the difference observed between yeast and fly septins is species dependent. Interestingly, only septin hexamers could bind to the 5%PIP2 SLBs, although in a non-reproducible manner. The addition of PS to the SLB made the binding of hexamers reproducible and was necessary to trigger octamer binding to 20%PS+5%PIP2 SLBs. This shows that PS and PIP2 have a synergistic effect on binding septins.

4

We then tested septin binding by TEM imaging where septins were incubated on lipid monolayers. On 5% PIP2 lipid monolayers, we observed that both hexamers and octamers bound and polymerized, in contrast with QCM-D assays on 5%PIP2 SLBs. This discrepancy likely stems from the experimental design. In QCM-D, there was a flow of septin oligomers over the SLB, while for TEM the septin incubation was done in a bulk solution without any flow. The flow likely removes weakly bound septins that did not have the opportunity to polymerize yet. This is further evidenced by the fact that the membrane-bound septin is dislodged from the SLB when high-salt septin buffer is added. Upon depolymerization, septins apparently become weakly bound to the SLBs, leading to a complete removal by the flow. This interpretation could be further tested by repeating the QCM-D experiments on 5% PIP2 bilayers at higher septin concentrations, so that the rate at which septins polymerize increases, minimizing the effect of the flow. By TEM we observed more septin octamers binding on 20%PS lipid monolayers than on 100%PC monolayers but polymerization only occurred when PIP2 was present. This observation suggests that the synergistic effect between PS and PIP2 arises from the ability of PS to recruit septin oligomers, through electrostatic interactions [96], and of PIP2 to trigger septin polymerization upon binding. By recruiting septin oligomers, PS increases the local concentration of septin on the membrane, increasing the effective septin polymerization rate. It would be interesting to asses septin binding via QCM-D or spectroscopic ellipsometry in absence of flow and at higher septin concentration [236], which is difficult in the commercial QCM-D assay with flow due to the high sample volume demand. Combining those techniques with AFM or TEM to check for septin polymerization at high septin concentration on 20%PS bilayers would allow to test whether PS simply recruits septins via electrostatic interactions.

It is known that binding of septins to a guanosine nucleotide (GTP or GDP) is crucial for septin-membrane binding [99, 224], and it has even been proposed based on structural studies that the binding of SEPT3 subfamily members (such as SEPT9) could enhance or permit septin binding [150]. To assess this possibility we check the effect of incubating septin oligomers on SLBs of varied lipid composition in the presence versus absence of excess 1mM GTP. We found that on SLBs that can trigger septin polymerization, such as

5%PIP2 and 20%PS+5%PIP2, the addition of GTP significantly enhanced the ability of septin hexamers to reproducibly bind 5%PIP2 SLBs and slightly increased it on 20%PS+5%PIP2 SLB. From our results, we can conclude that the presence of GTP increases septin binding. At this point we do not have a full explanation. From the knowledge that SEPT6 subfamily members do not hydrolyze GTP while SEPT2, SEPT7, and SEPT3 subfamily members do [79], we can assume that SEPT6 is bound to GTP after purification whereas SEPT2, SEPT7 and SEPT9 are bound to GDP (Chapter 2). Therefore, septin-bound GDP caould potentially be exchanged by freshly added GTP in SEPT2, SEPT7, and SEPT9 [167]. To be sure that the effect of increased membrane binding comes from the addition of GTP, future experiments are needed to characterize the nucleotide state of the septin complexes by using spin columns with radiolabeled nucleotides [243, 244].

Then we aimed to study the structure that the septin-bound filaments formed. Using TEM of septins on lipid monolayers and AFM of septins on lipid bilayers. On 5%PIP2 lipid monolayers, both septin hexamers and octamers formed a mesh of paired and single filaments, but with differences in the filament distribution. For octamers, single and paired filaments were locally parallel to each other but their distribution was otherwise unorganized. Two layers of filaments were present, with single and paired filaments being present in both layers. Similar two-layer septin filament formations have been observed for human septin octamers before [97]. In contrast, the hexamers formed a much more ordered double network with single filaments running in parallel in one layer and paired filaments in the second layer running in perpendicular to the single filaments. Furthermore, the distances between the hexamer paired filaments were conserved at around the length of a single hexamer (~24nm [83, 102]), showing a periodicity that suggests that a single region of the hexamers, likely the coiled-coils as suggested before [97, 208, 236], guides the cross-hatching patterning. We next did AFM on 20%+5%PIP2 SLBs. Septin octamers formed a similar pattern as on the monolayers and as in previous work [97]: a dense network of filaments with no obvious order. In contrast, hexamers formed a bundle-based meshwork with an apparent local order. A similar bundles-based network has been observed before for fly septin hexamers [96]. However, the human hexamer bundles were more curved and the surface was more densely packed than for fly hexamers at similar septin hexamer concentrations. To test whether two layers were present, as suggested by the cross-hatched patterns seen in TEM, we measured the height of the septin film for both hexamers and octamers. We did this using three methods. First, if all the septin filaments form two layers, we would expect two types of pixel values in the AFM, one for the background and one for the two-layered septin. Indeed, the distribution of pixel values showed a bimodal distribution (Fig. 4.5). Assuming the first peak to correspond to the background and setting its center height to 0nm, the second peak showed values between 5 and 10nm. Since human septin hexamers and octamers both formed very densely packed films the size of the background peak was quite small, making it more difficult to detect. The 5-10nm height of the second peak therefore likely represents an underestimate. Still, the height appears higher than the 4nm height of single septin filaments, consistent with more than a monolayer. Given the inaccuracy of the height histogram, we manually searched for regions with lower septin surface density, and measured the height of individual filaments. For both hexamers and octamers, single bundles/filaments had an approximate height of ~8-10nm, indeed suggesting the formation of a two layer network.

Finally, we used the Sauerbrey equation as a last check to find the height of the septin film from the final frequency shift from the QCM-D experiments, and found heights of 10-16nm, suggesting again the presence of two layers. However, these values should be carefully interpreted, because the Sauerbrey equation is only applicable to uniform, dense, and rigid films.

TEM and AFM results both indicated that septin hexamers and octamers form morphologically different films on lipid layers (Fig. 4.9). This finding is independently corroborated by the mechanics of the adsorbed film, as measured by QCM-D. The rate of decrease of the softness of the films as a function of surface coverage during the initial steps of the binding process was equal for septin hexamers and octamers. However, once the negative frequency shift $-\Delta f$, a proxy for the surface coverage, increased above 50Hz, the rate of decrease of softness decreased for the octamers while it remained constant for the hexamers, leading the hexamers to form a stiffer film than the octamers. The bundle-based network of hexamers observed by AFM is indeed probably stiffer than the filament-based network of the septin octamers. Interestingly, this final stiffer network for the hexamers was only observed in the presence of GTP and on SLBs, since in the TEM experiments on monolayers we observed a filament-based network. In agreement with these findings, earlier work showed that fly septin hexamers also formed a filament-based network on lipid monolayers and a bundle-based network on lipid bilayers [96]. All this suggests that septin filaments may form two morphologically different membrane-bound films: a bundle-based and a filament-based one. But since septin hexamers can form both types, bundle-based and filament-based films, the oligomer type is not the only controlling mechanism. It is therefore important to further explore how other environmental conditions, such as the presence of GTP or the type and composition of the lipid layer control the film formation.

Finally, we used particle-based simulations to study what factors govern the formation of the bundle-based hexamer films. In the simulations we considered four main parameters, nucleation rate, elongation rate, paired nucleation rate, and alignment of adjacent filaments. We considered filament pairing because of two main reasons. First, Szuba et al. [96] found that coiled-coils, which govern septin pairing, are important for the formation of a bundle-based network in case of fly septin hexamers. Second, the QCM-D results suggest that the first steps of the formation of bundle-based and filament-based networks are the same. Since TEM imaging showed that hexamers on lipid monolayers form filament-based networks containing paired filaments, we think it is likely that paired filaments are also important for the bundle-based network. The simulation revealed that to form networks of long paired filaments, growth and paired nucleation rates needed to be much higher than the nucleation rate, which seems to be consistent with a nucleation-elongation polymerization model. Comparing the AFM results with the results from the simulations with alignment, high elongation rate, and high paired nucleation rate, we can see how the formed networks are similar (Fig. 4.10). In both images we find abundant long and curved and locally aligned fibers. However the AFM images show bundles while the simulations clearly show single and paired filaments. This difference could stem from tip convolution during AFM imaging, which would make single, paired, and aligned filaments appear thicker than they are and not differentiable when they are too close.

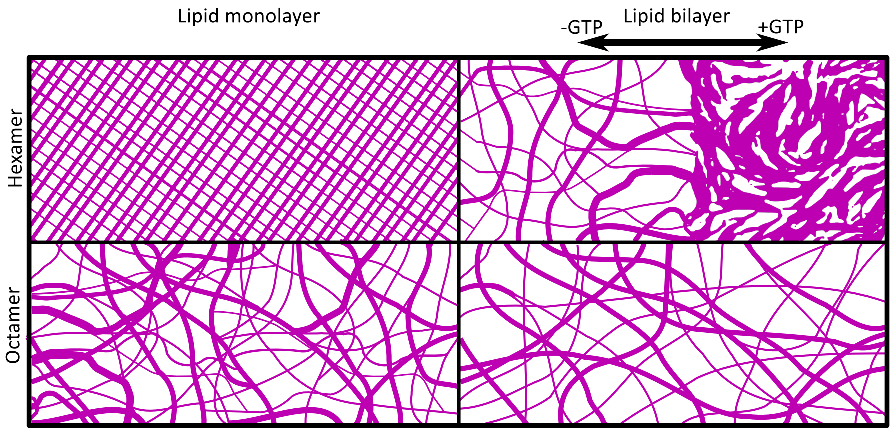

Figure 4.9. Morphologies of membrane-bound septin networks. Diagram showing the different types of morphologies that septin networks can acquire depending on the oligomer length (vertical axis), the type of membrane (horizontal axis), and the presence or absence of GTP (arrow). Octamers only form filament-based networks consisting of unordered single and paired filaments. Hexamers on monolayers form filament-based networks ordered into a cross-hatching pattern with paired filaments in one direction and single filaments in the other. Hexamers on bilayers in the absence of GTP likely form a filament-based network (only indirectly observed by QCM-D, not yet confirmed by AFM). Hexamers on bilayers in the presence of GTP form bundle-based networks.

Despite the interesting results coming from these simulations, we think that there is still room for improvement. First, the simulations consider that only one layer is formed, while we show that the septin films consist of two layers. Second, many of the filaments in the simulations are partially paired, which does not seem to be the case for septin paired filaments observed by TEM imaging here nor in previous literature [82, 96, 208]. Likely the simultaneous binding of septin oligomers to the lipid membrane and to a membrane-bound septin filament would make the rate of paired nucleation even higher than the rate of growth, leading to a more complete pairing. Finally, in the simulations septin filaments are not allowed to cross each other. This is likely the case when membrane binding is strong, and this condition favors the alignment needed to form the bundle-based network. However, testing the option of allowing septin filaments to cross each other could lead to the formation of the filament-based network. Identifying if this is is the case and what are the parameters that govern when filaments align or cross each other is vital to understand when each type of network forms.

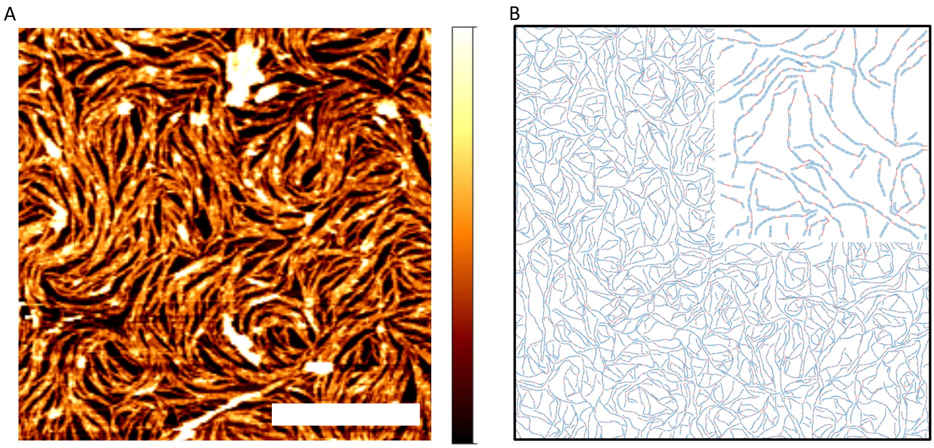

Figure 4.10. Comparison of the networks obtained by AFM and the simulations. A. Representative atomic force microscopy (AFM) images illustrating the network morphology observed for 120 nM septin hexamers organizing on a 20%PS+5%PIP2 SLB. Scale bar is 2µm. B. Example result of the simulation with $\mathbf{k}_n$ = **1**s^{-1}, $k_p = 10^4\,s^{-1}$, $k_g = 10^4\,s^{-1}$, considering alignment (α=2π). Red shows single filaments while blue shows paired filaments. Inset shows a close up. Fields of view between A and B are of the same size.

4

4.4. Materials and methods

All chemicals unless specified otherwise were obtained from Merck KGaA.

4.4.1. Purification of human septin complexes

Human septin oligomers were purified and their quality was checked as detailed in chapter 2. We used septin hexamers with a subunit order of SEPT2-SEPT6-SEPT7-SEPT7-SEPT6-SEPT2 and septin octamers with a subunit order of SEPT2-SEPT6-SEPT7-SEPT9_i1-SEPT9_i1-SEPT7-SEPT6-SEPT2. Septins were fluorescently tagged with msfGFP on the C-terminus of SEPT2. For purification, SEPT2 contained a his_6-tag at its N-terminus, and SEPT7, for hexamers, or SEPT9, for octamers, contained a Strep-II-tag at its C-terminus.

4.4.2. Small unilamellar vesicles preparation

The first step to prepare SLBs is to make small unilamellar vesicles (SUVs) that will rupture on a surface, forming a surface-adsorbed unilamellar lipid bilayer [232]. We used three types of lipids to prepare the SUVs, namely 1,2-dioleoyl-sn-glycero-3-phospho-(1'-myo-inositol-4',5'-bisphosphate) (ammonium salt) (PIP2) (Merck KGaA, #850155P), 1,2-dioleoyl-sn-glycero-3-phosphocholine (DOPC) (Merck KGaA, #850375C), and 1,2-dioleoyl-sn-glycero-3-phospho-L-serine (sodium salt) (DOPS) (Merck KGaA, #840035C), all from Avanti Polar Lipids.

Following earlier methods [96], lipids were mixed in a glass vial in the specified mole proportions in either chloroform, when PIP2 was absent, or in a 20:9:1 chloroform:methanol:water mixture, when PIP2 was present. The solvent was evaporated using a stream of N_2 followed by overnight incubation in a desiccator. The dried lipid film was dissolved in buffer to give a total lipid concentration of 0.25mM. The SUV buffer was either

F-buffer pH 7.4 (20mM Tris HCl, 2mM $MgCl_2$, 50mM KCl, 1mM DTT) or, if PIP2 was in the mixture, NaCi buffer pH 4.8 (50mM citrate, made of equal molarity trisodium citrate and citric acid mixed in a 2:3 volume ratio, 50mM KCl, 0.1mM ethylenediaminetetraacetic acid). The acidic citrate buffer was used to reduce the charge on the PIP2 head groups, thus promoting SLB formation [245]. The lipids were resuspended by four cycles of 1 min vortexing and 5 min incubation at room temperature. For AFM only, the solution underwent 12 freeze-thaw cycles to promote vesicle rupture.

Finally, SUVs were obtained by sonicating the lipid solution at room temperature using an Ultrasonic homogenizer series HD 2000.2 sonicator equipped with a BR30 cup resonator (Bandelin) at 10% amplitude for 30 minutes (total sonication time) with pulses of 5s on and 5s off to avoid excessive heating.

4.4.3. Sample preparation

We polymerized septin on SLBs by rapidly diluting them 6-fold from the high (300mM) KCl storage buffer that prevents polymerization into the same same buffer, but without KCl. The reduced salt concentration induces polymerization [83]. In preparation, we first diluted the septin complexes to a concentration 6 times higher than the desired final concentration in septin buffer. In parallel, we prepared a 5x pre-mix of septin polymerization buffer (58.25mM Tris-HCl pH 7.4, 5.83mM $MgCl_2$, and 5mM DTT). Just before the septin addition onto the SLB, the 5x pre-mix septin polymerization buffer was diluted 5 times and the septin was diluted 6 times in the same solution to give septins in F-buffer. When used, GTP (Merck KGaA, #10106399001) dissolved in F-buffer pH 7.4 at a stock concentration of 100mM was added in this final dilution step to reach a final concentration of 1mM.

4.4.4. QCM-D experiments

Silicon-coated QCM-D sensors (Quantum design, Q sensor QSX-303) were cleaned in a UV/ozone cleaner (Ossila, Cat. # L2002A3) for 20 minutes. After, the sensors were immediately mounted in the flow module (Quantum design, QFM 401) of the Q-Sense E4 system. Then, the resonance frequencies and dissipation constants for overtones 5 to 11 were calibrated as per the manufacturer's instructions and SLB buffer was added to the flow system. The steps from removing the sensors from the UV/ozone cleaner to buffer arriving on the sensor were done within 15 minutes to maintain surface hydrophilicity. The SLB buffer (NaCi-SLB for SLBs containing PIP2 or F-SLB buffer in absence of PIP2) was identical to the SUV buffer, but with a higher KCl concentration (150 mM) to promote SUV rupture and SLB formation. We kept adding SLB buffer at 20μL/min until the frequency and dissipation shift signals stabilized, which usually took ~20 minutes. Next, we immediately formed the SLB. To do so, we first diluted the pre-formed SUVs 4-fold in SUV buffer, but with a KCl concentration of 183.33 mM, to give a final buffer composition matching that of the NaCi-SLB or F-SLB buffer. Since the experiment works in continuous 20μl/min flow conditions, we recommend to prepare at least 700μL of diluted SUVs. Once the SLB was formed [232, 233], as can be noted by the stabilization of the frequency change at around -25Hz, and the dissipation at around $0.1*10^{-6}$ after an initial peak in both signals, we washed the SLB with F-buffer until ~2min later we noted a change in both frequency and dissipation due to the change in buffer composition.

Then, we diluted the septins as described above to give 1mL of 50nM final septin complex concentration and immediately added them to the flow system at 20μL/min. Once the septin solution was finished, we added septin buffer to the system to induce septin depolymerization (due to the presence of 300mM KCl) to test for the reversibility of membrane binding.

After finishing the experiment, the system was thoroughly washed by sequentially running 2% Sodium dodecyl sulfate (SDS), Milli-Q water, ethanol, and Milli-Q water, each for 5 minutes at 300μl/min. Then, the system was dried by keeping the flow at 300μl/min without adding any solution. Finally, to allow reuse of the sensors, they were washed for at least 30 minutes by submerging them in 2% SDS, thoroughly rinsed with Milli-Q water and blow-dried with N_2 gas.

4.4.5. TEM experiments

We produced septin-coated supported lipid monolayers on EM grids by forming a lipid monolayer at the air-water interface of a solution of 50nM septin complexes inside a well and then transferring it onto a transmission electron microscopy grid [246, 247]. To do so, we first prepared 100μL or 30μL-wells. The 100μL-wells consisted of lids of 0.5mL Eppendorf tubes. The 30μL-wells are the wells in the Microwell Staining Mold (Ted Pella, Cat. # 103), which we cleaned between uses by sonicating for 5 minutes in ethanol, and subsequently in MilliQ water in a bath sonicator (Branson Ultrasonic Bath). At room temperature, we dissolved the lipids with the desired species composition in chloroform. We used a total lipid concentration of either 0.005mM or 0.01mM, with comparable results. Next, we added 100μL or 30μL of septins in polymerization buffer, prepared as explained above, to the well. To form the monolayer, we then dropped 2μL of the lipid mixture on the well using a 5μL Hamilton syringe. The well is then incubated at room temperature for at least one hour to bind the proteins to the lipid monolayer. Subsequently, an EM-grid (QuantiFoil, QF300 R1.2/R1.3 or C support Cu400) is placed with a crossover tweezer on top of the well for 2 seconds. The monolayer with attached proteins will adhere to the grid [247]. Finally, the grids were fixed and stained by adding 3μL of 2% uranyl acetate in water and blotting after 30-60 seconds with filter paper. We used either EM-grids with the standard carbon layer on a copper support (QuantiFoil, C support Cu400) or EM-grids designed for cryo-EM (QuantiFoil, QF300 R1.2/R1.3). The latter were used to increase the contrast, since the lipid monolayer spans over the holes in the carbon [247]. Then, the electron beam strikes only the lipids and proteins stained with uranyl acetate within the holes. However, the monolayers over the holes are fragile since they lack support. For this reason, when using the Cryo-EM grids, we did not wash the sample before staining.

4.4.6. TEM image analysis

We manually detected the filaments for the septin hexamers incubated on 5% PIP2 lipid monolayers. We did this by tracing the filament by eye with a linear spline in FIJI [154]. Unfortunately, we only could trace paired filaments, since single filaments showed too low contrast. We manually identified the paired filaments by their thickness. Next, we calculated the closest distance, from edge of one filament to edge of the adjacent filament, between each filament and its adjacent filaments along the filament length. The code for calculating this closest distance between filaments can be found at https://github.com/djimderidder/2021imageAnalysisMEP. For the angle measurements for the septin hexamer meshworks, we used the angle tool from FIJI to manually calculate the acute angle between crossing single and paired filaments.

4.4.7. AFM experiments and image analysis

Silicon wafers (BT-electronics, Silicon Wafer 4” N(Arsenic) Prime) were cut into 10x10cm squares, rinsed with Milli-Q water, ethanol, and Milli-Q water, and dried with N_2 gas. After, the substrate was glued with two-component epoxy glue (Bison Kombi Snel-Rapide) to a microscope slide (Menzel Gläser). Next, we rendered the silicon wafer surface hydrophilic and removed any organic contaminants by treating with UV/ozone at 75 Watt 100 mTorr O_2 for 5 minutes (Plasma Prep III, SPI). Within 5 minutes of treating the wafers, we drew a ring with grease (Sigma Aldrich, Z273554) on the treated silicon wafer surface, wherein we immediately added 100 μL of the pre-formed SUVs dissolved in NaCi-buffer. Incubating the SUVs for 30 minutes resulted in the formation of an SLB on the silicon wafer through vesicle rupture. Remaining vesicles were washed out by replacing 50μL of solution with 50 μL of F-buffer six times. Next, we polymerized 60nM or 120nM septin complexes for at least 20 minutes at room temperature on the SLB in 100 μL F-buffer. This step was followed by washing out unbound septin by replacing 50μL of solution with 50 μL of F-buffer six times and leaving 100 μL. Finally, to reduce septin interactions with the AFM tip, we fixated the sample with 1 wt% glutaraldehyde (Sigma Aldrich, #G7651) and similarly washed six times with F-buffer. Earlier work [96] with fly septins showed that GTA fixation does not change the structure of the membrane-bound septin meshwork.

AFM images were acquired using a Nanowizard 4 XP Bioscience (Bruker) with a silicon cantilever (ScanAsyst-Fluid+; Bruker) with a nominal spring constant of 0.35N/m and sharp tips with a nominal radius of 2nm. using the JPK Fast Scanner cantilever holder (Bruker). We used quantitative imaging mode (QI mode) with a maximum applied force of 1.5pN, an amplitude of 50-100nm, a scan rate of 3-5ms/pixel (depending on the amplitude), and a resolution of either 512x512px or 1024x1024px.

The AFM images were processed using Gwyddion [248]. We first corrected for sample tilt by second-order flattening the images. Next, we corrected for scan line artifacts by aligning the rows and correcting for scars. Finally, we exported the processed AFM data to an Excel file and performed the additional analysis with custom-written code in Python, which can be found at https://github.com/djimderidder/2021imageAnalysisMEP. First, we manually sorted the images based on morphology to find artifact-free (protein aggregates and imaging artifacts) images containing filaments. To analyse the height profiles, we did a non-linear least-squares fit (SciPy package) of a bimodal distribution to the histogram of the height for each image. For the analysis of the height of single bundles/filaments, we did plot profiles of manually drawn lines crossing a bundle/filament between voids in the image.

4.4.8. General simulation setup

Below we outline our approach to model the assembly of septin filaments on supported lipid bilayers (SLBs). During the simulation, septin filaments can nucleate, grow and pair, following rules described below. Importantly, all simulation events, whether nucleation, growth, or paired nucleation, can only occur if they do not result in an overlap or intersection of septin subunits. Otherwise, the corresponding simulation events are discarded.

The parameter values are summarized in Table 4.1.

Table 4.1. Model parameters.

Parameter	Used value	Reference value
Persistence length l_p	$1\,\mu m$	$1.08 - 1.38\,\mu m$ (A. gossypii) [249]
Simulated box (2d) $L_x = L_y$	$5\,\mu m$	$5\,\mu m$; FOV in AFM exp.
Subunit length hexamers l_s	24 nm	25 nm [76]
Subunit length octamers l_s	32 nm	
Subunit width d	4 nm	5 nm [76]
Subunit reservoir N_{res}	3×10^4	-
Alignment angle α	$0 - 2\pi$	-
Nucleation rate k_n	$1 - 10^4 s^{-1}$	-
Growth rate k_g	$1 - 10^4 s^{-1}$	-
Paired nucleation rate k_p	$1 - 10^4 s^{-1}$	-

First simulation event: filament nucleation

A nucleation event is characterized as the mutual binding of two subunits on the membrane. This event generates a membrane-bound filament, consisting of two septin subunits (cf. Fig. 4.6A). To simulate this process, we begin by setting the positional angle of the first septin subunit that we draw from a uniform distribution ranging between $[-\pi, \pi)$. Next, we generate an orientational offset, denoted as δ_ϕ, between the two subunits. This offset is generated from a normal distribution with a mean of 0 and a standard deviation of $\sqrt{2l_s/l_p}$, where l_s is the subunit length and $l_p = 1\,\mu m$ [249] is the persistence length of the filament. We also assign growth directions to the two subunits so that further septin subunits extend the filament nucleus in opposite directions. Importantly, during nucleation, we also determine randomly to which side paired nucleation will possibly occur. In this way, paired nucleation events can only happen on the same side over the whole length of the filament.

Second simulation event: filament growth

A growth event is characterized by the binding of a subunit to one of the available ends of a membrane-bound filament. The number of available filament ends a equals the number of all unconnected filament ends where the binding of a subunit does not lead to the intersection of the subunit with another filament. In a growth event, we first randomly select one available filament end that is going to be extended by an additional subunit. Secondly, we determine the orientation of the newly added subunit. To represent the orientation deviation, we generate a random value from a normal distribution with a mean of 0 and a standard deviation of $\sqrt{2l_s/l_p}$. We add the orientation deviation to the orientation of the preceding subunit to obtain the orientation of the newly added subunit (cf. Fig. 4.6A). In this way, we simulate the growth of semiflexible septin filaments as a persistent random walk with persistence length l_p [250].

Filament alignment vs growth inhibition: To reflect the experimental observation of filaments growing bound to the surface without intersecting, we prohibit intersecting filaments in the simulation. Instead, when filaments meet, they can either align or stop growing (cf. Fig. 4.6A). A contact region is defined between a growing and non-growing filament if the centers of their subunits are closer than the subunit length l_s. If there are more than two subunits within the contact region, we assume that the closest subunit is triggering alignment. Alignment occurs when the angle under which the filaments meet is smaller than the alignment angle α, otherwise growth stops. If alignment occurs, the orientation of the nearest subunit is adopted and an offset is added to it, drawn from a normal distribution with a mean of 0 and a standard deviation of $\sqrt{2l_s/l_p}$.

Paired filament growth: During a growth step, if the center of the newly added subunit is closer to the center of an adjacent subunit compared to the center of the growing subunit, paired filament growth can happen. In this context, the growing subunit is defined as the subunit to which the new subunit is to be added. Paired growth will happen if the growing subunit is paired and the adjacent subunit is unpaired. Moreover, to avoid overlaps, the newly added subunit has to be at least 5 nm apart from the growing subunit. In this case, instead of freely extending the growing subunit by one subunit, as described previously, the adjacent unpaired subunit is then paired. In this way, filaments can grow paired (cf. Fig. 4.6A).

Third simulation event: filament paired nucleation

Paired nucleation involves the binding of a subunit to an unpaired subunit of a membrane-bound filament. However, in contrast to growth events, the added subunit does not bind longitudinally but instead in parallel to the target subunit (cf. Fig. 4.6A). To initiate a paired nucleation event, we randomly select a subunit from the pool of unpaired subunits p, including all subunits that have not been paired with another subunit yet. It is important to note that each subunit can be paired with at most one other subunit. The side of the filament to which paired nucleation occurs is the side that was already determined for the entire filament during nucleation. The newly added subunit is positioned at a distance of 2 nm of the target subunit with the same orientation. Additional subunits can bind to this subunit from both ends.

Dynamics of filament growth

In order to simulate the dynamics of septin filament growth, we make use of the Gillespie algorithm [251]. We implement three different reaction rates for the three simulation events that can occur: the nucleation rate k_n, the growth rate k_g and the paired nucleation rate k_p. The typical parameter values are summarized in Table 4.1. We define the propensities β_i of the three possible simulation events that drive the dynamics of filament assembly [252] as follows:

$$\beta_1 = k_n \cdot s \cdot (s-1), \tag{4.2}$$

$$\beta_2 = k_g \cdot s \cdot a, \tag{4.3}$$

$$\beta_3 = k_p \cdot s \cdot p. \tag{4.4}$$

β_1 defines the propensity for nucleation, β_2 the propensity for growth and β_3 the propensity for paired nucleation, where s is the number of free subunits in the bulk that can potentially bind to the membrane, a is the number of available filament ends to which free subunits can bind to and p is the number of unpaired filament subunits with which free subunits can be paired.

In order to determine the time τ until the next simulation event occurs, we draw a random number r_1 from a uniform distribution between 0 and 1 and calculate $\tau = \ln(1/r_1)/\beta_\Sigma$, where $\beta_\Sigma = \sum_i \beta_i$ is the sum of all propensities. After the time τ the simulation event i occurs if $\beta_{i-1}/\beta_\Sigma \leq r_2 < \beta_i/\beta_\Sigma$ is fulfilled, where $\beta_0 = 0$ and r_2 is a random number drawn from a uniform distribution between 0 and 1.

During the simulation, we track the time, the number of free subunits, the number of filament ends and the number of unpaired filaments. We simulate the assembly of septin filaments with a finite reservoir of subunits N_{res} until the reservoir is completely empty and the simulation stops.

4.5. Supplementary information

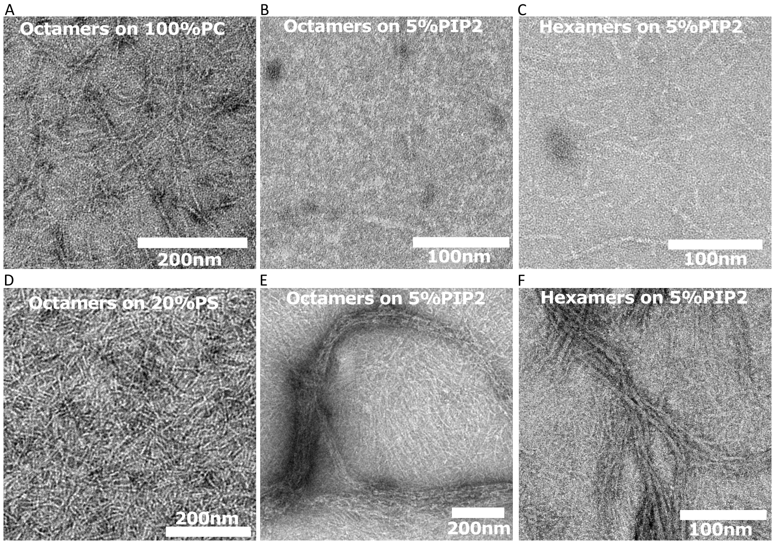

Figure S4.1. TEM images of septin complexes on lipid monolayers of different lipid composition. A. 50nM septin octamers incubated on 100%PC lipid monolayer. B. Corresponding image for 5%PIP2 lipid monolayer. C. 50nM septin hexamers incubated on 5%PIP2 lipid monolayer. D. 50nM septin octamers incubated on 20%PC lipid monolayer. In all panels A-D, we observe a few short and scattered filaments on the monolayer. E. Same as B, but showing a sample region with monolayer-anchored septin bundle. F. Example of monolayer-anchored bundles for septin hexamers.

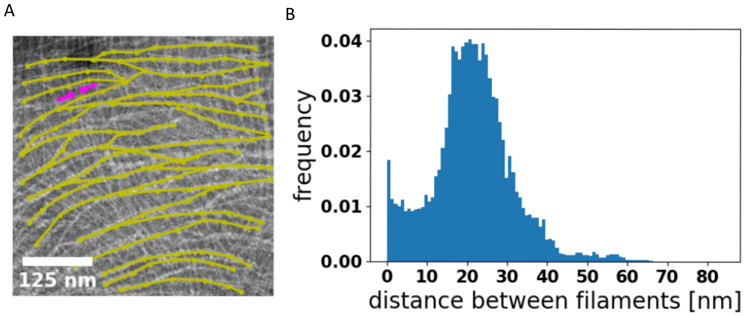

Figure S4.2. Measurement of the distances between paired filaments in septin hexamer meshworks formed on 5%PIP2 monolayers. A. Representative TEM image of a septin hexamer meshwork on a 5%PIP2 monolayer with the manually detected paired filaments as yellow lines. The pink arrows point to a single filament recognizable by its ~4nm width. B. Histogram (N= 9 images from 3 samples. # bins=100) showing the measured distance between neighbouring detected paired filaments. Note the peak at 0nm and the peak at 24nm, representing the filaments coming together and the typical distance between the paired filaments, respectively.

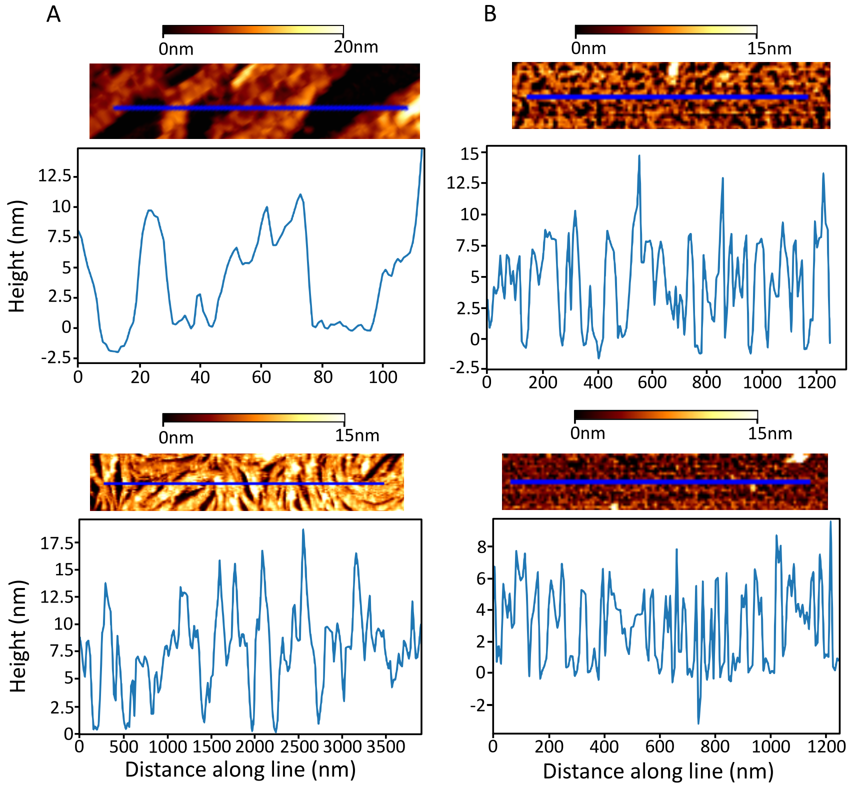

Figure S4.3. Examples of 8nm high bundles and filaments in the septin networks on 20%PS+5%PIP2 SLBs. Representative images and plot profiles along the blue lines for two independent samples of 120nM septin hexamers (A) and 60nM septin octamers (B) binding to 20%PS+5%PIP2 SLBs. Individual bundles (in A) and filaments (in B) show a height between 8 and 12nm.

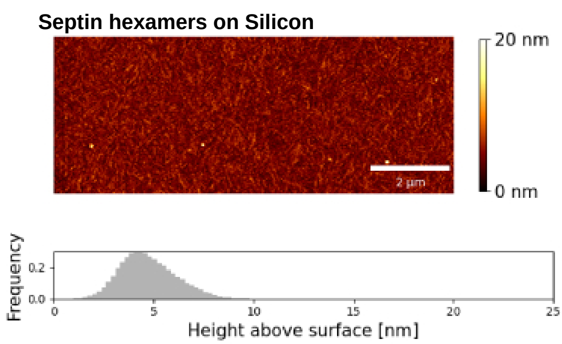

Figure S4.4. AFM of septin hexamers in the absence of an SLB. Representative atomic force microscopy (AFM) images and corresponding height histogram showing 120 nM septin hexamer organization on a bare silicon substrate. Since we could not observe two peaks, we used the minimum height value as 0.

Acknowledgements

We thank Jeffrey den Haan for his help with protein purification. F.F. gratefully acknowledges funding from the Kavli Synergy program of the Kavli Institute of Nanoscience Delft.

4

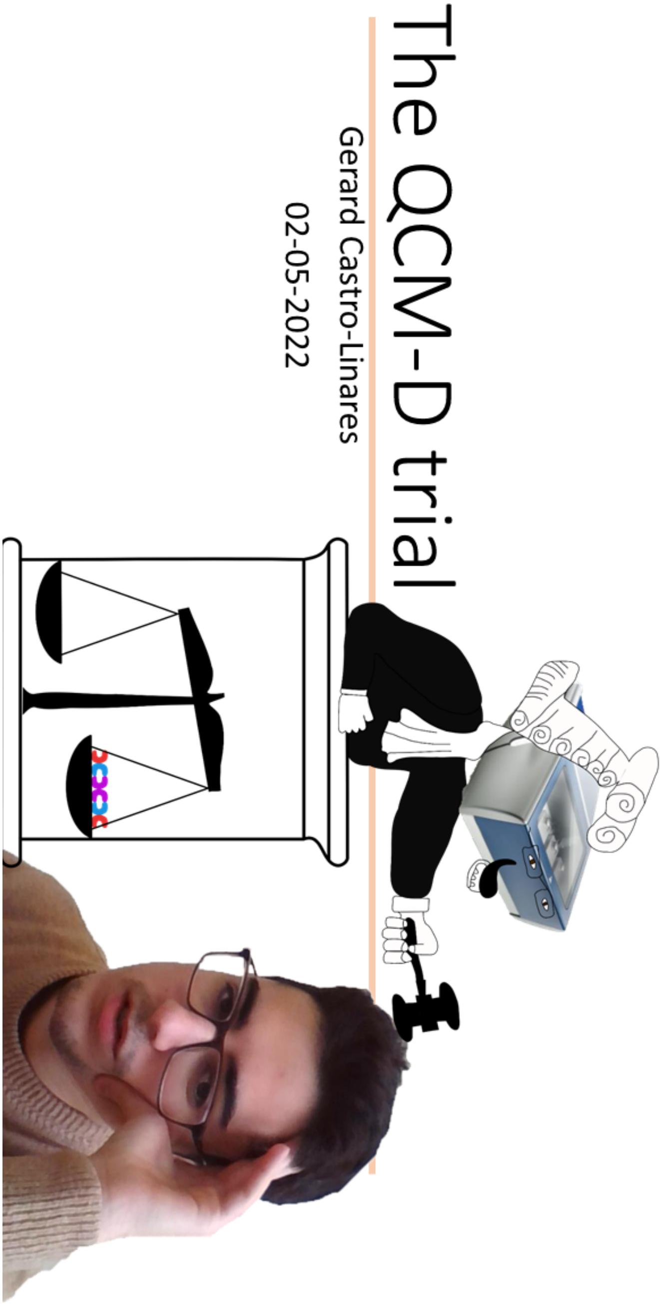
The QCM-D trial
Gerard Castro-Linares
02-05-2022

Chapter 5

Human septins exhibit lipid and curvature sensitivity in binding to cell-sized vesicles

5

Recent evidence suggests that septin cortical networks may play a direct structural and mechanical role in the cell cortex. To explore this possibility, we utilized emulsion Droplet Interface Crossing Encapsulation (eDICE) to form Giant Unilamellar Vesicles (GUVs) where we either encapsulate septin complexes inside or add them to the outside of the vesicles. We then used confocal imaging to determine the effect of lipid composition and membrane curvature on septin-membrane binding and to test whether septins can reshape free-standing lipid membranes. We show that human septin octamers and hexamers subtly differ in their ability to bind negatively charged membranes. We also observed a synergistic effect in septin recruitment for DOPS and PIP2 lipids, and found that PIP2 is absolutely required for septin binding. Interestingly, septin binding on the vesicle inside was independent of vesicle diameter (4 to 10 µm), suggesting binding is curvature-insensitive in cell-sized vesicles, but septins bound on the outside generated periodically spaced membrane spikes or bumps. We conclude that, while at the cell scale septins are insensitive to the size of the membrane curvature, they can still distinguish between positive and negative curvatures.

This chapter is based on a manuscript with the same name by Gerard Castro-Linares, Katerina Kourkolou, Elise Perton, Marcos Arribas Pérez, and Gijsje H. Koenderink which is currently in preparation for publication. Experiments were designed in collaboration by Gerard Castro-Linares and Marcos Arribas Pérez. Experiments were performed by Katerina Kourkoulou, Elise Perton, Gerard Castro-Linares and Marcos Arribas Pérez. Katerina Kourkoulou wrote the membrane localization analysis script and did the analysis under the supervision of Gerard Castro-Linares and Marcos Arribas Pérez. Gerard Castro-Linares and Katerina Kourkoulou wrote the manuscript while all other authors gave feedback.

5.1. Introduction

The shape of mammalian cells is defined by the cytoskeletal networks that are associated with the cell surface. The actin cortex, which is a thin network of actin filaments located beneath the plasma membrane, plays a central role in shaping the cell surface and determining its mechanical properties [253]. In addition to actin filaments, the actin cortex also contains molecular motors, membrane-actin anchoring proteins, actin nucleators, crosslinkers, and other regulatory proteins [47]. Together, these components make the shape of animal cells highly dynamic and adaptable to external stimuli in a variety of physiological contexts, such as cell migration and tissue morphogenesis.

The mammalian cell cortex contains a second group of cytoskeletal proteins known as septins [76]. Septins contribute to many vital functions in the cell, such as cell division [106], cell-cell adhesion [130], cell motility [119], tissue morphogenesis [131], and protection against bacterial infection [77]. These proteins form small hetero-oligomers composed of septins from different subfamilies [76, 86, 96, 102, 133], which vary in length depending on the species. For instance, human septins form both hexamers and octamers [85]. These hetero-oligomers serve as the basic building block for apolar filaments [254] that interact with the cell membrane [96, 98, 207], actin filaments [101, 102, 130, 144], and microtubules [103]. The presence of septin on the cortex has been found to be important for membrane integrity and mechanical stability [98, 119, 255]. For example, septins are vital for reinforcement of cell-matrix adhesions during *Drosophila* development [256] and for cell rounding during cell division [120]. However, the fact that septins can bundle and crosslink actin filaments (Chapter 6 and [101, 102]), and anchor actin to reconstituted model biomembranes (Chapter 7 and [144]) has made it difficult to determine whether these membrane strengthening functions come from a direct binding of septins to the membrane, by anchoring the actin to the membrane, or by simply strengthening the actin cortex. A recent study by Laplaud et al. [257] used an external magnetic field to pinch the cortex of dendritic cells between two beads. Intriguingly, they found that when actin polymerization was impeded, the measured thickness of the cortex remained higher (5 nm) than expected for a naked membrane (~92nm). This observation suggests that proteins present in the cell cortex, other than actin itself, may have a more direct influence on the membrane than previously thought. We hypothesize that, thanks to their polymerizing and membrane-binding abilities, septins are good candidates to fulfill this role.

Cell-free studies have shown that septins have the ability to directly bind lipid membranes, which is conserved from yeast to mammals (Chapter 4 and [82, 96, 97]). Yeast septins have been shown to recognize phosphatidylinositols (PI) lipids with different phosphorylation states [82, 95, 99, 100, 217, 218]. In case of fly septins, electrostatic interactions were shown to be sufficient to drive membrane binding and polymerization, as shown by their ability to bind not only phosphatidylinositol 4,5-biphosphate (PIP2), an important signaling lipid in animal cells [219–221], but also phosphatidylserine (PS), a negatively charged lipid that makes up about ~20% of the inner leaflet of the plasma membrane [25]. In contrast, as described in chapter 4, we found that human septin complexes can only polymerize on membranes containing PIP2, although PS synergistically reinforces this binding.

Interestingly, septins are one of the few proteins that are able to sense micrometric curvature of membranes [95, 108], with other curvature-sensitive proteins being sensitive at the nanometer scale. Bridges et al. [95] found that yeast septins localize preferably to the site with highest curvature of branching yeast *Ashbya gossypii*, while human septins localize preferentially to the base of protrusions in mammalian cells [95, 127, 128]. Bridges et al. [95] also found that both yeast and human septins could bind to differently sized beads coated with a supported lipid bilayer (SLB), with maximal binding to beads of ~ 1μm in radius. Later, they also found that membrane binding causes yeast septins to form filaments that orient in a curvature-dependent manner [230]. Yeast septins bound along the long axis of SLB-coated cylinders of a small (100-400nm) radius, while increasing the cylinder radius (600-2000nm) allowed the septins to turn and align with the axis of principal curvature. Beber et al. [98] performed related studies with yeast septin complexes, but using SLB-coated wavy substrates to study selectivity for positive and negative curvatures. When encountering regions of positive curvature, such as the crests or hills of the waves, yeast septins formed filaments bound preferentially along the long axis of the substrate, avoiding the curvature. Conversely, when encountering regions of negative curvature, such as the valleys or troughs of the waves, the septins formed filaments bound perpendicularly to the long axis of the substrate, favoring the curvature. This indicates that septins avoid positive curvatures and prefer to bind to negative curvatures. When these experiments were repeated with human septin octamers [97], these were also found to prefer negative curvatures. At low concentrations (8.7nM), human septin octamers formed filaments preferentially bound to the valleys of the wavy pattern, and as the concentration increased (>26nM) they started to form filaments bound to the hills of the SLB. Interestingly, when the concentration increased even more (87nM), a second layer of septin filaments, placed perpendicularly to the first layer, appeared. At the highest concentration tested, filaments of the lower layer (directly bound to the membrane) were distanced around ~30nm while the distances between filaments of the upper layer was ~20nm. This is in contrast with yeast septins, which formed a single layer at high (100 nM) concentration [98].

Interestingly, septins not only sense membrane curvature, but also generate curvature. The research described above used SLBs on silicon surfaces, which hamper membrane deformation. Lipid vesicles instead provide a free-standing model bilayer, which permits to investigate the effect of septin binding on membrane shape. When yeast or human septin octamers were incubated on the outside of giant unilamellar vesicles (GUVs), they deformed the vesicle [97, 100]. Yeast septins formed membrane spikes when bound to the outside of GUVs [98], while human septin octamers formed regularly spaced bumpy membrane deformations on the GUV, making the vesicles wavy [97].

The fact that septins bind directly to lipid bilayers forming either a filamentous ([82, 96, 97, 100] and Chapter 4) or bundle-based ([96] and Chapter 4) meshwork together with the observations described above that septins can reshape GUV membranes suggests that they could directly bind and reinforce the cell membrane. Despite the fact that septins localize to the cell membrane being confined to the interior of the cell (except when they bind to infecting bacteria [77]), no *in vitro* reconstitution research has been done with septins encapsulated inside GUVs. Therefore, in this chapter we encapsulate septins inside GUVs and compare how they interact with the membrane in comparison with the situation where septins are added outside the GUVs. First, we encapsulated septin complexes inside

GUVs with varying lipid compositions to examine if the lipid specificity demonstrated on SLBs in Chapter 4 is the same for free-standing membranes. Then, we examined the curvature sensitivity of septins from two points of view. First, we compared whether GUV-encapsulating septins bind differently to GUV membranes of different size, to check whether septins are sensitive to curvature at smaller scales (0.04-0.33μm^{-1}) than previously examined (0.31-6.67μm^{-1}) [95, 97, 98, 230]. Secondly, we examined whether septins can differentiate curvature sense by either encapsulating the septins inside of the GUVs or incubating them on the outside of the vesicles.

5.2. Results

5.2.1. GUV production with eDICE

In this work we aimed to encapsulate septins inside GUVs. Two main classes of techniques exist for protein encapsulation, namely swelling-based methods and emulsion-based approaches. Here we decided to use the emulsion-based eDICE approach, which was recently shown to be highly efficient at generating high yields of GUVs with encapsulated cytoskeletal proteins [258]. We specifically used emulsion droplet interphase crossing encapsulation, or eDICE [258]. This technique is a variation from the most classically used continuous droplet interphase crossing encapsulation, or cDICE [259]. eDICE is based on transforming water-in-oil emulsion droplets stabilized by a lipid monolayer into vesicles by centrifugally driving the droplets across a lipid-stabilized oil-water interphase where they acquire a second lipid monolayer and hence transform into GUVs (Fig. 5.1). This procedure allows for a quick encapsulation, useful for time sensitive experiments, since it only takes around 30sec to make the emulsion. It is also useful for temperature sensitive experiments because the solutions can be kept at a specific temperature in the tubes and then the GUVs are formed quickly. This is especially useful for cytoskeletal proteins like septins, where long incubation in the final buffer at physiological temperatures will cause premature polymerization in solution before GUV formation is complete.

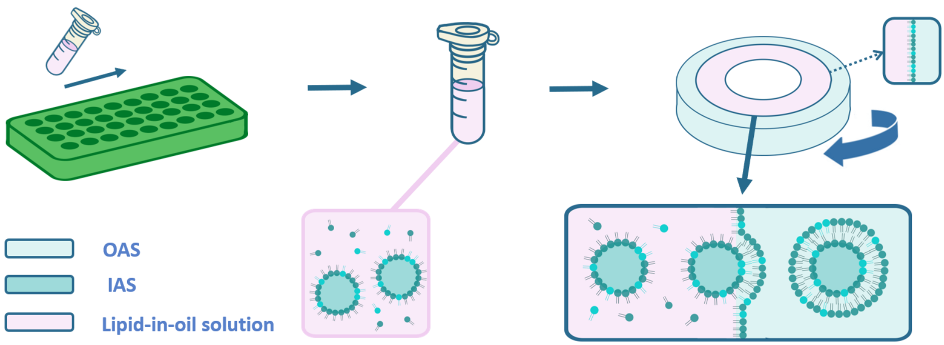

Figure 5.1. eDICE schematic. After addition of the inner aqueous solution (IAS) in a lipid-in-oil solution, rapid rubbing on a rough surface leads to the formation of an emulsion (left-middle). The pre-formed droplets are then added in a spinning chamber where a lipid monolayer has previously formed between the lipid-in-oil solution and the outer aqueous solution (OAS). The centrifugal forces push the droplets to cross the interface, leading to the formation of GUVs (right).

Using eDICE, we were able to generate both empty GUVs, which we used for testing binding of septin complexes to the outer surface, and GUVs encapsulating septin complexes. In both cases, the quality of GUVs was assessed through confocal microscopy, where the GUV yield, size, and membrane quality were examined. An example image is shown in Fig. 5.2A. Despite batch-dependent variations in sample quality and density, eDICE almost always produced a high yield of GUVs with a wide but consistent vesicle radius distribution (4-20µm, with an average of ~7µm, Fig. 5.2B). However, other lipid structures and objects were commonly observed.

In all samples several types of artifacts were observed. First, we could see dust particles (Fig. 5.2C). Free-floating lipid aggregates, seen as bright fluorescent specks (Fig. 5.2D) or oil droplets (Fig. 5.2E), were also observed. Often, large immobile lipid aggregates of different sizes were attached to the vesicles (Fig. 5.2F). Multilamellar structures were often encountered among the GUVs (Fig. 5.2G), or long lipid tubes (Fig. 5.2H). Often, small bright lipid aggregates diffused around within the GUVs' lumen (Fig. 5.2I) or smaller vesicles were encapsulated within the GUVs (Fig. 5.2L). On occasion, the membranes of the GUVs were attached to neighboring vesicles and lipid aggregates, forming large clusters (Fig. 5.2F), or they presented lipid pockets (Fig. 5.2K) or other secondary membrane structures observed as bright spots (Fig. 5.2J). In the latter case, septin often localized in these regions independent of membrane composition, possibly trapped within the formed lipid structures (Fig. 5.2J, inset). The percentage of these artifacts varied per sample, indicating that eDICE is highly sensitive to environmental conditions and manual handling during preparation. To overcome this issue, at least 3 independent samples were prepared for each membrane composition of interest, and, if an automatic analysis was needed, rigorous filtering was implemented to isolate only clean-looking vesicles.

5.2.2. Septin encapsulation efficiency

To assess the efficiency of eDICE in encapsulating septins within GUVs, we used quantitative fluorescence microscopy. Specifically, we encapsulated 800nM of 15% msfGFP-labeled septin hexamers in high-salt septin buffer, to prevent septin polymerization ([102] and Chapter 2), within GUVs composed of a neutral lipid bilayer, to prevent septin binding ([96] and Chapter 4). We calibrated the septin signal by measuring the fluorescence intensity for a series of 15% msfGFP-labeled septin hexamer solutions at different concentrations (0, 200nM, 400nM, 600nM, 800nM, 1000nM) (Fig. 5.3). Septin has a high affinity for glass surfaces (see Chapter 4). Therefore, to prevent septin sticking while imaging the septin bulk solutions (Fig. 5.3A), we passivated the surface with an SLB made of neutral lipids. Nevertheless, we could see some clusters of septin bound to the surface of the glass. This was probably due to bilayer defects too small to resolve with confocal microscopy. Despite these small defects, we obtained a good linear relation (R^2=0.97) between fluorescence intensity (in a.u.) and concentration, with a proportionality constant of 0.0018nM^{-1} (Fig. 5.3B).

The GUVs formed by eDICE qualitatively showed a good encapsulation of the septin hexamers (Fig. 5.3C). Occasionally, we could see some GUVs that had septin accumulated to lipid clusters on the membrane. Since this accumulation could deplete the septin signal within the GUV's lumen, we manually excluded those vesicles from the analysis. Then we measured the septin signal intensity within the GUVs by averaging the pixel intensities in

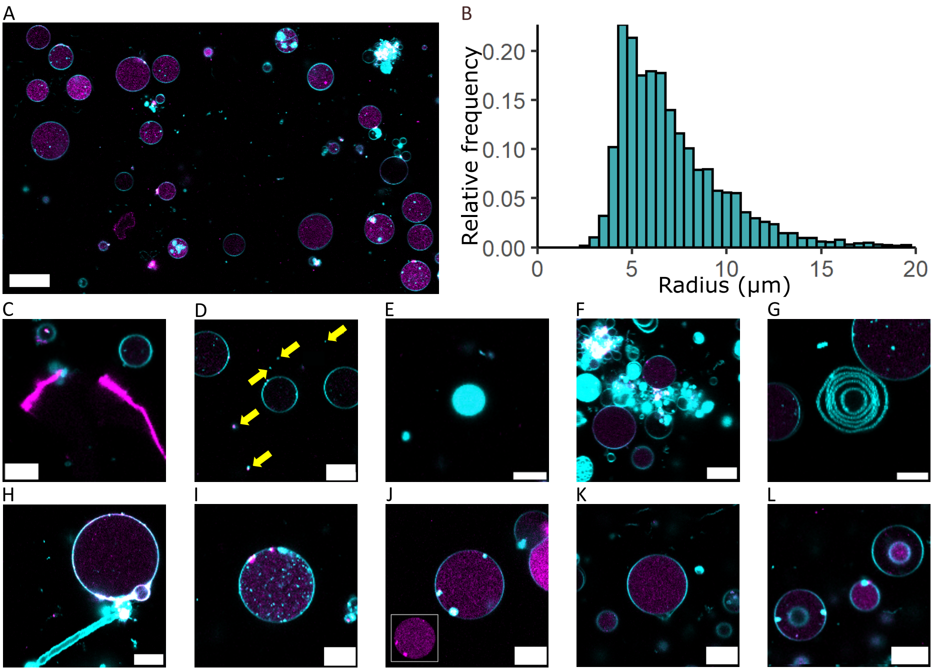

Figure 5.2. Septin-encapsulating GUVs produced by eDICE. A. Typical confocal region of a GUV sample prepared with eDICE. Overlay of the lipid (cyan) and the septin channel (magenta). The GUV membrane composition is 79.75:20:0.2:0.05 PC:PS:Biotin-PE:Rhodamine-PE weight fractions and the inner aqueous solution contains a nominal concentration of 800nM of human septin octamers. Scale bar is 25µm. B. Cumulative (from 39 samples) radius distribution of ~3000 GUVs of different lipid compositions with either hexamers of octamers encapsulated. C-L. Examples of artifacts found together with vesicles in the samples. Different images come from different samples with different membrane compositions and encapsulated content. C. Un-encapsulated septin bundles or septin aggregation on dust particles. D. Small lipid aggregates (yellow arrows). E. Oil droplets. F. Large lipid aggregates attached to vesicles. G. Multilamellar structures. H. Lipid tubes. I. Small free-floating lipids inside GUVs. J. Lipid clusters on the membrane. In this case, septin signal is also present in the same location, as shown in the inset image. K. Lipid pockets. L. Encapsulated smaller vesicles. Scale bars for C-L are 10µm.

the lumen of the GUVs within 90% of their radius. These mean intensities were converted into concentrations using the proportionality constant determined from the bulk samples. The distribution revealed an average internal septin hexamer concentration of 1000nM, which is unexpectedly high given that the nominal concentration in the IAS before encapsulation was 800nM. (Fig. 5.3D). This discrepancy is likely due to an underestimation of the proportionality constant caused by the presence of the surface-bound aggregates in the bulk solutions. The calculated distribution was found to be broad, with approximately 14% of the vesicles encapsulating more than double the nominal concentration. Furthermore, the distribution was asymmetrical, with 63% of vesicles containing septin concentrations higher than the peak value. A similar phenomenon has been previously observed for the encapsulation of actin using eDICE [258], indicating that this apparent supersaturation is a characteristic feature of this GUV production method.

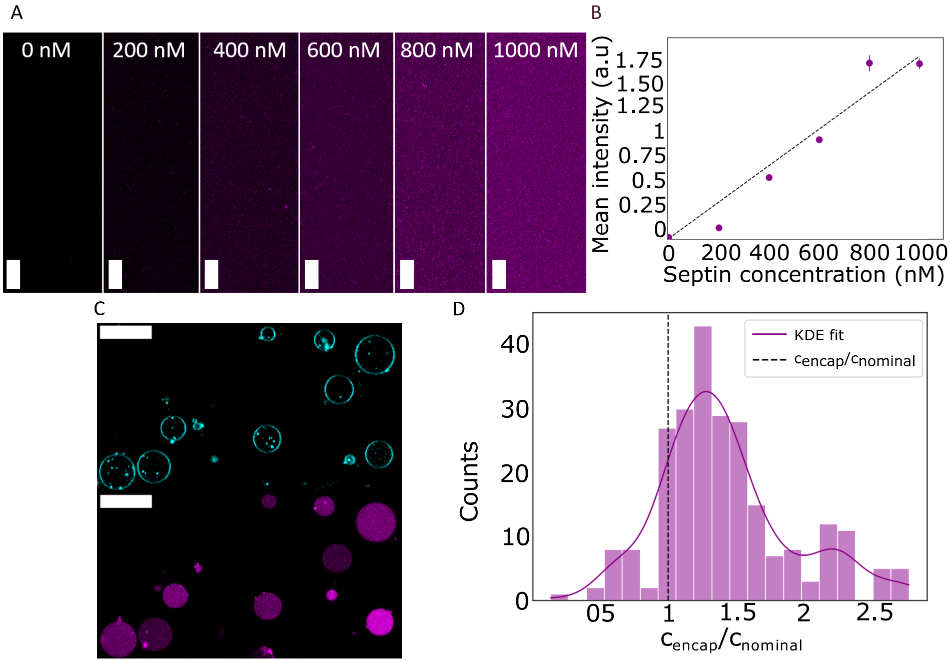

Figure 5.3. Encapsulation efficiency of septin hexamers in GUVs formed by eDICE. A. Example regions of each septin (magenta) solution used for the conversion of pixel intensities to septin concentration. Scale bars are 10 µm. B. Calibration curve (dashed line) obtained after linear fit of the average pixel intensities per septin solution versus the corresponding nominal septin concentration (magenta points), yielding a proportionality constant A = 0.0018nM^{-1} (R^2=0.97). Standard deviations (two repeats) of the mean intensities are in most cases smaller than the point size. C. Confocal image of the membrane (cyan) and septin, showing septin hexamers encapsulated inside GUVs in a high salt buffer that inhibits septin polymerization. Membrane composition was 99.75:0.2:0.05 DOPC:Biotin-PE:Rhodamine-PE. Scale bar is 20µm. D. Histogram and corresponding kernel density estimation (KDE) fit of the septin concentration found per GUV normalized by the nominal encapsulated concentration ($C_{nominal}$ = 800nM), marked by the dashed line. $N_{vesicles}$ = 244.

5.2.3. DOPS and PIP2 synergistically promote binding of septins to the inner leaflet of GUVs

In order to understand the affinity and lipid specificity of human septin complexes to free-standing membranes, we next studied the localization of septins to the membrane inside GUVs for different lipid compositions. We based the membranes on the neutral phosphatidylcholine (PC) lipids DOPC or POPC (see methods), and included the negatively charged phosphatidylserine (PS) lipid DOPS, and/or PIP2. We tested membrane binding of 15%msfGFP-labeled septin hexamers and octamers at a nominal concentration of 800nM for neutral membranes (100%PC), and for negatively charged membranes containing either 20wt%DOPS (20%PS), 5wt%PIP2 (5%PIP2), or a combination of 20wt%DOPS with 1wt%, 3wt%, or 5wt%PIP2 (20%PS+1%PIP2, 20%PS+3%PIP2, 20%PS+5%PIP2, respectively). These lipid proportions are comparable to concentrations found in the plasma membrane of cells [260, 261] and were similar to the ones tested on SLBs in Chapter 4.

For neutral 100%PC GUVs, an homogeneous septin hexamer and octamer intensity was observed inside the vesicle's lumen (Fig. 5.4A and B, respectively, top panels). This finding is consistent with our observations on neutral SLBs in Chapter 4, where septins likewise did not bind. In a large proportion of the GUVs, however, septin was found clustered together with lipid clusters (Fig. 5.5A). This effect was also observed in the presence of PS and/or PIP2, as shown in Figure 5.4A (hexamers) and Figure 5.4B (octamers), indicating that either septin is accumulated in these lipid pockets or that bundled septin is able to make small deformations of the membrane. In case such clusters were observed, the vesicle was removed from further analysis (see Section 5.4.9). Unlike the 100%PC GUV samples, GUVs with negatively charged membranes showed two types of vesicles. One type was enriched with septin signal along the membrane, while a second type resembled the GUVs in 100%PC samples with an homogeneous signal within the lumen. For GUVs having septin on the membrane, z-stacks demonstrated that septin was uniformly distributed across the entire membrane surface, with occasional septin-lipid clusters found at specific segments (Fig. 5.5B), similarly to some of the clusters observed in the 100%PC samples (Fig. 5.5A). To prevent false positives in the localization analysis due to the septin-lipid clustering, vesicles with increased angular profile variance were discarded and the membrane-bound septin signal was taken as the median value (see section 5.4.9).

To analyze the localization of septin in the GUVs, we computed radial profiles obtained by averaging over 360° (see Fig. 5.12A for a schematic). The radial profiles of the membrane and septin signals for a typical 100%PC vesicle with encapsulated septin complexes are shown in Figure 5.5D. The membrane profiles clearly showed a single major peak representing the membrane location. The septin radial profile showed a high and constant intensity of septin from the center of the GUV, reflecting the presence of septin in the lumen of the vesicle. Closer to the membrane, this intensity decreased (Fig. 5.5D) until it approached zero outside of the GUV. As clearly seen when comparing the membrane and septin profiles, the septin intensity decreased at the location of the GUV membrane itself. This effect reflects the spherical shape of the vesicles: because the GUV surface is curved, septin complexes near the membrane are not present throughout the whole confocal slice, causing a decrease in intensity at the membrane (Fig. S5.1). Thus our findings show that in 100%PC GUVs, septin complexes are homogeneously distributed within the lumen of the

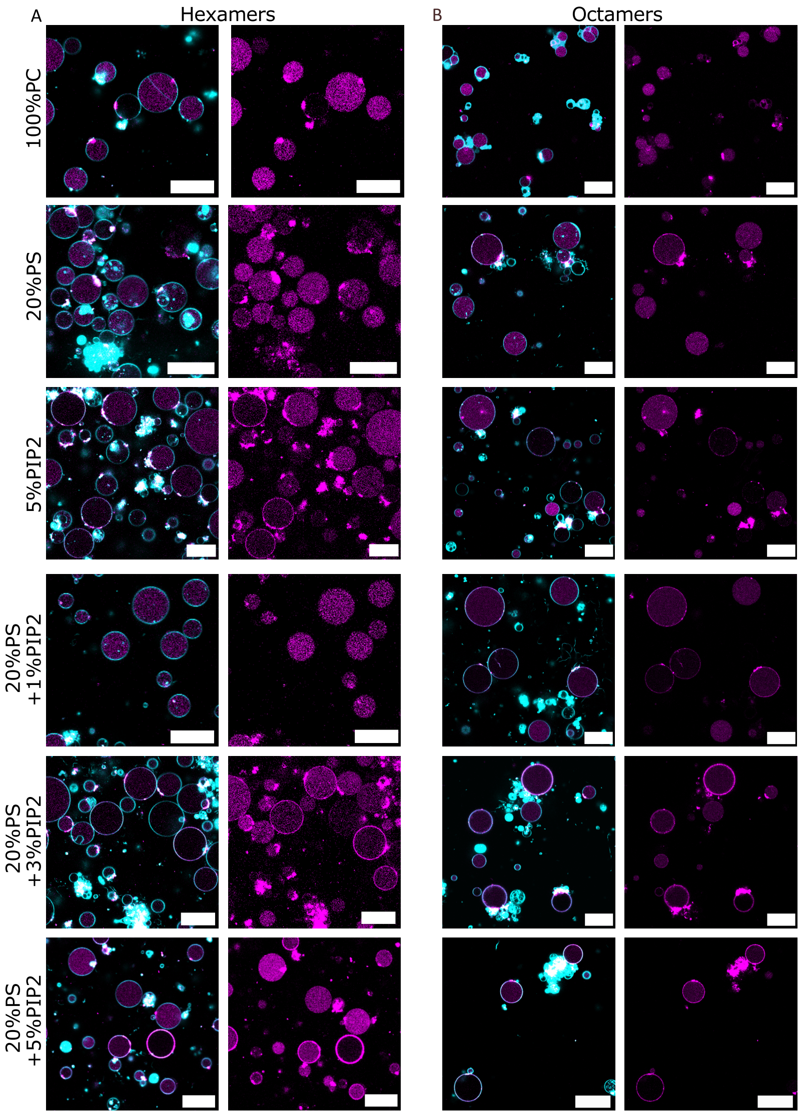

Figure 5.4. Overview of GUVs with encapsulated septin. Representative confocal images of GUVs (cyan) of different lipid compositions encapsulating 800nM human septin (magenta) hexamers (A) or octamers (B). From top to bottom: 100%PC, 20%PS, 5%PIP2, 20%PS+1%PIP2, 20%PS+3%PIP2, and 20%PS+5%PIP2. Scale bars are 25μm.

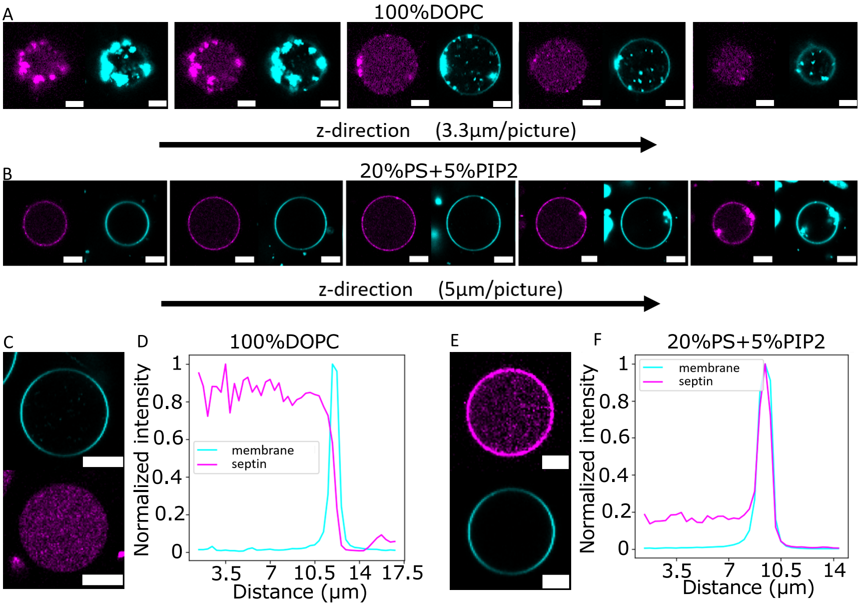

Figure 5.5. Septin localization in 100%PC and 20%+5%PIP2 GUVs. A. Confocal z-stack of a 100%PC GUV displaying septin localization only to lipid clusters. Scale bar is 5µm. B. Confocal z-stack of a 20%PS+5%PIP2 GUV displaying largely homogeneous localization on the membrane for all heights, with only occasional localization in lipid clusters. Scale bars are 10µm. C. Representative confocal image of a 100%PC GUV (cyan) encapsulating human septin complexes (octamers, in the specific example, in magenta). Scale bars are 10µm. D. 360° averaged radial profile of the lipid and the septin channel for the GUV in C. E. Representative confocal image of a 20%PS+5%PIP2 GUV encapsulating human septin complexes (octamers, in the specific example). Scale bars are 5µm. F. 360° averaged radial profile of the lipid and the septin channel for the GUV in E.

GUV. By contrast, the radial profile of septins in GUVs with septin localization at the membrane indeed consistently showed a peak that colocalized with the membrane (Fig. 5.5F).

In order to test whether the lipid composition influenced membrane binding, we quantitatively analyzed the septin localization. For that, we used a combination of the GUV analysis toolbox, DisGUVery [262], which we used to detect the GUVs, and a home-written software, that we used for further analysis. Details of the analysis can be found in section 5.4.9 and in Figure 5.12. After detection of the GUVs, we thoroughly checked the correctness of the detection, the radial profiles, and the angular profiles of each detection in order to remove from the analysis any oil droplet, GUVs with artifacts, incorrectly detected GUVs, empty GUVs, and out of focus GUVs. After this, we calculated a localization parameter, L (defined in Eq. 5.1), which compares the signals at the membrane versus the lumen. A value below 0 indicates that the lumen has a higher septin intensity than the membrane. A value of 0 indicates equal septin intensity at the membrane and at the lumen, while a value of 1 indicates that all septin intensity is on the membrane.

The distribution of L values for each condition is shown in Figure 5.6A. As expected, the L values for septin localization for 100%PC GUVs were negative, confirming that septins do not bind neutral membranes. This situation changed when the membrane contained negatively charged lipids, in which case some GUVs had L values below 0, meaning no septin on the membrane, and other GUVs had L values above 0, meaning membrane localization. From the values of L, we estimated the percentage of GUVs with septin localized to the membrane. In principle, choosing a threshold value for L of 0 should be enough to detect membrane localization given that the septin signal decreases near the membrane whenever it does not bind. However, the fact that the septin's fluorescent signal is low and that small septin-lipid clusters might not be properly detected, makes this threshold value impractical. To avoid false positives, we visually inspected randomly selected GUVs to decide on the threshold value of $L>0.16$ for membrane localization of septins. This value corresponds to the situation where the septin signal at the membrane is 20% higher than in the lumen.

The data revealed a clear similarity between septin hexamers and octamers: both were unable to bind 100%PC GUVs, but displayed lipid composition-dependent levels of binding to GUVs containing negatively charged lipids (Fig. 5.6B). When GUVs contained a single negatively charged lipid species, only a small fraction of GUVs had septin localized to the membrane (~10-25%). When both PS and PIP2 lipids were present, the fraction of GUVs having membrane-bound septins increased to around ~50%. This demonstrates that there is a synergistic effect between DOPS and PIP2 on the binding of septins to GUV membranes. We also observed some notable distinctions between septin hexamers and octamers. Septin hexamers bound to only about a quarter of the 5%PIP2 GUVs and ~10% of the 20%PS GUVs (Fig. 5.6B). In contrast, septin octamers bound to ~15% of the 5%PIP2 GUVs and ~24% of the 20%PS GUVs, showing a similar or even higher binding for PS alone than for PIP2 alone. Furthermore, adding just 1%PIP2 to the GUV membrane had drastically opposite effects on hexamers and octamers: hexamers showed low (~2%) binding to 20%PS+1%PIP2 GUVs whereas octamers exhibited a major increase in binding to around ~50%, reaching a similar level as observed in 20%PS+3%PIP2 and 20%PS+5%PIP2. It seems counterintuitive that hexamers would bind more to 20%PS bilayers than to 20%+1%PIP2

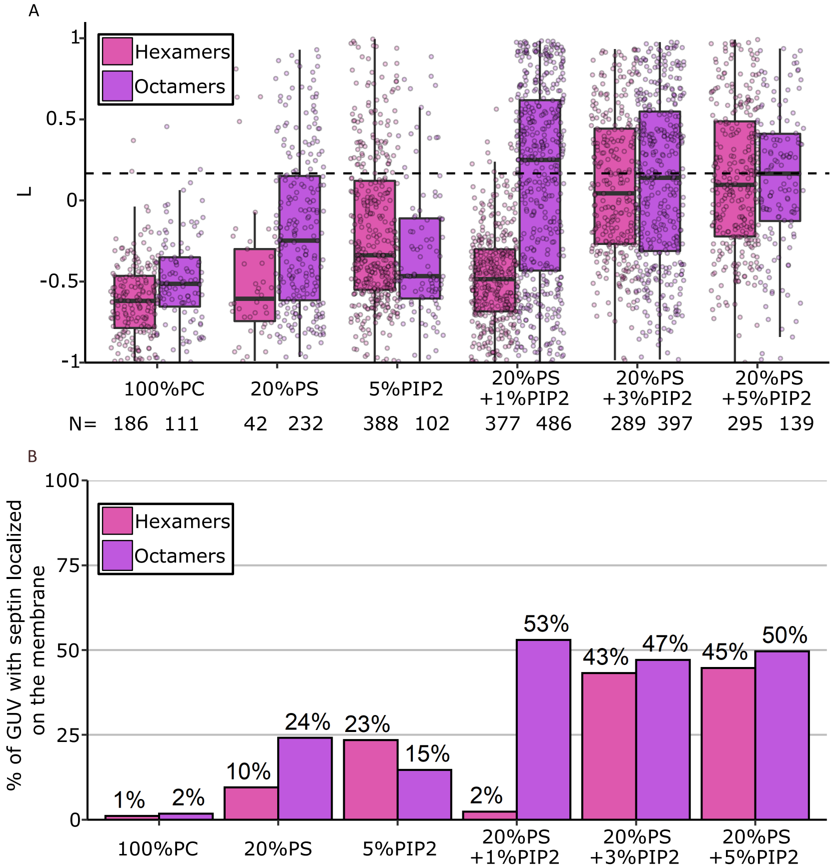

Figure 5.6. Analysis of the localization of encapsulated septin complexes on the membrane of GUVs. A. Distribution of the localization parameter L calculated with Eq. 5.1 for GUVs of different lipid compositions, for septin hexamers and octamers. Dashed horizontal line at 0.16 indicates the threshold chosen to decide if septin is localized to the membrane of GUV. Values below -1 have been removed from the analysis. Results are presented as box and whiskers plots, where the box represents the 25th and 75th percentiles, and the line inside the box indicates the median; the whiskers indicate the 5th and 95th percentiles. B. Classification of GUVs based on the analysis in panel A. All vesicles with L values above the dashed line in A are categorized as having membrane-localized septins.

bilayers. Looking at the L-distribution in Figure 5.6A, we can see that the 20%PS condition has a limited size (N=42) and only 4 of the GUVs showed membrane-binding, suggesting that this throws off the average. We think that in both conditions, 20%PS and 20%PS+1%PIP2, the hexamers did not significantly bind to the membrane. Notably, hexamers required the addition of >3wt% PIP2 in conjunction with 20%PS to generate a binding as strong as octamers. These findings suggest that, while there is a synergistic effect between PIP2 and PS for both septin hexamers and octamers, octamers have a higher binding affinity for negatively charged lipid membranes.

5.2.4. Septin binding to the inner leaflet of GUVs is size-independent

Since yeast septins were previously shown to exhibit curvature-specific binding to membranes with positive curvatures, with preferential binding to SLB-coated spherical beads of 0.5-1.5μm in radius [95], we tested whether we could detect any difference in the binding of septins to the inside of differently sized GUVs. We looked at the percentage of GUVs with septin localized on the membrane for lipid compositions with maximal membrane localization (20%PS+3%PIP2 and 20%PS+5%PIP2) for different vesicle radii (Fig. 5.7). We observed vesicles exhibiting a localized signal for both septin hexamers and octamers across all produced radii. Focusing on the range of 4 to 10μm radius, which encompasses the majority of the vesicles, and utilizing a binsize of 0.5μm, the percentage of vesicles with localized septin remained constant at 20-60% (Fig. 5.7B). The limited number of vesicles outside this radius range made reliable analysis unfeasible. Hence, we could not observe any correlation between localization and vesicle size from our data.

5.2.5. Septins reshape the GUV membrane when binding to the outer leaflet of GUVs

Previous research found that yeast [98] and human octamers [97] reshape the membrane of GUVs by creating spikes or bumps, respectively, when binding from the outside. However, when we encapsulate human septin complexes inside GUVs, the membrane remains spherical and no such deformations can be observed. One important factor for membrane deformations is likely the amount of excess membrane, which depends on the osmolarity difference between the inner and outer solution. Both in the previous experiments with septins added outside [97, 98] (~5mOsm/kg) and in our experiments with septins inside (~16mOsm/kg), the osmolarity difference was small. Therefore, the lack of deformations with septins encapsulated inside GUVs cannot be explained by the difference in osmolarity between the experiments. Alternative explanations for the different outcome of septins being inside versus outside could be either because eDICE forms GUVs with membrane impurities that inhibit reshaping, since previous work used gel swelling or electroformation [97, 98], or because the septin complexes are able to distinguish positive from negative curvature, and only deform membranes exhibiting their unpreferred positive curvature [97, 100]. To distinguish between these two possibilities, we formed GUVs with eDICE and added septin complexes to the outer solution at the same nominal concentration (800nM) as in the experiments with the septins inside. We found that if the GUV membrane contained 100%PC, both septin hexamers (Fig. 5.8A) and octamers (Fig. 5.8B) polymerized in solution, and did not show any interaction with the membrane. Instead, if the membrane composition was 20%PS+5%PIP2, both hexamers and octamers bound

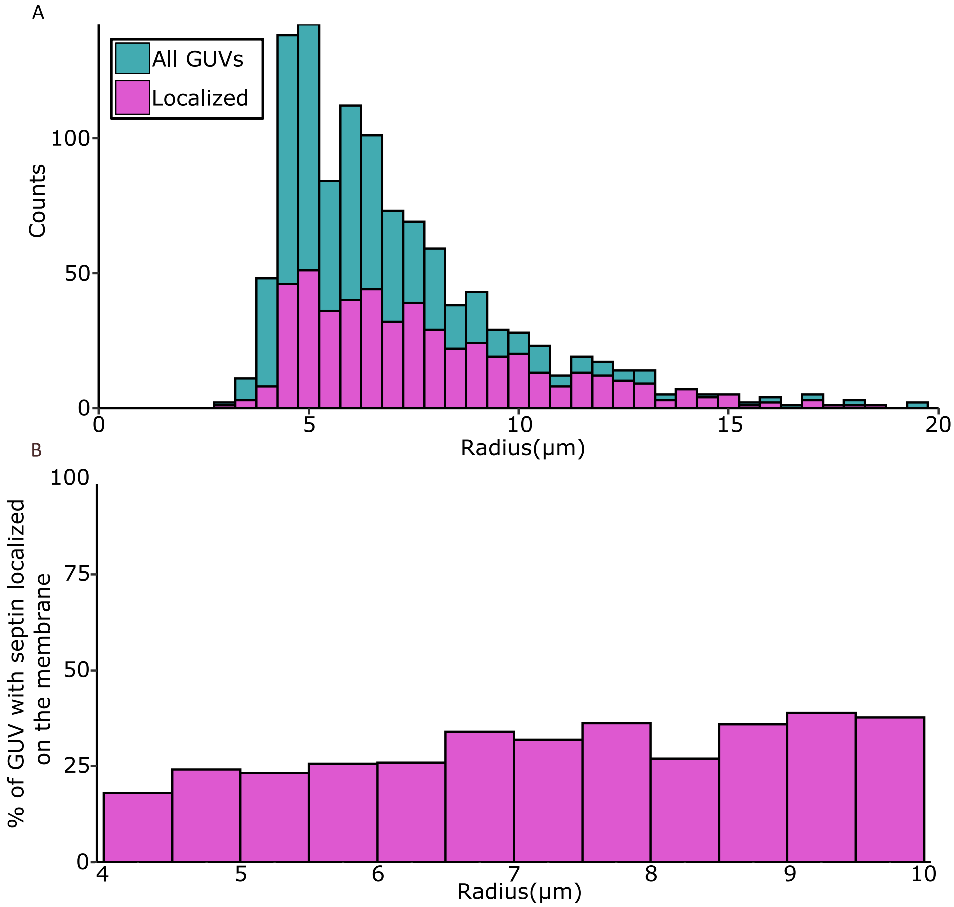

Figure 5.7. Analysis of the localization of encapsulated septin on the membrane of differently sized GUVs. A. Accumulated radius distribution of all the vesicles of compositions 20%PS+3%PIP2 and 20%PS+5%PIP2 (cyan) along with the radius distribution of only the vesicles with membrane-localized septin (magenta). B. Percentage of 20%PS+3%PIP2 and 20%PS+5%PIP2 GUVs with membrane-localized septins for different radius between 4 and 10μm.

to the GUV (bottom panels of Fig. 5.8A and B, respectively) within the first few minutes (Fig. S5.2).

In the 20%PS+5%PIP2 samples, we could see intriguing dotted patterns forming on the membrane of the GUVs (insets on the far right in Fig. 5.8) in ~60-90% of the GUVs, depending on the sample. Maximum Z-projections of these GUVs revealed that these dotted pattern were present in both the septin and the lipid images for both hexamers and octamers (Fig. 5.9A and B, respectively). These dotted patterns were also clearly observed both at the top and bottom surfaces of the GUVs for both hexamers and octamers (Fig. 5.9C and D, left). Interestingly, focusing on the equator of the GUV revealed that these dotted patterns were actually deformations in the form of either sharp ~1 μm long spikes towards the lumen of the GUV (Fig. 5.9C and D, top) or smaller ~0.5μm long bumps (Fig. 5.9C and D, bottom). Both types of deformations were observed in GUVs in the same sample, but each single GUV contained either spikes or bumps. We did not observe any difference in the frequency of appearance of spikes versus bumps between hexamers and octamers. By visual inspection, we observed a periodicity in distances between the dots (in the dotted pattern of the surface) as well as in the distances between the spikes/bumps (on the equator). To check this quantitatively, we manually measured these distances (Fig. S5.3) and found that they were around ~1μm with a wide distribution between 0.5μm and 1.7μm (N=10 GUVs, 5 for hexamers and 5 for octamers, from two experiments for each septin complex). Interestingly, the distances between these deformations on smaller GUVs were slightly smaller (~0.2μm smaller) than in larger GUVs, but the small number of analyzed GUVs did not allow for a systematic analysis. This shows that both septin hexamers and octamers are able to reshape GUVs when binding from the outside, similarly as reported recently for human septin octamers [97]. We note that the osmotic mismatch in our experiments was much larger (~111mOsm/kg, corresponding to a theoretical excess area of ~33%) than in previous reports [97, 98] (~5mOsm/kg). This suggests that the excess area is not a major factor in the vesicle reshaping.

Finally, on rare occasions we observed septin complexes, especially octamers, forming or localizing to other deformations on GUVs. First, both septin hexamers and octamers formed bumps with a larger ~0.9μm amplitude and irregular spacing on some GUVs when compared to the pattern described above (Fig. S5.4A and B). Septin octamers were able to bind or generate lipid tubes from the surface of some GUVs (Fig. S5.4C and D). Rarely, septin octamers deformed the GUVs into non-spherical shapes, while also maintaining the bumpy deformations (Fig. S5.4E and F). However, due to the small amount of data that we acquired for these experiments, we cannot conclude whether octamers differ from hexamers in this respect.

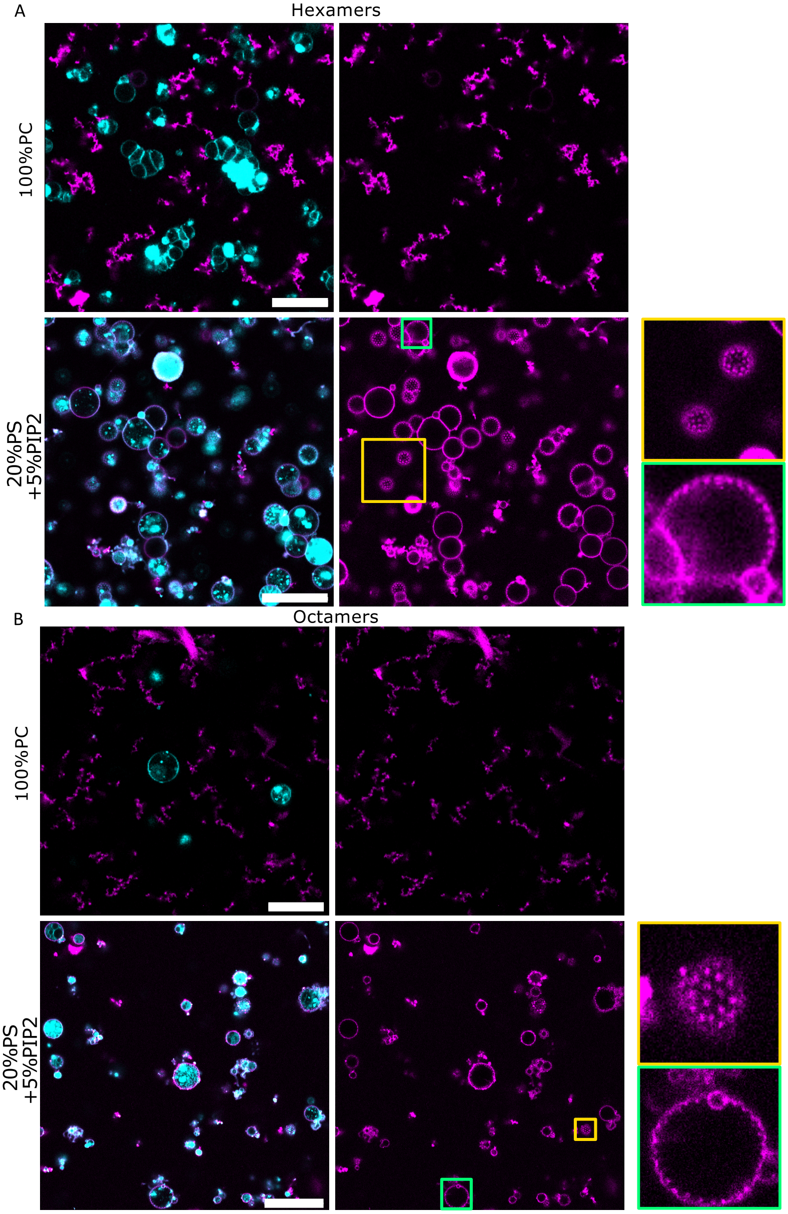

Figure 5.8. Septin localization on the outside of 100%PC and 20%PS+5%PIP2 GUVs. A. Representative confocal image of septin (magenta) hexamers interacting with GUVs (cyan) from the outside. Septin hexamers bundled in solution when exposed to 100%PC GUVs (top) but bound to the membrane when exposed to 20%PS+5%PIP2 GUVs (bottom). Inset shows a dotted pattern on the septin image only for 20%PS+5%PIP2 GUVs, both on the surface at the pole and at the equator of GUVs. Yellow or green squares around the inset images represent their location in the overview image. B. Corresponding images for septin octamers. Scale bars are 25µm.

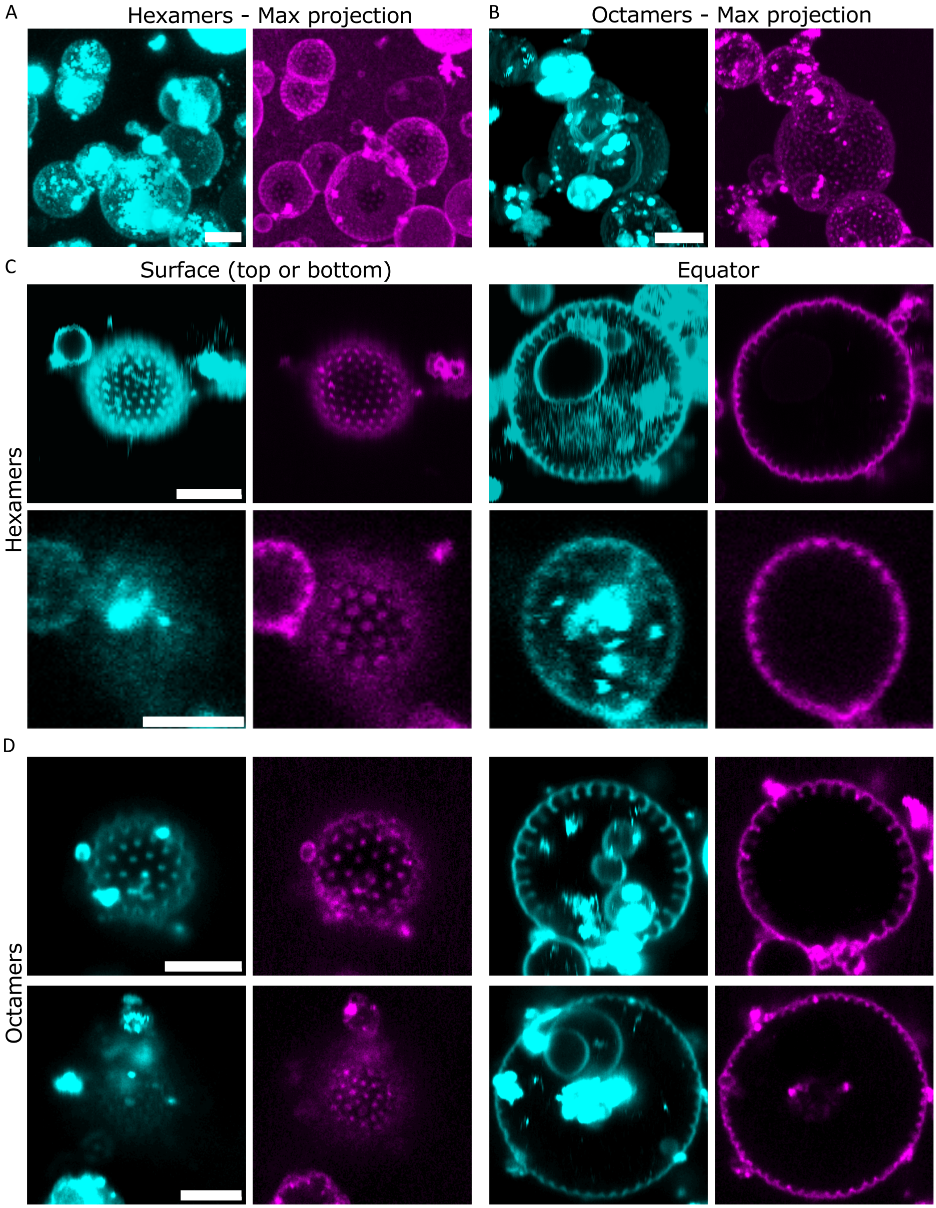

Figure 5.9. Septin complexes reshape the membrane of GUVs composed of 20%PS+5%PIP2. A. Maximum confocal Z-projections of septin hexamers (right, magenta) binding to the outside of GUVs (left, cyan) showing a dotted pattern. B. Corresponding projections for octamers. C. Single confocal images of the surface (top or bottom) and the equator of GUVs reshaped with either spikes (top) or bumps (bottom). D. Corresponding images for octamers. Scale bars are 5µm.

5.3. Discussion

In this chapter we explored how human septin hexamers and octamers interact with unilamellar lipid vesicles formed by eDICE. We were able to encapsulate septins inside GUVs, which, to our knowledge, has never been reported before. We found that eDICE produces vesicles with high yield, but with variable amounts of other lipid structures that need to be carefully excluded from analyses. The GUVs produced with eDICE had a reproducible but polydisperse size distribution, with a radius ranging from 4-20µm. This size range can be interesting to investigate how encapsulated content affects differently sized vesicles. Additionally the GUVs are polydisperse in terms of septin content, corroborating recent work with actin actin [258]. We found that encapsulating 800nM human septin hexamers resulted in GUVs having a spread of concentrations between 400 and 2000nM, peaking at around 1000nM. The explanation for the shift of the peak concentration as compared to the nominal concentration is likely that our calibration using a series of septin solutions was offset by septin aggregation. However, if we assume the peak is centered around 800nM, we would still have a broad spread between 200nM and 1800nM. This broad distribution can be useful to explore how proteins at different concentrations affect the membrane. However, careful concentration control does not seem possible with the current eDICE method and requires other protein encapsulating methods, such as OLA [263, 264].

5

To understand how septin-membrane binding might differ between supported and free-standing lipid bilayer, we then encapsulated septins in GUVs of different membrane compositions. We found that human septin octamers only bound to the membrane of GUVs in the presence of negatively charged lipids, and that they were able to bind both PS and PIP2 membranes, similar to what was previously reported for fly septins [96]. In contrast, we found that septin hexamers could only bind to the GUV membrane when PIP2 was present. Apparently, septin hexamers and octamers bind differently to lipid bilayers. Our findings with GUVs showing that septin octamers can bind PS are in apparent contrast with our Quartz Crystal Microbalance with Dissipation monitoring (QCM-D) results for SLBs from Chapter 4. On SLBs, neither octamers nor hexamers could bind when only 20mol%DOPS was present, although PS did synergistically promote membrane binding together with PIP2. We see three possible explanations for this discrepancy.

First, the experimental design is different in the two assays. On SLBs, we used septins at concentrations between 60nM and 120nM. From TEM experiments, we concluded that PIP2 is necessary for septins to polymerize on a lipid layer. Likely, septins only weakly bind to DOPS by electrostatic interactions because binding is not strengthened by polymerization. The QCM-D measurements of septin binding to SLBs are done in flow and with a much lower (50nM) concentration of septin complexes than in the GUV assays to avoid bundling in solution before septins reach the SLB-coated QCM-D sensor. The flow in the QCM-D experiments could remove any weakly bound septins from the 20mol%PS SLBs, so binding cannot be detected. By contrast, in the GUV assays, septins are present at high (~800nM) concentration and without flow, potentially allowing us to observe an equilibrium membrane-bound septin pool. The higher septin concentration inside GUVs may potentially also enhance the septin concentration at the membrane enough to promote septin polymerization. This idea has some precedence in our own observations that microtubule-binding allows polymerization-incompetent septin mutants to bind and affect microtubules (Chapter 3), and in prior studies showing that membrane-binding promotes polymerization of polymerization-incompetent yeast septins [152] and that high septin concentrations promote polymerization of human septins in high salt buffer [89].

A second possible explanation for the PS-dependent binding of octamers being different for SLBs versus GUVs could be the physical differences between these two types of bilayers. Having a support slows down lateral diffusion of lipids in SLB membranes and can affect lipid phase behavior as compared to free-standing GUV membranes [265–267], which could affect septin binding. Furthermore, septin binding could be dependent on membrane tension. This is an effect that could be investigated in GUVs by varying the osmotic mismatch between the inner and outer solution.

Finally, a third possible explanation is that septin hexamers and octamers could actually differ in their ability to bind lipid membranes. Recent evidence shows that septin octamers are the ones binding to actin stress fibers [103] and microtubules [103] in cells, and we show in this thesis that septin octamers bundle actin (Chapter 6) and bind microtubules (Chapter 3) at much lower concentrations than hexamers. The presence of SEPT9 in octamers could improve membrane binding over that of hexamers, as suggested before [150], but this would only have an impact at higher concentrations. Since the fluorescent signal of septin in fluorescence microscopy tends to be low, a technique that does not rely on fluorescence is needed to systematically check the effect of septin concentration on membrane binding. For instance, using QCM-D under no-flow conditions, would allow us to increase the septin concentration. If under these conditions, septins can still not bind 20%PS SLBs, the different type of bilayer (supported versus free-standing) is apparently important. Instead, if now septins do bind to 20%PS SLBs, septin hexamers and octamers apparently behave differently.

Having established the lipid specificity of septin binding, we examined how septin binding depends on the curvature of the GUVs. First, we examined if the size of the curvature itself could affect the membrane binding. We were able to obtain GUVs with radii ranging from 3 to 25µm (Fig. 5.2B). We found that the percentage of vesicles exhibiting septin localization at the membrane remained constant (40-60%) for GUVs containing 20%PS+3%PIP2 and 20%PS+5%PIP2, indicating that there was no preference for curvature in our samples. Our system's curvatures (0.33μm^{-1} to 0.04μm^{-1}) were lower than those that have been shown to be detectable by septins (0.31-6.67μm^{-1} [95, 97, 98, 230]), even in the case of our smallest vesicles. This suggests that septins may lose their sensitivity to curvature in this size range. Another explanation could be that the high concentration of septins that we used (800nM) may have obscured any preference for curvature. This concentration is much higher than the 90nM septin octamer concentration required for the formation of a saturated double-layered meshwork on SLBs on wavy solid substrates [97, 98]. Therefore, our vesicle membranes may have been saturated, making it difficult to detect any preferred curvature.

Despite this lack of curvature-size sensitivity, we found that human septin hexamers and octamers are able to detect the sense of the curvature. When septins bind to the inside of the vesicles, they experience a concave, or negative, curvature; whereas binding to the outside gives a convex, or positive, curvature. We found a striking difference between binding inside and outside. When binding from the inside, we could see a round

5

membrane without obvious membrane deformations. We did observe lipid clumps colocalized with septin, which could either represent septin-driven deformations or septin-driven aggregation of lipid clumps that were often present in the GUV interior. When septin complexes bound to the outside of the GUVs, they showed a striking pattern of ~1μm spaced spiky/bumpy deformations, which resembled deformations observed before for yeast octamers [98] (Fig.5.10B) and human octamers [97] (Fig.5.10D).

Both Nakazawa et al. [97] and we find that human septins form deformations towards the lumen of the GUVs. In contrast, yeast septins formed ~1μm long spikes towards the outside of the GUV (Fig.5.10B) that were irregularly spaced at an average distance of 4μm but with a wide distribution between 2 and 6μm. This distinctive behavior is probably due to the distinct organization of yeast and human septins on lipid bilayers. As shown in Nakazawa et al. [97] and in Chapter 4, human septins (hexamers and octamers) tend to form a 2-layered mesh of single and paired filaments, while yeast octamers form a single layer of paired filaments cross-bridged by single octamers [98, 152]. However, we also see a small difference between the deformations reported here and the ones reported by Nakazawa et al. [97]. In our study we find either spikes or bumps (Fig.5.10A and B, respectively) at a distance of ~1μm, while Nakazawa et al. found only bumps (Fig.5.10D) at a distance of around 3μm. We see three possible reasons.

First, Nakazawa et al. [97] worked with an osmolarity mismatch of only ~5mOsm/kg. This mismatch is similar to that in our experiments with the septins inside, where the mismatch was ~16mOsm/kg. In contrast, in our experiments with the septins outside, we had a larger mismatch of around ~111mOsm/kg, which gives a larger membrane excess area [268] (~5.5% for the septins inside versus ~33.8% for the septins outside) that could facilitate more abundant and larger-amplitude deformations, in the case of the spikes. This larger mismatch in osmolarity could have also led to the formation of non-spherical GUVs and the lipid tubes (Fig. S5.4C-F) and perhaps even the smaller vesicles inside the GUV's lumen seen in (Figs. 5.8 and 5.9), considering that upon shrinkage GUVs can lose membrane by creating smaller GUVs inside [268]. Second, we used a lipid composition consisting of 74.95%DOPC, 20%PS, 5%PIP2, and 0.05% Rhodamine-PE, while Nakazawa et al. used 56.5% EggPC, 15% Cholesterol, 10% DOPE, 10% DOPS, 8%PIP2 and 0.5% Bodipy TR ceramide. The use of 15% cholesterol, which is known to increase the bending rigidity of POPC membranes [269], could lead to smaller and less abundant deformations. Third, the GUV formation technique could also have a big impact. Nakazawa et al. used electroformation or gel-assisted swelling to produce GUVs [270], methods that do not require any oil. In contrast, in order to be able to directly compare results with septins inside versus outside the GUVs, we used eDICE. It is currently unknown whether the oil used during eDICE ends up in the GUV membrane, but if present, it could affect the mechanical properties of the membrane [271, 272]. To distinguish between these three possibilities it would be interesting to repeat our experiments with septins outside with a smaller osmolarity mismatch, and, conversely, to increase the osmolarity mismatch when the septins are inside. In addition, using electroformation and/or gel swelling with our lipid composition, osmolarity mismatch, and buffer compositions, could help to test the influence of the GUV formation technique.

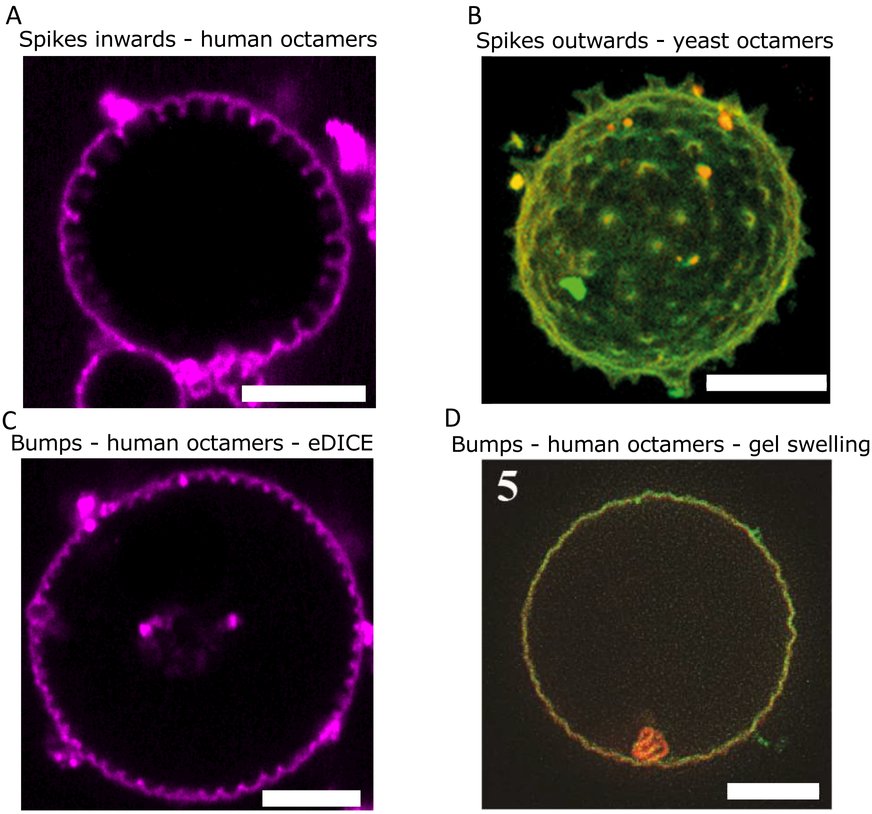

Figure 5.10. Comparison of the membrane deformations produced by yeast and human septin octamers. A. Representative single confocal image of the equator of a GUV showing spikes towards the lumen in the presence of 800nM human septin octamers. Experiment from this study. Only septin (magenta) image shown. B. 3D reconstructions of confocal images of a GUV showing spikes outwards in the presence of 600nM yeast septins octamers. Image extracted from [98]. Red shows the GUV membrane while green shows the septin. C. Representative single confocal image of the equator of a GUV showing bumps in the presence of 800nM human septin octamers. Experiment from this study. Only septin (magenta) image shown. D. Representative confocal microscopy image of the equator of a GUV showing bumps in the presence of 176nM human septin octamers. Image extracted from [97]. Red shows the GUV membrane while green shows the septin. For A, C, and D scale bars are 5µm. In B, scale bar is 10µm.

5

In addition to GUV experiments, both Beber et al. [98] and Nakazawa et al. [97] also did experiments with yeast or human octamers, respectively, on SLBs supported by a wavy surface. They found that both types of septin species prefer binding to negative curvatures. Thus when septins bind to the outside of GUVs, they may potentially deform the membrane in order to bind to their preferred negative curvature. However, septin complexes are small rods with 4nm in width and 24nm or 32nm in length for hexamers or octamers, respectively. Such small complexes are unlikely to detect the small curvature of vesicles with more than 2µm in radius, although single-molecule imaging suggests that yeast septin octamers bind with curvature-specific kinetics [230, 273]. However, we and others have shown that septins polymerize on lipid layers (Chapter 4, and [82, 96–

98, 152, 230]). Longer micron-long filaments such as the ones septins form on membranes are apparently able to detect the sense of curvature on giant vesicles, as it seems to give them their curvature sensitivity when binding SLB-coated beads, cylinders, and wavy surfaces with smaller curvatures than GUVs [97, 98, 106, 230]. Furthermore, rigid septin meshworks [96, 97] could be strong enough to reshape free-standing lipid membranes. Therefore, we think the ability of septins to polymerize on lipid bilayers gives them the ability to detect the sense of membrane curvature and to reshape the membrane to locally generate regions with their preferred negative curvature, forming the observed spikes and bumps.

It will be interesting to explain these fascinating findings by theoretical modeling, using continuum modeling of membrane-bound liquid crystals (as in [97]) or using molecular dynamic simulations (as in [274]) for a more microscopic modeling. Modeling could provide insight in the interplay of septin curvature sensing, membrane mechanics, and septin meshwork mechanics in the shape and amplitude of septin-driven membrane deformations. Finally, septin's ability to maintain their preferred curvature on membranes could explain how they might mechanically support lipid bilayers, but this remains to be tested by measuring the mechanical properties of septin-encapsulating-GUVs (see Chapter 8).

5.4. Materials and methods

All chemicals were obtained from Merck Sigma unless specified otherwise.

5.4.1. Purification of human septin complexes

Human septin oligomers were purified and their quality was checked as detailed in chapter 2. We used septin hexamers with a subunit order of SEPT2-SEPT6-SEPT7-SEPT7-SEPT6-SEPT2 and septin octamers with a subunit order of SEPT2-SEPT6-SEPT7-SEPT9_i1-SEPT9_i1-SEPT7-SEPT6-SEPT2. Septins were fluorescently tagged with msfGFP on the C-terminus of SEPT2. For purification, SEPT2 contained a his$_6$-tag at its N-terminus, and SEPT7, for hexamers, or SEPT9, for octamers, contained a Strep-II-tag at its C-terminus.

5.4.2. Lipid preparation for eDICE

We used several types of lipids to prepare the GUVs, all from Avanti Polar Lipids. First, the basic component for the membranes was either 1,2-dioleoyl-sn-glycero-3-phosphocholine (DOPC) (Merck KGaA, Cat. #850375C) or 1-palmitoyl-2-oleoyl-sn-glycero-3-phosphocholine (POPC) (Merck KGaA, Cat. #850457C). DOPC and POPC were used interchangeably as they only differ in the saturation of the alkyl chains that are within the hydrophobic core of the GUV bilayer, while the same headgroup is exposed to the aqueous solutions. Second, we used the anionic lipids 1,2-dioleoyl-sn-glycero-3-phospho-(1'-myo-inositol-4',5'-bisphosphate) (ammonium salt, and purified from brain) (PIP2) (Merck KGaA, Cat. #840046X), and 1,2-dioleoyl-sn-glycero-3-phospho-L-serine (sodium salt) (DOPS) (Merck KGaA, Cat. #840035C). To visualize the membrane we used 1,2-dioleoyl-sn-glycero-3-phosphoethano-lamine-N-(lissa-mine rhodamine B sulfonyl) (Rhodamine-PE) (Merck KGaA, Cat. #810150C). Finally, to bind the GUVs to the surface of the imaging chamber, we used 1,2-dioleoyl-sn-glycero-3-phosphoethanolamine-N-(biotinyl) (sodium salt) (Biotin-PE) (Merck KGaA, Cat. #870282C).

We used different lipid compositions to probe lipid specificity of septin binding (see Table 5.1). To promote septin binding, we added 20wt% DOPS and/or PIP2 at 1wt%, 3wt% or 5wt%. We always included 0.05wt% Rhodamine-PE to image the GUV membrane. In case GUVs were attached to the surface, we added 0.2wt% Biotin-PE. Finally, the rest of the membrane was composed of DOPC. Note that the lipid percentages are expressed in terms of weight%. In contrast, in Chapter 4, we used mole%. This leads to the use of different ratios, where 5wt%PIP2 is ~3.6mole%, 3wt%PIP2 is ~2.2mole%, 1wt%PIP2 is ~0.7mole%, and finally 20wt%PS is ~19mole%.

Table 5.1. Lipid compositions. Left column displays the abbreviation for the corresponding lipid composition. Percentages are expressed as weight%. If Biotin-PE was used, 0.2% of DOPC was removed to accommodate the addition of 0.2% Biotin-PE.

Abbreviation	DOPC	DOPS	PIP2	Rho-PE
100%PC	99.95	0	0	0.05
20%PS	79.95	20	0	0.05
5%PIP2	89.95	5	5	0.05
20%PS+1%PIP2	78.95	20	1	0.05
20%PS+3%PIP2	76.95	20	3	0.05
20%PS+5%PIP2	74.95	20	5	0.05

5

To prepare the lipid-in-oil solution for eDICE, first, enough lipids to give 0.2mg/mL total lipid concentration in 7mL of final solution were dried in a glass vial under a stream of N_2 gas, and incubated o/n in a dessicator. Since the presence of moisture in the lipid solution is known to be detrimental for the quality of GUVs formed with droplet interphase crossing encapsulation methods [259], we took several precautionary measures. First, we always wrapped Teflon tape around the screw of the glass vials to tighten the sealing once the cap is on. Second, the following day, the lipid vial was placed inside a glovebox with an ambient humidity of ~0.5-2%. Inside the glovebox, we prepared a 5.3:1.2 volumetric ratio mix of silicone oil (Merck KGaA, Cat. #) and mineral oil (Merck KGaA, Cat. #), respectively. We then dissolved the dried lipid films in 50µL of chloroform and diluted them with 400µL of decane. Next, we added 6.5mL of the oil mix to each lipid vial while continuously mixing by vortexing. Finally, we removed the vials containing the lipid-in-oil solution from the glovebox, sealed them with parafilm, and sonicated them in an ice bath for 15 minutes using a bath sonicator (Branson 2510 Ultrasonic Cleaner, Marshall Scientific) to break down any remaining lipid clumps.

5.4.3. eDICE

In order to produce GUVs, we used emulsion droplet interphase crossing encapsulation, or eDICE [258]. To generate the vesicles, we need the lipid-in-oil solution described above, and three aqueous buffers. First, the inner aqueous solution (IAS) was the buffer to be encapsulated into the GUVs. The IAS contained either 6.5% optiprep or 200mM sucrose to increase the density of the solution, necessary for the GUV formation [259]. No apparent difference was observed between the use of either of the chemicals. The outer aqueous solution (OAS) was a glucose solution designed to keep a close osmolarity to the IAS to avoid osmotic shock, so its concentration depended on the osmolarity of the IAS (see each type of experiment below). Finally, the vesicle buffer (VB) stabilized the OAS pH at a value of 7.4 after GUV formation.

The GUV preparation was conducted at room temperature (24℃±1℃) using a spinning chamber setup as described in [259]. We first set the spinning chamber to rotate at 2000rpm (corresponding to a motor voltage of 14.5V on our device), added 700µL of OAS, and carefully added 5mL of the oil solution. Next, 1 mL of lipid-in-oil solution was set aside in a 2mL Eppendorf tube. Droplets of IAS with a monolayer of lipids were created in the 1mL lipid-in-oil solution through manual emulsification, which involved adding the IAS and scratching the Eppendorf tube vigorously over an Eppendorf holder 10-15 times. Next, we pipetted 1mL of the emulsion into the spinning disc and centrifuged it for 3 minutes to allow the droplets to cross the lipid monolayer formed at the oil-water interface and transform into GUVs.

After GUV formation, the spinning chamber was stopped by gradually reducing the motor voltage and we carefully removed most of the oil phase from the edge of the chamber's opening while gradually tilting the disc. Then, we added 233 µL of VB to the aqueous phase. We concentrated the GUVs by resting the spinning chamber at a 45° angle for at least 15 minutes so the GUVs sunk. To pick up the GUVs, we cut a 200µL pipette tip to minimize shear forces and pipetted the solution from the corner of the tilted spinning disk, cleaned the pipette tip of residual oil, and transferred the GUV-containing solution into an Eppendorf tube. After a 5 minute incubation, we pipetted the GUVs from the bottom of the tube and transferred them into the imaging chambers with a cut pipette tip, as specified in later sections. We did this 5 minute incubation in a tube since we found this helps decreasing the amount of lipid clusters in the sample.

5

5.4.4. Septin encapsulation efficiency

We first prepared a 800nM septin hexamers containing 15% msfGFP-labeled solution in septin buffer (20mM Tris pH 7.4, 2mM $MgCl_2$, 300mM KCl, 1mM DTT) to prevent polymerization (see Chapter 2). We complemented this buffer with complemented with 1mM 6-hydroxy-2,5,7,8-tetramethylchroman-2-carboxylic acid (TROLOX) to prevent blinking, 1mM Protocatechuic acid (PCA) and 0.05mM Protocatechuate 3,4-dioxygenase (PCD) as a photobleaching protective mix, and 6.5% optiprep. We encapsulated the septin solution in 100%DOPC GUVs with biotin-PE. Since the IAS had an osmolarity of 604 ± 3 mOsm/kg, as measured by a freezing point osmometer (Osmomat 3000, Gonotec), we prepared an OAS of 625mM glucose and a vesicle buffer of 475mM glucose and 80mM Tris pH 7.4, which had osmolarities of 628 ± 3 mOsm/kg and 651± 2 mOsm/kg osmolarity, respectively.

To provide a calibration curve, we prepared septin hexamer bulk solutions of six different septin concentrations (0, 200, 400, 600, 800, 1000nM) in the same buffer composition as the encapsulated septins. The septin bulk solutions were initially prepared with double concentrations and were diluted two-fold when added to the imaging chambers (see below). Prior to the preparation of the solutions, septin stocks were airfuged for 15 minutes at 149000 g (Air-driven Ultracentrifuged, Beckman Coulter) to remove any septin aggregates.

To prevent septin from binding the surface of the imaging chamber, the samples were placed in custom-made wells on glass slides (#1 Cover Glass, Corning) passivated with 100% DOPC SLBs (see 4.4). Initially, the glass slides were cleaned for 10 minutes in a base piranha solution (5% hydrogen peroxide, 5% ammonium hydroxide) (see Chapter 3). The slides were then washed with MilliQ water and dried with a nitrogen gun. The wells were prepared by cutting the bottom of PCR tubes and gluing them top-down on the glass slides. Once the glue was set, we added the small unilamellar vesicle solution, prepared as in Chapter 4, to form the SLB, adding 5mM $MgCl_2$ to facilitate SLB formation. The wells were covered with lids of 500μL eppendorf tubes and kept in a humid box at all times prior to imaging to prevent evaporation. After an incubation of at least 30 minutes, the wells were washed twice with 100μL of septin buffer and twice more with 3:1 OAS:VB in the case of the wells meant for the GUV sample. The buffers were then partly removed, leaving 20μL to prevent the SLBs from drying. 20μL of the septin bulk solutions were added for two-fold dilution in the well. Similarly, 20μL of the GUV sample were pipetted in the well containing the 3:1 OAS:VB.

5.4.5. Membrane localization

For the membrane localization experiments, we prepared GUVs with the lipid compositions listed in Table 5.1 encapsulating 800nM septin hexamers or octamers in buffer conditions that permit polymerization (50mM KCl, see Chapter 2). To avoid polymerization of septin before they were inside the GUVs, we prepared a septin mix composed of 85% dark septin complexes and 15% msfGFP-labeled septin complexes at a total septin concentration of 4800nM in septin buffer. Then we prepared a 5x septin polymerization buffer (5xSPB) made of 83.33mM Tris-HCl at 7.4 pH, 8.33mM $MgCl_2$, 5mM DTT, 5mM GTP, 2.5mM MgATP, 5mM TROLOX and 5mM PCA.

Once the spinning disk was ready with the OAS and the lipid-in-oil solution, we finished preparing the IAS, to ensure that the septins only started polymerizing once encapsulated inside the GUVs. The IAS was prepared by mixing, in this specific order: MilliQ water (enough to top up to the final desired volume, usually 25μL, so 6.08μL), 20% 5xSPB (1:5 dilution, 5.4μL), 0.05μM PCD (0.27μL), 6.5% optiprep (1.75μL), 33.3% G-buffer (5mM Tris-HCl 7.8 pH, 0.2mM $CaCl_2$; 9μL) and 16.67% Septin mix (1:6 dilution, 4.5μL). This yielded a final composition of IAS of 20mM Tris pH 7.4, 1.66mM Tris pH 7.8, 2mM $MgCl_2$, 50mM KCl, 1mM DTT, 1mM GTP, 0.5mM MgATP, 1mM PCA, 1mM TROLOX, 0.05μM PCD, 6.5v% optiprep, 0.067mM $CaCl_2$, and 800nM total septin concentration (15% msfGFP-labelled). After the IAS was prepared, we emulsified it into the lipid-in-oil solution as fast as possible and pipetted it into the spinning disk, which took around 10-20 seconds.

Since the IAS had an osmolarity of 176 ± 5mOsm/kg, we prepared the OAS and the VB to have a slightly higher osmolarity. The OAS, made of a solution of 190mM glucose, had an osmolarity of 188±2mOsm/kg. The VB was made of 20mM glucose and 80mM Tris pH 7.4 and had an osmolarity of 199±3mOsm/kg, which gave an osmolarity mismatch of ~16mOsm/kg, leading to a final excess area of ~5.6% [268].

The samples were placed in ibidi 18-well μ-slides. For GUV immobilization on the imaging surface, the wells were previously passivated by incubation with 1mg/ml of a 1:1 BSA:BSA-biotin solution in Milli-Q for at least 15 minutes at room temperature, followed by incubation with 1mg/ml of Neutravidin in 3:1 OAS:VB for at least 5 minutes. Subsequently, the wells were washed with 3:1 OAS:VB twice. 40μL of the prepared GUV samples were pipetted in each well that already contained 40μL 3:1 OAS:VB for 1:2 dilution. Alternatively, the wells could also be passivated with β-casein. For this, we incubated the wells with 50μL 1mg/mL β-casein for at least 30 minutes, and directly dried the wells with a nitrogen gun. This passivation, however, does not allow for the immobilization of the GUVs since the GUVs could not bind to the casein.

5.4.6. Adding septins to the outside of GUVs

We first prepared empty GUVs, containing only IAS buffer. The IAS was composed of 20mM Tris pH 7.4, 50mM sucrose, 6.5%optiprep and had an osmolarity of 129±1mOsm/kg. The OAS was a 150mM glucose solution with an osmolarity of 156±2mOsm/kg. The VB contained 67mM Tris pH 7.4, and 6.7mM $MgCl_2$, and had an osmolarity of 128±1mOsm/kg. After sinking, 45μL of GUVs were added into β-casein passivated wells.

Prior to adding the septins to the imaging wells with the GUVs, we complemented the outer solution by adding 5μL of 10x extra mix (9.8mM Tris pH 7.4, 0.98mM $MgCl_2$, 24.5mM Tris pH 7.4, 10mM DTT, 10mM GTP, 10mM TROLOX, 10mM PCA, 0.5mM PCD). To avoid osmotically shocking the GUVs and to ensure proper mixing, we added this mix slowly across the whole well and incubated it for 5 minutes. Then, we slowly added 8.3μL of a septin mix made of 15% msfGPF-labelled 4800nM septin complexes in septin buffer. This yielded a final osmolaity of the outside solution of ~240±3mOsm/kg, which gave an osmolarity mismatch of ~111mOsm/kg, leading to a final excess area of ~34% [268]. After this, we started imaging as soon as possible.

5

5.4.7. Confocal imaging

The samples were imaged on an inverted Leica Stellaris 8 point scanning confocal microscope using a 63x glycerol immersion objective, a white light laser, and HyD detectors operated in analog mode. Rhodamine and msfGFP were excited sequentially at 573nm (1.5% intensity and 2% gain) and 489nm (23% laser intensity and 80% gain), respectively. Images were acquired with line accumulation set to 2.

To obtain calibration data for the septin encapsulation efficiency experiment, 5 images of 2048x2048px were collected for each septin bulk solution. The images were all taken at approximately 7μm height from the imaging surface, determined using the reflection observed in an xzy mode. Then, at the same height from the surface and using the same imaging settings, multiple regions of the GUV sample were collected.

For the assessment of septin localization on the membrane at either the inside or the outside of the GUVs, a series of two-dimensional image regions were collected for each sample. The regions were all taken at approximately 7μm height from the imaging well surface. This height corresponds approximately to the average vesicle radius, so that the majority of vesicles are at their equatorial plane. Additionally, z-stacks with a Z-distance of either 0.5 or 1μm were also collected.

5.4.8. Septin encapsulation efficiency analysis

For each septin bulk solution, the average signal of the 5 collected regions was calculated and, assuming a linear relation between pixel intensity values and septin concentration of the form: $I_{sept}(c_{sept}) = A \cdot c_{sept}$, the proportionality constant A was determined using a code written in Python using the numpy least square fitting to obtain the calibration curve.

The positions and radii of the GUVs were detected using DisGUVery [262], an open-

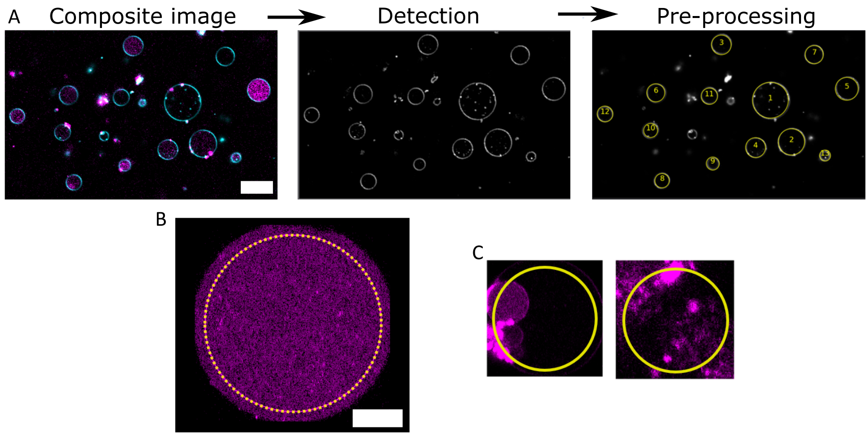

Figure 5.11. Analysis workflow of GUV samples for the quantification of septin encapsulation. A. A two-channel confocal image (membrane: cyan, septin: magenta) was acquired at 7 µm height from the coverslip. The image was pre-processed with Gaussian smoothing and edge enhancement. The vesicle positions and radii were obtained with DisGUVery [262]. Scale bar: 20 µm. B. The average intensity of the septin signal was calculated within a circular ROI with a radius equal to 90% of the vesicle radius (yellow dashed line) and converted to concentration using the calibration curve obtained from the septin bulk solutions (Fig. 5.3B). Scale bar: 5 µm. C. Examples of rejected GUVs due to erroneous GUV detection (left) or the presence of septin aggregation (right).

source software specialized in the analysis of GUVs. The collected raw images were imported in the DisGUVery software and pre-processed with a 2D Gaussian smoothing of kernel size 15 and edge enhancement of a kernel size of 30. Subsequently, the Circular Hough Transform detection method [275] was implemented for the detection of the vesicles (Fig. 5.11A). The parameters selected for the detection were Edge threshold: 30, Hough threshold: 30, Min. vesicle distance: adjusted per image based on the vesicle density, Min. radius: 10, Max radius: 200.

Then, the detected vesicle positions were imported in a custom Python script, where circular ROIs were created, concentric to each GUV and with radii of 90% of the respective vesicle radius (Fig. 5.11B), to avoid underestimation of the septin signal due to misaligned GUV detection. After visual inspection of the drawn ROIs, false detections and GUVs that included large septin aggregates of the membrane were rejected, as in these cases the homogeneous septin signal in the lumen does not correspond to all the encapsulated content (Fig. 5.11C). For the remaining vesicles, the pixel intensities within the ROI areas were then averaged for each vesicle, providing a distribution of encapsulated septin concentration after conversion using the determined proportionality constant A.

5.4.9. Membrane localization analysis

A custom-written Python script was developed (available at the repository `https://github.com/kkourkoulou/membrane-localization-quantification`), aiming to quantify the localization of encapsulated septin on the GUV membranes, allowing for comparisons between different membrane compositions.

Initially, the raw confocal images corresponding to the membrane channel were imported in the DisGUVery software [262] for vesicle detection. After a pre-processing step of image smoothing by convolution of the original image with a 2D Gaussian function of kernel size 3, the Circular Hough Transform detection method [275] was implemented for the detection of the vesicles. The parameters selected for the vast majority of the images were: Edge threshold: 35, Hough threshold: 35, Min. vesicle distance: 30, Min. radius: 10, Max radius: 80, with slight modifications for improved detection based on the density and clarity of each sample.

The raw confocal images corresponding to the membrane and the septin channel were then imported in the Python script together with the information of the vesicle positions and radii found by DisGUVery. Subsequently, for each vesicle, 360 equally-spaced radial paths were created starting from the detected vesicle centre. The path length was 1.5 times the length of the detected vesicle radius to account for possible membrane deformations and detection misjudgments in the placement or size of the vesicles by DisGUVery. Along each radial path, the signal intensity of both the membrane and the septin channel were measured with a one-pixel step size. The individual radial intensity profiles calculated in this manner were then averaged for all angles to obtain a collective radial profile for the vesicle while at the same time reducing the effect of noise (Fig. 5.12A). The background signal was subtracted from the collective radial profile to obtain the corrected mean radial profile of the vesicle. For the calculation of the background signal, a mask was created locally using the Li threshold [276] in a square of sides equal to 3 times the vesicle diameter centered on the vesicle under study. The threshold was applied locally to account for variations in the background signal over the wide region of the considered image. Closed contours of the mask were then filled in to efficiently avoid the signal of the vesicle lumen and of possible surrounding lipid aggregates or segments of other vesicles found in this area. The background signal for each of the channels was then calculated as the average of the corresponding signal intensity in the remaining area (Fig. 5.12B). The Li threshold was chosen after visual inspection of the performance of seven different options available in the filters module of the scikit-image Python package (Isodata, Li, Mean, Minimum, Otsu, Triangle and Yen) for a subset of randomly chosen sample images.

From the calculated radial intensity profile, the position of the membrane borders was re-defined using the peak detection function find_peaks of the scipy Python package, requiring a minimum height of 10units, a minimum distance from other peaks of 5units, and a prominence of 1. These parameters were chosen after trials and visual inspection of randomly chosen sample images. The membrane's position was considered to be the position of the detected peak. However, in dense samples the membranes of neighboring vesicles or lipid aggregates could result in the detection of multiple peaks in that region. To account for that possibility and avoid overestimation of the size of the vesicle, the heights of the last two or three (if present) peaks detected outside the vesicle radius found in DisGUVery were compared and the tallest peak was considered to correspond to the membrane position. The width of the membrane area was then taken as the chosen peak's width at half-maximum and the inner and outer borders of the membrane were thus determined (Fig. 5.12A). Subsequently, the angular profile of the vesicle along the membrane contour was calculated by averaging the pixel intensities within the detected membrane ring for each angle.

In order to study the localization of septin on the membrane, it was necessary that the vesicles were in focus and did not include lipid pockets, significant deformations, or other artifacts that could interact and interfere with the protein, such as encapsulated lipid aggregates, clusters of small vesicles on the membrane, multilamellar structures or lipid tubes. However, the sample quality varied significantly and such artifacts were often encountered, as well as other objects present in the outer buffer such as lipid aggregates, oil droplets, or crowded clusters of vesicles. Consequently, as the Circular Hough Transform method is based on edge and circularity detection, such unwanted objects were also falsely detected.

To ease the process of eliminating these undesired detected structures in the large collected datasets, an automatic rejection process was incorporated in the script. With it, individual vesicles were marked with appropriate comments based on the related type of artifacts reflected in the behaviour of the radial and/or the angular profile. The marked objects were subsequently removed and the remaining GUVs were isolated and analyzed. Detected objects were rejected if any of the following criteria was satisfied:

- Vesicles were crossing the image borders or some of the radial paths for the calculation of the intensity profiles extended further than the image margins (Fig. 5.12C.a).
- No septin signal was present inside the vesicle or septin signal was too low and dominated by noise. Condition chosen after visual inspection: Maximum of the septin signal inside the vesicle was lower than 5 a.u.
- No membrane peaks were detected with the chosen parameters. Intended to reject lipid aggregates, oil droplets and dense lipid clusters that present a rather uniform signal rather than a peak corresponding to clear circular membrane border as in the case of GUVs (Fig. 5.12C.b).
- The detected membrane was wider than at least 1/4 of the vesicle radius. Intended to reject the vesicles that are out of focus (Fig. 5.12C.c).
- Peaks were detected inside the GUV lumen. Intended to disregard vesicles with encapsulated lipid aggregates that might interact with the encapsulated septin and interfere with septin localization (Fig. 5.12C.d).
- The average lipid signal from the centre to the inner membrane border was larger than 1/3 of the signal at the membrane peak. Intended to avoid vesicles that contain large lipid aggregates or that encapsulate smaller vesicles (Fig. 5.12C.e).
- The average lipid signal outside the outer membrane border was larger than 40% of the signal at the membrane peak. Intended to reject vesicles that are part of large vesicle/lipid clusters (Fig. 5.12C.f-g).
- The relative standard deviation (RSD) of the septin angular intensity profile was higher than 0.8. Intended to avoid vesicles with significant deformations, lipid pockets or large aggregates on the membrane, where it is unclear whether septin is localized due to binding or trapped in lipid compartments (Fig. 5.12C.h). The threshold value of the RSD was chosen through visual inspection, aiming to be able to detect

such scenarios but avoid simultaneous rejection of vesicles with no clusters but with high variations in the angular profile due to noise.

After the rejection of unwanted objects and prior to the quantification of localization, an additional correction was necessary to avoid any effects of noise magnification due to multiple counting of the central pixels. From manual observation of the data, the removal of the two central pixels in the radial profile seemed sufficient (Fig. 5.12D).

To assess whether septin localizes at the membrane and quantify the localization, we formulated a definition that considers the normalized difference between the septin signal at the membrane and the septin signal in the lumen:

$$L = \frac{\tilde{I}_m - \bar{I}_c}{\tilde{I}_m} \tag{5.1}$$

where $\tilde{I}_m$ corresponds to the median of the septin intensity signal within the width of the detected membrane and $\bar{I}_c$ corresponds to the average septin signal of a central area of radius equal to 1/4 of the detected vesicle radius (Fig. 5.12E).

5

We calculated the median of the fluorescent intensity within the detected membrane width, instead of the average, because the mean is sensitive to overestimation if there are small septin clusters on the membrane. In such regions, since the septin colocalized with a membrane cluster, it is unknown whether septin localized due to lipid affinity or physical entrapment. Thus, calculation of the median provides us with a value that is representative of the homogeneous septin signal observed for the majority of the membrane segments. In contrast, as the septin signal away from the membrane is uniform, taking the average value within a concentric central segment is sufficient.

To accommodate for comparisons between different vesicles of the same or different samples, the calculated $\tilde{I}_m - \bar{I}_c$ difference needed to be normalized. As overall the septin signal was low and variable among GUVs, we chose to normalize by the median signal at the membrane so that L is bounded, in practice (see section 5.2.3), between any negative value and 1. This normalization additionally facilitates a convenient qualitative classification of the vesicles, based on whether septin localization is present or absent. Specifically, when $\tilde{I}_m \leq \bar{I}_c$ or equivalently $L \leq 0$, it is obvious that there is no septin localization on the membrane, while for $0 < L \leq 1$ some septin localization is detected. In order to avoid misjudgement and to only include vesicles with clear homogeneous localization, the threshold value $L = 0.16$ was chosen. This value corresponds to $\tilde{I}_m = 1.2\bar{I}_c$ and was chosen after visual inspection of randomly chosen vesicles in order to avoid false assessments due to the signal present in the lumen area of the radial intensity profiles (Fig. 5.12F). The calculated distributions of L values for each composition were statistically compared using the Mann-Whitney U test.

5.4.10. Measurement of the distances between deformations

The distances between the deformations on the GUVs with septins incubated outside and the vesicle radii were measured with FIJI. We manually draw lines between the centers of adjacent dots on the surface (top or bottom) of the GUVs or between the tip of adjacent spikes/bumps on the equator of the GUV. We then measured the distance of each line.

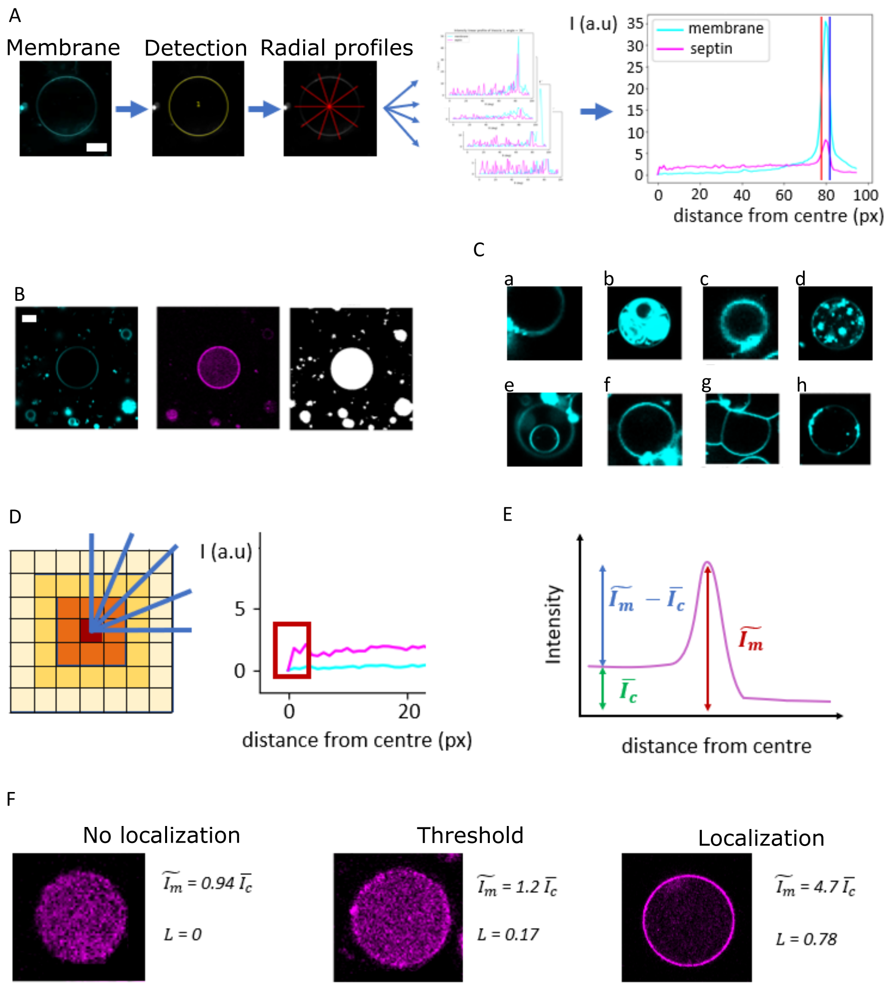

Figure 5.12. Analysis for the quantification of septin localization inside GUVs. A. After detection of the vesicle positions (yellow line), 360 equally spaced radial intensity profiles were calculated (red lines), and then averaged to obtain a collective radial intensity profile for each vesicle. The borders of the membrane (vertical red and blue lines) were identified as the width at half maximum of the detected peak. B. A mask (white on the right image) was created locally for the calculation of the background noise using the Li threshold [276]. The background of each channel (membrane: cyan, septin: magenta) was calculated by averaging in the unmasked region. C. Example images of rejected DisGUVery detections. D. The pixel grid centered at the vesicle center is depicted, with the 1st (red), 2nd (orange), 3rd (yellow), 4th (light yellow) initial pixels. As all radial profiles (blue) originate from the centre, the initial pixels are multi-counted. The effect reduces as the lines grow further from the center and as the number of pixels averaged for a specific radius increases. In the zoomed-in image of the radial profile of A., the bias from the multi-counting is visible (red rectangle). E. Visualization of Eq. 5.1. L was defined as the ratio of the blue over the red height. F. Three different vesicles displaying no localization, signs of localization and clear localization, respectively. Scale bar are 10 µm.

Examples of this can be seen in Figure S5.3B. The radius was measured as half the manually measured diameter.

5.5. Supplementary information

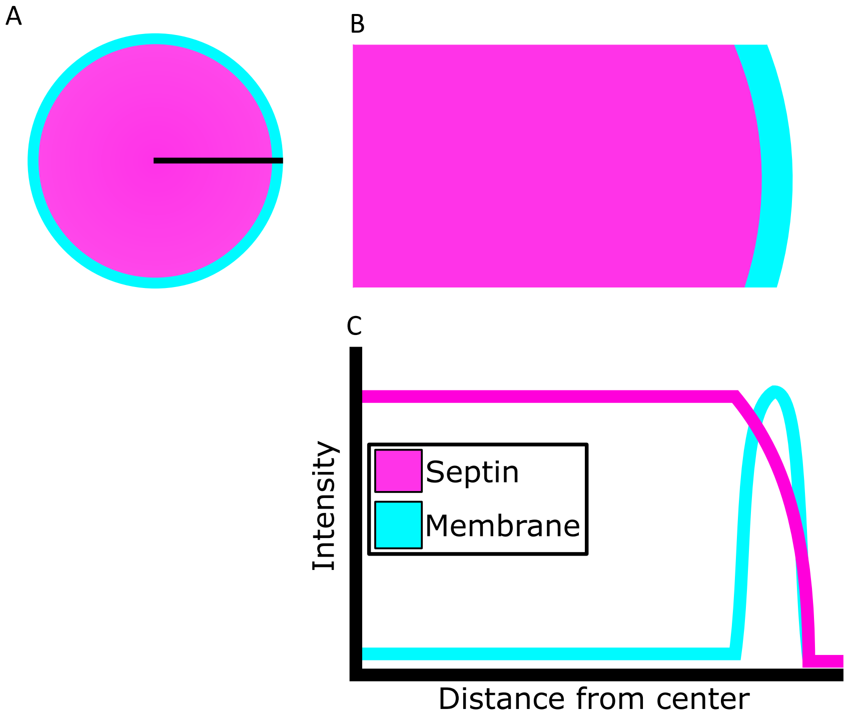

Figure S5.1. Decrease of the septin intensity close-by the GUV membrane when septin does not localize to the membrane. A. Representation of a GUV (cyan) with septin (magenta) encapsulated, as seen by confocal microscopy. B. Representation of the confocal slice taken along the black line in A. C. Representation of the radial profile produced by the confocal slice in B. As there is less septin per unit of distance on the Z direction close to the GUV membrane, the measured confocoal fluorescence intensity decreases.

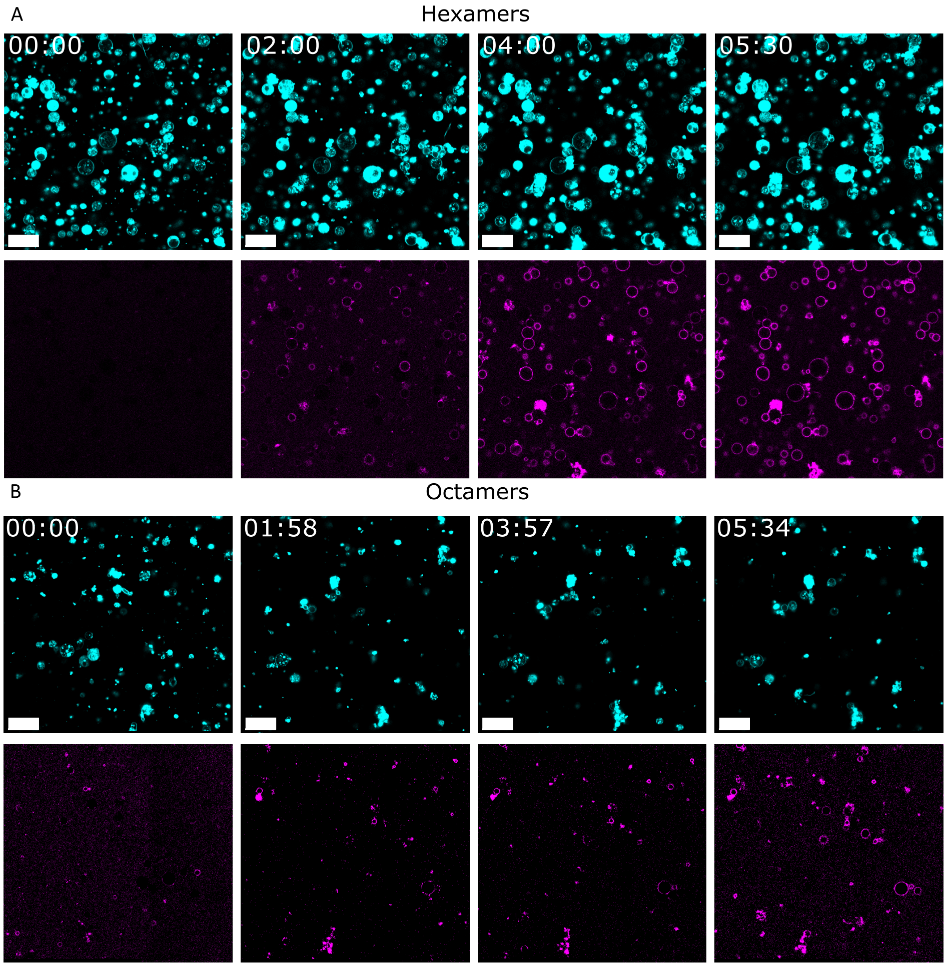

Figure S5.2. Timelapse confocal image series of septin complexes binding to the outside of GUVs. A. Septin hexamers (magenta) binding to GUVs (cyan) with a lipid composition of 20%PS+5%PIP2. Time is denoted in the top left corner of each image as min:sec. B. Same for septin octamers. Scale bars are 25μm.

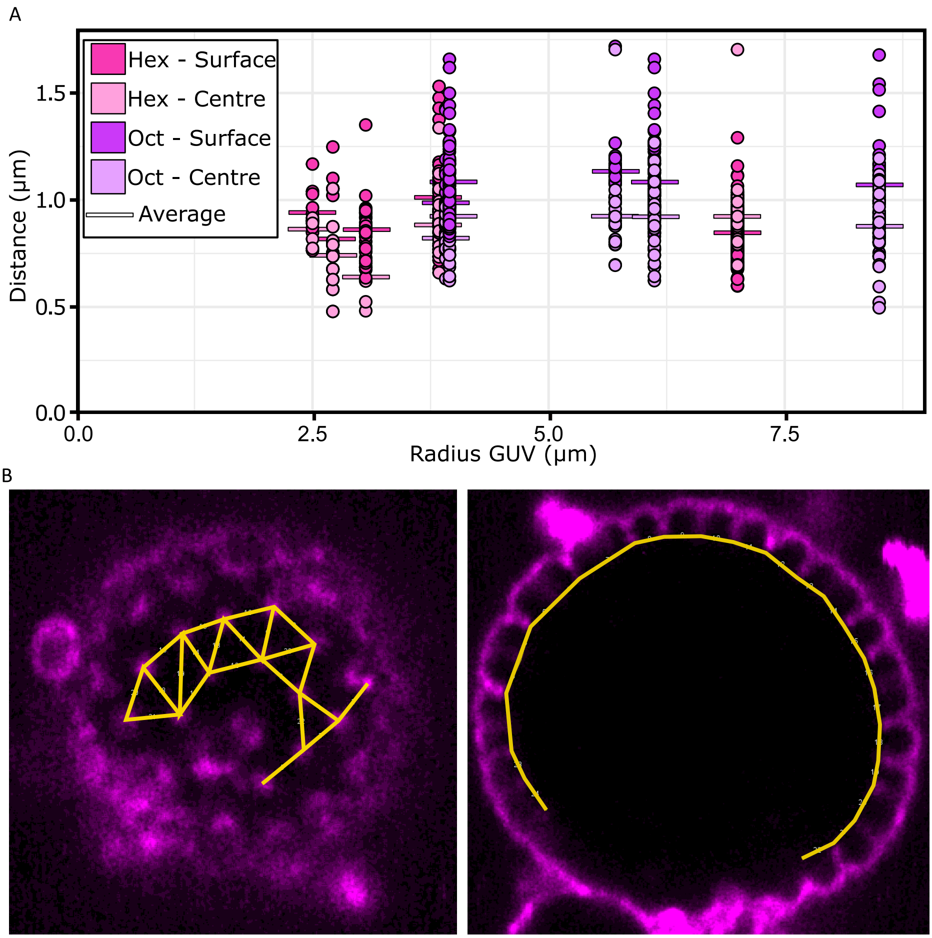

Figure S5.3. Distance between the septin-mediated deformations o the GUV membrane. A. Scatter plot showing distances between the dots on the surface (top or bottom, darker color) or between the tip of the spikes/bumps on the equator (lighter color) against the radius of the GUV these distances were measured from, for both hexamers (pink) and octamers (purple). Single dots represent single distances between dots/spikes/bumps and horizontal lines represent the average of the distances for each given radius (N = 10 GUVs, 5 for hexamers and 5 for octamers; from 2 independent experiments). Due to to the small amount of GUVs counted, each single radius represents a single GUV (with some overlap between 3.5 and 4µm). B. Example images showing the manually drawn lines used to measure the distance between the dots on the surface (left, bottom surface in the shown example) or between the spikes/bumps observed in equatorial confocal slices (right).

5

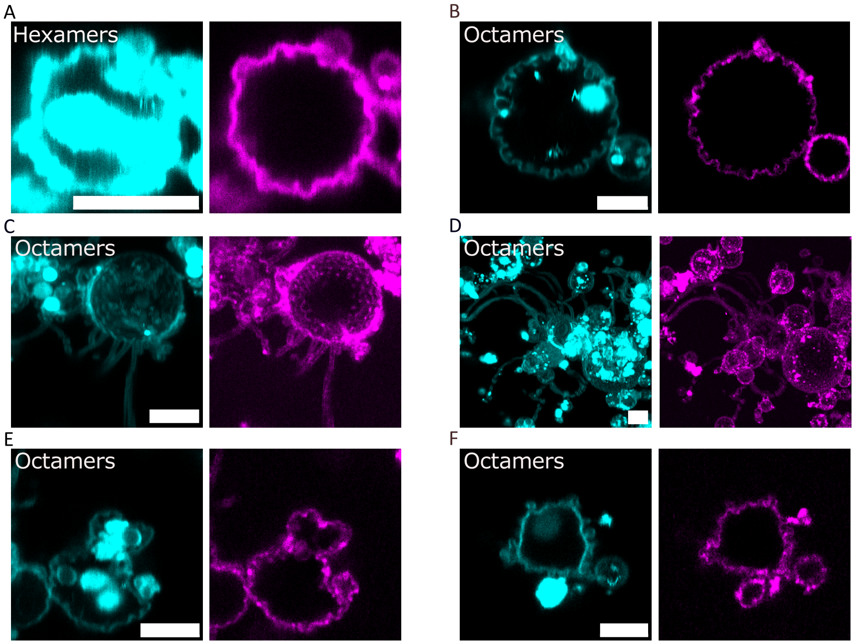

Figure S5.4. Alternative, more rare structures formed when septin complexes bound to the outside of GUVs. A and B. Representative single confocal images of bumps with larger amplitude than typically (~0.9µm) and irregular spacing formed on GUVs (cyan) by both septin (magenta) hexamers (A) and octamers (B). C. and D. Maximum confocal Z-projections of septin octamers localizing to membrane tubes. E and F. Representative single confocal images octamers localizing to GUVs that are non-spherical while also displaying bumps. Scale bars are 5µm.

Acknowledgements

We thank Jeffrey den Haan for his help with protein purification. We also thank bachelor students Britta Bor and Suzanne van de Schaft for their invaluable help setting up the assays and acquiring initial data. We thank Aurelie Bertin, Manos Mavrakis, and Koyomi Nakazawa for useful discussions.

5


Deciphering human septin-
membrane interactions
19-04-2021
Gerard Castro-Linares
Research plus

Chapter 6

Septin octamers regulate myosin-driven contraction by modulating actin bundling and crosslinking in a concentration-dependent manner

Dynamic cellular processes such as cell division and migration critically depend on contractile actin-myosin networks. Septins are gaining recognition as a protein family that regulates the contractility of these networks. Observations in cells showed that septins regulate the contractility of actin-based structures by direct interactions with actin and myosin, with potential involvement of accessory proteins, and through crosstalk with signaling factors. It is challenging to disentangle these different regulatory roles of septins in the full complexity of the cell. Here we test how septins may regulate actomyosin contraction in the absence of any accessory proteins, by reconstituting a minimal cell-free model system combining human septins, actin filaments and muscle myosin-2 thick filaments. We show that septin hexamers and octamers both are able to tightly bundle actin filaments, forming interconnected networks of composite septin/actin bundles. High septin concentrations hamper myosin-driven contraction because the actin-bound septins immobilize the myosin filaments. By contrast, low septin concentrations promote long-range myosin-driven contraction by crosslinking the actin network. Our findings show that septin can inhibit or permit myosin activity depending on the extent of septin-mediated crosslinking of the actin network.

The experiments for this chapter were designed by Gerard Castro-Linares with the help of Lucia Baldauf, who also provided the myosin TEM images in Figure S6.2. Experiments, analysis, and writing were performed by Gerard Castro-Linares.

6.1. Introduction

The actin cytoskeleton plays a fundamental role in powering cell and whole-body movements in animals. This movement is essential for embryo development, proper functioning of the immune system, tissue repair, and more, making it essential for the overall health and survival of cells and organisms [277]. The basis of this movement is the interaction of myosin, specifically myosin-2, with diverse filamentous actin structures, such as the cell cortex, stress fibers, or sarcomeres [278, 279]. Myosin-2 is a molecular motor protein that uses the hydrolysis of ATP to generate a powerstroke that moves the myosin head domain towards the plus end of the actin filament it binds to [280]. Since myosins self-organize into bipolar filaments, this movement can slide pairs of actin filaments past one another to drive contraction. Despite myosin's ability to generate movement, there is a need for other actin binding proteins (ABP) to translate this movement to the scale of the cell and the body. ABPs can modulate the contractility of the actin network by affecting the crosslinking, polymerization, and turnover of actin filaments, as well as the recruitment and activity of myosin-2 motors [47].

One such ABP is septin, a cytoskeletal GTP-binding protein. In mammalian cells, septins are part of actin stress fibers [105, 144, 281], contractile actin rings [119, 281, 282], and the cell cortex [120, 142]. In human cells, septins are present in the form of hexameric and octameric complexes [83–85]. It was recently shown that specifically the octamers are responsible for actin stress fiber stabilization [144]. These stress-fiber localized septin octamers are involved in the reinforcement of stress fiber organization [105, 109, 283], the maturation of focal adhesions [109], and the anchoring of the stress fibers to the membrane [144]. The proper septin-mediated crosslinking of the stress fibers is important for stress fiber contractility and cell migration [109]. On the cell cortex, septins bind preferentially to branched actin networks such as lamellipodia [127] and phagocytic cups [128]. Cortical septins serve different cell-dependent roles related to the contractility of the cortex [119, 284], via the cross-linking of the cortical network [284] and the stabilization of cell junctions [285, 286]. Through these roles, septins participate in single- and collective-cell migration [215, 216] of fibroblasts and endothelial cells as well as in collective cell movements in developing embryos [213, 287, 288]. Cortical septins also contribute to cell division [119, 120, 214] via distinct mechanisms [282]. Specifically, septins play important roles during cell rounding [119, 120], constriction of the actomyosin ring [121–124], and midbody abscission [125, 126]. It has been observed that knockdown of SEPT7, which is required for forming septin complexes, leads to incomplete cleavage furrow ingression [119]. Knockdown of SEPT9, which is required for forming octamers, can slow or stop cell division, or even kill dividing cells [119]. Septins are recruited to the cytokinetic furrow during early stages of cytokinesis by anillin [124]. Once on the ring, they participate in the activation of non-muscle myosin II [121] to drive contractile ring contraction. Removing septins from the contractile ring, by either sequestering it [121] or not allowing anillin to recruit it [122], still allows for the formation and constriction of the ring. However, without septin, once constriction has finished, the cleavage furrow retracts before the intercellular bridge stabilizes, showing septin's importance for midbody formation. In the midbody, septins form a double ring that organizes the ESCRT system for midbody abscission [125, 126]. Despite this evidence that septins do not participate in the contractile ring formation, during cellularization of *Drosophila melanogaster* embryos, a process very similar to cell division [289], septins are crucial for the correct formation and compaction of the contractile rings [101]. In the absence of septin hexamers, actin formed polygonal arrays of loosely packed bundles of poorly oriented actin filaments, indicating that septins serve a crosslinking role [101].

Cell-based studies have provided evidence that septins participate in actin crosslinking [101, 102, 105, 109, 283, 284], but there is not much research on the mechanism of the septin-actomyosin interaction. Indeed, the mechanisms of action of septins in cells have been difficult to decipher due to the diversity of septin complexes with distinct roles in different cell types [75, 282], and the interaction of septin complexes with other cell components, such as the cell membrane [95, 96, 98], microtubules [103, 148], signaling proteins such as myosin kinases [121], and the presence of accessory septin-binding proteins such as the Borg family [104, 141, 164]. *In vitro* reconstitution has been successfully used as a tool to dissect some of these interactions thanks to the use of a simplified environment with a controlled protein composition. Several studies showed that purified septins can bind and crosslink actin filaments [101, 102]. Kinoshita at al. [133] first reported that recombinant mammalian septin hexamers (composed of SEPT2, SEPT6, and SEPT7) show no detectable affinity for F-actin in cosedimentation and fluorescence imaging. They proposed that anillin is needed to mediate actin and septin interactions. Two later studies, however, reported that both fly hexamers [101] and human hexamers and octamers [102] bind actin filaments and bundle them into curved fibers [101, 102]. By crosslinking actin, septins may potentially regulate actomyosin contractility since higher crosslink densities promote longer-ranged contraction [290, 291]. One study showed that purified SEPT2 directly binds myosin, suggesting that septins may regulate contractility by recruiting myosin to actin structures [121]. So far, there are no *in vitro* studies testing the combined effect of septin-actin and septin-myosin interactions on actomyosin network contraction.

6

Prompted by the evidence that septins can crosslink actin, here we aim to understand how human septin hexamers and octamers are able to bundle actin and how this crosslinking activity impacts myosin-based contraction of actin. To do so, we used contraction assays where preformed myosin-2 filaments were incubated with actin bundled made in the presence of different amounts of recombinant septin complexes. We used muscle myosin 2 for experimental convenience, since it can can be readily isolated in large quantities from rabbit skeletal muscle. The majority of *in vitro* contraction assays have similarly used muscle myosin 2 [291–294]. General principles should be the same as for nonmuscle myosin filaments. However, exact details may differ, because of differences in myosin bipolar filament length (~300nm in case of nonmuscle myosin-2 [295] versus ~1.5μm for muscle myosin [296]), motor processivity (with a duty ratio of ~0.05 for single skeletal muscle myosins versus ~0.8 for nonmuscle myosin-2, depending on the isoform [297–299]), and speed (~7μm/s for skeletal muscle myosins versus ~0.3μm/s for nonmuscle myosin-2, depending on the isoform [297]). Our findings establish a possible direct role of septins in myosin-based contraction of tight actin bundles even in absence of regulatory proteins. This mechanism may play a role in bundled actin structures such as stress fibers and contractile rings and in crosslinked structures such as the actin cortex.

6.2. Results

6.2.1. Septin oligomers tightly bundle and curve actin

Prior biochemical reconstitution studies have demonstrated the ability of fly and human septins to bind and bundle actin filaments [101, 102]. In this study, we investigated the ability of human septin hexamers and octamers to bundle actin filaments. To accomplish this, we copolymerized 1μM actin with different concentrations of septin hexamers and octamers ranging from 10nM to 800nM on a neutral lipid bilayer-coated surface that prevents septin binding. Subsequently, we visualized the samples using TIRF microscopy (Fig. 6.1A).

We saw that at the highest concentrations (800nM and 500nM), both septin hexamers (Fig. 6.1C) and octamers (Fig. 6.1D) completely converted the actin filaments to bundles. The signal of the actin (top row, yellow) clearly showed thicker filaments in the presence of septin than in its absence (Fig. 6.1B). Additionally, these bundles were highly curved, as observed before [101, 102], even forming loops and rings. The septin image (bottom row, magenta) showed exactly the same structures as the actin image and, in addition, a dotted pattern characteristic of septin bundles or complexes bound to defects in the lipid bilayer (see section 6.4) that are too small to show up by fluorescence microscopy in the lipid bilayer channel. The septin-actin bundles were connected, forming a meshwork. Our findings demonstrate that septin oligomers bundle and crosslink actin filaments.

6

At low concentrations (300nM and lower), septin octamers could bundle actin more efficiently than septin hexamers. At 300nM, the septin-actin bundles formed by septin hexamers (Fig. 6.1C) were short and isolated, unlike the connected networks seen at higher septin concentrations. In contrast, the bundles in the presence of septin octamers were indistinguishable from the 800nM condition (Fig. 6.1D). Human octamers could completely bundle actin down to a septin complex concentration of 100nM, while in the presence of 100nM hexamers, actin filaments looked the same as in the absence of septin (Fig. 6.1B).

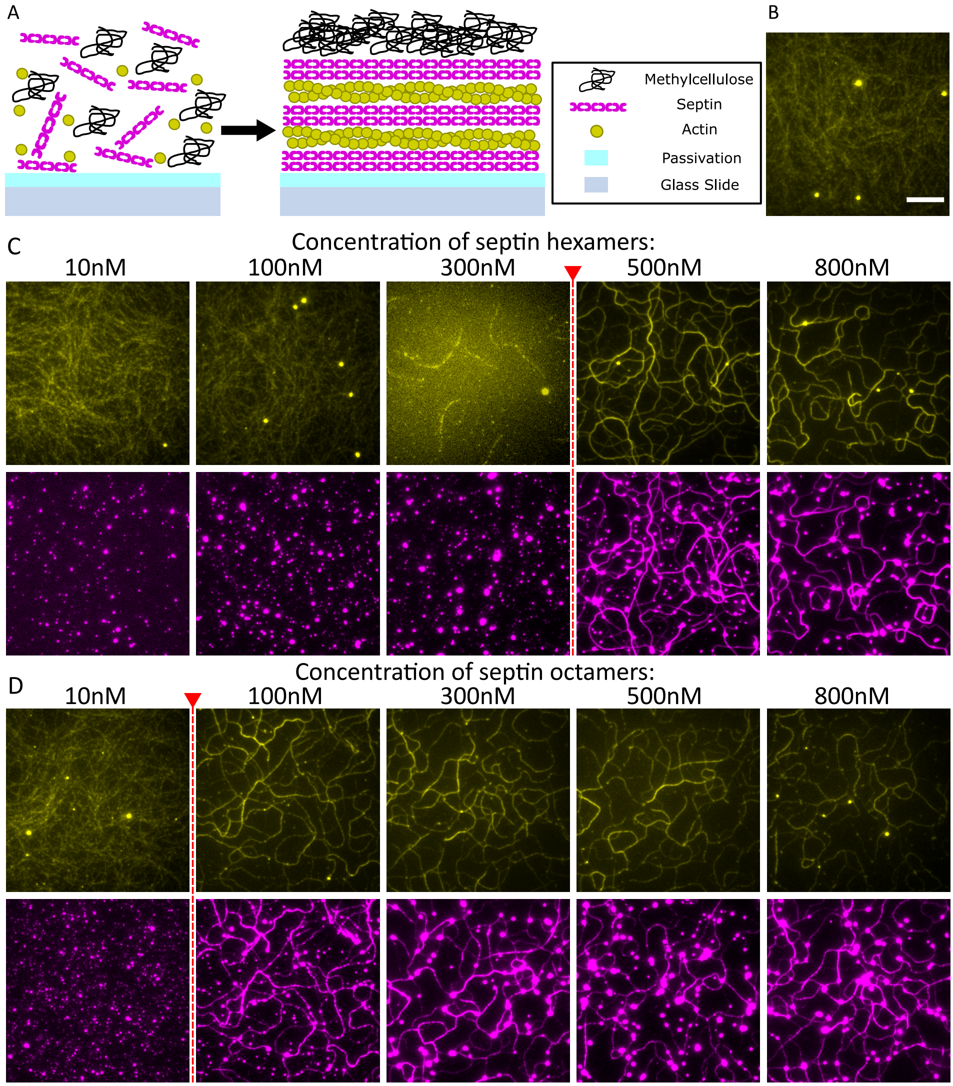

Figure 6.1. Bundling of actin filaments by human septin hexamers and octamers at different concentrations. A. Schematic representation of the experiment. Septin oligomers and actin monomers are mixed and immediately added into a passivated flow channel. There they co-polymerize and methylcellulose crowds them to the surface for visualization by TIRF microscopy. B. Representative images of actin (yellow) polymerized in the absence of septin complexes. C. Representative images of actin co-polymerized with the specified concentrations of human septin hexamers. D. Corresponding images with human septin octamers. For C and D, red arrowhead with dashed line indicates the transition point from which we can clearly start to observe septin-actin bundles. Scale bar is 10μm.

To visualize the bundle ultrastructure and test if there is any observable difference between bundles formed with septin hexamers versus octamers, we used TEM. We imaged bundles formed at 800nM, because both septin complexes completely bundle the actin filaments at this concentration, and also at 300nM, because at this concentration octamers completely bundle actin while hexamers cannot. A first obvious observation is that the network of septin-actin bundles observed with TIRF microscopy (Fig 6.1) is not seen by TEM (Fig. 6.2). We believe that this difference originates from the differences in sample handling. The bundles imaged by TIRF form undisturbed within the flow channel upon insertion of G-actin and septin oligomers. In contrast, the bundles imaged by TEM needed to be similarly formed in an Eppendorf tube but then extensively handled, first by pipetting them onto the TEM grid followed by repeated washing and fixation steps. This extra handling likely disrupts the network, separating and isolating the connected fibers into single bundles. Nevertheless, we could clearly observe the septin-actin bundles by TEM under the same conditions where we also observed them by TIRF. At 800nM, both hexamers and octamers bundled most of the actin, as shown by the high density of bundles observed at low magnification for both septin complexes (left panels in Fig. 6.2A,C) of a fairly uniform width of 128±17nm (Fig. S6.1A). Occasionally, we observed thicker bundles (200-350nm in width). These bundles usually split into several bundles of the more commonly observed smaller width (Fig. 6.2A and C, right), explaining the network formation seen in the fluorescence imaging (Fig. 6.1). At 300nM, septin octamers bundled the actin to form extensive and curved fibers (left panel in Fig. 6.2B) with a similar width as at 800nM (119±11nm, Fig. S6.1A). As seen in the right panel of Figure 6.2B, we also encountered more loosely bundled or even completely unbundled actin filaments, indicating that insufficient septin was present to bundle all the actin. By contrast, septin hexamers at 300nM rarely formed tight bundles. Most of the actin was unbundled or loosely bundled (Fig. 6.2D, left and right). On the rare occasion where we found a bundle, these had a thickness of 89±26nm (Fig. S6.1A). For both septin complexes at 300nM, we observed a common structure where the end of some bundles opened up and freed single actin filaments, as seen in the center images of Figure 6.2B and D. This suggests that, when insufficient septin is present to bundle all the available actin, septin accumulates at the middle of the bundles.

The images of tight bundles formed with 800nM septin complexes had enough quality to distinguish single filaments running in parallel (Fig. 6.2). To test whether we could distinguish septins from actin filaments and whether septins form filaments, we measured filament widths and compared them with the width of septin filaments in bundles formed solely of septin (as described in Chapter 2) and with the width of single actin filaments (Fig. S6.2A and C). Septin and actin filaments have rather distinct widths. Septin filaments have an expected width of 4nm (see chapter 4 and also [83, 102] and can form paired filaments having a width of ~10nm (see chapter 4 and also [82, 99]) and a height of ~4nm. Actin filaments have an expected width of 7nm [300]. The results of our width measurements are summarized in Figure S6.1B and Table S6.1. The filaments in the septin-actin bundles were all thinner (on average 4.4±0.8nm for hexamers and 5.7±0.5nm for octamers) than actin filaments (9.3±0.7nm in our TEM images). The average filament width of the hexamer-actin bundles is close to that of single septin hexamer filaments (~4.5), suggesting that the filaments that we observe are predominantly septin hexamer filaments. This observation implies that the actin filaments that, according to the TIRF results, are also part of the bundle are buried underneath either alone or with more septin filaments. Our observations furthermore suggest that the septin hexamers form filaments because the 4nm filaments run along the length of bundles are clearly longer than single hexamers

(~24nm [83, 102]). In case of the octamer-actin bundles, we observed a broader distribution of filaments widths (Fig. S6.1B), with some having a similar thickness as actin filaments (~9nm), others having a similar thickness as octamer filaments (~4nm), and the majority in between (~5-7nm). The thinner filaments are likely septin filaments that, similarly to the hexamer-actin bundles, are also polymerized since they are longer than single octamers (~32nm [82]). The other filaments can either be actin filaments with a smaller apparent width than isolated actin filaments due to the tightness of the bundle, or paired septin octamer filaments that are rotated towards the center of the bundle, exhibiting a lower width than expected (~13nm [208]).

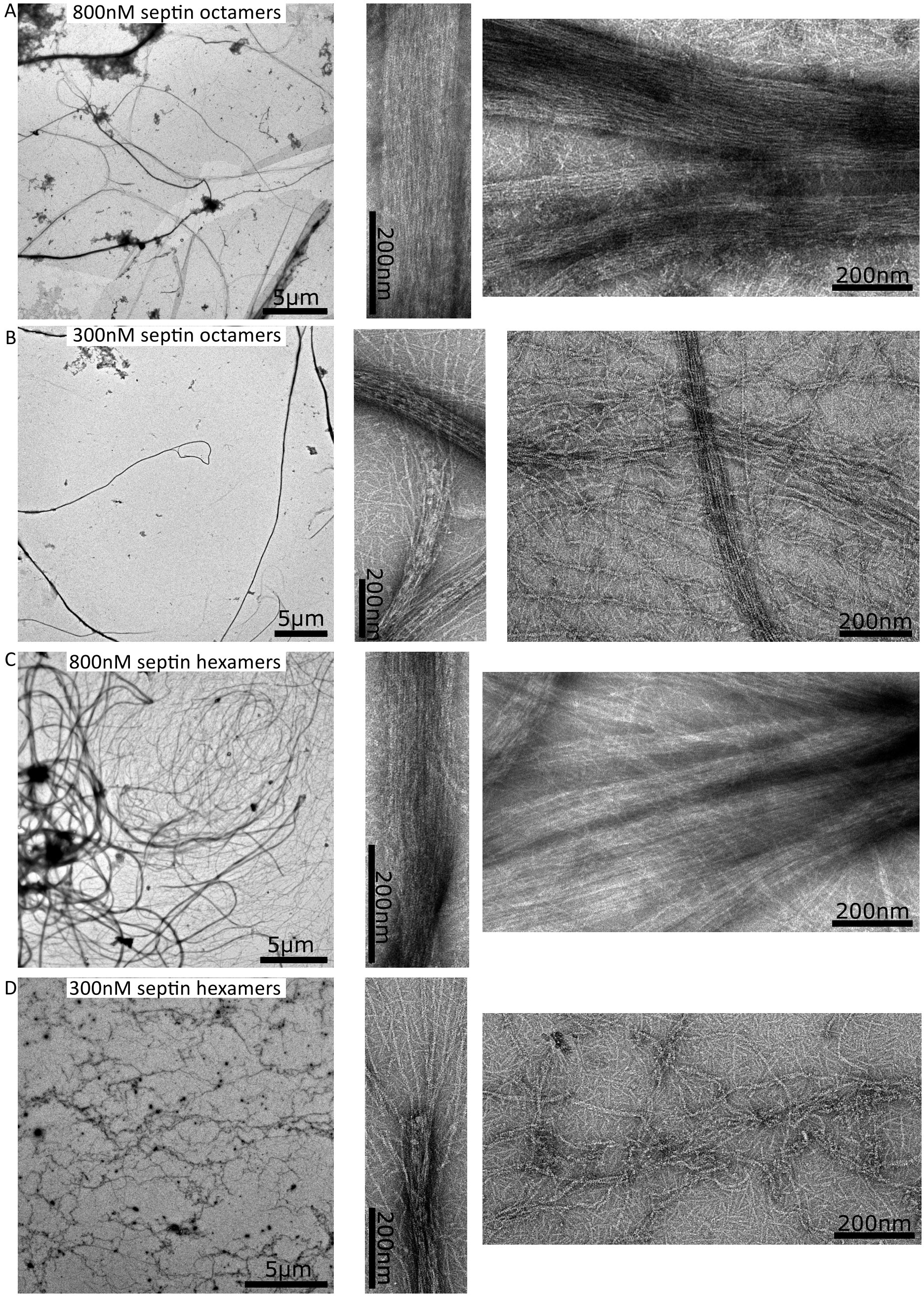

Figure 6.2. High resolution imaging of septin-actin bundles by TEM. Left panels show an overview of the sample, center panels show a detailed close up of a single bundle where single filaments can be observed, and right panels show a close up of the sample to reveal the details of the formed structures. A and B. Representative images of actin polymerized together with 800nM (A) or 300nM (B) human septin octamers. C and D. Representative images of actin polymerized together with 800nM (C) or 300nM human (D) septin hexamers.

6.2.2. Septin octamers induce rapid actin bundling

To study how septins bundle actin filaments, we next performed time-lapse imaging of the bundling process. For this, we first polymerized 1μM of actin inside an imaging chamber and then added the septin oligomers (Fig. 6.3A). Since we observed that octamers bundle actin more efficiently than hexamers and given the evidence that octamers play a dominant role in cell division [119] and stabilization and anchoring of stress fibers [144], we continued the experiments with just octamers.

Figure 6.3B shows a time-lapse imaging series of 300nM septin octamers bundling actin. We see that, as expected from the previous results, all the actin in the TIRF field is bundled, forming a network of septin-actin bundles. This bundling occurred surprisingly fast, since in less than 30 seconds after the addition of septin octamers, we already see bundles in the actin image. At ~15 sec after septin addition, small dots of octamers can be observed in regions where several actin filaments were close to each other. Instead of binding randomly across the yet-to-form bundle, the septin-covered region elongated from the spot where it initially localized (Fig. 6.3B and C). This phenomenon is readily apparent in the septin kymograph (Fig. 6.3C), where the septin signal exhibits a clear pattern of growth from the points of initial binding, rather than appearing randomly. This observation is consistent with the TEM images showing that actin-septin bundles are tight in the middle but often splay out with single actin filaments at the ends. The presence of a hazy/blurry region at the early times in the actin kymograph (Fig. 6.3C) indicates that actin filaments were initially free to move around. Binding of octamers immediately stopped the filaments' movement, as shown by the disappearance of the blurry pixels upon appearance of septin. This indicates that the persistence length of the bundle is much larger than that a single actin filament. Additionally, the binding of octamers also increased the signal of actin, indicating that several actin filaments came together to bundle (Fig. 6.3D). Finally, the increase of the septin signal on the kymographs (Fig. 6.3C and D) shows an accumulation of septin on the bundles after their initial formation. This accumulation is, however, limited and appeared to saturate at 5-fold the initial septin signal after ~4min. This accumulation of septin, but not of actin, is in agreement with the observation that only septin filaments are present on the outside of bundles from our TEM imaging.

When we repeated the experiment with a lower septin octamer concentration of 100nM, we again observed complete bundling of actin and accumulation of septin octamers (Fig. S6.3), similar to the 300nM condition and consistent with the results of Figure 6.1. The process, however, took longer, since it did not start until ~40sec and end until ~2min. This is probably due to the fact that a lower concentration of septin decreases the probability of oligomers finding the actin filaments.

When we reduced the octamer concentration further to 10nM (Fig. 6.4), the septins partially bundled the pre-polymerized actin filaments. This is an interesting observation, since septin octamers at 10nM were unable to bundle actin during co-polymerization (Fig. 6.1). As shown in figure 6.4A, ~1min after the octamers were added, some spots of septin started to appear in regions with a high density of actin filaments, similarly to the 300nM condition. Over time, more spots appeared and elongated (Fig. 6.4B), leading to the bundling of actin filaments along the regions with high actin filament density. Towards the end of the bundling process, the situation differed from the 300nM condition. Sparse actin-septin bundles of limited length connected by unbundled actin filaments free of septin (or with a small amount of septin not visible under these imaging conditions) were present. The presence of this unbundled actin is also shown in the kymograph (Fig. 6.4B), which clearly shows actin signal in a region completely free of septin signal. We initially see a cloud of signal, concurrent with the haziness in the kymograph from the actin filaments moving, and as septin binds, there is a step where the actin signal slightly increases and stays constant. Meanwhile, the septin signal increased without ever reaching a plateau during the imaging time. This shows that septin octamers at 10nM can bundle pre-formed actin filaments in a similar manner as at 300nM, but to a lesser extent due to a sparsity of septin octamers.

6.2.3. Septin octamers tune myosin-2 activity on actin filaments in a concentration-dependent manner

In order to test how septin-mediated actin bundling impacts myosin-driven contraction, we moved to contraction assays with skeletal muscle myosin-2. For comparison, we first performed control experiments with septin-free actin bundles created by crowding with methylcellulose [301]. We polymerized actin in the imaging chamber, added 0.3% methylcellulose, and then waited 5 minutes so the actin could bundle (Fig. 6.5A). After adding 25nM preformed myosin-2 thick filaments, we observed a remodeling of the bundles (Fig. 6.5). The myosin-2 thick filaments moved along the actin bundles, as seen in time-projections (Fig. 6.5C), and in kymographs (Fig. 6.5D,E). Myosin motility remodeled the actin network into asters (Fig. 6.5F), radial arrays of actin filaments. A similar aster formation process has been observed in several prior studies [291, 302–304] and was explained by plus-end directed motility and end-dwelling of myosin motors on actin filaments [291].

6

To study the effect of septin octamers on the contraction of actin bundles, we performed contractile assays with actin bundled by 300, 100, and 10nM septin octamers. For this, we built upon the experiments shown in section 6.2.2 and, after the bundling process was finished, added preformed muscle myosin-2 filaments. In strong contrast with the assay using methylcellulose-bundled actin, myosin had no effect on the septin-actin bundles formed with 300 nM septin octamers for more than 20 minutes (Fig. 6.6). Moreover, myosin, although it bound to septin-actin bundles, did not move or unbind (Fig. 6.6B).

To understand this surprising behavior, we obtained higher resolution images by TEM (Fig. 6.6C). We first examined the interaction of myosin filaments with actin filaments alone or with septin octamer bundles alone (Fig. S6.2B). This is motivated by evidence that nonmuscle myosin II can directly interact with SEPT2 and septin hexamers [121]. Figure S6.2D shows the interaction of unbundled actin filaments with myosin filaments. We observe large radial structures reminescent of the asters observed by TIRF imaging. This shows that in our system myosin filaments can remodel actin filaments into asters despite the lack of crosslinkers, which are known to promote aster formation [290, 305]. Figure S6.2E shows the combination of septin octamer bundles and myosin filaments. We can clearly distinguish septin bundles from myosin filaments, since the latter are thinner, shorter and less curved. Strikingly, the septin octamer bundles displayed a pattern of darkened regions (cyan arrowheads in Fig. S6.2E). Such a periodic pattern is absent in EM images of septin octamer bundles (Fig. 6.2 and Chapter 2). Therefore, the darkened regions, which looked like spherical clumps of protein, must be myosin filaments that, when binding to the bundle, bent or otherwise lost their typically elongated shape. Unfortunately, we could not distinguish if the darkened regions are formed of myosin filaments with the current resolution. In some instances (green arrowheads in Fig. S6.2E), we can observe some myosin filaments overlapping with the septin bundle.

We next combined actin, myosin and septins. Similarly to the sample preparation for TIRF imaging, we prepolymerized actin, added the septin octamers to bundle the actin and incubated for ~30min, and finally added the myosin filaments and incubated for ~3min. We then adsorbed the sample onto a TEM grid and stained with uranyl acetate. Figure 6.6C reveals the co-existence of septin-actin bundles, septin complexes not binding to actin, and myosin filaments. Interestingly, all of the septin-actin bundles showed a periodic pattern of unidentified darkened regions, similarly to the septin-myosin samples in absence of actin (Fig. S6.2C). In some regions (Fig. 6.6D, right side, second and third images), we observed elongated structures reminiscent of muscle myosin-2 filaments, buried in-between some of the bundle-forming filaments of the septin-actin bundle, supporting our hypothesis that the darkened regions are myosin filaments. Our observations suggest that myosins may bind to actin-bound septins rather than to the actin directly. We hypothesize that the septins on the surface of the actin bundles prevent myosins from moving along the actin.

To test this hypothesis, we lowered the septin concentration to produce actin bundles that are connected by septin-free actin filaments. For actin-septin bundles produced by 100 nM septin octamers, we observed a similar behavior as with 300nM. The myosin filaments progressively accumulated on the bundles and did not move along the bundles, and did not remodel them (Fig. S6.3). When we reduced the concentration of septin octamers further to 10nM, the situation changed. After around 8min, the network of bundles formed by the septin and the actin started to move. Soon after, an out of focus cloud made of septin-actin bundles moved across the imaged region; in less than 2 minutes the septin-actin bundles were completely moved out of the field of view, indicative of contraction (Fig. 6.7A and C). In this whole process, the myosin was difficult to see, either because not much myosin bound to the bundles or because myosin quickly unbound (Fig. 6.7B). The top kymograph in figure 6.7B shows moving myosin particles (red arrowhead), and immobile ones (purple arrowheads). The time that it took for the myosin filaments to start remodeling the network was much longer (~6min) than in the control in the absence of septin complexes (<1.5min). Thus at low concentration, septins crosslink the actin network without completely covering the actin filaments, permitting contraction.

When we observed similarly prepared samples by TEM, but mixed and incubated in solution before depositing on an EM grid, we observed asters (Fig. 6.7C), resembling those observed in the absence of septin complexes (Fig. S6.2D). The filaments emanating from the asters (Fig. 6.7D) also resembled those seen in the absence of septin complexes (Fig. S6.2D). In regions where the myosin did not form asters, we could see single actin filaments that, in some occasions, came together forming a short and thin bundle (Fig. 6.7E and F). In these regions, myosin filaments could be observed between bundles and actin filaments. In some regions (Fig. 6.7E and F), we saw bundles with darkened regions similarly to the 300nM condition (Fig. 6.6C). These observations confirm that at low (10nM) septin octamer concentration, myosin is able to interact with actin filaments and contract them into asters.

6

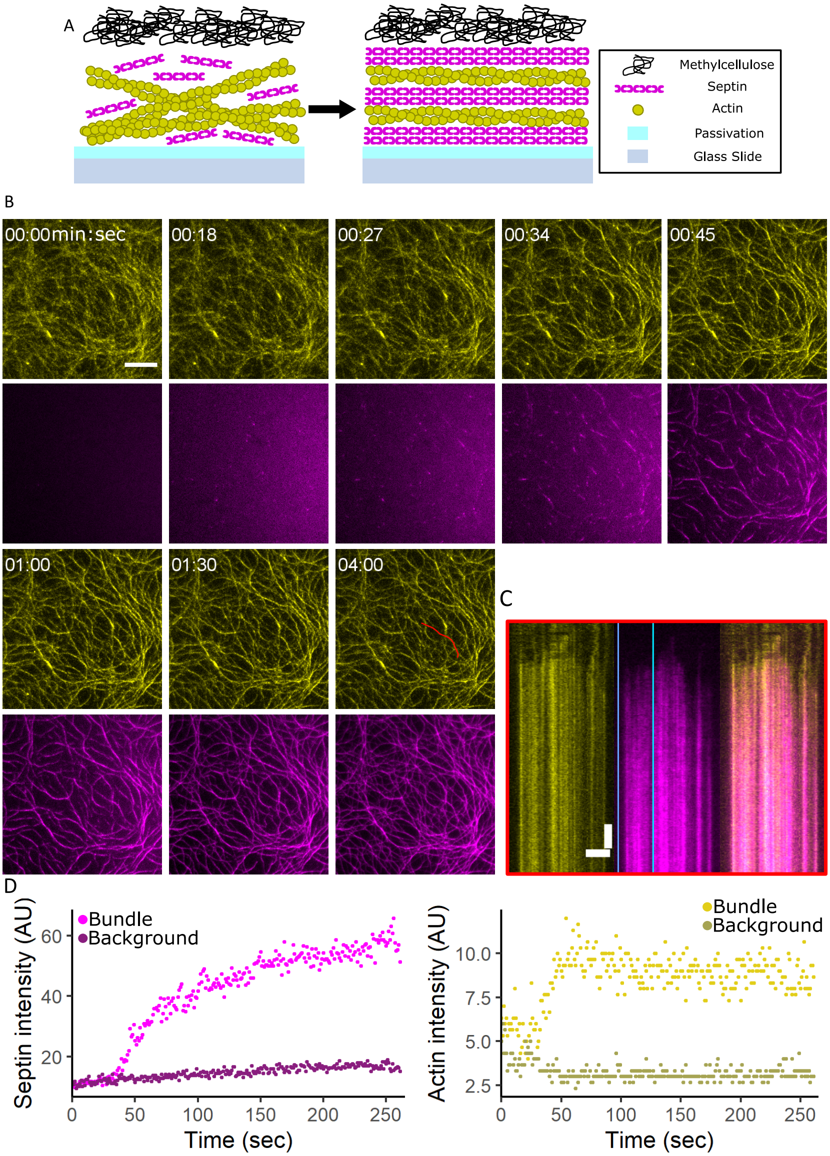

Figure 6.3. Bundling of pre-formed actin filaments by 300nM human septin octamers. A. Schematic representation of the experiment. First, actin is polymerized in a passivated imaging chamber. Then, unpolymerized septin octamers are added. Methylcellulose crowds the actin filaments and the septin-actin bundles to the surface so we can image the bundling process using TIRF microscopy. B. Representative time-lapse imaging series of 300nM septin octamers (magenta) bundling F-actin (yellow). Scale bar is 10µm. C. Kymograph of the red line in B, showing the formation of a single septin-actin bundle. Horizontal scale bar is 4µm. Vertical bar is 25 seconds. D. Fluorescence intensity profiles along the vertical blue lines in the septin kymographs in B, showing how septin accumulates on the bundles over time (left), while actin signal is constant as soon as a bundle is formed at t>50s (right). 'Bundle' represents the light blue line, while 'background' represents the dark blue line drawn outside of the bundle region of the kymograph.

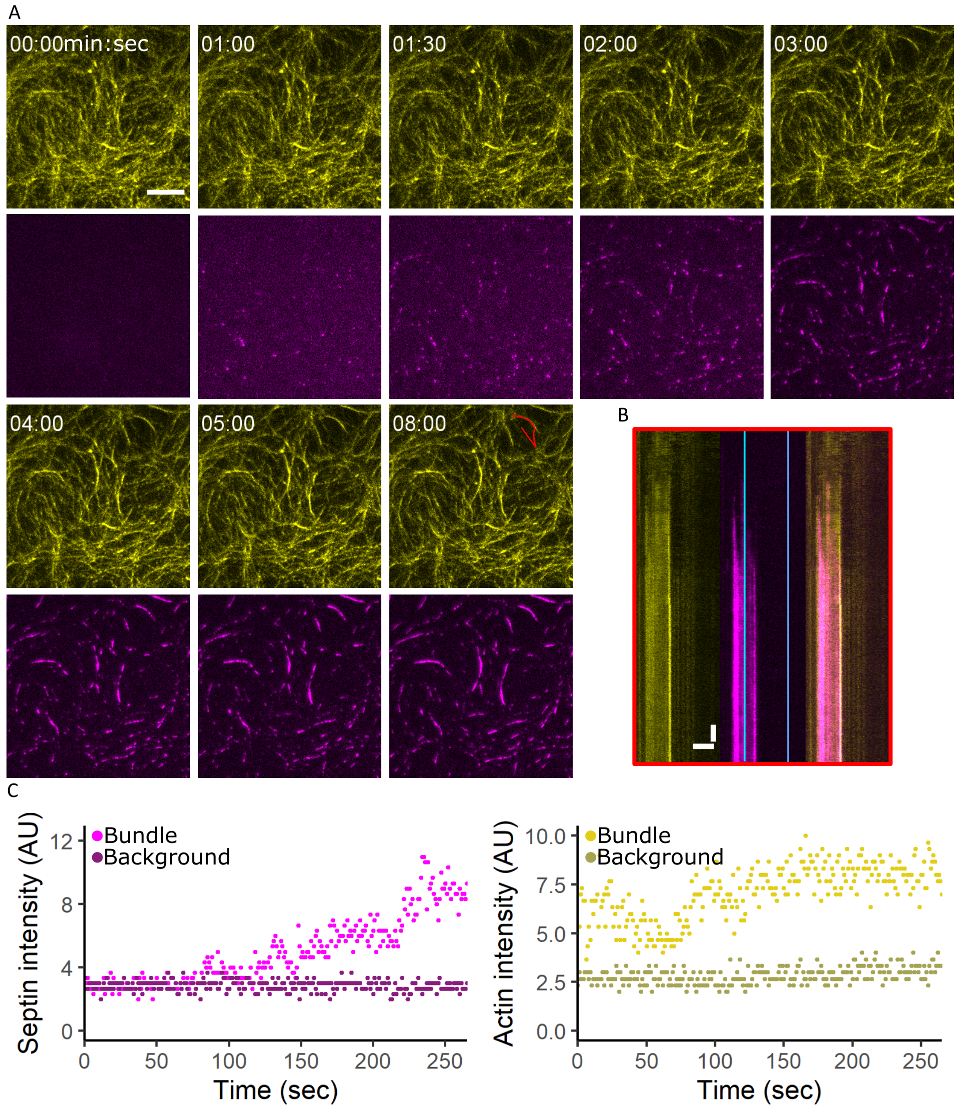

Figure 6.4. Bundling of pre-formed actin filaments by 10nM human septin octamers. A. Representative time lapse image series of 10nM septin octamers (magenta) bundling F-actin (yellow). Scale bar is 10µm. B. Kymograph of the red line in A, showing the formation of a single septin-actin bundle. Horizontal scale bar is 4µm. Vertical bar is 25 seconds. D. Fluorescence intensity profiles along the vertical blue lines in the septin kymograph in B, showing how septin accumulates on the bundles over time, while actin does not. 'Bundle' represents the light blue line, while 'background' represents the dark blue line drawn outside of the bundle region of the kymograph.

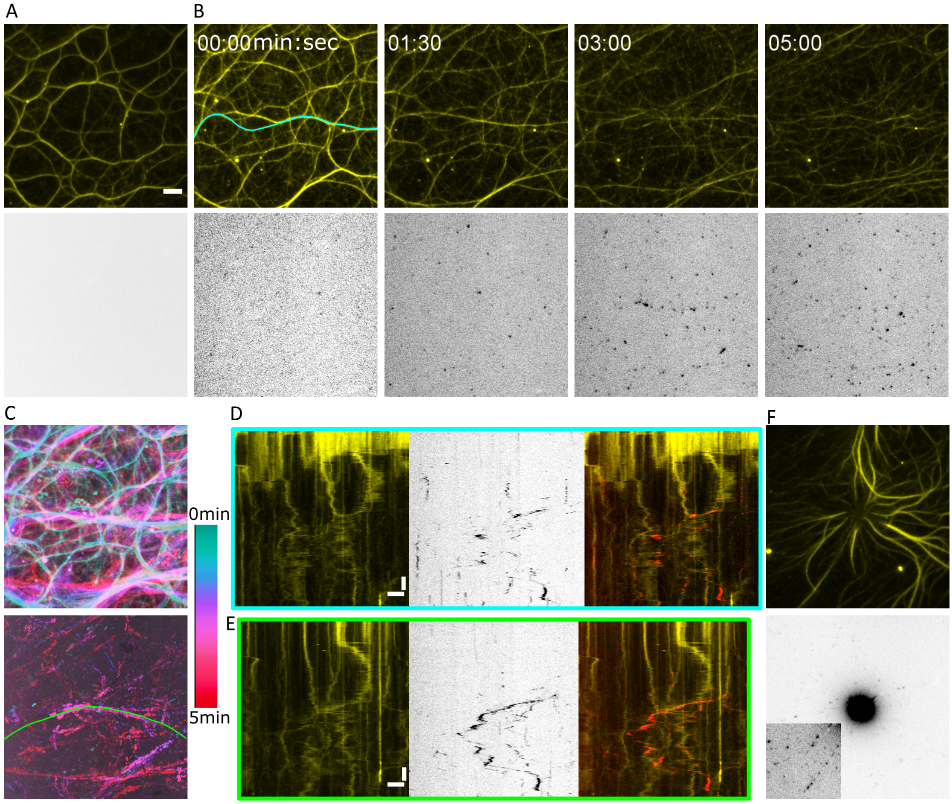

Figure 6.5. Activity of preformed muscle myosin-2 filaments on methylcellulose-bundled actin filaments. A. Representative time-lapse images series of actin bundles (yellow) after adding 25 nM myosin at t=0. B. Corresponding time lapse images of myosin (gray, inverted for improved contrast). Time is denoted as min:sec in the top left of each actin image. Scale bar is 5μm. Cyan line in the 0:00 min actin image represents the line used to make the kymograph in D. C. Time-colored projection of the timelapse from B showing how the actin bundles moved and deformed (top); and the regions in which myosin moved (bottom). Green line shows the line used to build the kymograph in E. D. Kymographs of the cyan line in B showing how the bundle observed at time 0:00 moves due to the myosin activity. E. Kymograph of the green line showing how the myosin moved along the actin bundles. Horizontal scale bar is 5μm. Vertical bar is 25 seconds. F. Asters formed by the activity of the myosin, 10 minutes after. The inset in the bottom left is a contrast-enhanced part of the image to show myosin on the actin bundles moving towards the center of the aster.

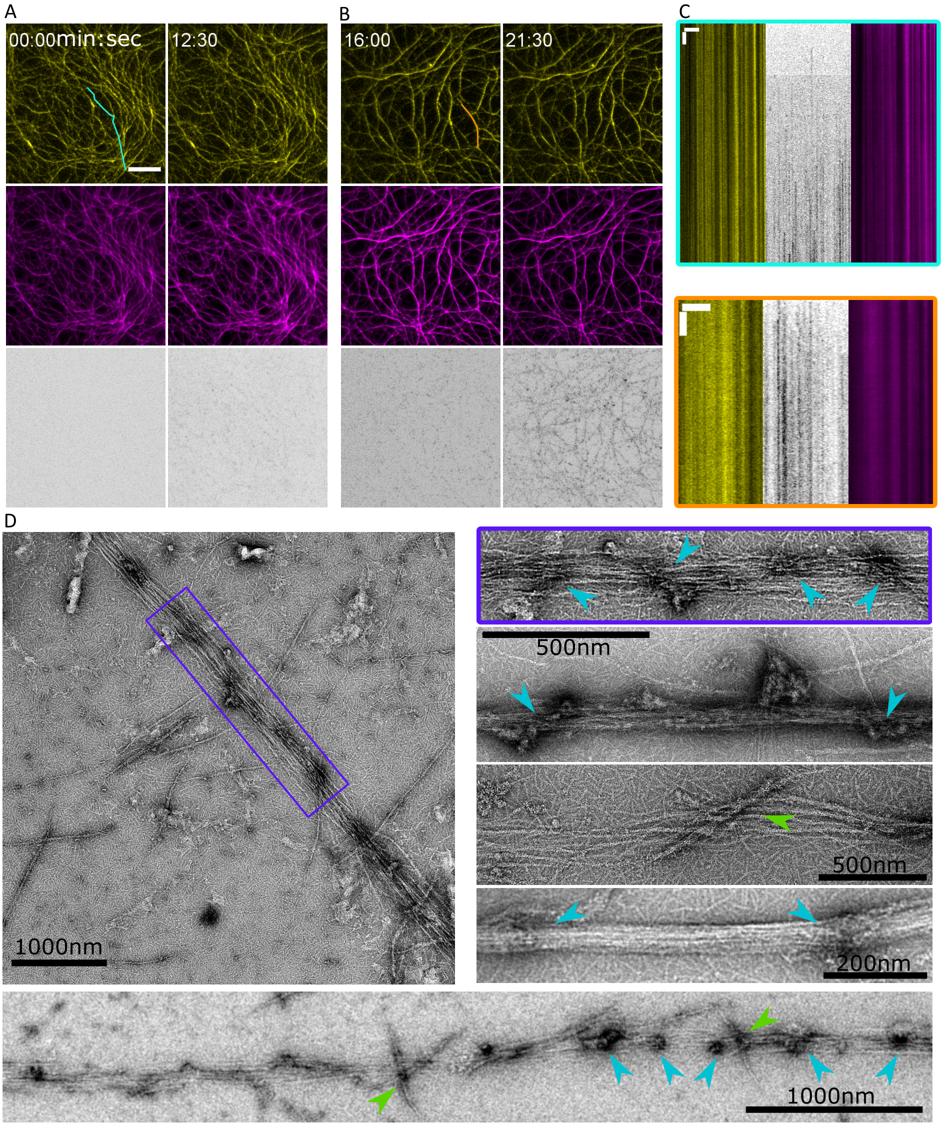

Figure 6.6. Activity of preformed muscle myosin-2 filaments on actin filaments bundled by 300nM septin octamers. A and B. Representative time-lapse image series of assembled myosin (gray, inverted for enhanced contrast) interacting with actin (yellow) bundled by 300nM septin octamers (magenta). Time is denoted as min:sec in the top left of each actin image. Panel A shows same region as in Figure 6.3, while panel B shows a different field of view for the same sample. Scale bar is 10µm. Cyan and orange lines in the 00:00 and the 16:00 images of A and B, respectively, represent the lines used for the kymographs in panel C. C. Kymographs showing myosin binding to septin-actin bundles and not moving for the cyan line in A (top) and orange line in B (bottom). Horizontal scale bar is 5µm. Vertical bars are 40sec. D. TEM images of preformed myosin filaments interacting with septin-actin bundles. Top-left: overview. Top-right and bottom:close ups. Top-right shows a close up of the boxed region on the top-left image. Septin-actin bundles present darkened regions as indicated with the cyan arrowheads. Some myosin filaments can also be seen on top of the bundles, as indicated with green arrowheads.

6

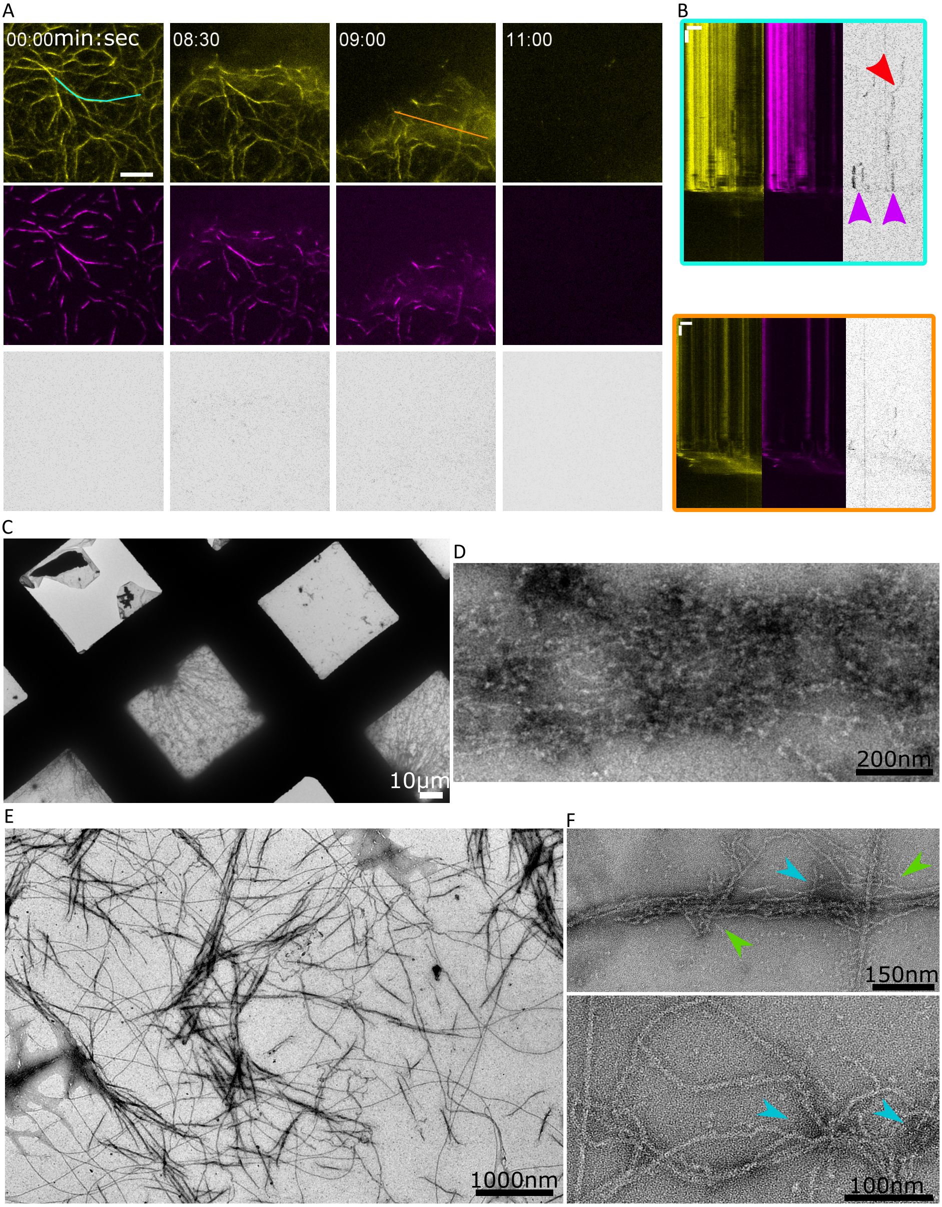

Figure 6.7. Activity of preformed muscle myosin-2 filaments on actin filaments bundled by 10nM septin octamers. A. Representative time-lapse image series of myosin filaments (gray, inverted for enhanced contrast) interacting with actin (yellow) bundled by 10nM septin octamers (magenta). Time is denoted as min:sec in the top left of each actin image. Scale bar is 10µm. Cyan and orange lines in the 00:00 and the 9:00 images represent the lines used for the kymographs in B. B. Kymographs of the cyan (top) and orange (bottom) lines in A. Red arrowhead indicates mobile myosin, while purple arrowheads indicate immobile myosin. Horizontal scale bars are 5µm. Vertical bars are 40sec. C. Overview of the TEM grid showing the formation of asters. D. Close up of filaments emanating from the asters. E. Overview image of a different region of the same TEM grid as in panel C, where myosin did not form asters. F. Close up of a thin bundle (top) and of unbundled actin filaments (bottom), showing darkened regions (cyan arrowheads) and myosin filaments (green arrowheads) on top of the actin structures, in a aster-free region.

6.3. Discussion

In this chapter we aimed at using a minimal cell-free system to study how septins may regulate actomyosin contraction in absence of regulatory accessory proteins. We first investigated the actin bundling ability of human septin hexamers and octamers. We used TIRF microscopy and TEM to image co-polymerized septin/actin bundles. We found that both septin hexamers and octamers bind and bundle actin filaments. These bundles were often curved, as described before for fly septin hexamers [101] and human septins [102]. TIRF images showed that the bundles formed an interconnected network. TEM images mostly showed isolated bundles, consisting of closely spaced parallel filaments. Bundles formed at high (800nM) concentrations of septin complexes frequently split into thinner septin-actin bundles at their ends, explaining the interconnectivity of the network seen by TIRF. The extensive sample handling required for TEM sample preparation likely disrupted these connections, resulting in isolated bundles in TEM images

Interestingly, septin octamers displayed a higher bundling ability than hexamers. With TIRF microscopy, we observed septin-actin bundling and the formation of interconnected networks starting at a concentration of 100nM for octamers, compared to 500nM for hexamers. With TEM, only the octamers could make long-interconnected bundles at 300nM, while hexamers at the same (oligomer) concentration rarely formed bundles. One potential explanation could be that septin octamers, being longer (32nm [149]) than hexamers (24nm [82, 83]), could potentially bind more stably to actin filaments. In case all septin subunits contribute equally to actin binding, the bundling capacity should be equal for octamers and hexamers for an equal total concentration of septin subunits. However, we observe that septin octamers at 100nM, corresponding to 800nM monomers, can bundle actin better than 300nM hexamers, corresponding to 1800nM monomers. Therefore, the different lengths of the two types of septin complexes alone cannot explain the observed difference in bundling ability. This suggests that, SEPT9, a SEPT3 subfamily member unique to the octamers, enhances the bundling capacity of octamers by either bringing a unique actin binding sequence or by changing the physico-chemical properties of the complex. This idea is consistent with previous research that showed that the N-terminus of SEPT9 can bind and bundle F-actin [130], although we note that this research was carried out with SEPT9 monomers and fragments thereof. We found by TEM that actin/septin bundles contained ~4nm wide filaments consistent with the expected width of septin filaments, that were clearly longer than single septin complexes. Silva Martins et al. [144] showed that on actin stress fibers, septin octamers likewise form filaments. Future work will need to reveal the actin binding domain of septin. Currently, only the microtubule binding site (in Chapter 3 and [103]) and the Borg3 binding site [89] of septin oligomers are known.

Time-lapse imaging revealed that septins nucleate bundles at places where actin filaments are in close proximity, and the bundles then elongate from this point by further recruitment of septins. At highest septin concentrations tested (300 and 100nM), bundling was complete, while at low septin concentration (10nM), free actin filaments were left between the septin-actin bundles. This result was again recapitulated by TEM imaging, since at 300nM, all hexamer-actin bundles and some octamer-actin bundles opened up and split into single actin filaments at their ends. We could observe this splitting even at concentrations where the bundling was complete according by TIRF (300nM octamers). This is probably due to the handling process that leads to the breakage of the network, as described above.

Interestingly, TIRF imaging revealed that after the bundles are formed, the signal of actin remains constant while the signal of septin increases, indicating that septin is accumulating on the bundles. We examined the width of the filaments within the septin-actin bundles imaged by TEM. We found that, on average, all filaments were thinner than actin filaments and closer in width to septin filaments. For bundles formed in presence of hexamers, we only detected filaments with a width of 4 nm, corresponding to the expected width of septin oligomers [83, 102]. In contrast, the width of the filaments in the octamer-actin bundles had a broader distribution composed of some filaments with a similar width as septin filaments, a few filaments with a width similar as actin filaments (~9nm), and a majority of the filaments with an intermediate width (~5-7nm). This intermediate width is in between the width of a single septin filament and that of an actin filament or a SEPT2-SEPT2-mediated paired filament (~13nm [208]). This wider distribution can be explained by the presence of actin filaments or septin paired filaments on the exterior of the octamer-actin bundles together with single octamer filaments. An actin filament is a double helix [306] of ~10nm in diameter, whereas an octamer paired filament has a cross-section of ~13nm and measures only ~4nm in thickness, forming a flat structure. We speculate that the rotation of the paired filaments towards the center of the bundle hides part of the paired filament, showing a thinner apparent width on TEM images, which would not be the case for the more symmetric actin filaments. Due to the time-dependent accumulation of septin octamers observed in our timelapse experiments, and the fact that only septins appear to be present on the exterior of the hexamer-actin bundles, we think that it is more likely that single and paired octameric filaments, and not actin filaments, are found on the exterior of the octamer-actin bundles. However, we have no direct proof. To test whether actin filaments and septin filaments are indeed segregated in this way, cryoEM together with tomography is needed to resolve the 3D structure of the septin-actin bundles. To definitively distinguish septin from actin in the bundles, chemically specific labeling is needed, either by immunolabeling on EM or or by superresolution fluorescence microscopy with septin and actin tagged with distinct dyes.

6

In order to understand the impact of septin-mediated bundling on myosin-driven contraction, we next performed contraction assays. For this, we added preformed muscle myosin-2 thick filaments to preformed F-actin filaments that had been previously incubated with septin octamers at a high (300nM), intermediate (100nM), or low (10nM) concentration, and imaged them with TIRF microscopy and TEM. At high and intermediate septin octamer concentration, we observed that myosin filaments did bind to the septin-actin bundles, but did not move along them. The TEM imaging showed a unique pattern of darkened regions on both septin-actin bundles and septin-only bundles, only observed when myosin filaments were present. Occasionally, myosin filaments were found buried in-between bundle-forming filaments. All this evidence, together with previous work showing that SEPT2 can directly bind myosin [121], strongly suggests that septin is indeed able to interact with myosin. The use of a lower concentration of septin (10nM) leaded to a much lower density of septin-actin bundles. In this case, myosin did move along actin filaments and remodeled the network into asters, suggesting that in this case myosin can directly bind actin. However, this contraction occurred at a lower speed than for the septin-free control.

Overall, we observe a non-monotonic effect of septins on the contractility of actin networks. A similar non-monotonic effect has also been observed for actin crosslinker proteins. There is a region of optimal crosslinker concentrations where myosin can contract actin *in vitro* [290, 304, 307–311] and in cells [312]. Thus, if septins primarily acty as crosslinkers, at high and intermediate septin octamer concentrations (300nM and 100nM), the network may be too stiff for myosin to contract it, whereas lower septin octamer concentration (10nM) may be more optimal for contraction. However, septins introduce additional complexities. First, they form filaments that co-assemble with actin filaments, unlike conventional actin crosslinker proteins. Second, they have the ability to bind myosin filaments. Thus we envision a scenario where septins modulate contraction by different mechanisms depending on their concentration, as illustrated by Figure 6.8. In the absence of septin-mediated crosslinking, myosin filaments are able to bind and move along actin filaments, resulting in local formation of asters [290] (Fig. 6.8A). When septins are added at low concentration, they crosslink the actin network and thus increase network connectivity (Fig. 6.8B). This function resembles that reported for conventional actin crosslinkers, except that in this case, myosins will be immobilized in case they bind to a septin-covered actin bundle. Septin-mediated crosslinking causes the resulting forces to be transmitted over long distances, promoting long-range contraction. In contrast, when septins are present at high concentration, they will bundle the actin filaments, creating septin-covered bundles that immobile myosin (Fig. 6.8C).

6

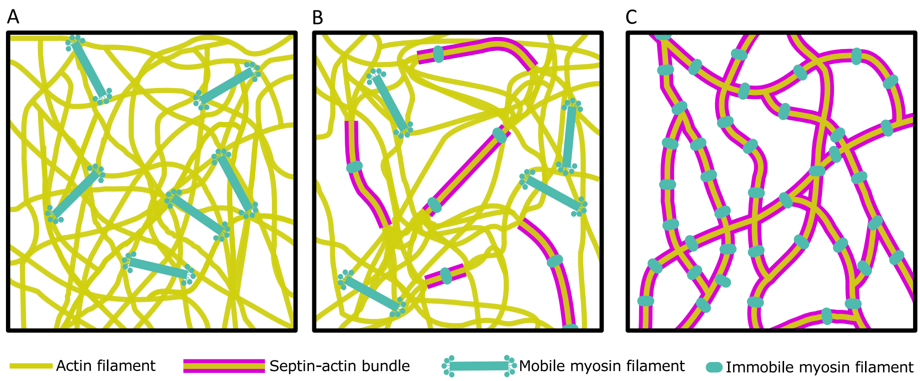

Figure 6.8. Proposed mechanism to explain how septin octamer-mediated actin crosslinking can tune the activity of myosin in a concentration-dependent manner. A. In the absence of septin, myosin can bind and move along actin filaments, causing local contraction at high enough myosin concentration. B. At low concentration, septin can act as a crosslinker that promotes myosin-driven actin contraction by enhancing network connectivity. On septin-covered actin bundles, myosins are immobilized. C. At high concentrations, septin completely bundles the actin and immobilizes the myosin on the bundles, inhibiting contraction.

In this chapter, we found that septin directly bind and polymerize on septin-actin bundles. This has been also observed in cells [144], but in that case it was unclear whether they bind directly or require an accessory protein. We also found that septins have a non-monotonic effect on myosin activity, permitting contraction at low concentration, while inhibiting contraction at higher concentrations. This is in contrast with previous research in cells that found that septins promote myosin activity, although these studies did not systematically titrate the septin concentration but compared wild type and septin knock-down situations [109, 121–124]. Most of the research on the interplay of septin on acto-myosin structures has been done in non-muscle cells. As their own name describes, non-muscle cells use non-muscle myosin-2 instead of muscle myosin-2. Non-muscle myosin-2 molecules form minifilaments composed of tens of myosin motors [295] whereas muscle myosin molecules form thick filaments consisting of hundreds of motors [296]). The fact that these myosins have different properties might contribute to the contradiction between our *in vitro* work versus work on in cells. Another factor different from our *in vitro* assays is that septins may exert additional contraction-promoting effects, for instance by scaffolding kinases [121] and recruiting other accessory proteins. To resolve how septin-actin and septin-myosin interactions play out in cells, the *in vitro* experiments should hence be repeated in the future with non-muscle myosin-2.

6.4. Materials and methods

6.4.1. Proteins

All chemicals were obtained from Sigma Aldrich unless specified otherwise.

Septin

Human septin oligomers were purified and their quality was checked as detailed in chapter 2. We used septin hexamers with a subunit order of SEPT2-SEPT6-SEPT7-SEPT7-SEPT6-SEPT2 and septin octamers with a subunit order of SEPT2-SEPT6-SEPT7-SEPT9_i1-SEPT9_i1-SEPT7-SEPT6-SEPT2. Septins were fluorescently tagged with msfGFP on the C-terminus of SEPT2. For purification, SEPT2 contained a his_6-tag at its N-terminus, and SEPT7, for hexamers, or SEPT9, for octamers, contained a Strep-II-tag at its C-terminus.

Actin

Unlabeled and Atto-647 labeled rabbit skeletal muscle actin were purchased from Hypermol (Cat. # 8101-03 and 8158-02, respectively). Following the supplier instructions, we dissolved the lyophilized actin to a final concentration of 23.8μM in MilliQ water, resulting in a final buffer composed of 2mM Tris pH 7.8, 0.4mM ATP, 0.1mM Dithiothreitol (DTT), 0.08mM $CaCl_2$ and 0.2% unspecified disaccharides. After a 2h incubation on ice, the solution was cleared by centrifuging at 148,000g for 1h. The actin concentration remaining after clarification was checked by UV absorption measurements at 290nm using a Nanodrop 2000c spectophotometer (actin's extinction coefficient ϵ_{290}=0.617 $Lmg^{-1}cm^{-1}$ [313]). The G-actin solution was aliquoted, snap-frozen and stored at -80℃ until use. Before use, actin aliquots were quickly thawed and stored on ice for up to two weeks. Aliquots were incubated for at least 2h on ice to depolymerize any F-actin [314].

Muscle Myosin-2

Skeletal muscle myosin-2 was purified in house from psoas rabbit muscle tissue following a previously described protocol [315]. The entire procedure was done either in a cold room, on ice, or in a fridge, to prevent protein degradation. Briefly, after removing residues of connective tissue, muscle tissue was minced using a meat grinder. Myosin was then extracted by mechanically agitating the mince for 15min in a high ionic strength phosphate buffer (150mM KH_2PO_4 pH 6.5, 300mM KCl, 20mM EDTA, 5mM $MgCl_2$, 1mM ATP) and subsequent filtering of the mince through a cheese cloth. Myosin, actin, and actin binding proteins were precipitated by slowly diluting the eluate with MilliQ water until a concentration of ~30mM KCl was obtained. Removal of contaminant proteins was achieved by two sequential dialysis steps against buffers of decreasing KCl concentration (from 1M to 600mM on the first step and from 3M to 600mM in the second step), alternating with precipitation in MilliQ water and following resuspension. Finally, myosin was stored at -20℃ in a buffer containing 25mM KH_2PO_4 pH 6.5, 300mM KCl, 0.5mM DTT, and 50v/v% glycerol.

Myosin was fluorescently labeled using N-hydroxysuccinimide (NHS) ester amide reactive DyLight550 (ThermoFischer Scientific, Cat. # 10387779) following the supplier's protocol with typical labeling ratios (determined by UV/vis spectroscopy) of 1-2 dyes per protein. Labeled myosin was stored in the same buffer and at the same temperature as unlabeled myosin. Just before use, 50μL of a mixture of 95mole% unlabeled and 5mole% labeled myosin was dialyzed for at least 2h at 4℃ against myosin buffer (20mM Tris pH 7.4, 300mM KCl, 4mM $MgCl_2$, and 1mM DTT) using a 20kDa cutoff 0.5mL slide-A-lyzer dialysis cup (Thermo Fisher scientific, Cat. # 88402) to remove the glycerol. The protein was then centrifuged for 20min at 148,000g to pellet any aggregated protein. The protein concentration was then measured by UV absorption at 280nm (extinction coefficient myosin ϵ_{280}=0.249μM−1cm−1 [315]).

6.4.2. Preparation of passivated flow channels

Flow channels were prepared as detailed in chapter 3. Briefly, 2x20mm parafilm strips were sandwiched, separated by ~3mm, between a base piranha cleaned glass slide and coverslide. The parafilm was then melted at 120℃ to fix the flow channel. Once the channels had cooled down, as shown by the parafilm turning opaque again, we passivated the surface. We either formed an inert Supported Lipid Bilayer (SLB) composed of 100% DOPC lipids (see Cchapter 4) or performed subsequent incubations with PLL-PEG-biotin and κ-casein (see Chapter 3). As soon as liquid were introduced into the flow channels, these were left in a humid chamber to avoid drying. We used a 100-eppendorf tube -20 freezer box where the holes were filled with water and the devices were placed on top of small PDMS squares to avoid direct contact of the device with the water.

6.4.3. Preparation of passivated imaging chambers

Passivated chambers for fluorescence micoscopy were prepared by sticking a pre-cut eppendorf tube to a coverslide. First, we cut the lid and the bottom of a 500μL eppendorf. We then used 2-component epoxy glue (Bison, Cat. # 6305950) to stick the eppendorf tube, from the side where the lid was attached, to a base piranha cleaned (see chapter 3.4) coverslide. Once the glue was set, we immediately passivated the surface by subsequent incubations with PLL-PEG-biotin and κ-casein (see chapter 3.4). To do so, we first incubated the channels with 40μL of 0.2 mg/mL Poly(L-lysine)-graft-biotinylated PEG (SuSoS, Cat. # CHF560.00) in MRB80 buffer for 10 minutes, and next washed the chambers with

200μL of F-buffer (20mM Tris pH 7.4, 2mM $MgCl_2$), 50mM KCl, and 1mM DTT). After the final wash, 20 μL of the remaining solution were removed and 1mg/mL κ-casein (Sigma-Aldrich, Cat. # C0406) in F-buffer was added. After incubation for at least 10 minutes, we washed twice with 200μL F-buffer. Just before loading the samples, 20μL of solution was removed. We then added the sample in F-buffer to the pre-existing volume of F-buffer, diluting the sample. We therefore prepared the sample stock solution at double the concentration of all components not present in F-buffer. The imaging chambers were stored at all times in the same type of box as the flow channels.

6.4.4. Septin-actin bundle formation for TIRF microscopy

Septin-actin bundles were formed by either co-polymerizing septin oligomers and G-actin or by polymerizing septin oligomers in the presence of pre-polymerized F-actin, as described in each individual subsection of the results.

For all experiments, we first prepared a mix of labeled and unlabeled protein. For actin, we mixed 90% unlabeled skeletal muscle rabbit actin with 10% ATTO-647 skeletal muscle rabbit actin in G-buffer (2mM Tris pH 7.8, 0.2mM $CaCl_2$, and 1mM DTT) to a total G-actin concentration of either 5μM (for experiments with flow channels) or 10μM (for experiments with passivated imaging chambers). For septin, we mixed 90% unlabeled septin complexes with 10% msfGFP septin complexes in septin buffer (20mM Tris pH 7.4, 2mM $MgCl_2$, 300mM KCl, and 1mM DTT) to a concentration of either 6 times (for experiments with flow channels) or 12 times (for experiments with passivated imaging chambers) higher than the desired final concentration.

To co-polymerize septin oligomers with G-actin, we followed a process similar to the one described in chapter 2.2. Briefly, we prepared a 5x septin polymerization buffer (5xSPB) containing all the necessary components except the proteins. This 5xSPB contains (83.3mM Tris-HCl pH 7.4, 8.3mM $MgCl_2$, 5mM DTT, 5mM GTP, 5mM ATP, 0.75w/v% Methylcellulose, 5mM Protocatechuic acid (PCA), 5mM 6-hydroxy-2,5,7,8-tetramethylchroman-2-carboxylic acid (TROLOX)) for the flow channels and (83.3mM Tris-HCl pH 7.4, 8.3mM $MgCl_2$, 10mM DTT, 10mM GTP, 10mM ATP, 10mM PCA, and 10mM TROLOX) for the imaging chambers. Note that for the imaging chambers, the methylcellulose was not included in the 5xSPB. Then, in this specific order, we mixed MilliQ water (enough to top up to the final desired volume), 20% 5xfluoSPB (1:5 dilution), 0.05μM (for flow channels) or 0.1μM (for imaging chambers) Protocatechuate 3,4-Dioxygenase (PDC, sigma-Aldrich, Cat. # P8279), 0.3% methylcellulose (only for the imaging chambers), 20% Actin mix, and 16.67% Septin mix (1:6 dilution). This mix was immediately inserted into the flow channels or 1:1 diluted into the imaging chambers containing F-buffer (see above). This gives a final buffer composition of 20mM Tris pH 7.4, 2mM $MgCl_2$, 50mM KCl, 1mM DTT, 1mM GTP, 1mM ATP, 0.15% methylcellulose, 1mM PCA, 0.05μM PCD, 1mM TROLOX, 1μM actin and a final concentration of septin complexes in the range of 10nM to 800nM, as specified in the Results. We typically prepared 10μL for the flow channels and 20μL for the imaging chambers. PCA and PCD are oxygen scavengers used to protect the sample from bleaching and from photodamage [316, 317]. TROLOX inhibits blinking [318]. Methycellulose is a crowding agent that crowds the actin filaments/bundles to the surface for TIRF imaging. The final mixture was then immediately added into the flow channels or the imaging chambers to avoid disrupting the bundled network. The flow channels were sealed with Dow Corning® high-vacuum silicone grease (Sigma-Aldrich, Cat. # Z273554), while the imaging chambers were closed with their cut lids to avoid drying.

To pre-polymerize actin and then add the septin oligomers, we followed a similar approach. We mixed the volumes specified above of MilliQ water, 5x master buffer, PCD, methylcellulose, and the actin mix. We incubated this mixture for at least 1h to allow the actin to polymerize and then added the septin mix. Following this process, the final buffer specified above is only completed after adding the septin. Therefore, the actin is polymerized in a slightly different buffer composed of 20mM Tris pH 7.4, 2mM $MgCl2_2$, 0.72mM DTT, 1.2mM GTP, 1.2mM ATP, 0.18% Methycellulose, 1.2mM PCA, 0.06μM PCD, 1.2mM TROLOX, and 1.2μM actin.

6.4.5. Septin-actin bundle formation for TEM

To prepare septin-actin bundles for TEM imaging, we prepared the samples in the same way as for the TIRF flow channels but did not include PCA, PCD, TROLOX and methylcellulose. In this case, before adsorbing the protein onto the TEM grid, the samples were mixed and incubated in an eppendorf tube. To prepare the sample, a TEM grid (QuantiFoil, C support Cu400) was first glow discharged (GloQube, Quorum Technologies Ltd.). During the glow discharging, a parafilm strip was first laid out on a clean surface. Next, two 20μL drops of F-buffer, one 10μL drop of MilliQ water, and one 4μL drop of 2%uranyl acetate were carefully pipetted onto the parafilm strip, one on top of the other, creating a column of drops. This process was repeated in parallel to create multiple columns of drops. After the glow discharging, 5μL of sample was pipetted onto the glow discharged TEM grid and incubated for 1min. After the incubation, we blotted the sample drop (avoiding complete drying) by carefully absorbing the liquid with a filter paper from the side, washed twice with F-buffer by placing the EM grid on one of the F-buffer drops and blotting, washed once with the MilliQ water drop, and stained by picking up the 4μL drop of 2% uranyl acetate. The drop of uranyl acetate was incubated on the grid 30-45 seconds and the sample was blotted to dryness. This sample was then ready to image.

6.4.6. Timelapse bundling assays

To image how septin bundled actin, we polymerized actin alone in an imaging chamber as described above. We then imaged the actin to check that it had properly polymerized, crowded to the surface, and not bundled by methylcellulose [301]. Next, we added the septin oligomers and started imaging as soon as possible. We imaged as fast as the microscope allowed (1frame/sec) until the septin completely bundled the actin or for at least 15min. Microscope settings for TIRF imaging are described in section 6.4.8.

6.4.7. Myosin contraction assays

Before use, we first assembled myosin thick filaments. We made a 6-fold dilution of the dialyzed myosin monomers into F-buffer, while considering the contributions of the myosin buffer (see above), which with a 6x dilution adds 3.33mM Tris pH 7.4, 0.67mM $MgCl_2$, 0.17mM DTT and 50mM KCl to the final solution. We prepared the myosin dilution by first pre-mixing Tris pH 7.4, $MgCl_2$, DTT and MQ and then adding the myosin that came out of the dialysis. The resulting solution was incubated at room temperature for at least

30min to allow the myosin to form filaments. The final concentration of myosin in this mix is different in every experiment, due to the different concentrations coming out of the dialysis. The concentration is thus calculated by UV absorption as described in section 6.4.1.

For the myosin contraction assays, we first imaged septin-mediated actin bundling, as described before, and then added the myosin filaments. To do so, we prepared a mix of assembled myosin, ATP, creatine kinase, and creatin phosphate. This mix was prepared aiming to the addition of 50nM assembled myosin, 1mM ATP, 0.2mM creatine kinase, and 10mM creatine phosphate to volume of sample already present in the imaging chamber. We then immediately started imaging at 0.66frames/sec. Microscope settings for TIRF imaging are described in section 6.4.8.

For imaging myosin-actin samples with TEM, the samples were prepared in the same way as for TIRF imaging, but in an eppendorf tube. After incubating the myosin with the septin-actin bundles for ~3min, we deposited the samples onto TEM grids as described in section 6.4.5. TEM imaging settings are described in section 6.4.9.

6.4.8. TIRF imaging, processing, and analysis

Imaging was done using an inverted Nikon Eclipse Ti-E microscope with perfect focus system, equipped with a FRAP/TIRF Ilas ^{2} system (Gataca Systems), an oil immersion objective (Nikon Plan Apo λ 100× NA 1.45), and a EMCCD camera (Photometrics). Image acquisition was controlled using MetaMorph (Molecular Devices). We used lasers (all from Cobolt) with wavelengths of 488nm (~15% intensity, 50-100ms exposure time), 561nm (~2% intensity, 10-30ms exposure time), and 642nm (~15% intensity, 50-100ms exposure time), which were set to an angle yielding a penetration depth of ~100nm. Images were processed with FIJI [154]. The time-colored projection was made using the temporal-color code plugin of FIJI. Kymographs were built using the reslice tool of FIJI over the lines manually drawn shown in the corresponding figures.

6.4.9. TEM imaging, processing, and analysis

Imaging was done using a JEM-1400plus microscope (JOEL) equipped with a 4k X 4k F416 CMOS camera (TVIPS) and operated at an acceleration voltage of 120kV with magnifications between 100x and 60000x. Images were processed with FIJI. First, images were denoised using the "smooth" tool of FIJI, which applies a 3x3 average filter. Width measurements were taken from the non-smoothed image by manually drawing a line perpendicular to the long axis of the bundle or the filament, from the start to start of the darkened pixels in each side generated by the defocus halo on each side of the bundle or filament (Fig. S6.1C and D). If the borders were not clear, the bundle/filament was skipped.

6.5. Supplementary information

Table S6.1. Widths of filaments within septin bundles and septin-actin bundles measured in TEM images. The table shows the mean, standard deviation, and 95% confidence interval for single actin filaments, filaments within septin hexamer or octamer bundles, and filaments within septin-actin bundles with either hexamers or octamers.

	Actin	Hexamers	Octamers	Hexamers+actin	Octamers+actin
Mean (nm)	9.279	4.436	3.959	4.437	5.668
Standard deviation (nm)	1.628	0.576	0.504	2.040	1.858
Confidence interval (nm)	0.658	0.238	0.195	0.824	0.534

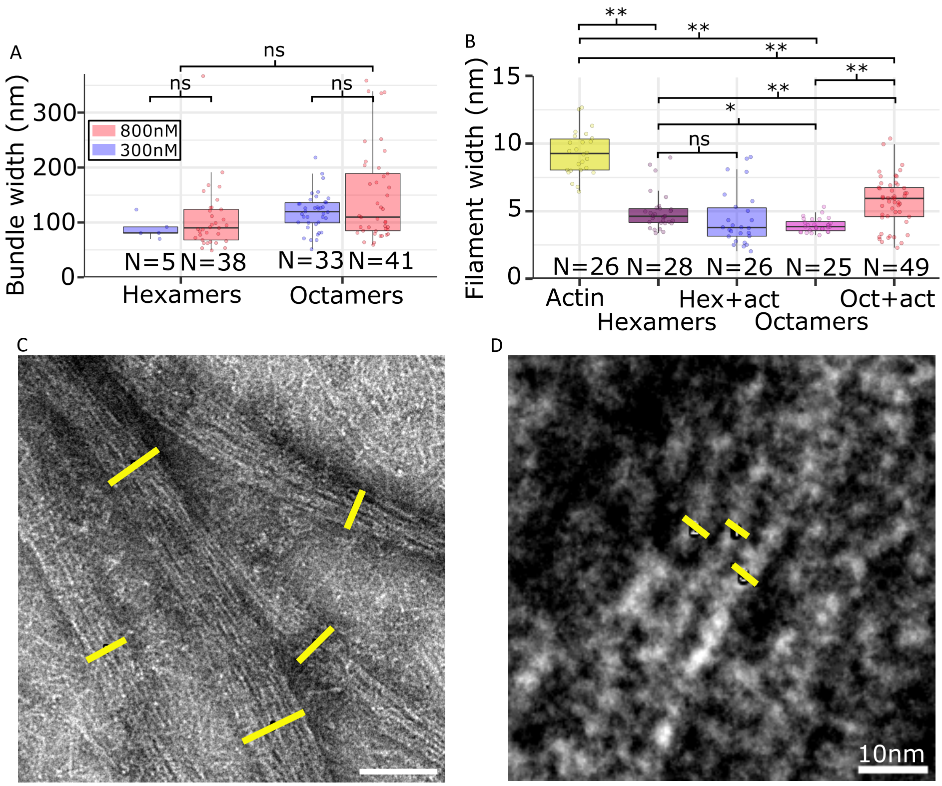

Figure S6.1. Width of septin-actin bundles and width of filaments within these bundles. A. Width of septin-actin bundles imaged with TEM as in panel C and D. The number of bundles for the 300nM hexamers condition is low due to the scarcity of bundles in the sample. Results are presented as box and whiskers plots superposed with individual data points including outliers (red: actin co-polymerized with 800nM septin complex, light blue: actin co-polymerized with 300nM septin complex). Two-tailed t-test with p-values adapted to use the Bonferroni correction (* p<0.0083, ** p<0.00083, ns=non-significant). Clearly defined bundles from 5-8 images taken at 1,000-30,000x were measured per condition from at least 2 independent replicates. B. Width of single actin filaments (formed in the absence of any other protein), of filaments in either hexamers-only or octamers-only bundles, and of filaments in copolymerized septin and actin. Results are presented as box and whiskers plots superposed with individual data points including outliers (yellow: actin filaments, purple: hexamers bundles, light blue: actin-hexamers bundles, pink: octamer bundles, red: actin-octamers bundles). Two-tailed t-test with p-values adapted to use the Bonferroni correction (* p<0.005, ** p<0.0005, ns=non-significant). Clearly defined filaments from 5-8 images taken at >30,000x were measured per condition from at least 2 independent replicates. C. Representative image of a bundle (actin and 800nM septin octamers) with yellow lines displaying examples of measured bundle widths. D. Representative image of a septin-actin bundle (300nM septin octamers) with yellow lines displaying examples of measured filament widths.

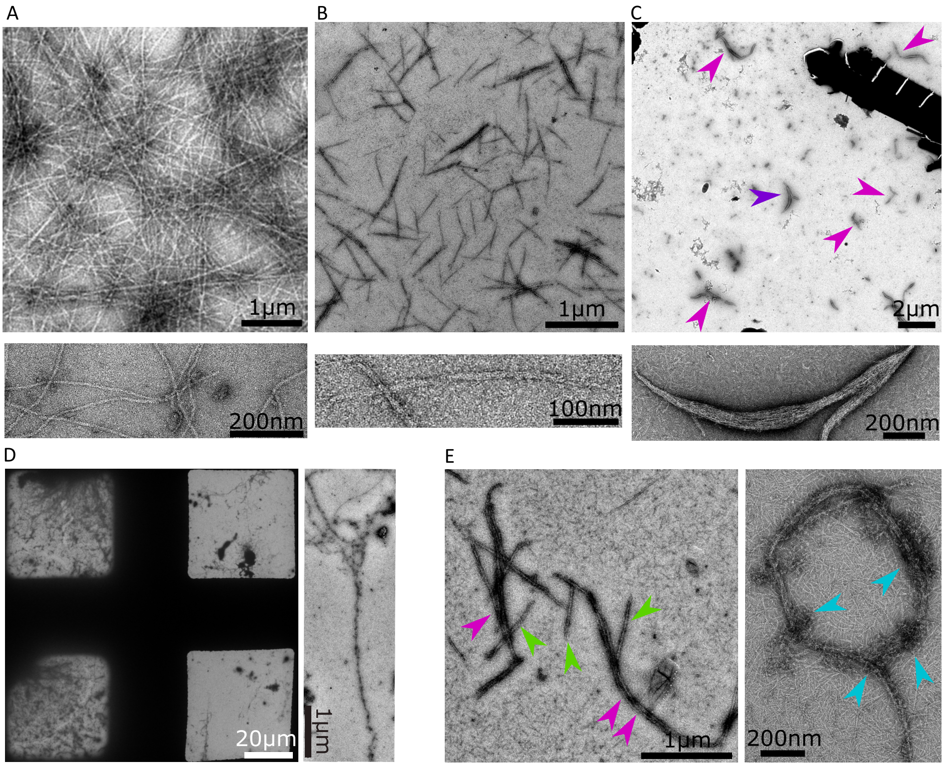

Figure S6.2. TEM images of actin filaments, preformed muscle myosin-2 filaments, septin bundles, and combinations of the myosin filaments with either actin or septin bundles. A. Representative images of 1µM F-actin. The top image shows an overview, while the bottom image shows a magnified region with a lower density of filaments. B. Representative images of preformed muscle myosin-2 filaments. The top image shows an overview, while the bottom image shows a magnified view of a single filament. C. Representative images of polymerized septin octamers at 300nM. The top image shows an overview of the sample with many septin octamer bundles, as highlighted by the pink arrowheads. The bottom image shows a magnified view of the bundle indicated by the purple arrowhead. The large dark structure in the top-right is a uranyl acetate crystal. D. Representative images of a sample of F-actin incubated for 15min with muscle myosin filaments. The left image shows an overview of the sample. In the two squares on the left, radial structures resembling asters can be seen. On the left, actin filaments not forming a radial structure can be seen. Right image shows a magnified view of actin filaments on the periphery of the radial structure. D. Representative images of a sample of septin bundles incubated for 3min with muscle myosin filaments. The left image shows several septin bundles (magenta arrowheads) coexisting with myosin filaments (green arrowheads). The image on the right shows a magnified view of a single septin bundle that contains several darkened regions (cyan arrowheads).

6

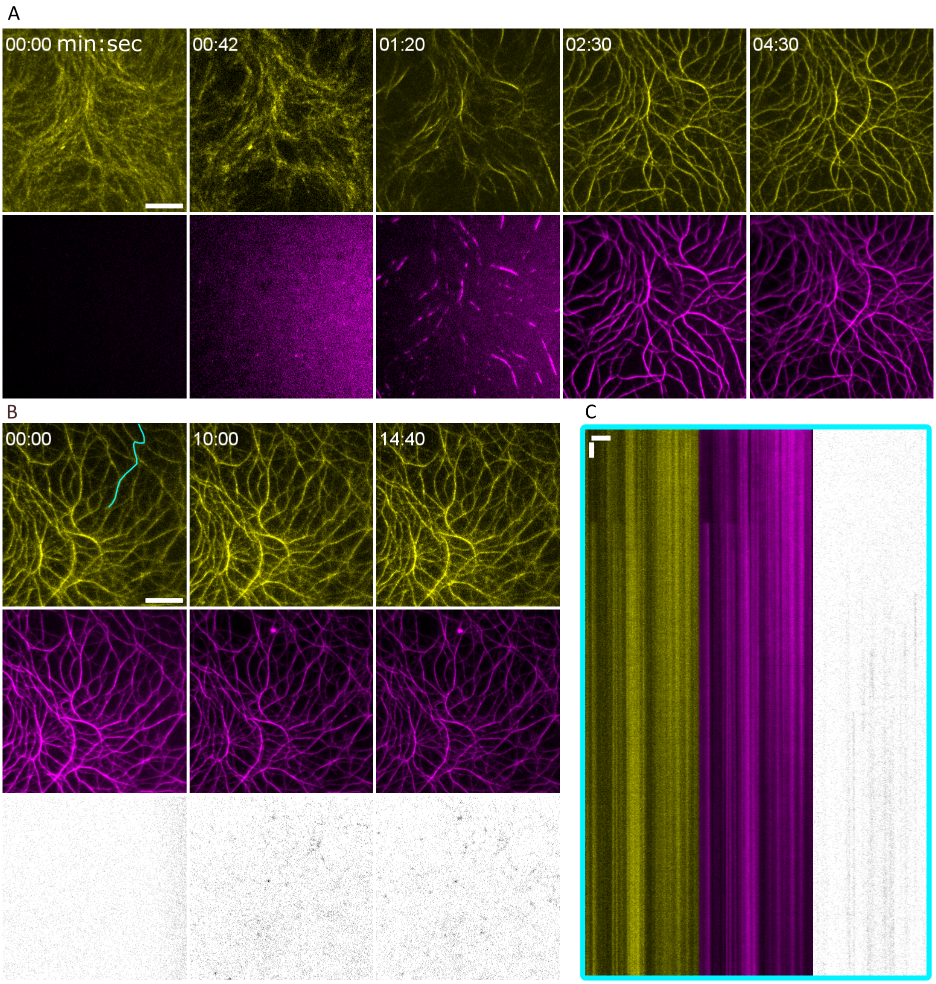

Figure S6.3. Bundling of pre-formed actin filaments by 100nM human septin octamers and further activity of myosin filaments on them. A. Representative time lapse image series of 100nM septin octamers (magenta) bundling F-actin (yellow). Time is denoted as min:sec in the top left of each actin image. Scale bar is 10µm. B. Representative time lapse image series of myosin filaments (gray scale, inverted to increase contrast) interacting with actin (yellow) bundled by 100nM septin octamers (magenta). C. Kymograph of the cyan line in B, showing the accumulation of immobile myosin filaments on the septin-actin bundle. Horizontal scale bar is 5µm. Vertical bar is 25 seconds.

Acknowledgements

We thank Jeffrey den Haan for his help with protein purification. Lucia Baldauf for her help on designing some experiments, knowledge on the use of actin and myosin, and discussion. Marcos Arribas Pérez, SaFyre Reese, and Elise Perton for assistance during some fo the experiments. Laurens Dijkstra for early septin-actin bundling experiments. Manos Mavrakis for useful discussions about the data.

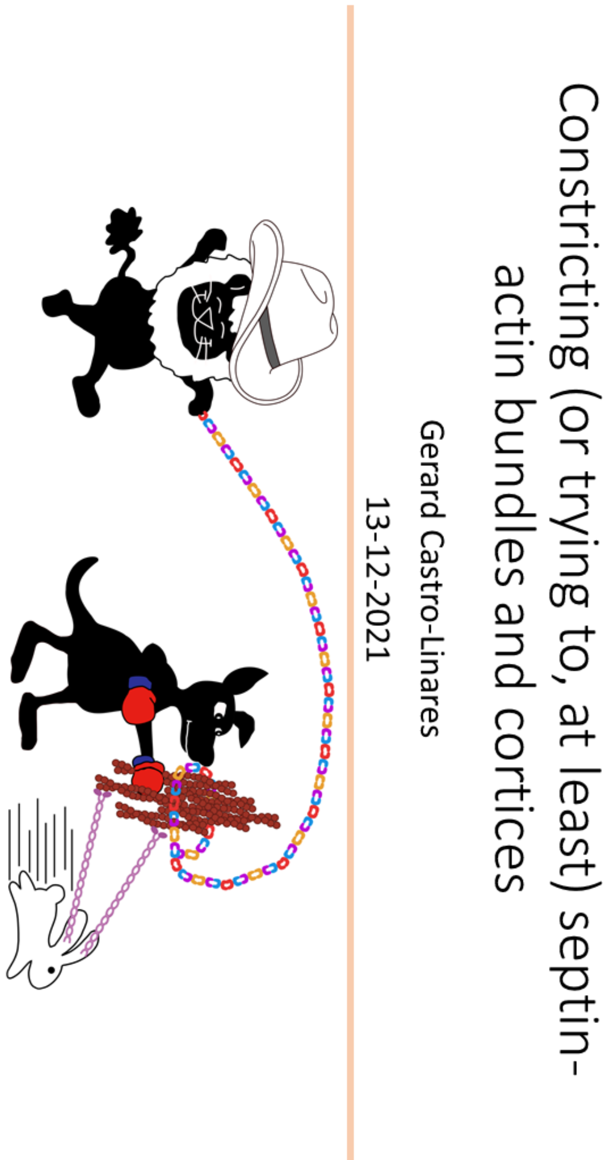
Constricting (or trying to, at least) septin-actin bundles and cortices
Gerard Castro-Linares
13-12-2021

Chapter 7

Septins anchor actin filaments and bundles to lipid membranes

Building a synthetic cell is becoming not only an interesting engineering challenge, but also a toolbox to understand the basic mechanisms that govern the cell's functioning. One important aspect is the support of the cell membrane, which needs to withstand internal and external mechanical stresses, while also needing to undergo regulated shape changes during cell division and migration. In animal cells, mechanical support and cell reshaping are partly controlled by the cell cortex, a network based on actin filaments organized by actin-binding proteins that reinforces the membrane but can also actively drive changes in membrane shape. In this context, building a synthetic actin cortex can contribute to understanding the minimal components needed for its functions in cell membrane support. In this Chapter, we explore the possibility of building a synthetic actin cortex via the interaction of septins with both lipid bilayers and actin. We found that septin is indeed able to anchor actin filaments and bundles thereof to supported lipid bilayers and giant vesicles, forming a cortex-like structure. Adding the actin nucleator protein Arp2/3 led to the formation of membrane-bound asters.

This study was designed in close collaboration between Gerard Castro-Linares and Marcos Arribas Pérez. Experiments and analysis were performed by Gerard Castro-Linares and Elise Perton. Elise Perton worked under the joint supervision of Gerard Castro-Linares and Marcos Arribas Pérez. The supported bilayer part of this Chapter has been partly (Fig. 7.1) published in *Martins et al. Human septins organize as octamer-based filaments and mediate actin-membrane anchoring in cells, JCB, 2023*

7.1. Introduction

Building a synthetic cell from the bottom-up has emerged as a powerful approach to investigate the fundamental principles underlying cellular life. By deconstructing the complexity of real cells into a minimal set of components, this approach enables the systematic dissection of the roles of individual components and their interactions in cell function [10, 11]. This reductionist approach allows researchers to uncover new principles of cell organization, regulation, and behavior, and to test hypotheses that are difficult to address in real cells due to their complexity and heterogeneity. The basic toolbox for synthetic biology is to develop cell-inspired modules that drive different functions of the cell [319], that are later combined to build a fully functional synthetic cell.

One important function of cells that must be mimicked in synthetic cells is their ability to control their shape and mechanical stability, and to engineer morphogenetic processes such as cell division [23, 32, 320]. The shape and mechanical properties of cells are essential for their proper function, since they allow cells to perform division, migration, phagocytosis, and many other crucial functions. Bacterial and plant cells are characterized by their rigid and defined shapes, which are maintained by a cell wall [18–20]. In contrast, animal cells lack a cell wall and instead rely on the cytoskeleton, a dynamic network of filaments that determines cell shape and provides mechanical support [22, 23, 321]. The cytoskeleton is composed of four types of filament-forming proteins: actin, microtubules, intermediate filaments, and septins [76, 322]. In particular, the cell cortex is a specialized cytoskeleton-based structure which is responsible for maintaining cell shape and mechanical stability by actively reshaping and mechanically supporting the fragile cell membrane [47, 321]. The cortex is composed mainly of actin filaments, which are crosslinked and organized by a variety of actin-binding proteins (ABP). Important ABPs for cell shape control and mechanical stability are actin crosslinkers, that make a cohesive network of actin filaments, actin anchors, that couple the cortex to the cell membrane, actin nucleators, that define the architecture and density of the actin meshwork, and motor proteins, that actively reshape the cortex [43, 47, 323–325].

7

In order to build a synthetic cell with an actin-inspired actin network, we must select a minimum set of cortex components to be expressed from a synthetic genome inside giant unilamellar vesicles (GUV), that are cell-sized liposomes. However, the expression of multiple proteins using *in vitro* transcription-translation systems is still a challenge [326, 327]. Additionally, the fact that actin requires posttranslational modifications [328], which are present in low amounts in bacteria [329], that it is poorly soluble in bacterial lysate [330], and that it is prone to degradation by bacterial proteases [330], has made it impossible to express actin in the commonly used bacterial-based transcription-translation systems [326]. Therefore, synthetic actin cortices have instead been studied by encapsulating purified actin and ABPs inside GUVs [259, 331–338]. Different methods of actin-membrane anchoring have been pursued, including direct binding by electrostatic interactions [339, 340] or biotin-streptavidin [337, 341, 342], or indirect binding via the His-tagged actin-binding domain of anillin [334] or via integral membrane proteins coupled to ankyrin and spectrin [343]. Interestingly, two recent studies by Baldauf et al. [258, 344] used a more physiological approach where they selectively nucleated actin at the membrane using Arp2/3, which generates branched actin networks, together with a membrane-bound activator.

Compared to the physiological situation, some important simplifications were made: as activator they used VCA, a fragment of N-WASP, and for membrane binding of VCA, they tagged VCA with a His-tag that recognizes Ni-NTA lipids in the membrane. They found that these synthetic actin cortices were dynamic and able to detect membrane curvature, form membrane protrusions, and stabilize the shape of the GUV. However, anchoring via the artificial His-Ni interaction makes the system non-physiological by immobilizing the cortex anchors to the membrane, so they can move in plane, but cannot bind and unbind [345, 346].

We aim to build upon the Arp2/3-mediated actin cortex system by anchoring the actin cortex via the physiological interaction between septin, actin, and the membrane. Septins are a recently acknowledged family of cytoskeletal proteins that form nonpolar filaments via the interaction of rod-shaped septin hetero-oligomers [76]. In human cells, septins form hexamers, composed of SEPT2-SEP6-SEPT7-SEPT7-SEPT6-SEPT2, and octamers composed of SEPT2-SEP6-SEPT7-SEPT9-SEPT9-SEPT7-SEPT6-SEPT2 [87, 88]. As described in Chapter 2 and in previous literature [102, 147], we are able to purify these pre-formed oligomers by recombinant expression in *Escherichia coli*. As shown in Chapters 4 and 5, septins are able to polymerize and bind to phosphatidylserine (PS) and phosphatidylinositol 4,5-biphosphate (PIP2)-containing supported lipid bilayers (SLB) and GUVs. Chapter 6 and previous work [102] showed that septin complexes are also able to bind actin filaments, crosslinking them at low concentrations (~10nM septin octamers), and bundling them at higher concentrations (>100nM septin octamers or >500nM septin hexamers). If septins are able to mediate actin and membrane interactions at once, they could act simultaneously as a membrane-actin anchor and an actin crosslinker, fulfilling two important cortical functions. Recent work showed that septins anchor actin stress fibers to the plasma membrane in adherent cells [144], strengthening our hypothesis that septins may act as a membrane-actin anchor. Additionally, the formation of a membrane-bound septin network could provide additional mechanical support to the GUV membrane, while their ability to curve membranes might also contribute to cell shape control.

In this chapter, we explore the possibility to form a septin-mediated actin cortex for synthetic cells by bringing together our work on septin-membrane binding (Chapters 4 and 5) and septin-actin binding (Chapter 6). First, we explored whether septin is able to anchor actin to a model lipid membrane by copolymerizing septin and actin on top of SLBs and inside GUVs. We show that in both systems, a meshwork of septin-actin bundles is anchored to the biomimetic membrane systems. Then, with the aim to tune the architecture of this cortex, we add the actin nucleator Arp2/3 and its activator VCA, showing the formation of membrane-bound cortices comprised of actin asters.

7.2. Results

7.2.1. Septin complexes anchor actin filaments to flat membranes

In Chapter 6 we investigated how septin complexes crosslink and bundle actin at different concentrations on top of inert SLBs composed of 100mol% DOPC (100%PC SLB). Since these inert membranes do not interact with septins, we crowded the resulting structures to the surface with methylcellulose to enable visualization by TIRF microscopy. To investigate whether septins can anchor actin to lipid bilayers, we replicated these experiments, but now using negatively charged SLBs containing 5mol% of the septin-binding lipid PIP2 (5%PIP2 SLB) (Chapter 4 and 5, and [96]) and removing the methylcellulose to avoid crowding (Fig. 7.1A). We performed these experiments with human septin octamers at a concentration of 300 nM. Figure S7.1 shows representative images of the SLBs generated in this chapter. The small lipid clusters observed did not show any systematic effect on septin localization, as judged from comparing signal co-localization. By using TIRF, which only illuminates a shallow (~100nm) region close to the surface, we expect to observe actin only if septin is anchoring it to the surface (Fig. S7.2). Figure 7.1C clearly shows that septin and actin were bound and immobilized on top of the 5%PIP2 SLBs, while only out of focus moving structures were seen on the 100%PC SLB. This shows that septin octamers are indeed able to interact simultaneously with actin and PIP2-containing SLBs, anchoring the actin to the membrane. Additionally, to check whether septins need to polymerize on the membrane before anchoring actin, we pre-polymerized septin octamers with actin the mixture a bulk solution, and then incubated it on top of the SLBs (Fig. 7.1B). On the 5%PIP2 SLBs, we could again observe the actin on the surface while only out-of-focus bundles were seen on the 100%PC SLB (Fig. 7.1D). This finding shows that septins do not need to polymerize on the membrane first. Interestingly, though, we could observe clear differences between the two types of experiments. When septin octamers and actin were co-polymerized on the 5%PIP2 SLB, we observed a network of thinner filaments than when the septin complexes and the actin were pre-polymerized. Additionally, in the co-polymerization experiments we observed a uniform septin signal along the whole membrane surface (with occasional smaller clusters), reminiscent of human and fly septins binding SLBs (Fig. S7.2B and C, and [96] for fly septins). In contrast, in the pre-polymerization experiments, all the septin octamers were sequestered in the septin-actin bundles, indicating that once bound to the actin, the septin do not unbind and relocalize to the lipid bilayer.

To further investigate how septins anchor actin to PIP2-containing bilayers, we conducted a series of experiments where we co-polymerized 1µM actin with varying septin concentrations (10nM, 100nM, 300nM, 500nM, 800nM), now comparing septin hexamers and octamers. To promote septin-membrane binding, we included 20mol%PS in the SLBs (20%PS+5%PIP2 SLBs) (Fig. 7.2A), which enhances binding to PIP2-containing SLBs as shown in Chapter 4 and 5. At the highest septin concentration of 800nM, both hexamers and octamers bound a mesh of septin-actin bundles to the membrane (Fig. 7.2B and C, respectively). As the septin concentration decreased, we observed distinct differences between hexamers and octamers. Septin hexamers (Fig. 7.2B) could still anchor actin bundles to the membrane at 500nM, but no septin could be observed on these bundles. At 300nM, only a few actin filaments were observed on the SLB. At even lower concentrations of 100nM and 10nM, we could not observe any surface-bound actin within the TIRF field, indicating that these concentrations are insufficient for membrane anchoring (Fig. 7.2B). Septins hexamers could still be seen bound to the surface, as illustrated by the homogeneous septin signal with dotted signal. In contrast, septin octamers were able to anchor a network of septin-actin bundles to the surface at all concentrations tested (Fig. 7.2C). We could only see a qualitative difference for the 10nM septin octamer sample, where we were unable to distinguish a septin signal on the surface-bound actin. Interestingly, this concentration-dependent difference between hexamers and octamers is consistent with

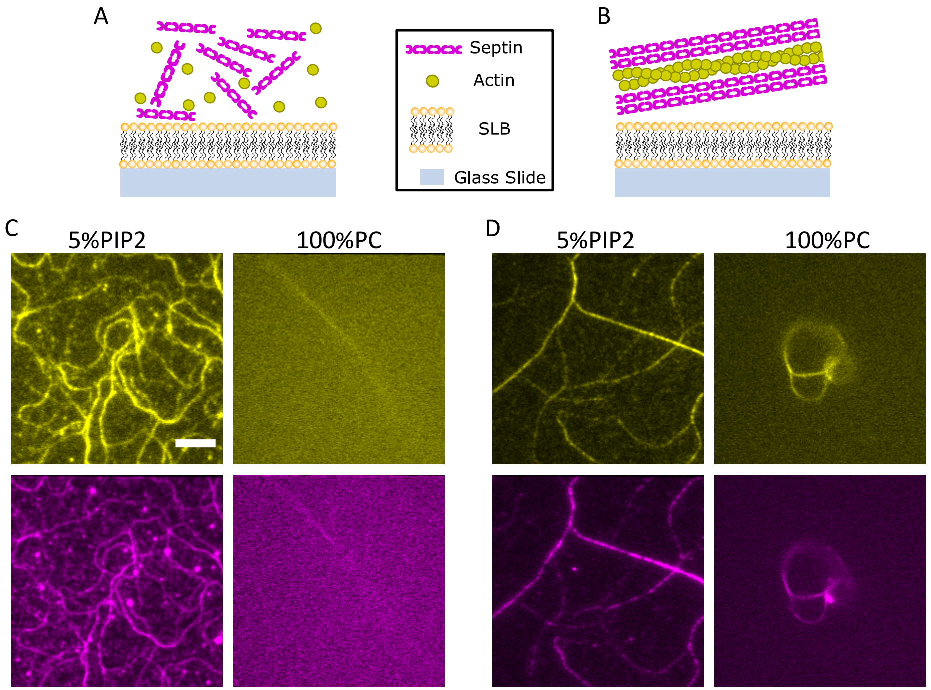

Figure 7.1. Septin octamer-mediated actin anchoring to 5%PIP2-containing supported lipid bilayers. A. Schematic representation of the experiments in panel C where actin and septin octamers are co-polymerized on an SLB. B. Schematic representation of the experiment in panel D where pre-formed actin-septin bundles are placed in contact with the SLB. C. Representative TIRF images of actin (yellow) and 300nM septin octamers (magenta) co-polymerized on top of 5%PIP (left) or 100%PC (right) SLBs. D. Corresponding images for pre-polymerized actin-septin bundles. Scale bar is 10μm.

the concentration-dependence of actin bundling in solution. As shown in Chapter 6, hexamers required concentrations above 300nM to bundle actin in solution, whereas octamers could bundle actin from 100nM when co-polymerizing with actin and even from 10nM if actin was pre-polymerized. Therefore, we cannot determine whether septin hexamers and octamers have different actin-anchorage ability or simply have a different actin-bundling strength.

7.2.2. Septin complexes anchor actin bundles to the inside of GUVs

Towards the aim of building a vesicle-based synthetic cell, we encapsulated 4μM actin together with different concentrations (0nM, 50nM, 100nM, 300nM, 500nM, and 800nM) of septin complexes inside cell-sized GUVs composed of 75wt%PC, 20wt%PS, and 5wt%PIP2 (20%PS+5%PIP2 GUVs) using the eDICE method, as described in Chapter 5. As shown in Fig. 7.3, confocal imaging revealed a strong effect of septin concentration on the localization and organization of actin inside the GUVs. In the absence of septins, actin displayed an homogeneous signal throughout the lumen that decreased close to the membrane, representing the curvature of the GUV (left-most column of Fig. 7.3). Sometimes, especially for GUVs smaller than 6μm in radius, we observed a shell of enhanced actin intensity at the periphery of the GUV (Fig 7.3). This type of spontaneous peripheral localization has been observed before [347, 348] and is a known consequence of confinement. Entropy favors a homogeneous distribution, but when the vesicle size is smaller than the persistence length of actin filaments (~10μm [349]) and their contour length, the enthalpic cost of filament bending forces the filaments to the periphery [348]. When actin was co-encapsulated with septin complexes at a low septin concentration (50nM or 100nM), we could again observe vesicles with either an homogeneous or a peripheral shell of the actin with occasional septin dots. When the septin complex concentration was raised to 300nM, we started to observe (rare) instances of GUVs harboring septin-actin bundles. At the highest concentrations of 500nM and 800nM of septin complexes, we frequently observed septin-actin bundles inside the GUVs. Interestingly, septin octamers (Fig. 7.3B) made thinner and more interconnected septin-actin bundles than septin hexamers (Fig. 7.3A).

Then, to understand whether septins were anchoring the septin-actin bundles to the GUV membrane, we classified the GUVs depending on whether or not the bundles localized on the GUV membrane. To do so, we visually inspected z-stacks of GUVs encapsulating actin together with the highest concentrations (500nM and 800nM) of septin complexes (N=90 for hexamers in Fig. 7.4A, and N=93 for octamers in Fig. 7.4B). We classified the GUVs in 3 groups: the network of bundles (1) completely colocalized, (2) partially colocalized, or (3) not localized with the GUV membrane. We found complete bundle localization to the membrane in the majority of the GUVs (62% for septin hexamers and 74% for septin octamers) (Fig. 7.4A and C). Most other GUVs showed partial colocalization (35% for septin hexamers and 26% for septin octamers), while only a small fraction of GUVs contained bundles that were completely detached from the membrane (2% for septin hexamers and 1% for septin octamers) (Fig. 7.4A and C, respectively). From the GUVs with partial bundle/membrane co-localization, for a high fraction (94% for septin hexamers and 96% for septin octamers) the bundles not localizing on the membrane were co-localized with small lipid aggregates (Fig. 7.4A and C, central column). Additionally, we noticed that bundles frequently localized to lipid clusters in the membrane. Indeed, in 97% of the GUVs with septin-actin bundles localized to the membrane, these bundles were localizing to regions with membrane clusters (Fig. S7.3). It is unclear whether these clusters are part of the GUV membrane or whether they are small lipid aggregates that are recruited to the membrane by septin. We also do not know if septin-actin bundles preferred to bind to pre-existing membrane clusters, or if they caused the clustering. Interestingly, we noticed that 20%PS+5%PIP2 GUVs tended to have fewer small lipid aggregates in the lumen if they had septin and actin inside than when septin was not present (Fig. 7.3), suggesting that septin-actin bundles could recruit the aggregates to the GUV membrane.

To test whether this septin-actin bundle localization at the membrane is due to septin anchoring, we performed the same manual analysis on inert 100%PC GUVs. To do so, we co-encapsulated 800nM septin hexamers or octamers and 4μM actin in GUVs composed of 99.75wt% PC, 0.05wt% rhodamine PE, and 0.2wt% biotin PE and took confocal z-stacks of 119 GUVs with septin-actin bundles (N=76 for hexamers in Fig. 7.4B, and N=43 for octamers in Fig. 7.4D), and classified these GUVs into the same three groups. In the majority of GUVs (97% for septin hexamers and 93% for septin octamers), the bundles partly localized to the membrane. In 5% of the GUVs with octamers, the bundles completely colocalized with the membrane, and in the rest (3% for septin hexamers and 2% for septin octamers), the bundles were completely detached from the membrane. Thus, septin-actin bundles rarely localize completely to the membranes of 100% GUVs, whereas they frequently localize completely to the membrane of 20%PS+5%PIP GUVs, suggesting that septins bundle and anchor actin to the membrane of GUVs in a PIP2 and PS-dependent manner.

7.2.3. Septin octamers anchor actin asters to lipid bilayers in the presence of the actin nucleator Arp2/3

We found that septin by itself is able to anchor actin bundles to a PIP2 and PS-containing lipid bilayer. We next wondered whether we could tune the architecture of the cortex-like structure by adding other ABPs, generating a more cell-like cortex. We chose to include the actin nucleator Arp2/3 and the Arp2/3-activating domain of murine N-WASP, VCA.

We again first tested this possibility on 100%PC and 20%PS+5%PIP2 SLBs imaged with TIRF microscopy. To do so, we mixed 5.5nM Arp2/3, 0.55μM VCA (based on previous literature [258, 344]), 0.9μM actin, and 700nM septin octamers. In these experiments we fluorescently labeled the SLB, to check its quality, actin, and either septin octamers or VCA, which were tagged with fluorophores excited at the same wavelength (msfGFP for septin and AlexaFluor 488 for VCA). We did all the experiments in the absence and presence of 0.15wt% methycellulose (MC), but here we only show the experiments in the presence of MC for cases where the actin structures were not anchored to the SLB. To check the effect of adding Arp2/3 and VCA on septin and actin separately, we first incubated actin and septin separately on a 20%PS and 5%PIP2 SLB with Arp2/3 and VCA. We observed no particular change in the septin signal on SLBs when Arp2/3 was added (Fig. 7.5A). The septin signal was homogeneous along the surface with occasional brighter spots. With actin, we observed an intricate network of filaments, with varying densities at distinct regions (Fig. 7.5B). We did not observe any indication of branching, but the higher densities made the network look differently than actin alone (see Chapter 6). The actin network was only seen in the presence of methylcellulose, indicating it was not membrane-bound.

Surprisingly, when the four components were all combined, we could see membrane-bound radial arrays of actin filaments of a radius of ~10μm (Fig. 7.5C). At the center of these asters, there was always a small dot of VCA, indicating that Arp2/3 might be nucleating the actin from the center of these arrays. The septin signal was higher on the aster than on the rest of the SLB, particularly on the center, but we could not observe any indication of the septin following the actin filaments going outwards. Similar actin asters have been observed before in the presence of Arp2/3 and fascin [350].

We then repeated this experiment on a 100%PC SLB and in the presence of MC, since in this case septin does not anchor the structures to the SLB (Fig. 7.5D). We could again see radial arrays of actin, but in this case there were fewer and thicker filaments emerging from the VCA-rich center, resembling stars. Septin was again enriched at the center, but we could now see it also enriched on the thicker arms. To test whether the lack of septin-mediated anchoring is what differentiates the asters from the stars, we designed an intermediate situation in which we polymerized all proteins in solution and in the absence of MC, and afterwards added them on the 20%PS+5%PIP2 SLB. In this situation, we could see a phenotype similar to the one observed in the absence of Arp2/3 and VCA, namely a mesh of anchored septin-actin bundles (Fig. 7.5E). We could, however, see that many more of the bundles crossed, or emerged, from a single point, reminiscent of the stars observed on the 100%PC SLB, indicating that the formation of asters is indeed dependent on membrane binding during actin and septin polymerization.

To understand more about the mechanism of formation of the membrane-bound asters, we performed two more experiments on 20%PS+5%PIP2 SLBs. In these experiments, we first pre-incubated the nucleator, Arp2/3, its activator, VCA, and one of the cytoskeletal proteins for 30 minutes in solution and in absence of MC. After the incubation, we added the other cytoskeletal protein and immediately flushed the mixture onto the SLB. When we incubated first septin octamers with Arp2/3 and VCA, we could again see membrane-bound asters with a ~10 um radius(Fig. 7.6A). In this case, however, we could see septin signal localized to most of the actin filaments moving outwards from the aster. This indicates that septin may have interacted with Arp2/3 and VCA during the incubation in solution, so, enhancing its binding to the polymerizing actin arms. When actin was added first, we could still see membrane-bound circular arrays, but the structures were double in size as compared to the previously described situation, had no obvious center, and septin could not be observed on the actin filaments, indicating that if septin is not present from the start of the polymerization process, the asters formed are more loosely packed (Fig. 7.6B).

Finally, we wondered if we could form these membrane-bound asters inside GUVs. To test this, we used eDICE to make GUVs with membrane compositions of either 100%PC or 20%PS+5%PIP2 encapsulating the four proteins. In the 20%PC+5%PIP2 GUVs we could see a variety of phenotypes (Fig. 7.7A and B). We could see that some of the GUVs contained a single clump of protein. These clumps contained actin and septin or VCA. Since septin octamers and VCA were labeled with fluorophores excited at the same wavelengths, we could not check if both proteins were present in the protein clump simultaneously. Other GUVs contained membrane-bound septin-actin bundles, a phenotype similar to the bundles formed in absence of Arp2/3 and VCA. Finally, we could see GUVs containing structures reminiscent of the asters seen in the SLB experiments, where bundles of actin (and septin, observed in experiments where we labeled it) emerged from a protein clump with either septin or VCA (we could not image both simultaneously). To further check if septin octamers interacted with Arp2/3 or VCA, we also encapsulated all the proteins except actin. In this case, we could only see clumps of proteins with no septin localizing to the membrane (as in Chapter 5), suggesting that Arp2/3 or VCA could be inhibiting septin-membrane interactions by binding septin. In contrast, in the 100%PC GUVs, we could only observe clumps of protein in most of the GUVs, indicating that the addition Arp2/3 and VCA lead to the polymerization of a single septin structure that could not be resolved by confocal microscopy.

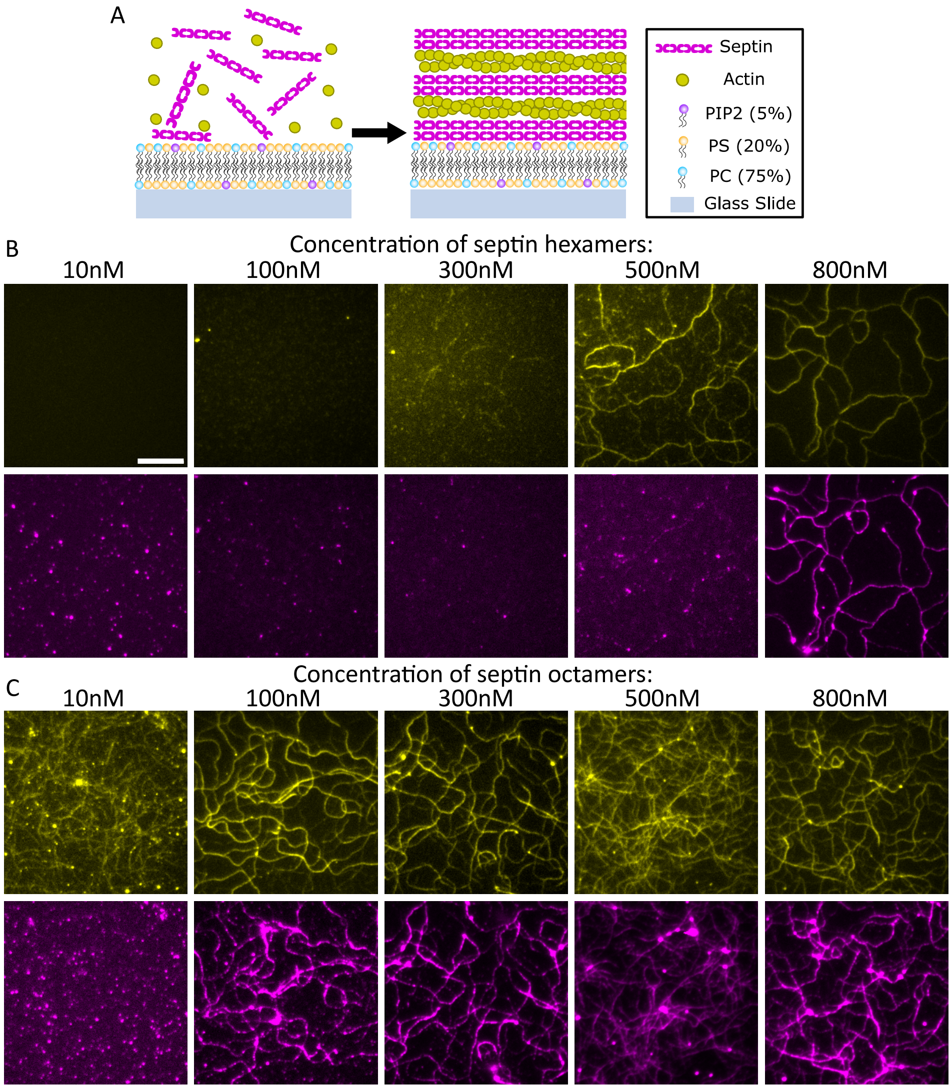

Figure 7.2. Anchoring of actin filaments to SLBs by human septin hexamers and octamers at different concentrations. A. Schematic representation of the experiments. Septin complexes are co-polymerized with actin on top of 20%PS+5%PIP2 SLBs. B. Representative TIRF images of actin (yellow) co-polymerized with the specified concentrations of human septin hexamers (magenta) on top of 20%PS+5%PIP2 SLBs. D. Corresponding images with human septin octamers. Scale bar is 10µm.

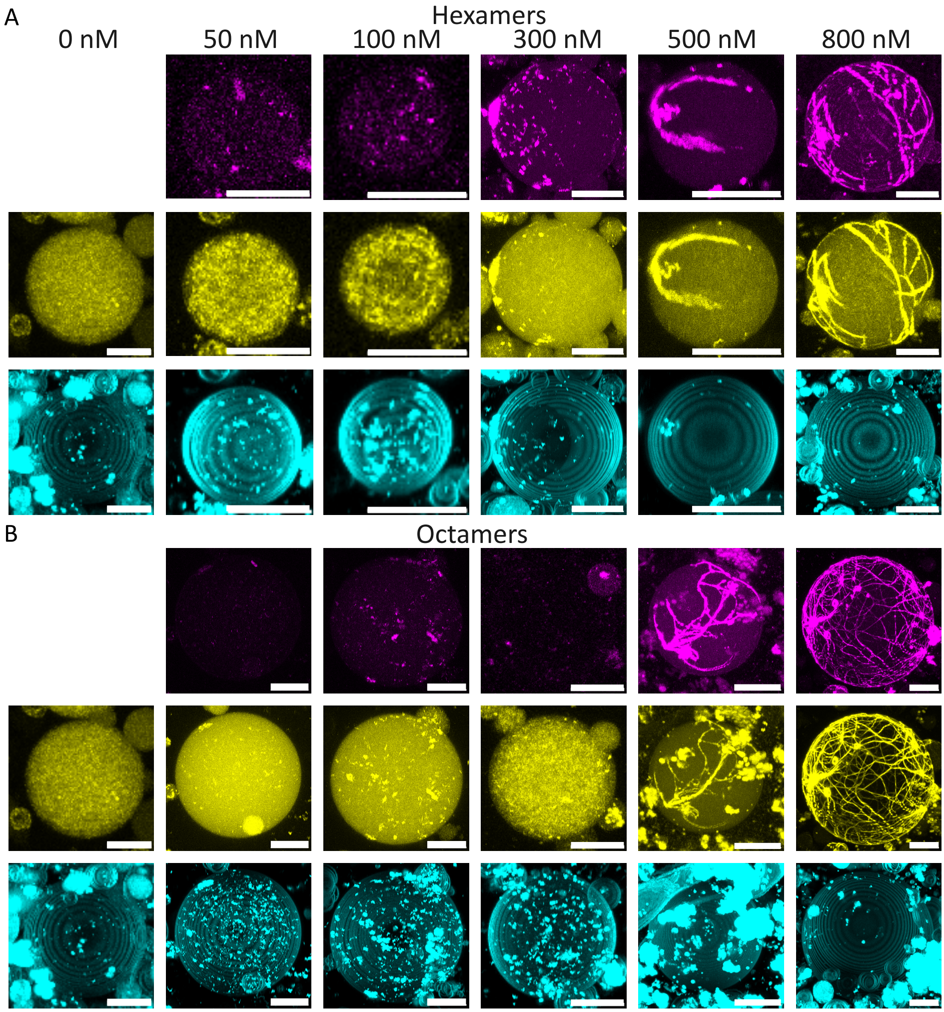

Figure 7.3. Anchoring of actin filaments to the inner surface of GUVs containing 20%PS+5%PIP2 by human septin hexamers and octamers at different concentrations. A. Maximum intensity z-projections of representative confocal Z-stacks of 4µM actin (yellow) co-polymerized with the specified concentrations of human septin hexamers (magenta) inside 20%PS+5%PIP2 GUVs (cyan). B. Corresponding images with human septin octamers. Note that bright and amorphous lipid structures are contaminating structures such as lipid droplets introduced by the eDICE method. Scale bar is 10µm.

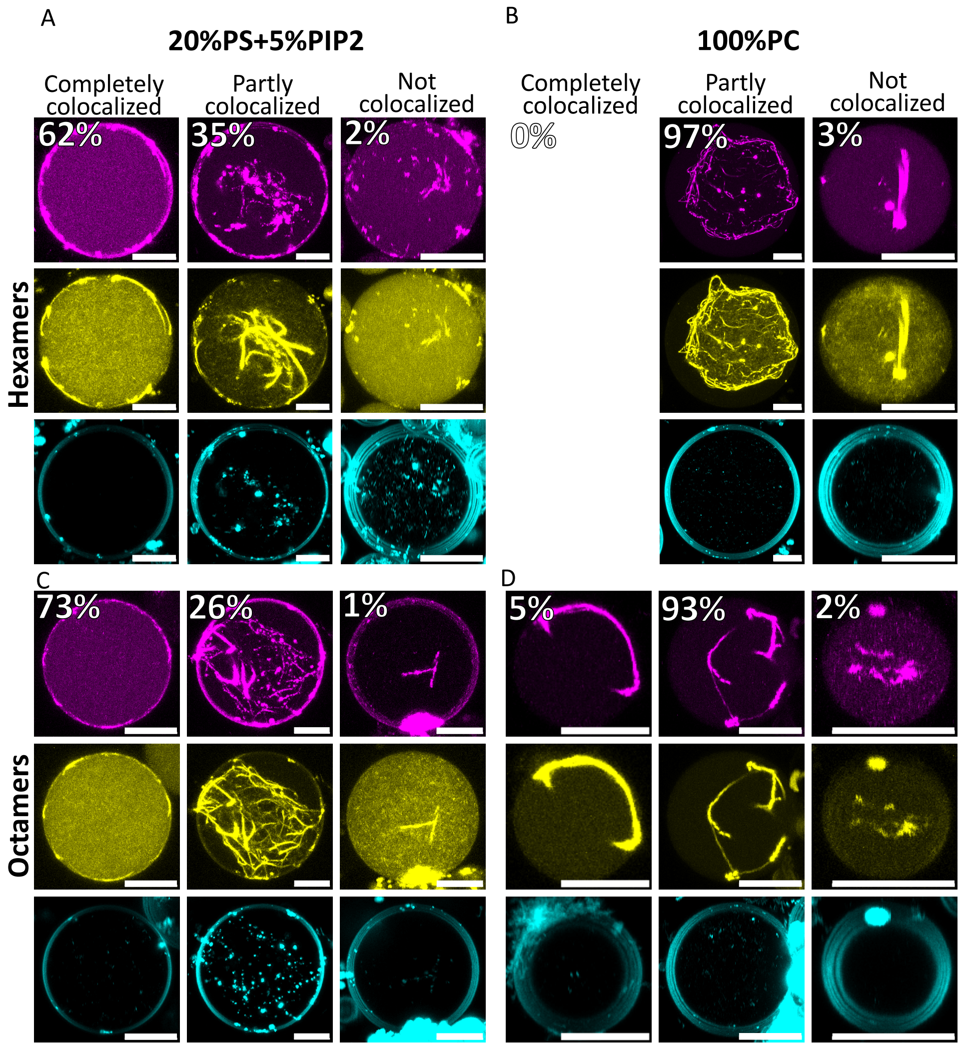

Figure 7.4. Localization analysis of the septin-actin bundles inside GUVs. A. Maximum intensity projections of the central 10 confocal slices (0.5 or 1µm step size) of representative z-stacks for each category of the classification of the localization of septin (magenta) hexamers-actin(yellow) bundles inside 20%PS+5%PIP2 GUVs (cyan). B. Corresponding images of the classification for 100%PC GUVs. C. Maximum intensity projections of the central 10 confocal slices of representative z-stacks for each category of the classification of the localization of septin octamers-actin bundles inside 20%PS+5%PIP2 GUVs. Corresponding images of the classification for 100%PC GUVs. Note that GUVs composed of 100%PC in B and D, have fewer small lipid aggregates in the lumen than those composed of 20%PS+5%PIP2 SLB in A and C. Scale bars are 10µm.

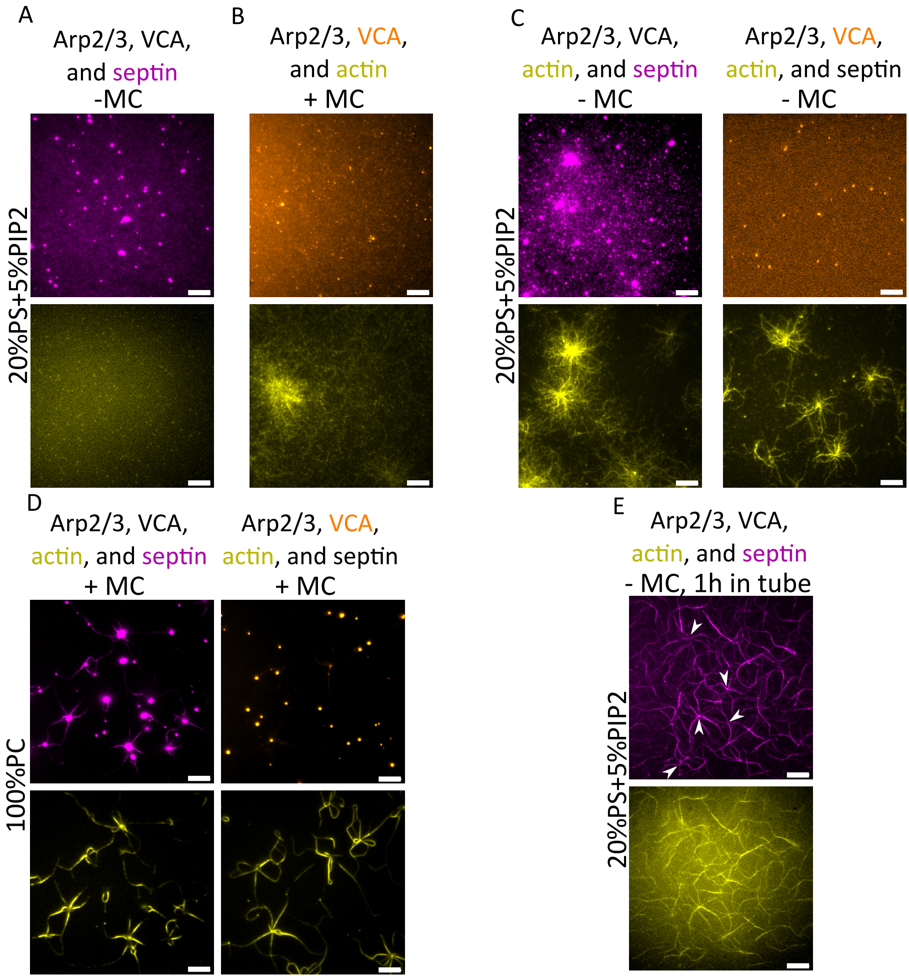

Figure 7.5. Formation of a septin octamer-anchored actin network on SLBs in the presence of Arp2/3 and VCA. A. Representative TIRF images of septin octamers (magenta) incubated with Arp2/3 and VCA on a 20%PS+5%PIP2 SLB in the absence of methylcellulose (-MC). B. Representative image of actin (yellow) incubated with Arp2/3 and VCA (orange) on a 20%PS+5%PIP2 SLB in the presence of 0.15wt% methylcellulose (+MC). C. Representative images of the incubation of the four proteins at once on a 20%PS+5%PIP SLB in the absence of methylcellulose. On the left septin is labeled, while on the right VCA is labeled. D. Representative images of the incubation of the four proteins on a 100%PC SLB in the presence of 0.15wt% methylcellulose. On the left septin is labeled, while on the right VCA is labeled. E. Representative image of the four proteins incubated together in solution for 1h and afterwards added to a 20%PS+5%PIP2 SLB in the absence of methylcellulose. The white arrowheads in E show the presence of aster-like structures. The experiments in D were done twice while the experiment in E was done only once. Scale bars are 10μm.

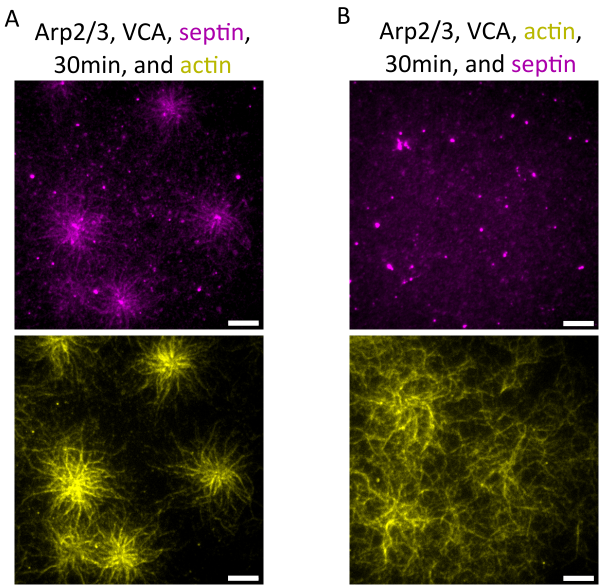

Figure 7.6. Pre-incubation of Arp2/3 and VCA with either actin or septin gives different aster morphologies. A. Representative TIRF image of the asters formed when septin octamers (magenta) are incubated for 30min with Arp2/3 and VCA before the addition of actin (yellow). B. Representative image of the asters formed when actin is incubated for 30min with Arp2/3 and VCA before the addition of septin octamers. Both experiments were done only once. Scale bars are 10µm.

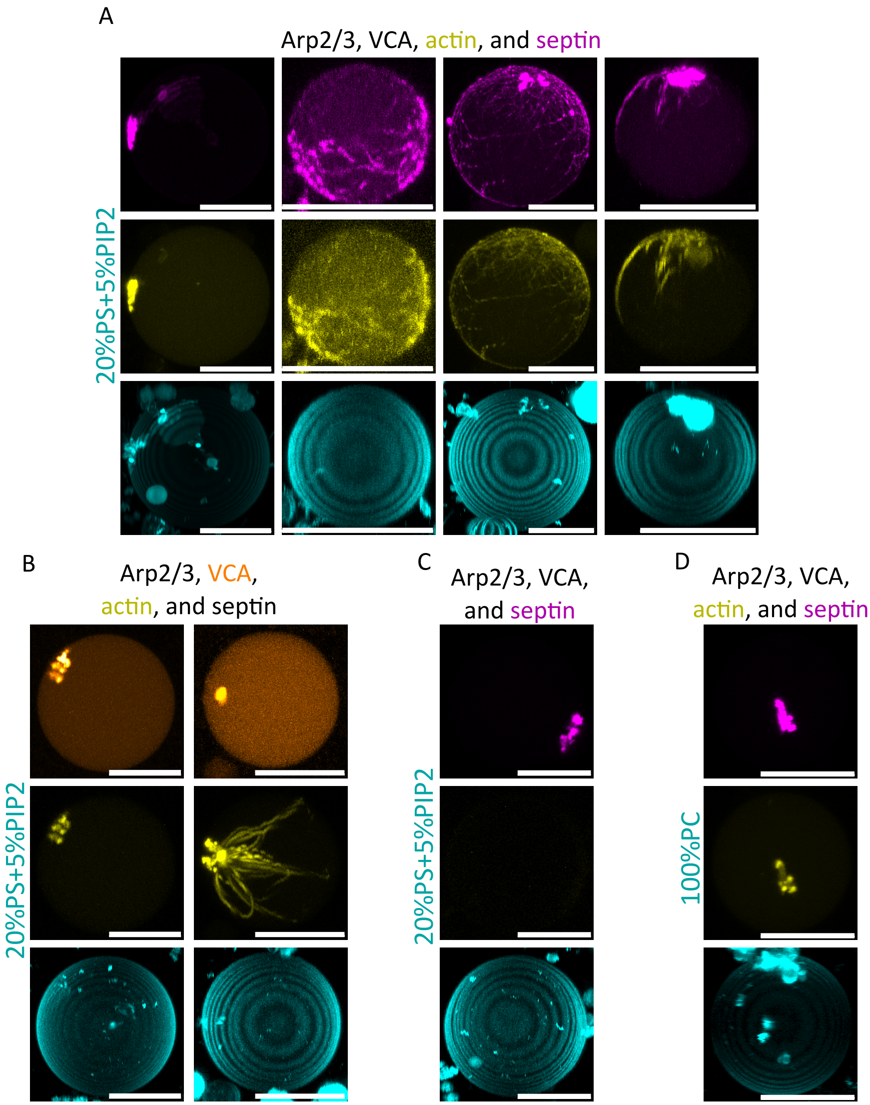

Figure 7.7. Encapsulation of actin, septin octamers, Arp2/3, and VCA in GUVs. A. Representative confocal images of 20%PS+5%PIP2 GUVs (cyan) encapsulating actin (yellow), fluorescent septin octamers (magenta), Arp2/3, and VCA. B. Corresponding images using unlabeled septin and fluorescent VCA (orange). C. Representative confocal images of 20%PS+5%PIP2 GUVs encapsulating fluorescent septin octamers (magenta), Arp2/3, and VCA. D. Representative confocal images of 100%PC GUVs encapsulating the same proteins as in A. Scale bars are 10µm.

7.3. Discussion

In this chapter we have explored the possibility to anchor an actin-based cortex-like structure to the membrane of a synthetic cell via simultaneous septin-actin and septin-membrane interactions. Elsewhere in this thesis, we found that septins bind to membranes containing PIP2, and they bind better if PS is also present (Chapters 4 and 5). From Chapter 6, we know that septin complexes can bundle actin at high concentrations (>500nM), while octamers start bundling actin already from lower (~10nM) concentrations. Therefore, in this chapter we first compared the actin-anchorage ability of septin octamers to 5%PIP2 SLBs and to 100%PC SLBs using TIRF microscopy. We found that septin-actin bundles were only observed on the 5%PIP2 SLBs. This shows that septins can indeed anchor actin filaments to a lipid bilayer, indicating that with septins alone, we can build a bundle-based cortex-like structure to mechanically support the synthetic cell membrane. Our findings also show that (1) the lipid- and actin-binding domains of septins are independent and (2) far enough from each other on the septin oligomer to permit both interactions at once. When septin octamer-actin bundles were first pre-formed in solution before incubation on SLBs, we found very similar results: the bundles were bound to the membrane only when PIP2 was present. Since we know that septins form filaments on the surface of septin-actin bundles (Chapter 6), this indicates that polymerization on the SLB is not critical for septin binding. Comparing the two experiments, we found that actin-septin bundles were more abundant and thinner when formed on the membrane instead of in solution. This is likely due to the formation process. In solution, polymerizing septin and actin filaments are able to move in 3D, leading to more interactions with other septin and actin filaments. On the SLBs, the septin filaments and associated actin filaments are immobilized, drastically decreasing the amount of potential interactions with other actin or septin filaments.

We next compared at what concentrations hexamers and octamers were able to anchor actin filaments on SLBs, using 20%PS+5%PIP2 SLBs to strengthen the septin-membrane interactions. We saw that septin hexamers were also able to anchor actin to the SLB, forming a similar bundle-based cortex-like structure as septin octamers. The octamer-mediated anchoring, however, led to a thinner and more interconnected network of bundles. When decreasing the septin concentration, we found that hexamers stopped anchoring actin at concentrations below 500nM, while octamers could anchor actin at all tested concentrations. However, at the lowest concentration of octamers tested (10nM), the surface-bound actin was thinner and no septin was seen colocalizing with it. These results are consistent with those of the actin bundling assay from Chapter 6, were we found that septin hexamers could bundle actin in solution only above 500nM, whereas septin octamers bundled actin from 10nM (if the actin was pre-polymerized). Therefore, we cannot at this stage conclude whether septin hexamers have different actin-anchorage ability or simply have a higher critical concentration for actin bundling. Interestingly, we see that at 10nM, septin octamers can anchor many actin filaments to the membrane, although only partially bundling them in solution. This may indicate that septin octamers have a stronger affinity for the 20%PS+5%PIP2 SLBs than for actin, forming first a network on the SLB to which actin filaments can later anchor. We could test this hypothesis by tuning the SLB composition to lower the percentages of PS and/or PIP2 and see whether this arrangement is replicated or whether septin would switch from being more an anchor to being more an actin bundler

Despite the ability of septin to anchor actin to lipid bilayers, by itself septin simply anchors a network of bundles. With the aim to tune this architecture and move to a more realistic cortex-like arrangement with shorter and more interconnected actin filaments [41, 123, 253, 351], we decided to use Arp2/3 and its activator VCA to nucleate branched actin networks. When we co-polymerized actin with Arp2/3, VCA and septin octamers on a 20%PS+5%PIP2 SLB, to our surprise, we found that septin now anchored actin asters to the SLBs. These asters had many thin actin filaments coming out of their center. On the 100%PC SLB, when crowding the bundles to the surface, we could see asters with only a few thicker actin bundles, which we termed stars. On the samples with asters, the septin signal was higher on the asters, especially in the center, but this signal did not show a well-defined structure and we could not see a clear colocalization with the actin filaments. On the samples with stars, however, we did observe septin decorating the actin arms, in addition to a high signal in the star center. VCA signal was high only in the center of both asters and stars. To learn about the mechanism of formation of these structures we varied the experimental process in three ways. First we copolymerized the actin and septin in the presence of Arp2/3 and VCA in bulk before adding onto the 20%PS+5%PIP2 SLB, and found that a network of septin-actin bundles was formed, with some bundles emanating from stars. This suggests that septin-membrane interactions are vital for the formation of asters. We then incubated Arp2/3 and VCA in bulk with either septin or actin for 30min, and then added the other cytoskeletal protein and incubated the mixture on the 20%PS+5%PIP2 SLB. We found that if septin was incubated with Arp2/3 and VCA first, asters were formed with the septin now clearly localizing to the actin filaments coming out of the center. This suggests that septin might interact with Arp2/3 and/or VCA, forming a cluster of the three proteins that can then interact with actin. This could lead to a higher local concentration of septin that helps it bind the actin filaments, giving a clear (instead of not well-cloudy) localization with the asters arms. Instead, if actin was co-polymerized with Arp2/3 and VCA first, we observed larger and less tightly packed structures, suggesting that to form proper asters (with filaments emanating from a center), septin is needed during actin polymerization.

Our observations are reminescent of earlier work of Haviv et al. [350], who found similar asters and stars when polymerizing actin in the presence of Arp2/3, VCA and the actin bundling protein fascin. They proposed that during the initial stages of polymerization, Arp2/3 and VCA start nucleating a seed of a branched actin network that will form the centre of the aster, and fascin then binds to allow formation of aster arms. Similarly, we propose that septins bind to the nascent aster centre thanks to its interaction with actin, and, as suggested by our observation of septin localizing better to the arms if previously incubated with VCA and Arp2/3, also to Arp2/3 and/or VCA. During aster nucleation, the Arp2/3 concentration is still high, favoring the formation of branched actin filaments. As the actin filaments grow, the available Arp2/3 pool in solution is depleted, favoring the formation of straighter filaments forming the aster arms (Fig. 7.8A). The actin bundler (septin for us, and fascin in [350]) then starts bundling the actin filaments. Since the actin in the aster center has more branched actin networks, which are more difficult to bend to promote bundling, only the straighter actin filaments coming out of the seeds are bundled, leading to the formation of the arms of the aster. To understand when we get asters versus stars depending on the lipid composition, we can use the same explanation as detailed above for the formation of septin-actin bundles that are thinner if they polymerize on the 20%PS+5%PIP2 SLB. Briefly, as the actin and septin filaments are immobilized due to their septin-mediated anchorage, they can only interact with a few filaments and would form thin bundles or remain as filaments (Fig. 7.8B), leading to aster formation (Fig. 7.8C). When polymerized on a membrane that does not bind septin or in the bulk, the actin and septin filaments can now freely move in 3D leading to more septin-mediated actin-actin interactions and therefore to the formation of thicker arms (Fig. 7.8D), leading to star formation (Fig. 7.8E). We should caution that this interpretation is speculative, since the experiments where we varied the timing and incubation conditions were only done once or twice.

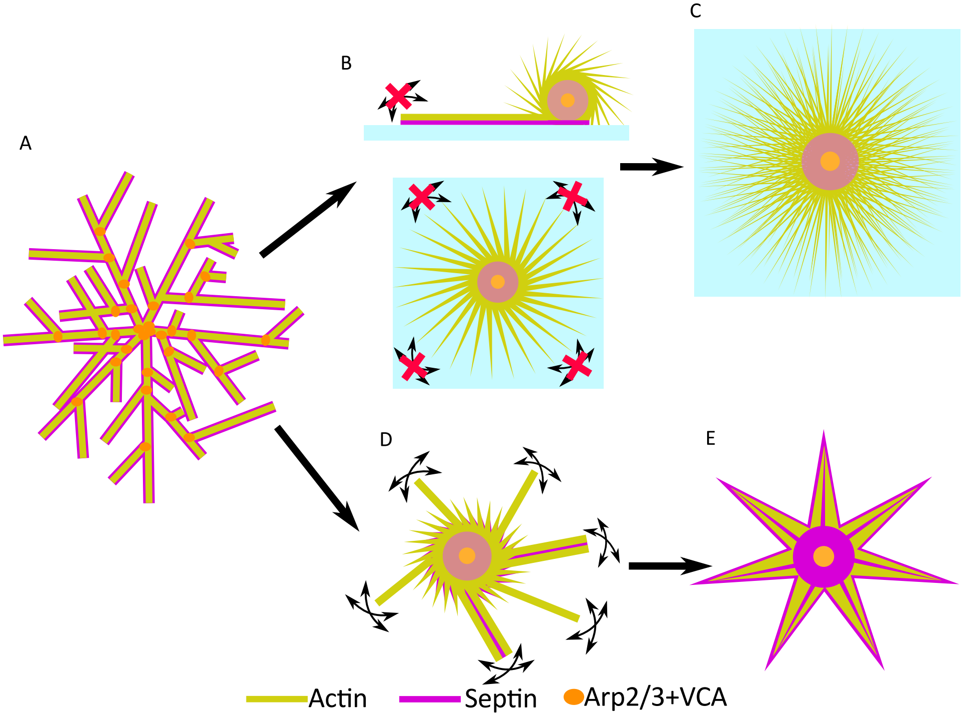

Figure 7.8. Proposed mechanism to explain how septin octamers mediate aster versus star formation. A. Nascent aster composed of actin (yellow), septin octamers (magenta), and Arp2/3+VCA (orange), consisting of short, branched actin filaments. B. If the nascent aster grows on a septin-binding lipid bilayer, it will be anchored by the septin octamers. In this case the actin filaments are immobilized by their anchorage to the surface and will only bundle by septin if two filaments grow together from the center of the aster. Top represents a lateral view, bottom represents a bird's eye view. C. The lack of lateral interaction and bundling will generate an aster, with many actin filaments coming out of the center. D. If the nascent aster grows in solution, the actin and septin filaments can move, leading to septin-mediated bundling by different filaments coming together. E. As a consequence of the bundling, the septin octamers bundle most of the actin filaments in a few arms, generating a star.

With the aim of building a synthetic cell, we finally encapsulated the septin and actin with and without Arp2/3 and VCA inside cell-sized vesicles using the eDICe method. We found very similar results compared to the SLBs experiments. When septin and actin were encapsulated together, we found bundle formation only above a nominal septin concentration of 500nM, in this case for both septin hexamers and octamers. These bundles were completely membrane-localized inside 60-70% of the 20%PS+5%PIP2 GUVs, but in only one of the 100%PC GUVs. This again shows that both septin hexamers and octamers can anchor a cortex-like structure to PIP2- and PS- containing lipid bilayers, and they can also do so inside cell-sized vesicles. However, since we used confocal microscopy to image the GUVs, we cannot be sure whether the bundles that we observe represent all the septin-anchored actin, or whether additional thinner filaments or bundles are also present but not seen due to the lower sensitivity of confocal microscopy as compared to TIRF microscopy. Using higher resolution techniques, such as electron microscopy or high resolution fluoresce microscopy (such as STED or STORM) would be useful to characterize the actin-septin networks more fully. When we encapsulated actin and septins together with Arp2/3 and VCA, we obtained some GUVs with aster-like structures attached to the membrane. At the same time we also observed GUVs containing either small clumps containing all the proteins or membrane-anchored septin-actin bundles, similarly to when Arp2/3 and VCA are not present. The variability in phenotypes across all the GUV experiments probably originates from variations in protein encapsulation efficiency. As reported by Baldauf et al. [258] and by us in Chapter 5, eDICE produces GUVs having a wide range of protein concentrations. Therefore, the phenotype observed when co-encapsulating multiple proteins likely depends on the stoichiometric ratios of these proteins.

Finally, the lack of septin on the membrane of 20%PS+5%PIP2 when encapsulating it with Arp2/3 and VCA, and the better localization of septin to actin filaments after preincubating it with Arp2/3 and VCA is initial indirect proof that septins might directly interact with Arp2/3. This could be very relevant for cells, since septins have been found to localize to regions of the cortex with branched actin networks [127, 128], and to actin regions nucleated with Arp2/3 [352, 353]. Further studying whether septins directly interact with Arp2/3 would give a deeper understanding of how septins could participate in forming structures such as lamellipodia [127] and phagocytic cups [128]. In particular, cosedimentation assays and higher resolution imaging of septin complexes incubated with Arp2/3 can give more insights into this possibility.

In summary, we have been able to use septin to build a cortex-like membrane-anchored actin structure. However, the architecture of the network does not resemble a real cortex. The cell cortex has several co-existing morphologies, ranging from disordered networks [41, 253, 351] to tightly packed bundles such as the contractile ring [123]. We do obtain anchored septin-actin bundles, but these are often curved and disorganized, unlike the contractile ring. Therefore more work is needed to tune the architecture of the septin-mediated actin cortex, and in particular to order the bundles into a ring and to form a network of shorter and crosslinked actin filaments that are uniformly distributed along the GUV membrane, which would potentially further reinforce the synthetic cell membrane. This could be done by playing with the timing at which the proteins are added, or by incorporating other ABPs that would further tune the architecture. Furthermore, having less thick bundles of actin and septin or single crosslinked actin filaments could make it possible for myosin to contract the actin network, since septin inhibits contraction of bundles (as shown in Chapter 6). Finally, to test whether actin-septin bundles can indeed reinforce the synthetic cell membrane, it will be interesting to perform mechanical measurements by fluctuation analysis or micropipette aspiration (see Chapter 8).

7.4. Materials and methods

All chemicals were obtained from Sigma Aldrich unless specified otherwise.

7.4.1. Proteins

Septin

Human septin oligomers were purified and their quality was checked as detailed in chapter 2. We used septin hexamers with a subunit order of SEPT2-SEPT6-SEPT7-SEPT7-SEPT6-SEPT2 and septin octamers with a subunit order of SEPT2-SEPT6-SEPT7-SEPT9_i1-SEPT9_i1-SEPT7-SEPT6-SEPT2. Septins were fluorescently tagged with msfGFP on the C-terminus of SEPT2. For purification, SEPT2 contained a his$_6$-tag at its N-terminus, and SEPT7, for hexamers, or SEPT9, for octamers, contained a Strep-II-tag at its C-terminus.

Actin

Unlabeled and Atto-647 labeled rabbit skeletal muscle actin were purchased from Hypermol (Cat. # 8101-03 and 8158-02, respectively). Following the supplier instructions, we dissolved the lyophilized actin to a final concentration of 23.8μM in MilliQ water, resulting in a final buffer composed of 2mM Tris pH 7.8, 0.4mM ATP, 0.1mM Dithiothreitol (DTT), 0.08mM $CaCl_2$ and 0.2% unspecified disaccharides. After a 2h incubation on ice, the solution was cleared by centrifuging at 148,000g for 1h. The actin concentration remaining after clarification was checked by UV absorption measurements at 290nm using a Nanodrop 2000c spectrophotometer (actin's extinction coefficient ϵ_{290}=0.617 Lmg^{-1}cm^{-1} [313]). The G-actin solution was aliquoted, snap-frozen and stored at -80℃ until use. Before use, actin aliquots were quickly thawed and stored on ice for up to two weeks. Aliquots were incubated for at least 2h on ice to depolymerize any F-actin [314].

Arp2/3

Porcine brain Arp2/3 complex was ordered from Hypermol (Cat. # 8413-01) and stored in a buffer containing 20 mM Tris, 150 mM KCl, 1 mM $MgCl_2$, 1 mM DTT, and 0.2 mM Na_2ATP at -80℃.

VCA-domain

A 10xHis-tagged VCA-domain of murine N-WASP was purified in-house from *Escherichia coli* Bl21 (DE3) following a described protocol [354]. The plasmid was a kind gift from Kristina Ganzinger (AMOLF). VCA was fluorescently labeled with AlexaFluor 488 C5 maleimide (Molecular Probes) following the retailer's protocol.

7.4.2. Reconstituting actin cortices on SLBs

In order to reconstitute septin-actin cortices on SLBs, we used small unilamellar vesicle (SUV) rupture to form SLBs inside custom-made glass flow channels as described in Chapters 4 and 6. Then we incubated the specified proteins on top of the SLBs.

7

SUV preparation

To make SLBs, we used the lipids 1,2-dioleoyl-sn-glycero-3-phospho-(1'-myo-inositol-4',5'-bisphosphate) (ammonium salt) (PIP2) (Merck KGaA, #850155P), 1,2-dioleoyl-sn-glycero-3-phosphocholine (DOPC) (Merck KGaA, #850375C), 1,2-dioleoyl-sn-glycero-3-phospho-L-serine (sodium salt) (DOPS) (Merck KGaA, #840035C), and to visualize the membrane we used 1,2-dioleoyl-sn-glycero-3-phosphoethanolamine-N-(lissamine rhodamine B sulfonyl) (Rhodamine-PE) (Merck KGaA, Cat. #810150C); all from Avanti Polar Lipids.

To prepare the SUVs, a lipid mixture in 20:9:1 chloroform:methanol:water containing 74.9mol% PC, 20mol% PS, 5mol% PIP2, and 0.1mol% rhodamine-PE (20%PS+5%PIP2) or a mixture in chloroform of 99.9mol% PC and 0.1mol% rhodamine-PE (100%PC) was dried under nitrogen in a glass tube. After an overnight incubation in a dessicator to remove any remaining solvents, we resuspended the lipid film in either F-buffer of pH 7.4 (20mM Tris HCl pH 7.4, 2mM $MgCl_2$, 50mM KCl, 1mM DTT) or, if PIP2 was in the mixture, NaCi buffer of pH 4.8 (50mM citrate, made of equal molarity trisodium citrate and citric acid mixed in a 2:3 volume ratio, 50mM KCl, 0.1mM ethylenediaminetetraacetic acid). The lipids were then resuspended by four cycles of 1 min vortexing and 5 min incubation at room temperature. Then, we transferred the lipid solution to an eppendorf tube and subjected the solution to ten freeze-thaw cycles. Finally, SUVs were obtained by sonicating the lipid solution at room temperature using an Ultrasonic homogenizer series HD 2000.2 sonicator equipped with a BR30 cup resonator (Bandelin) at 10% amplitude for 30 minutes (total sonication time) with pulses of 5s on and 5s off to avoid excessive heating.

SLB formation

7

Flow channels were prepared as detailed in chapter 3.4. Briefly, 2x20mm parafilm strips were sandwiched, separated by ~3mm, between a base piranha cleaned glass slide and coverslide (5% hydrogen peroxide and 5% ammonium hydroxide solution heated at 70℃ for 10 minutes). The parafilm was then melted at 120℃ to fix the flow channel. Once the channels had cooled down, as shown by the parafilm turning opaque again, we immediately formed the SLB by adding 10µL of SUV solution supplemented with 5mM $MgCl_2$, to promote vesicle rupture. As soon as solution was introduced into the flow channels, these were left in a humid chamber to avoid drying. After at least 30 minutes incubation, the channels were washed with 3 channel volumes (~30µL) of F-buffer.

Septin-actin cortex formation

We first prepared a mix of labeled and unlabeled protein. For actin, we mixed 90% unlabeled skeletal muscle rabbit actin with 10% ATTO-647 skeletal muscle rabbit actin in G-buffer (2mM Tris pH 7.8, 0.2mM $CaCl_2$, and 1mM DTT) to a total G-actin concentration of 5µM. For septin, we mixed 90% unlabeled septin complexes with 10% msfGFP septin complexes in septin buffer (20mM Tris pH 7.4, 2mM $MgCl_2$, 300mM KCl, and 1mM DTT) to a concentration 6 times higher than the desired final concentration.

We then followed a process similar to the one described in chapter 6. Briefly, we prepared a 5x septin polymerization buffer (5xSPB) containing all the necessary components except the proteins. This 5xSPB contains (83.3mM Tris-HCl pH 7.4, 8.3mM $MgCl_2$, 5mM DTT, 5mM GTP, 5mM ATP, 5mM Protocatechuic acid (PCA), 5mM 6-hydroxy-2,5,7,8-tetramethylchroman-2-carboxylic acid (TROLOX)). Then we mixed MilliQ water (enough to top up to the final desired volume), 20% 5xfluoSPB (1:5 dilution), 0.05μM (for flow channels) or 0.1μM (for imaging chambers) Protocatechuate 3,4-Dioxygenase (PDC, sigma-Aldrich, Cat. # P8279), 20% Actin mix, and 16.67% Septin mix (1:6 dilution), in this specific order. This gave a mix composed of 21.66mM Tris pH 7.4, 2mM $MgCl_2$, 50mM KCl, 1mM DTT, 1mM GTP, 0.5mM MgATP, 1mM PCA, 1mM TROLOX, 0.05μM PCD, 0.067mM $CaCl_2$, 1μM total actin concentration, and the septin concentrations specified in the Results section. This mix was immediately inserted into the flow channels. PCA and PCD are oxygen scavengers used to protect the sample from bleaching and from photodamage [316, 317]. TROLOX inhibits blinking [318]. The final mixture was then immediately added into the flow channels, and incubated for at least 1h at room temperature (~21℃). The flow channels were sealed with Dow Corning® high-vacuum silicone grease (Sigma-Aldrich, Cat. # Z273554).

Septin-actin-Arp2/3 cortex formation

As above, we first prepared the protein mixes. For actin, we mixed 90% unlabeled skeletal muscle rabbit actin with 10% ATTO-647 skeletal muscle rabbit actin in G-buffer to a total G-actin concentration of 5μM. For septin, we mixed 85% unlabeled septin octamers with 10% msfGFP septin octamers in septin buffer to a 6μM concentration. Then we diluted unlabelled VCA to 21.6μM and Arp2/3 to 0.22μM. Since septin and VCA were stained with fluorophores that are excited at the same wavelength, to image fluorescent VCA, we prepared the 6μM septin with only dark octamers (septin dilution), and the 70μM VCA with 20% AlexaFluor C5-VCA (VCA mix).

Then, we first prepared the perishable mix containing 5mM DTT, 5mM Trolox, 5mM PCA, 0.25μM PCD, 5mM GTP, and 2.5mM ATP in G-buffer. To prepare the sample, we subsequently mixed, in this specific order, MilliQ, 11.2 mM Tris-HCl pH 7.4, 1.2 mM $MgCl_2$, 17.6v% perishable mix, 2.5v% diluted Arp2/3, 2.5v% VCA (dilution or mix), 18v% actin mix, and 11.8v% septin octamers (dilution or mix), respectively. Unless specified otherwise, we waited 15 seconds between adding the actin and the septin. For experiments on 100% PC SLBs, we added methylcellulose at a final concentration of 0.13wt% (2wt% stock) just before the perishables mix. This resulted in a mix composed of 14.1mM Tris pH 7.4, 1.41mM $MgCl_2$, 44.1mM KCl, 1.32mM DTT, 0.88mM GTP, 0.44mM MgATP, 0.044mM PCA, 0.88mM TROLOX, 0.044μM PCD, 0.03mM $CaCl_2$, 0.88μM total actin concentration, 0.55μM VCA, 5.5nM Arp2/3, and 706nM total septin concentration. This mix was then, unless otherwise specified, immediately added to the SLB-coated flow channels, sealed with Dow Corning® high-vacuum grease, and incubated for at least 1h at room temperature.

TIRF imaging

Imaging was done using an inverted Nikon Eclipse Ti-E microscope with perfect focus system, equipped with a FRAP/TIRF Ilas² system (Gataca Systems), an oil immersion objective (Nikon Plan Apo λ 100× NA 1.45). Image acquisition was controlled using MetaMorph (Molecular Devices). We used lasers (all from Cobolt) with wavelengths of 491nm (~15% intensity, 50-100ms exposure time), 561nm (~2% intensity, 10-30ms exposure time), and 642nm (~15% intensity, 50-100ms exposure time), which were set to an angle yielding a penetration depth of ~100nm. Images were processed with FIJI [154] to tune the brightness and contrast for optimal visualization.

7.4.3. Reconstituting actin cortices inside GUVs

To make GUVs containing a septin-anchored actin cortex, we used eDICE, similarly as explained in Chapter 5.

eDICE

We used several types of lipids to prepare the GUVs, all from Avanti Polar Lipids. First, the basic component for the membranes was either DOPC or 1-palmitoyl-2-oleoyl-sn-glycero-3-phosphocholine (POPC) (Merck KGaA, Cat. #850457C). DOPC and POPC were used interchangeably as they only differ in the saturation of the alkyl chains that are within the hydrophobic core of the GUV bilayer, while the same headgroup is exposed to the aqueous solutions. Second, we used the anionic lipids PIP2 (purified from brain) (Merck KGaA, Cat. #840046X), and DOPS. To visualize the membrane we used Rhodamine-PE. Finally, to bind the GUVs to the surface of the imaging chamber, we used 1,2-dioleoyl-sn-glycero-3-phosphoethanolamine-N-(biotinyl) (sodium salt) (Biotin-PE) (Merck KGaA, Cat. #870282C). We used two lipid compositions, 74.95wt% PC, 20wt% PS, 5wt% PIP2, and 0.05wt% rhodamine-PE (20%PS+5%PIP2) or 99.95wt% PC and 0.05wt% (100%PC). To anchor GUVs to the imaging surface, we added 0.2wt% Biotin-PE in the place of PC.

First, we prepared the lipid-in-oil solution. To do so, we mixed enough lipids to give 0.2mg/mL total lipid concentration in 7mL of final solution, dried them in a glass vial with the screw wrapped with teflon tape under a stream of N_2 gas, and incubated o/n in a dessicator. Then, the vial was introduced into a glovebox. Inside the glovebox, we prepared a 5.3:1.2 volumetric ratio mix of silicone oil and mineral oil, respectively. We then dissolved the dried lipid films in 50μL of chloroform and diluted them with 400μL of decane. Next, we added 6.5mL of the oil mix to each lipid vial while continuously mixing by vortexing. Finally, we removed the vials containing the lipid-in-oil solution from the glovebox, sealed them with parafilm, and sonicated them in an ice bath for 15 minutes using a bath sonicator (Branson 2510 Ultrasonic Cleaner, Marshall Scientific) to break down any remaining lipid clumps.

The GUV preparation was conducted at room temperature (~21℃) using a custom-built spinning chamber setup as described in [259]. We first set the spinning chamber to rotate at 2000rpm (corresponding to a motor voltage of 14.5V on our device), added 700μL of outer aqueous solution (OAS), and carefully added 5mL of the lipid-in-oil solution. Next, 1 mL of lipid-in-oil solution was set aside in a 2mL Eppendorf tube. Droplets of inner aqueous solution (IAS) with a monolayer of lipids were created in the 1mL lipid-in-oil solution through manual emulsification, which involved adding the IAS and scratching the Eppendorf tube vigorously over an Eppendorf holder 10-15 times. Next, we pipetted 1mL of the emulsion into the spinning disc and centrifuged it for 3 minutes. After GUV formation, the spinning chamber was stopped by gradually reducing the motor voltage and we carefully removed most of the oil phase from the edge of the chamber's opening while gradually tilting the disc. Then, we added 233μL of vesicle buffer (VB) to the aqueous phase. We concentrated the GUVs by resting the spinning chamber at a 45° angle for at least 15 minutes so the GUVs sunk. To pick up the GUVs, we cut a 200μL pipette tip and pipetted the solution from the corner of the tilted spinning disk, cleaned the pipette tip of residual oil, and transferred the GUV-containing solution into an Eppendorf tube. After a 5 minute incubation, we pipetted the GUVs from the bottom of the tube and transferred them into the imaging chambers with a cut pipette tip. The imaging chambers were ibidi 18-well μ-slides with glass bottom. For GUV immobilization on the imaging surface, the wells were previously passivated by incubation with 1mg/ml of a 1:1 BSA:BSA-biotin solution in Milli-Q for at least 15 minutes at room temperature, followed by incubation with 1mg/ml of Neutravidin in 3:1 OAS:VB for at least 5 minutes. Subsequently, the wells were washed with 3:1 OAS:VB twice. 40μL of the prepared GUV samples were pipetted in each well that already contained 40μL 3:1 OAS:VB for two-fold dilution. Alternatively, the wells could also be passivated with β-casein. For this, we incubated the wells with 50μL 1mg/mL β-casein for at least 30 minutes, and directly dried the wells with a nitrogen gun.

Septin-actin cortex formation

For the experiments where septin and actin were the only encapsulated proteins, we prepared GUVs encapsulating 800nM septin hexamers or octamers and 4μM actin in conditions that permit polymerization (50mM KCl). To avoid polymerization of proteins before they were inside the GUVs, we prepared a protein mix composed of 85% dark septin complexes and 15% msfGFP-labeled septin complexes at a total septin concentration of 4800nM in septin buffer (septin mix) and a mix of 10% ATTO647-actin at a total concentration of 12μM (actin mix) in G-buffer. Then we prepared a 5x septin polymerization buffer (5xSPB) made of 83.33mM Tris-HCl at 7.4 pH, 8.33mM $MgCl_2$, 5mM DTT, 5mM GTP, 2.5mM MgATP, 5mM TROLOX and 5mM PCA.

Once the spinning disk was ready with the OAS and the lipid-in-oil solution, we finished preparing the IAS by mixing, in this specific order: MilliQ water (enough to top up to the final desired volume, usually 25μL, so 6.08μL), 20% 5xSPB (1:5 dilution, 5.4μL), 0.05μM PCD (0.27μL), 6.5% optiprep (1.75μL), 33.3% actin mix (9μL) and 16.67% Septin mix (1:6 dilution, 4.5μL). This yielded a final composition of IAS of 20mM Tris pH 7.4, 1.66mM Tris pH 7.8, 2mM $MgCl_2$, 50mM KCl, 1mM DTT, 1mM GTP, 0.5mM MgATP, 1mM PCA, 1mM TROLOX, 0.05μM PCD, 6.5v% optiprep, 0.067mM $CaCl_2$, 4μM total actin concentration, and 800nM total septin concentration. After the IAS was prepared, we emulsified it into the lipid-in-oil solution as fast as possible and pipetted it into the spinning disk.

Since the IAS had an osmolarity of ~177mOsm/kg, if optiprep was used, and ~330mOsm/kg, if sucrose was used, we prepared the OAS and the VB to have a slightly higher osmolarity. The OAS was made of a glucose solution with an osmolarity of ~189mOsm/kg (if the IAS had optiprep) or ~370mOsm/kg (if the IAS had sucrose). The VB was made of sucrose solution supplemented with 80mM Tris pH 7.4 and had an osmolarity of ~199mOsm/kg (if the IAS had optiprep) or ~380mOsm/kg (if the IAS had sucrose). The osmolarity mismatch lead to a theoretical excess membrane area of ~5% for the samples with optiprep and ~8% for the samples with sucrose [268]. We could observe no difference between the use of optiprep or sucrose.

Septin-actin-Arp2/3 cortex formation

We prepared the IAS similarly as for the TIRF samples, but with higher actin concentration. We used the same OAS and VB as for the eDICE experiments in the absence of VCA and Arp2/3. Briefly, we prepared the same perishables mix as for the TIRF experiments. Then we prepared the protein mixes: 10μM 10% ATTO-647 actin mix, 6μM 15% msfGFP-labelled septin octamer mix, 70μM unlabeled VCA dilution, and 1.31 μM unlabeled Arp2/3 dilution.

Once the spinning disk was ready with the OAS and the lipid-in-oil solution, we finished preparing the IAS by mixing, in this specific order: MilliQ water (enough to top up to the final desired volume, usually 25μL, so 4.56μL), 9 mM Tris-HCl pH 7.4 (1.38μL of a 200mM stock), 1 mM $MgCl_2$ (1.58μL of a 20mM stock), 176.5mM sucrose (1.8μL of a 3M stock), 17.6v% perishable mix (5.4μL), 1.7v% diluted Arp2/3 (0.96μL), 3.1v% diluted VCA (0.53μL), 35v% actin mix (10.8 μL), and 11.8v% septin mix (3.6μL). This yielded a final IAS containing 14.1mM Tris pH 7.4, 1.41mM $MgCl_2$, 176.5mM sucrose, 44.1mM KCl, 1.32mM DTT, 0.88mM GTP, 0.44mM MgATP, 0.044mM PCA, 0.88mM TROLOX, 0.044μM PCD, 0.03mM $CaCl_2$, 3.53μM total actin concentration, 2.21μM VCA, 22nM Arp2/3, and 706nM total septin octamer concentration. After the IAS was prepared, we emulsified it into the lipid-in-oil solution as fast as possible and pipetted it into the spinning disk.

Confocal imaging

The samples were imaged on an inverted Leica Stellaris 8 point scanning confocal microscope using a 63x glycerol immersion objective, a white light laser, and HyD detectors operated in analog mode. Rhodamine and msfGFP were excited sequentially at 573nm (1.5% intensity and 2% gain) and 489nm (23% laser intensity and 80% gain), respectively. Images were acquired with line accumulation set to 2.

We first took large two-dimensional image regions made of the combination of multiple 512x512px images for each sample to screen the GUV population. Then, we focused on imaging z-stacks with a Z-distance of either 0.5μm or 1μm to analyze the 3D structures formed inside the vesicles.

7.5. Supplementary information

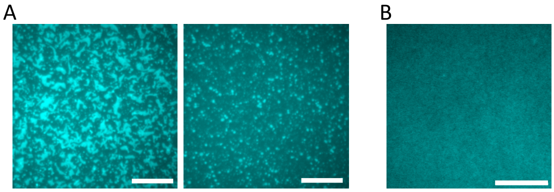

Figure S7.1. Representative examples of SLBs. A. Two examples of 20%PS+5%PIP2 SLBs imaged by TIRF microscopy. B. Corresponding image for a 5%PIP2 SLB. Brighter regions with more labeled lipid are likely due to the presence of lipid aggregates or multiple SLB layers. Scale bars are 10μm.

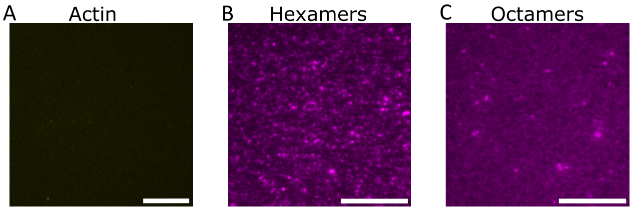

Figure S7.2. Actin and septin complexes alone polymerized on top of 5%PIP2 SLBs. A. representative TIRF image of 1μM actin polymerized on a 5%PIP2 SLB in the absence of a crowding agent. No actin is seen in the TIRF field, indicating that actin does not interact with the bilayer. B. Corresponding image of 250nM septin hexamers, demonstrating membrane binding. C. Corresponding image for 300nM septin octamers, again demonstrating membrane binding. Scale bars are 10μm.

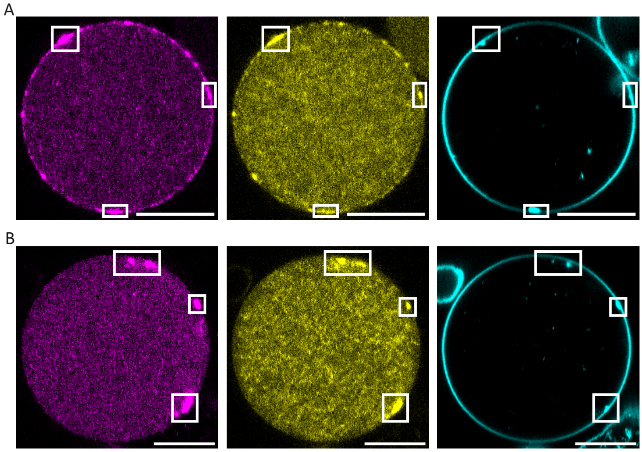

Figure S7.3. Septin-actin bundles in GUVs frequently localize to lipid clusters. A. Representative image of bundles of 800nM septin (magenta) octamer and 1µM actin (yellow) localizing to lipid clusters on the membrane of 20%PS+5%PIP2 GUVs (cyan). B. Corresponding images for 500nM septin hexamers. White boxes encircle lipid clusters co-localized with septin-actin bundles. Scale bars are 10µm.

Acknowledgements

We thank Jeffrey den Haan for his help with protein purification. We thank Katerina Kourkoulou for her involvement in some of the experiments and for useful discussions. Finally, we thank Kristina Ganzinger (AMOLF) for the kind gift of the VCA construct.

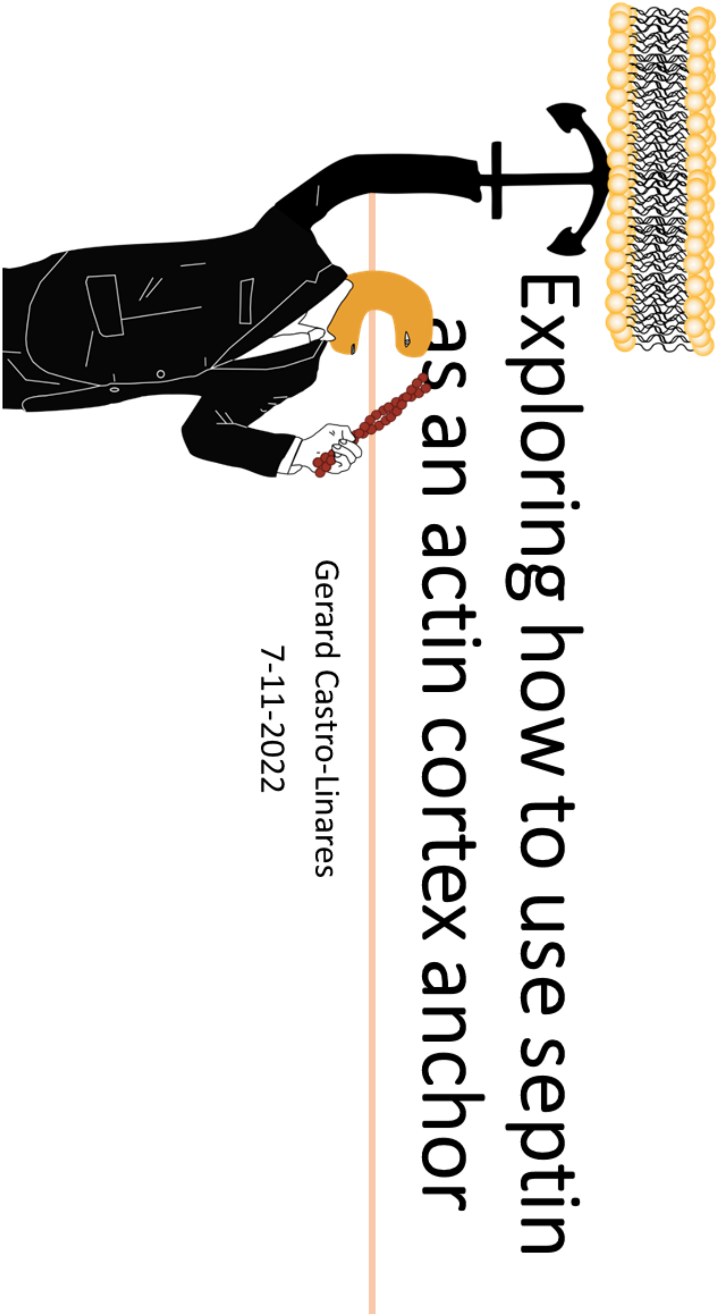
Exploring how to use septin
as an actin cortex anchor
Gerard Castro-Linares
7-11-2022

Chapter 8
Outlook

8.1. Introduction

Cells are the minimal living unit. Past research has shed light on the molecular building blocks that constitute a cell and on how their interactions drive the emergence of specific cell functions. However, we are still far from understanding the basic and minimal properties of life. The use of *in vitro* reconstitution emerged in the last century as a very useful tool to understand how cells function [7]. First, combining purified components can be used as a model of cellular functions, explaining their basic mechanisms. But secondly, new emergent properties that do not occur in cells can be discovered in reconstituted systems that have lower molecular complexity. These new properties can be useful to design modules for synthetic cells, which are emerging as a great tool to not only discover the minimal prerequisites and properties of cells, but also as a sandbox for fundamental research.

Motivated by these developments, in this thesis we investigated the interactions of septins with microtubules (Chapter 3), lipid membranes (Chapter 4 and 5), and actin and myosin (Chapter 6) using *in vitro* reconstitution. We focused on two aims: to understand the functions of septins in cells and to find emergent properties that can be used for the design of a cell shape control mechanism in synthetic cells. In this chapter, we discuss four further research directions to better understand the roles of septins in biological and synthetic cells. These research lines are: finding binding domains on septins, septin-mediated crosstalk, studying the mechanical properties of septin-bound membranes, and expressing septins from a synthetic genome in synthetic cells. In two of these particular research lines, we delve a bit deeper by explaining initial experiments that we have done, which can help guide future research.

8.2. In search of septin's binding domains

In Chapter 3 and [103], we have explored the interactions of septins with microtubules with a special focus on finding the microtubule binding domain (MBD) in septin complexes. We found that the unique N-terminus of SEPT9 is the MBD, while the common

Gerard Castro-Linares designed and performed the septin-action-microtubule crosstalk experiments. Katerina Kourkoulou performed the vesicle fluctuation analysis of GUVs encapsulating septin under the supervsion of Gerard Castro-Linares and Marcos Arribas Pérez.

N-terminus shared by SEPT9_i1 and SEPT9_i3 modulates this interaction by stopping unspecific interactions. These findings can be useful for cell and molecular biology by giving targets that can be mutated in septins to understand the role of the septin interaction in cells. But it can also be useful for the design of a synthetic cell. For example, by regulating the expression of SEPT9, we can control the effect of septin on microtubules: expressing septin hexamers can lead to microtubule dynamic arrest, expressing septin octamers with SEPT9_i1 can stabilize microtubules by reducing their shrinking speed, while expressing septin octamers with SEPT9_i3 can stop septin-microtubule interactions.

This illustrates how finding the specific domains of septins that interact with other components of the cell is of vital importance in the septin field. In the context of septin interactions with the membrane, there are three regions that have been proposed to mediate septin-membrane binding: a polybasic stretch of amino acids on the N-terminus of the SEPT2, SEPT3, and SEPT7 subfamilies [138, 222, 228], another polybasic region located in the GTP-binding domain and conserved in all subfamilies of septin [139, 229], and an alpha-helical domain located close to the polybasic domains [230]. However, these regions have been proposed based on experiments with monomeric septins or fragments thereof rather than intact oligomers. Since septins need to polymerize(Chapter 4, and [82, 96, 139]) and to form paired filaments [96] to bind lipid membranes, past results with monomers still need to be validated with oligomers, where the membrane-binding domain could be located elsewhere. Knowing that septins bind phosphatidylinositol 4,5-biphosphate (PIP2), a similar approach as used for microtubules can be used: bioinformatic analysis of the septin sequence in comparison with other PIP2-binding proteins such as ezrin or anillin [240, 355]. Using septin mutagenesis for *in vitro* reconstitution and *in vivo* experiments can then prove whether these domains are important for septin-membrane binding. Finally, as mentioned above, septin polymerization and pairing are critical for septin-membrane binding. Therefore, using high resolution imaging is crucial to check whether septins polymerize/-pair by themselves and on membranes depending on the domain under study.

8

Similarly, there is one report indicating that SEPT9 mediates septin-actin interactions [130]. This report points to the N-terminal region of SEPT9 (from amino acids 1-143), which also contains the MBD, as the actin binding domain. However, this study was based on SEPT9 alone, and we show that septin hexamers are also able to bind and bundle (Chapter 6 and [102]) actin, and even anchor (Chapter 7) it to membranes. Although, septin hexamers bundle actin less efficiently than octamers, it is clear that septin oligomers lacking SEPT9 can still bind actin. Therefore, more research is necessary to identify why septin oligomers bind and bundle actin filaments. We propose a similar approach of using bioinformatics to compare septins with other actin binding proteins (ABP), and then validating the hits with *in vitro* and *in vivo* experiments including high resolution imaging.

8.3. Septin-mediated crosstalk

Cytoskeletal crosstalk is recently gaining attention as a key player in many important cellular processes such as mechanical stability and cell shape control [69, 174, 175]. This crosstalk is mediated by molecules, called cytolinkers, that can bind simultaneously to two distinct types of cytoskeletal filaments [175]. Additionally, the crosstalk between the membrane and actin and microtubules is also important, not only to reshape the cell but also to control where this reshaping occurs, such as in cell division [174, 356, 357]. Septin, as a protein with the ability to directly interact with lipid bilayers, actin filaments, and microtubules, could potentially be an important cytolinker. Therefore, it is of the utmost importance to explore whether and how septin mediates crosstalk between important cellular components. Additionally, understanding how septins interact with multiple cell constituents at once is vital in order to use septin for synthetic biology since (1) the knowledge can be used for the design of synthetic cell modules and (2) to avoid septins having unspecific and unwanted interactions with other cell modules.

With this in mind, we have explored in Chapter 7 how septins mediate crosstalk between model lipid bilayers and actin filaments, and found that septins are able to anchor actin filaments and bundles to lipid membranes. This is a first step to build a synthetic cell cortex that can be tuned by changing the septin species, the septin concentration and adding other proteins, such as the actin nucleator Arp2/3.

In an animal cell-inspired cell division module, microtubules must separate the synthetic chromosomes and indicate where the midplane of the cell is, so the actin cortex can form a contractile ring to divide the cell. Therefore, is is vital to understand how septins could participate in this process. With this in mind, we performed initial experiments to study how septin octamers containing SEPT9_i1 (Oct_9i1) mediate crosstalk between actin filaments and microtubules. To do so, we grew microtubules from stable seeds attached to a coverslide, and then added a mix of Oct_9i1, tubulin, and G-actin (Fig. 8.1). As expected, septins quickly bound microtubules and started to follow their dynamics. Around ~10 minutes after adding the mix, the first actin bundles started to appear on top of the microtubules, and microtubules grew, so did the actin bundles (Fig. 8.1A and B). Around ~30 minutes later, septin and actin had formed a network of bundles. Colocalized with these bundles, we could observe microtubules that had stopped their dynamics (Fig. 8.1C and D).

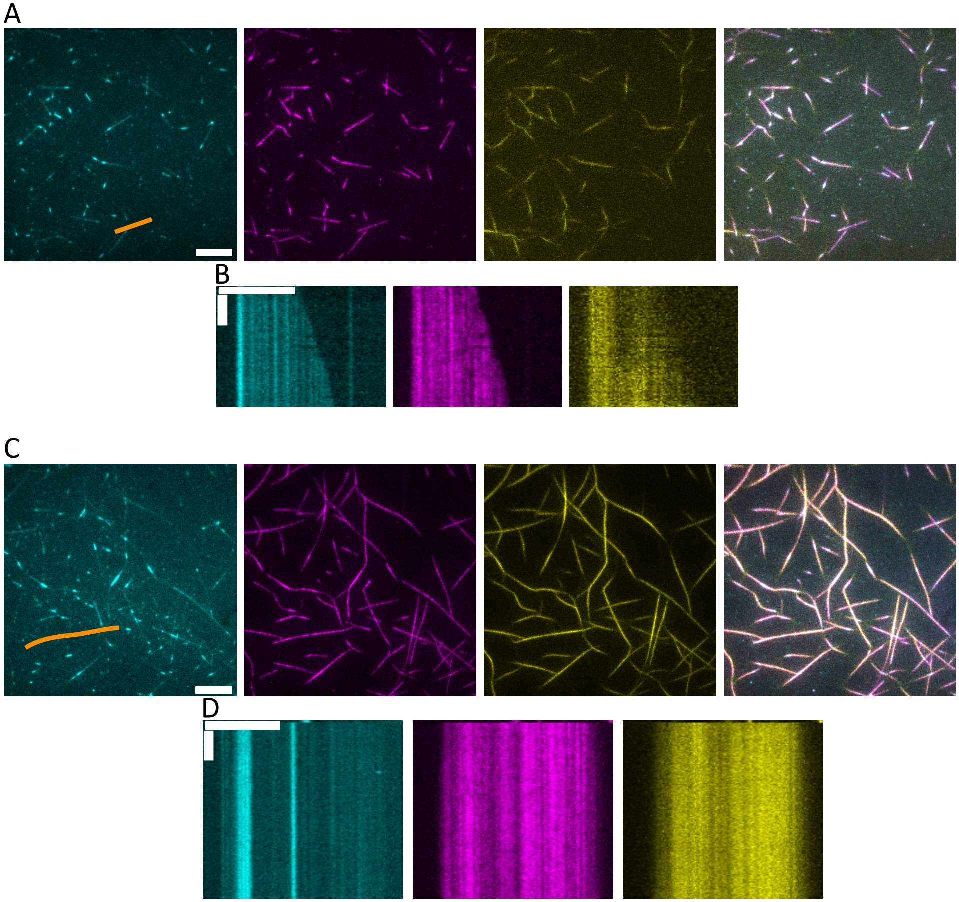

Figure 8.1. MT dynamic assay in the presence of Oct_9i1and actin. A. TIRF microscopy image showing microtubules (cyan), Oct_9i1 (magenta), and actin (yellow) in a septin-mediated microtubule-actin crosstalk experiment ~10min after the three components were combined. B. Representative kymograph (of the orange line in A) showing a microtubule, Oct_9i1 and actin growing in the same region ~10min after the three components were combined. C and D. Corresponding images and kymographs of the same sample ~30 minutes later. Horizontal scale bars are 10μm. Vertical bar is 25 seconds.

These results indicate that septin, specifically Oct_9i1, can indeed mediate actin-microtubule crosstalk, as found before for septin hexamers binding stable microtubule with stable or dynamic actin filaments [199]. However, these experiments have only been repeated twice, and there are multiple open questions. For instance, we do not know how the concentration of septin will affect this process by modulating the strength of the actin-microtubule binding. Additionally, it would be also be interesting to see how other types of septin oligomers affect this crosstalk. For instance, septin hexamers that stop microtubule dynamics by themselves, or septin octamers containing SEPT9_i3, that do not interact with microtubules. Exploring these possibilities could give ideas on how to tune actin-microtubule crosstalk in synthetic cells by controlling the amount and the type of septin expressed. Finally, these experiments were done in 2D, with microtubules anchored to the surface by the seed, and actin and septin crowded to the surface by methylcellulose. Moving these systems to 3D chambers imaged with confocal microscopy would provide a more physiological environment. Finally, moving this system to supported lipid bilayers (SLBs) or giant unilamellar vesicles (GUV) would be interesting to explore how septins mediate crosstalk between a lipid bilayer, that needs to be reshaped or mechanically stabilized, and actin or microtubules, with need to drive this reshaping or mechanical stabilization.

8.4. Mechanical properties of septin-bound membranes

As shown in Chapter 4, septins are able to directly bind lipid membranes forming either a filament-based or a bundle-based network. together with the ability of septins to reshape GUVs to bind to their preferred curvature (Chapter 5), this provides evidence that septins might reinforce a model lipid bilayer by themselves. This is important for the design of a synthetic cell, but also to study cell mechanics. In a recent study by Laplaud et al. [257] it was found that the stiffness and thickness of a cell membrane with impaired actin polymerization remained higher than what is expected for a naked membrane. This suggests that proteins other than actin could be forming a membrane-bound structure that reinforces the cell membrane. We think, and hope, that septins are a likely candidate to do so due to their ability to bind membranes and form a meshwork *in vitro*. To test this possibility, one would need to measure the mechanical properties of GUVs [358].

In our case, we used vesicle fluctuation analysis (VFA), which is a non-invasive approach to calculate the bending rigidity (κ) and tension (σ) of GUVs. Since the free-standing bilayer of a GUV is just a few nanometers thick, it is highly deformable and prone to thermally induced bending fluctuations known as undulations. Under low tension conditions, these fluctuations can be observed using light microscopy. This allows for the experimental determination of κ and σ, which set the amplitude of the fluctuations [269, 359–361]. We have performed initial VFA trials for GUVs encapsulating septin complexes, such as the ones prepared in Chapter 5. However, we encountered several problems. First, as detailed in Chapter 5, eDICE-produced GUVs encapsulate and are surrounded by several artifacts, such as lipid aggregates, membrane tubes and vesicle aggregation (Fig. 8.2A). We could thus only obtain a small set of GUVs for which we could measure the bending rigidity. And second, the setup required for imaging the septin-encapsulating GUVs at a framerate high enough for VFA presented spectral crosstalk between the lipid bilayer and the septin fluorophore, leading to an inability to distinguish between GUVs with and without septin on the membrane (Fig. 8.2B). Nevertheless, we managed to image and analyze between 6 and 9 GUVs per condition. We found that GUVs composed of 100% phosphatidylcholine (DOPC), which do not recruit septin, consistently had κ values from 8 to $14 k_B T$. In contrast, GUVs with membranes containing 20% phosphatidylserine (DOPS) and 5% PIP2 encapsulating either septin hexamers or octamers, had a wider distribution of κ values ranging from 10 to $35 k_B T$ (Fig. 8.2C). This suggests membrane-bound septins increase the bending rigidity of the membranes.

However, we also found that many of the GUVs in all the samples displayed no fluctuations, which is indicative of stiffer or more tense membranes. Therefore, we suggest that future research in this direction should use active mechanical manipulation

8

of GUVs [358], for instance by micropipette aspiration [362], acoustophoresis [363], or nanoindentation [333].

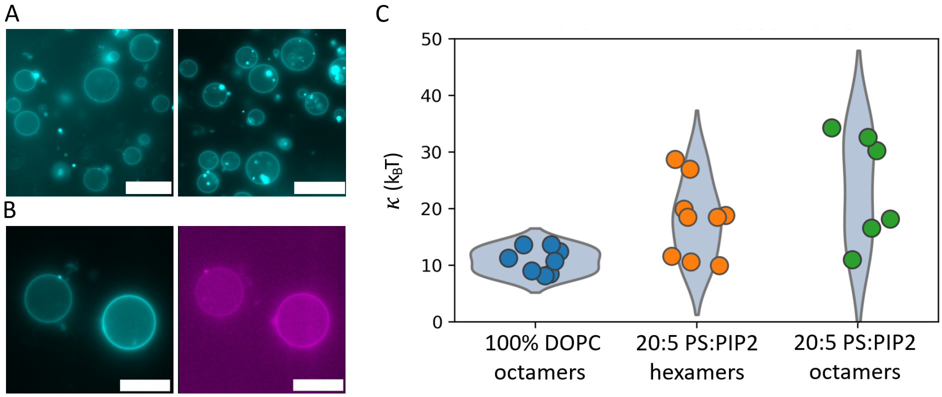

Figure 8.2. Measuring bending rigidity with VFA. A. Representative image of the septin-encapsulating GUVs showing several artifacts that hamper VFA. B. Representative image of a couple of septin-encapsulating GUVs illustrating the inability to distinguish between GUVs with or without membrane-bound septins due to spectral crosstalk in the VFA setup. C. Bending rigidities obtained for 100% DOPC GUVs encapsulating septin octamers (blue, N = 8 GUVs), and 20% DOPS + 5% PIP2 GUVs encapsulating either septin hexamers (orange, N = 9) or septin octamers (green, N = 6). Circles correspond to individual vesicles, while the gray area represents their distribution.

8.5. Expressing septins in synthetic cells

In order to use septins in synthetic cells it is of vital importance to express all the proteins and RNAs needed from a synthetic genome. In our systems we have used purified hexamers and octamers, as described in Chapter 2. During the purification process, we remove all the septin complexes that do not contain SEPT2 and SEPT7 (for hexamers) or SEPT9 (for octamers), yielding hexamers (mostly) and trimers or octamers (mostly) and tetramers. Therefore, we do not know what is the effect of having differently sized septin oligomers in the mixture. Purifying all septin oligomers produced in *Escherichia coli* is challenging because adding an affinity tag to a single septin subunit biases the purified oligomers towards containing that specific subunit. Therefore we propose to tackle two tasks at once by doing experiments in which septins are expressed in an *in vitro* transcription/translation system, preferably the well-defined PURE systems [364]. It is clear that PURE does not affect model lipid bilayers, since there is extensive research on encapsulating it in GUVs [327, 365, 366], even with cDICE [259]. However, it is not clear what is the effect of the PURE environment on other components, such as actin, microtubules (which cannot be expressed in current PURE systems) and septins. First, we should check the activity of these proteins in the PURE environment, to assess whether they can function properly. This can be done by simply polymerizing the purified proteins in PURE buffer. If polymerization is possible, two directions open. First, we can combine the purified proteins in the PURE environment to check whether the interactions described in the thesis are conserved. Second, the protein expression levels should be optimized in PURE. For septins, we can use the current bacterial-inspired PURE system. After expression, their oligomeric state and functional ability need to be assessed using the strategy detailed in Chapter 2. Future research could even explore how to build genetic networks that control the expression of septins to tune the oligomeric state and the subunit composition.

8.6. Materials and methods

All chemicals were obtained from Merck Sigma unless specified otherwise.

8.6.1. Purification of human septin complexes

Human septin oligomers were purified and their quality was checked as detailed in chapter 2. We used septin hexamers with a subunit order of SEPT2-SEPT6-SEPT7-SEPT7-SEPT6-SEPT2 and septin octamers with a subunit order of SEPT2-SEPT6-SEPT7-SEPT9_i1-SEPT9_i1-SEPT7-SEPT6-SEPT2. Septins were fluorescently tagged with msfGFP on the C-terminus of SEPT2. For purification, SEPT2 contained a his_6-tag at its N-terminus, and SEPT7, for hexamers, or SEPT9, for octamers, contained a Strep-II-tag at its C-terminus.

8.6.2. Dynamic microtubule assay with septin and actin

The dynamic microtubule assays were done similarly as in Chapter 3. Briefly, GMPCPP-stabilized microtubule seeds serving as a nucleation site for dynamic microtubules were prepared using an established double-cycle method [202]. Microtubule seeds were stored in MRB80 (80mM PIPES pH 6.8, 4mM $MgCl_2$, 1mM EGTA) supplemented with 10% glycerol, snap-frozen, and stored at -80℃ until use.

Before the experiment, we prepared flow channels by melting parafilm strips between base piranha-cleaned glass slides. After, we passivated the flow channels by subsequent 10 minutes incubations with 0.2mg/mL Poly(L-lysine)-graft-biotinylated Polyethylene glycol (SuSoS, Cat. # CHF560.00) in MRB80, 0.2mg/mL neutravidin (Thermo Fisher Scientific, Cat. # 10675574) in MRB80, 0.5mg/mL κ-casein (Sigma-Aldrich, Cat. # C0406) in MRB80, 1wt% Pluronic F-127 (Sigma-Aldrich, Cat. # p2443) in MRB80, and MRB80, in that order and without intervening washing steps. We then quickly thawed microtubule seeds, and incubated them for 5 minutes on the channel to anchor them to the surface. Microtubule polymerization was then induced by immediately flushing into the channel 20 µM tubulin (3% rhodamine-labeled tubulin) in a 5:1 volume ratio of MRB80:septin buffer (septin buffer: 20mM Tris pH 7.4, 2mM $MgCl_2$, 300mM KCl, and 1mM DTT) complemented with 0.5 mg/mL κ-casein to prevent unspecific interactions, 0.1% methylcellulose (Sigma-Aldrich, Cat. # M0512) as a crowding agent, 1 mM ATP (Sigma-Aldrich, Cat. # A9187), 1 mM GTP (Sigma-Aldrich, Cat. # G8877) and an oxygen scavenging system composed of 50 mM glucose(Sigma-Aldrich, Cat. # G8270), 200 µg/ml catalase (Sigma-Aldrich, Cat. # C30), 400 µg/ml glucose-oxidase(Sigma-Aldrich, Cat. # G6125), and 4 mM dithiothreitol (DTT) (Sigma-Aldrich, Cat. # 11583786001). After a 5 minute incubation, we added the same mix complemented with 100nM 10% msfGFP-labeled Oct_9i1 and with 1µM 10% ATTO-647 skeletal muscle rabbit actin in G-buffer (2mM Tris pH 7.8, 0.2mM $CaCl_2$, and 1mM DTT). Before flushing the solutions into the channel, they were airfuged for 5 minutes at 30 psi with a rotor at ~4℃ to remove any protein aggregates.

Imaging was done using an inverted Nikon Eclipse Ti-E microscope with perfect focus system, equipped with a FRAP/TIRF Ilas ² system (Gataca Systems), an oil immersion objective (Nikon Plan Apo λ 100× NA 1.45), and a EMCCD camera (Photometrics). Image acquisition was controlled using MetaMorph (Molecular Devices). We used lasers (all from Cobolt) with wavelengths of 488nm (~15% intensity, 50-100ms exposure time), 561nm (~15% intensity, 50-100ms exposure time), and 642nm (~15% intensity, 50-100ms exposure time), which were set to an angle yielding a penetration depth of ~100nm. Images were processed to set brightness and contrast for optimal visualization with FIJI [154]. Kymographs were built with the reslice tool in FIJI by reslicing a manually drawn line that went from the beginning of the microtubule seed to the tip of the microtubule in its maximum length.

8.6.3. Vesicle fluctuation analysis

GUVs encapsulating septin complexes were prepared exactly as in Chapter 5. In order to prevent the formation of lipid tubes by solvent evaporation, GUVs were only placed in the imaging chamber ~15 minutes before imaging. Vesicles were imaged with a Nikon Eclipse Ti microscope equipped with a digital camera (Orca-Flash 4.0, Hamamatsu) and monochromatic illumination with a LED light source (Spectra X, Lumencor), using a 100x oil immersion objective (Nikon, N.A. 1.40). In epifluorescence mode, time-lapse movies of 2000 frames were recorded at the equator of vesicles at an excitation wavelength of 555 nm (or 640 nm for the experiments with ATTO 655 DOPE) for the membrane channel and 470 nm for the septin channel with 50% and 75% LED intensities, respectively, with exposure times of 5 ms, 10 ms, 20 ms and 50 ms. To increase the number of fluctuating vesicles, the lid of the imaging chamber was removed for approximately 15-20 minutes to gradually increase the osmolarity of the sample's buffer through evaporation.

After acquisition of the time-lapse movies at the equatorial plane of the fluctuating vesicles, we employed a custom-written Python script made by Lennard van Buren [367] for the calculation of the bending rigidity and the membrane tension of each vesicle. The analysis of the data was based on five main steps: pre-processing to accommodate for membrane detection [262], tracking of the vesicle contour in time [262], calculating the corresponding fluctuation spectrum [368], selecting the appropriate mode regime for fitting to the theoretical spectrum [361, 368] and, finally, implementing the fitting for the acquisition of the membrane properties [368].


Anchorage of the cytokinetic ring
Gerard Castro-Linares
25-5-2020
Cell from: https://www.businessinsider.com/nikon-small-world-microscope-picture-winners-2016-10?international=true&r=US&IR=T#12-human-hela-cell-undergoing-cell-division-9

THE GALLERY OF

THE SEPTIN CIRCUS:

AN UNFORGETABLE SHOW OF CELLULAR COREOGRAPHY

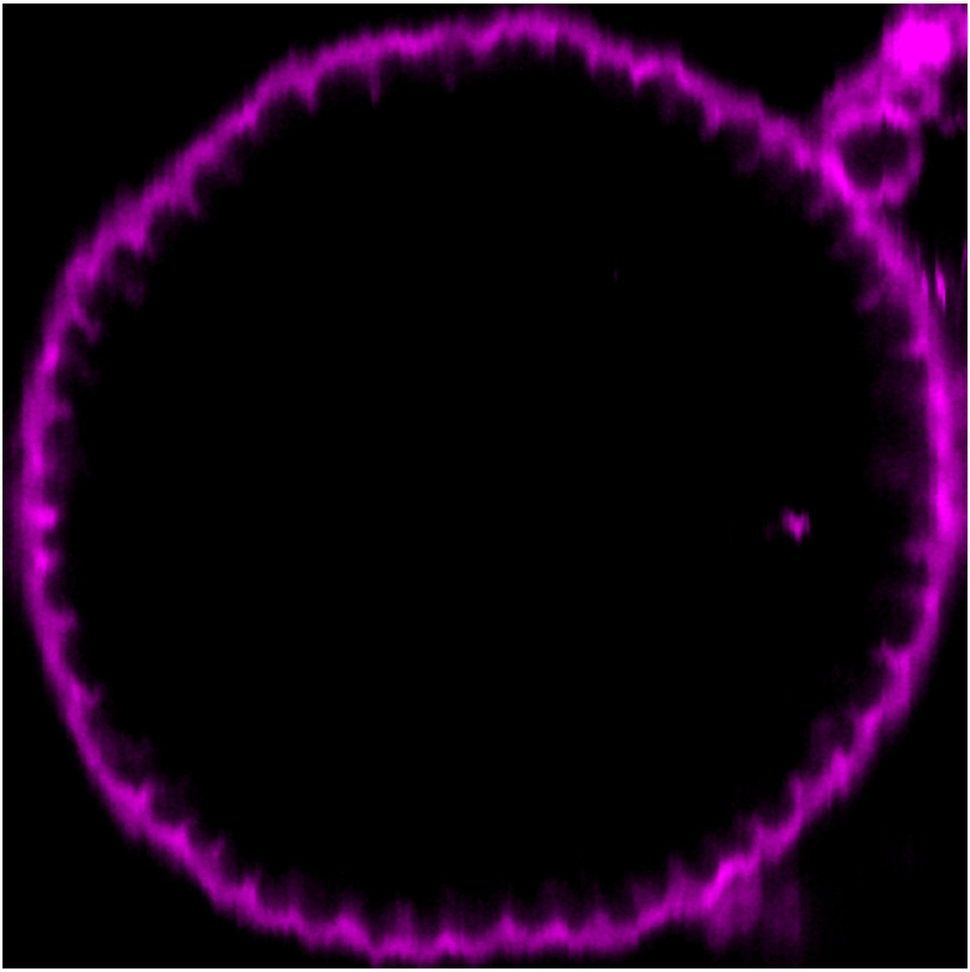

Do you know our lord the Golfball?

Gerard Castro-Linares

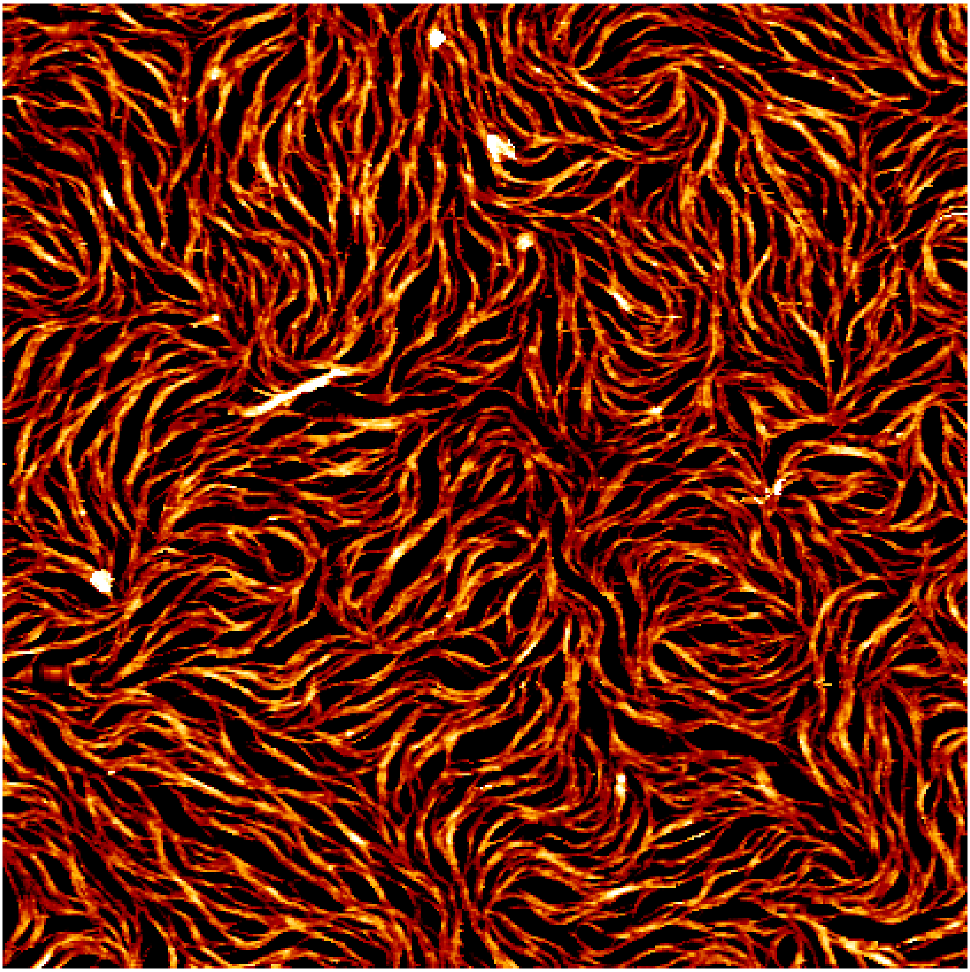

Objective

Djim de Ridder

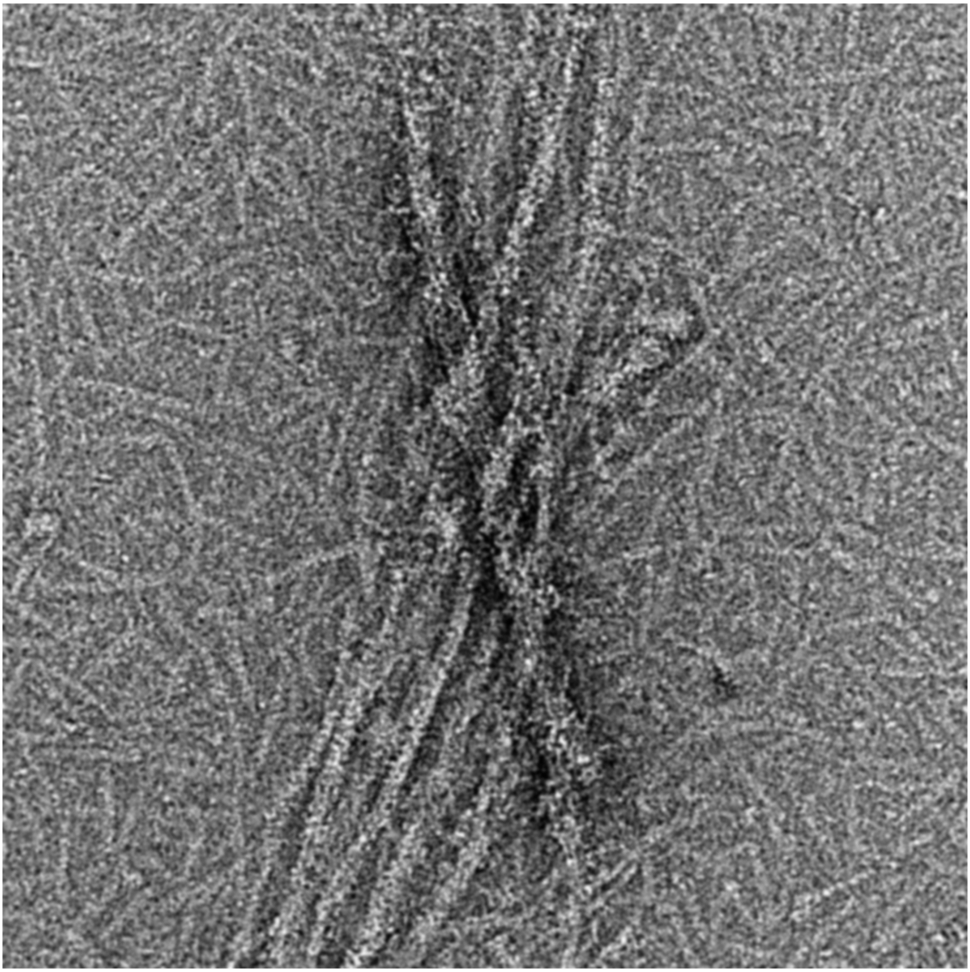

Trapped

Gerard Castro-Linares

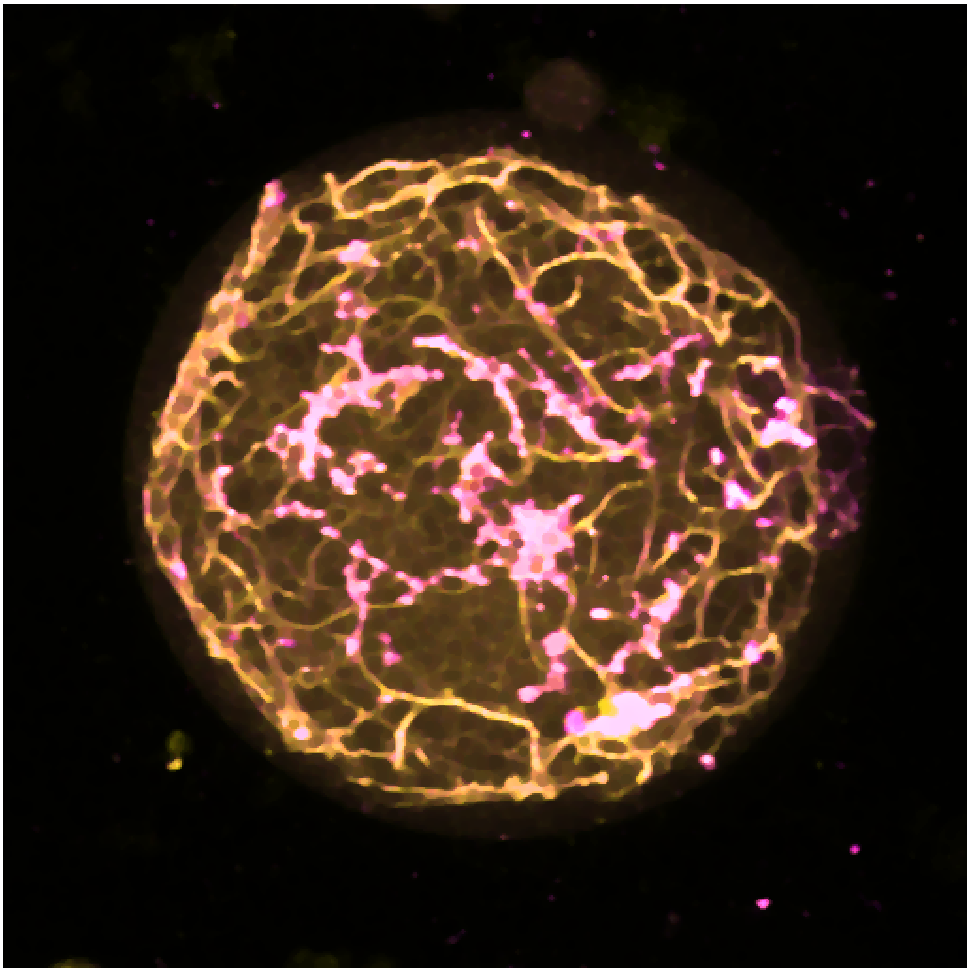

Dream

Elise Perton

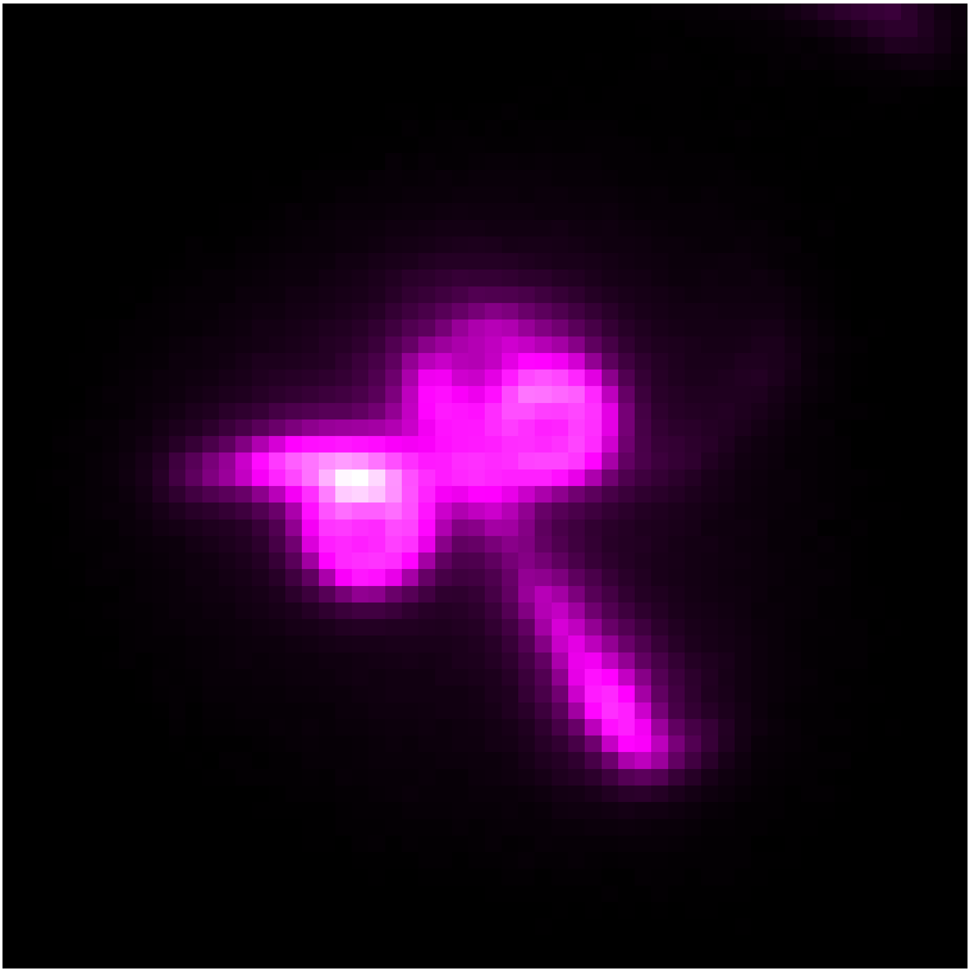

Naughty Boy

Gerard Castro-Linares

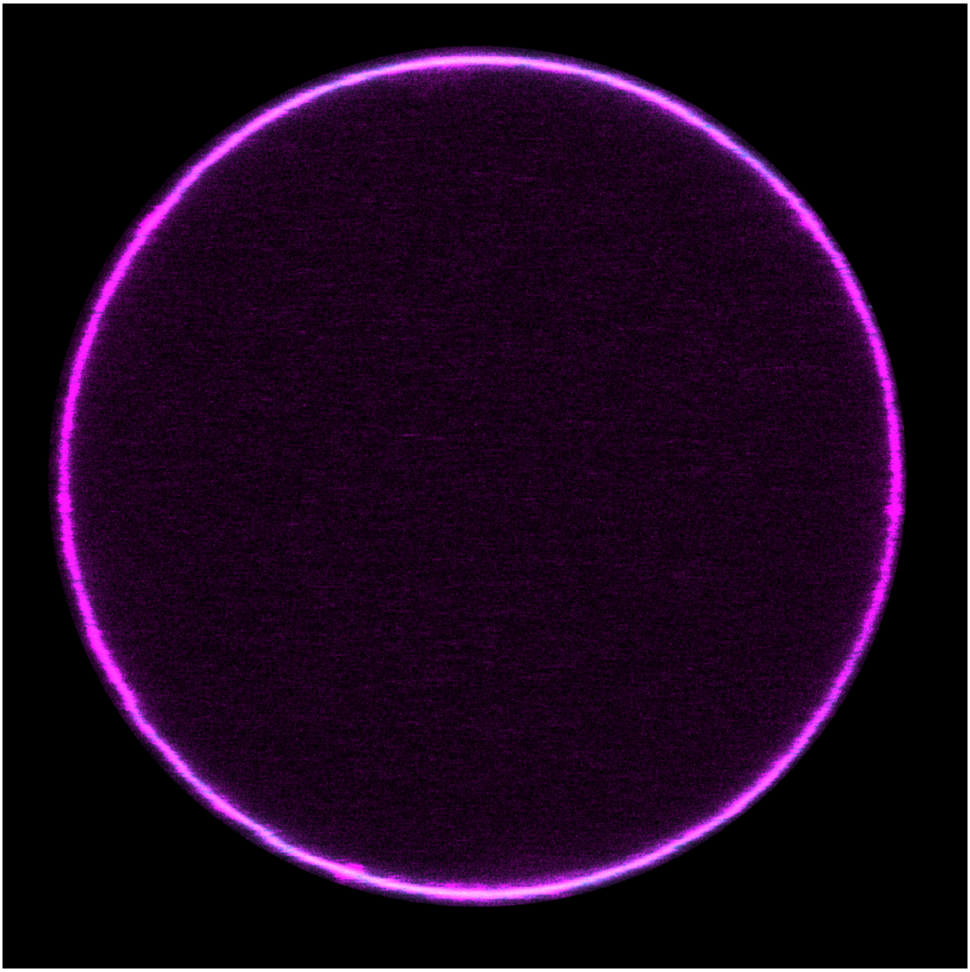

Meticulous

Katerina Kourkoulou

Last Septeam

Sonam Marapin

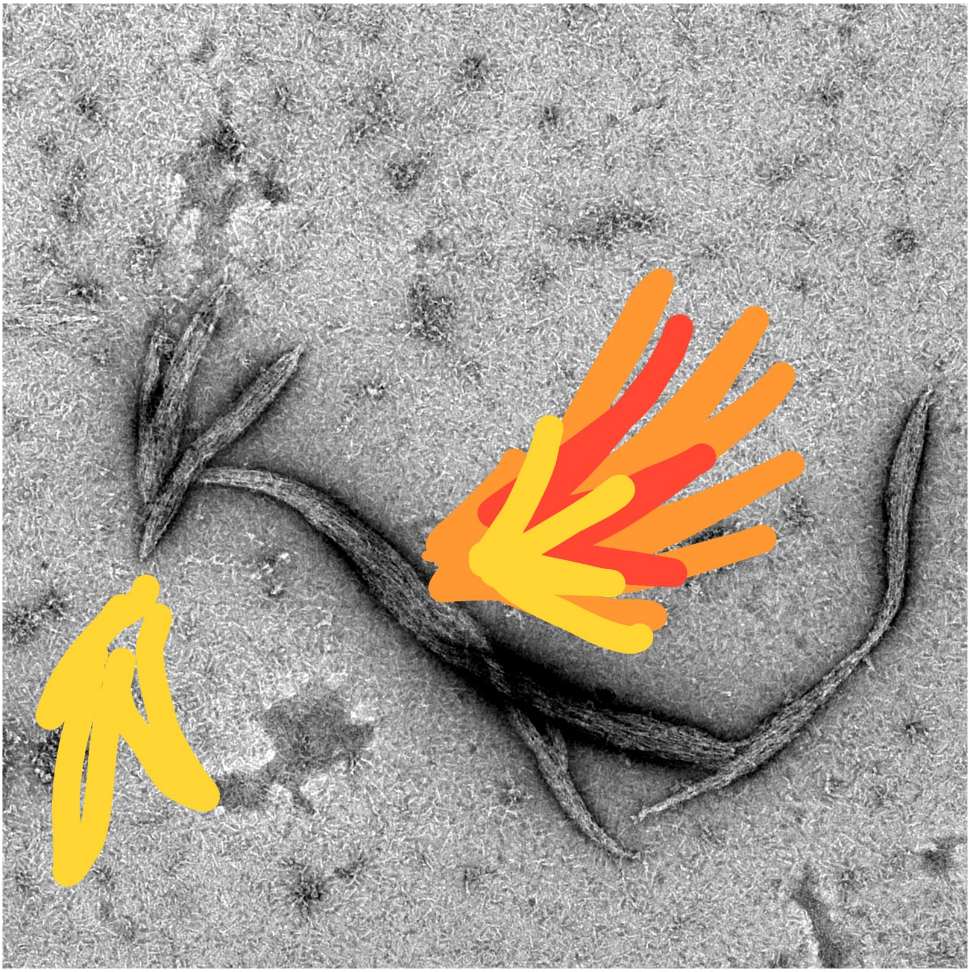

My little dragon

Gerard Castro-Linares and Lucia Baldauf

Box for the -80 freezer with the bottom holes covered with freezer tape, containing 96 wells filled up with water to 80% and PDMS squares used to place devices with flow channels made of parafilm strips sandwitched between a glass slide and a coverslide previously cleaned with base piranha

Gerard Castro-Linares

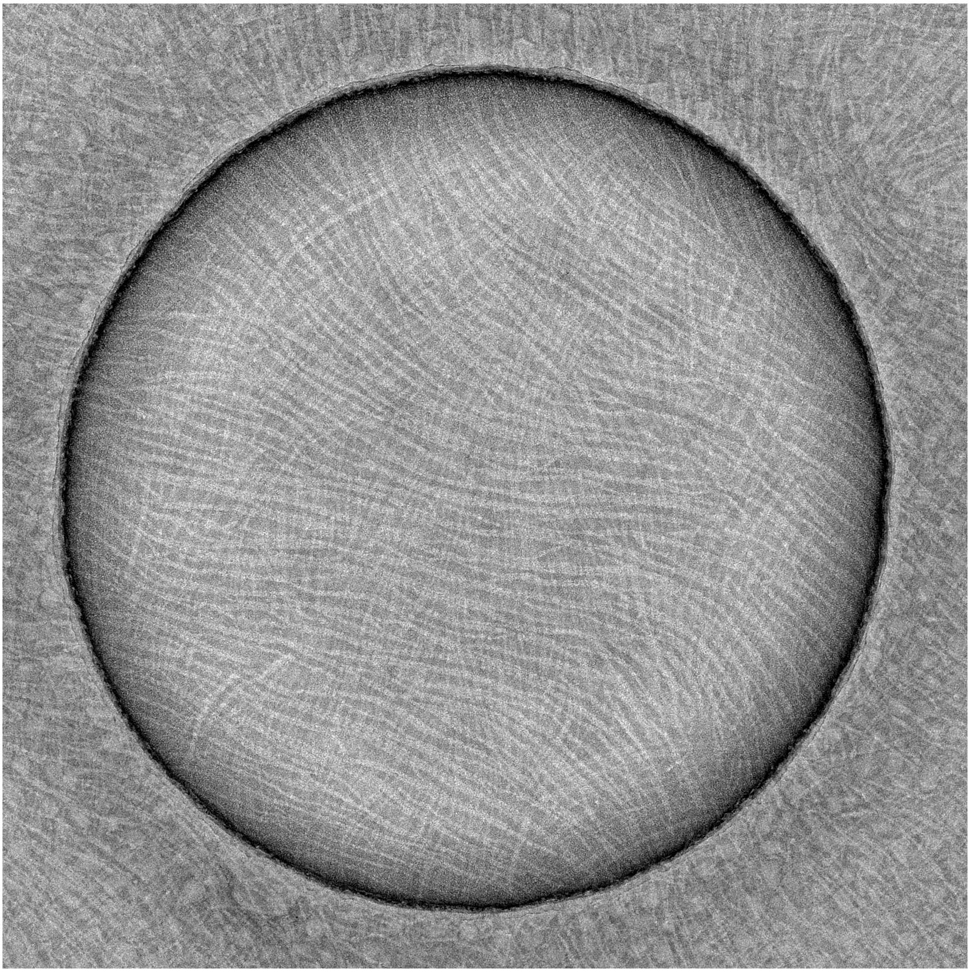

Circle of order

Djim de Ridder

Slippery slope

Irene Istúriz Petitjean

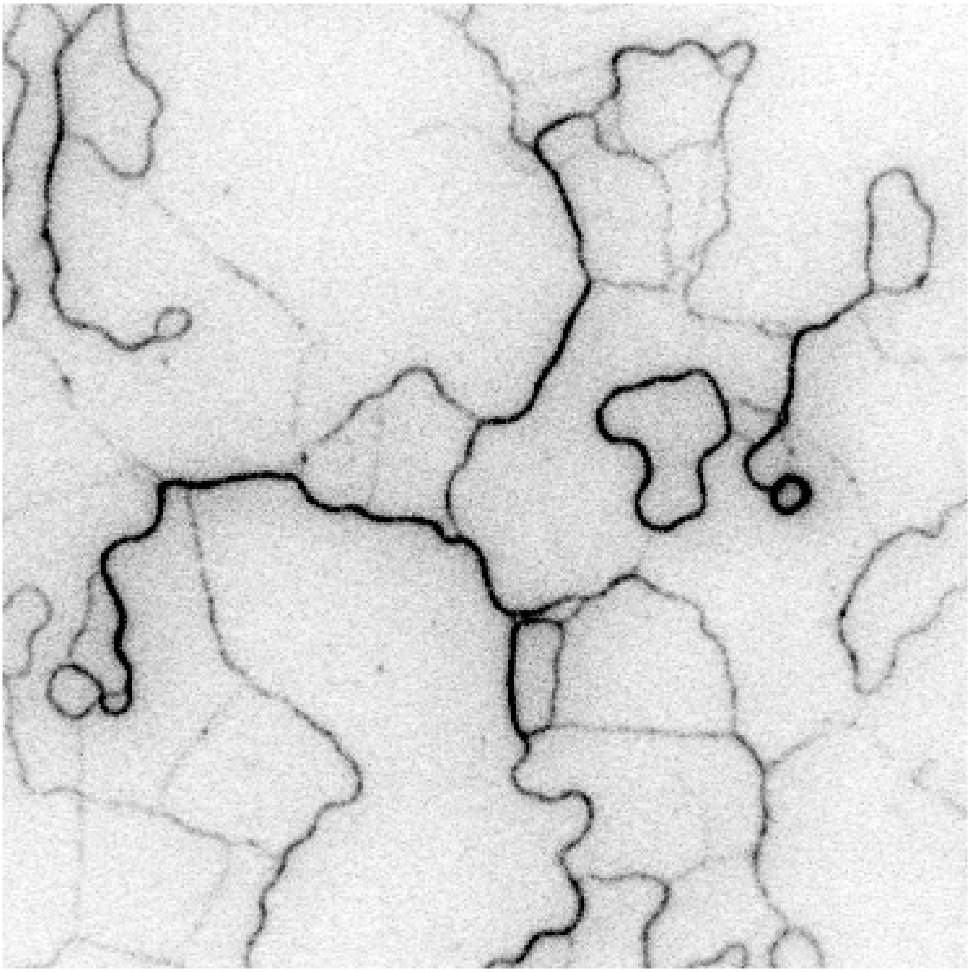

Starting waves

Gerard Castro-Linares

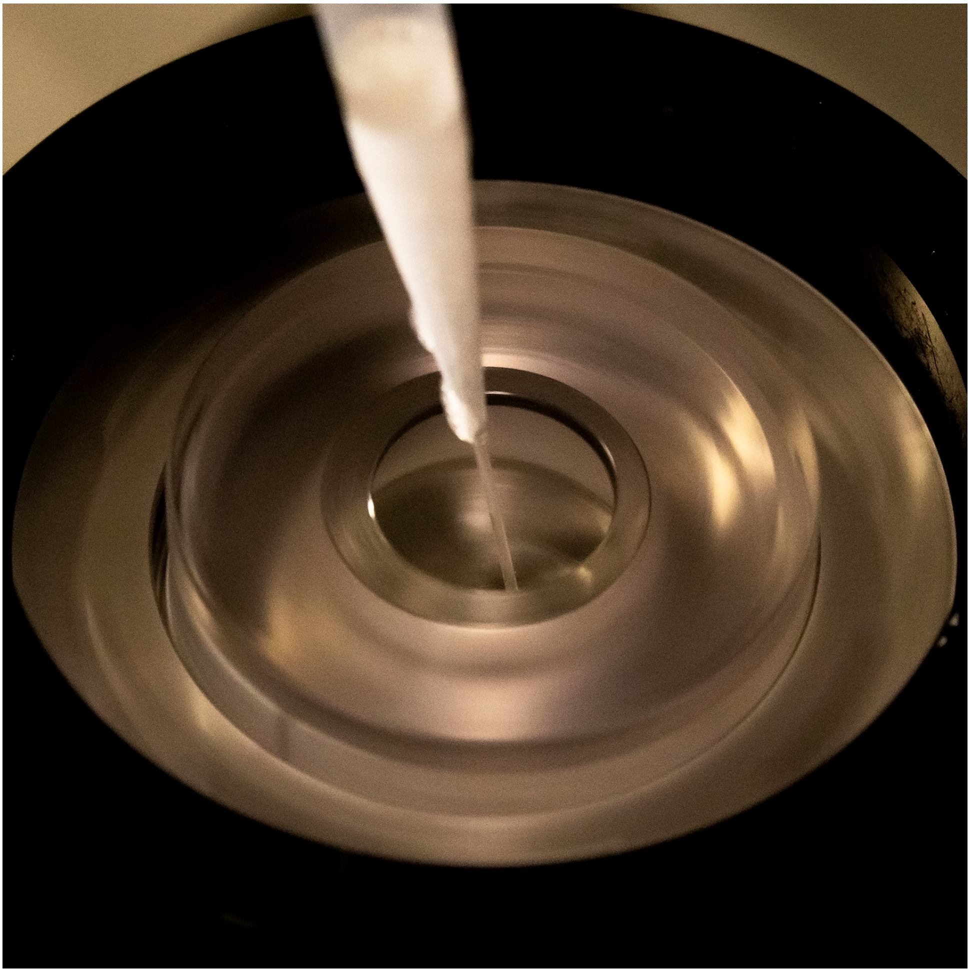

Stochasticity

Gerard Castro-Linares and Marcos Arribas Pérez

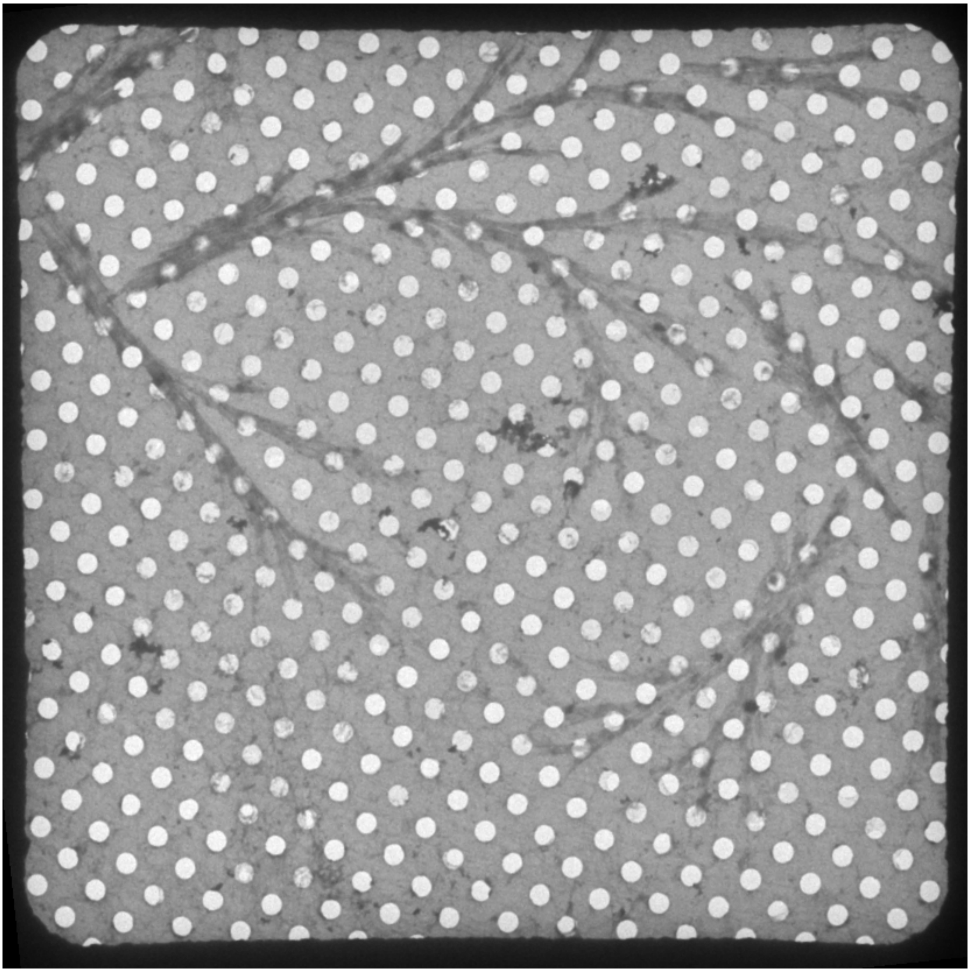

Needle in a haystack

Djim de Ridder

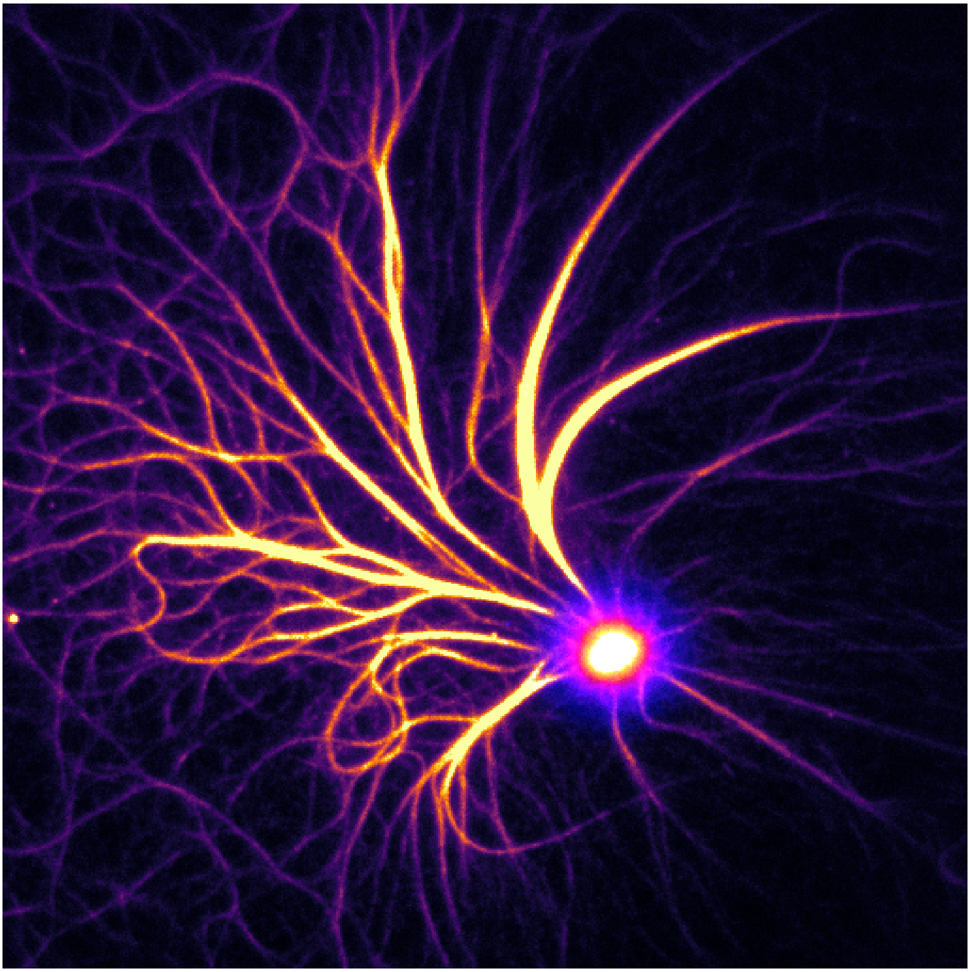

Race

Gerard Castro-Linares

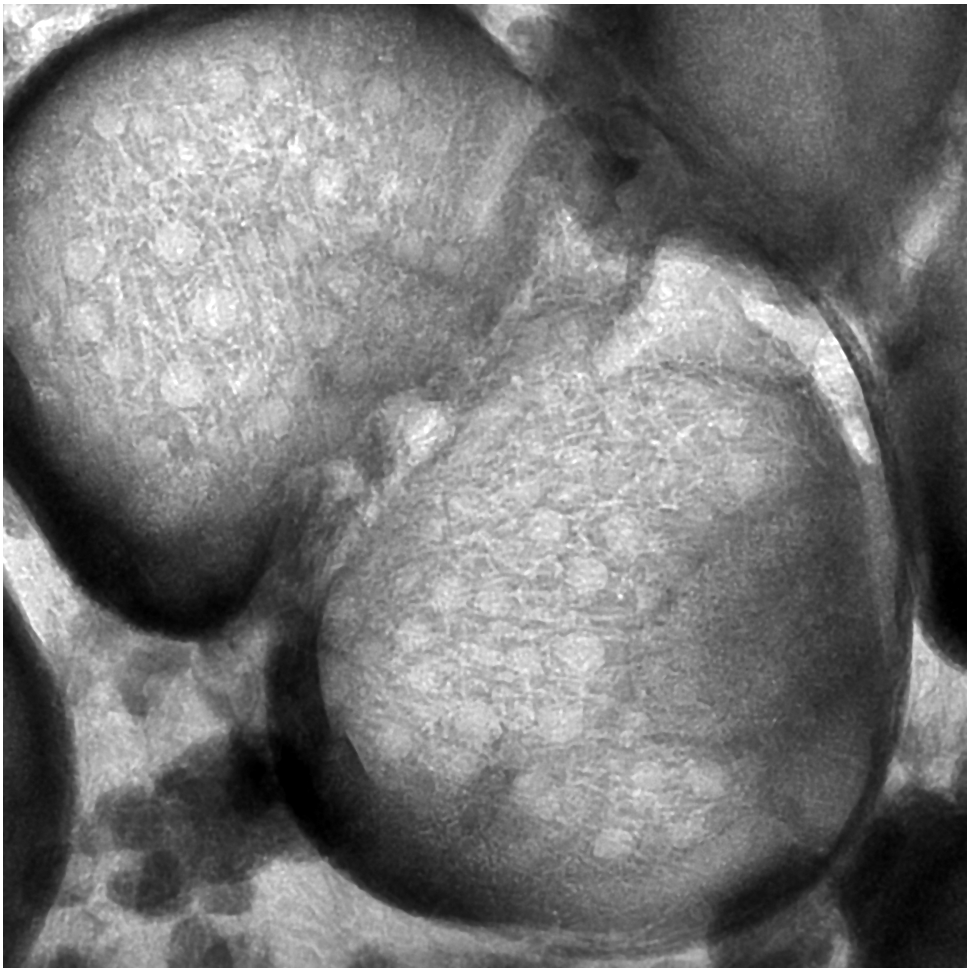

Field of view

Gerard Castro-Linares

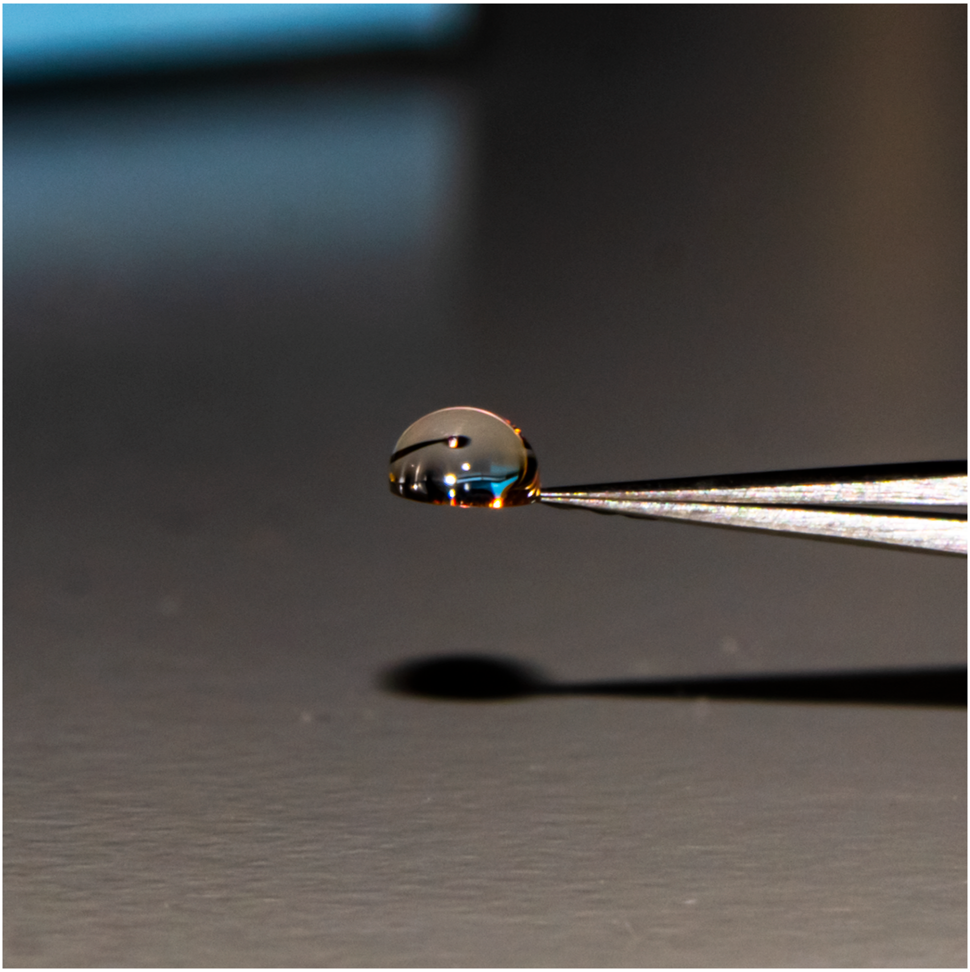

Strive

Gerard Castro-Linares

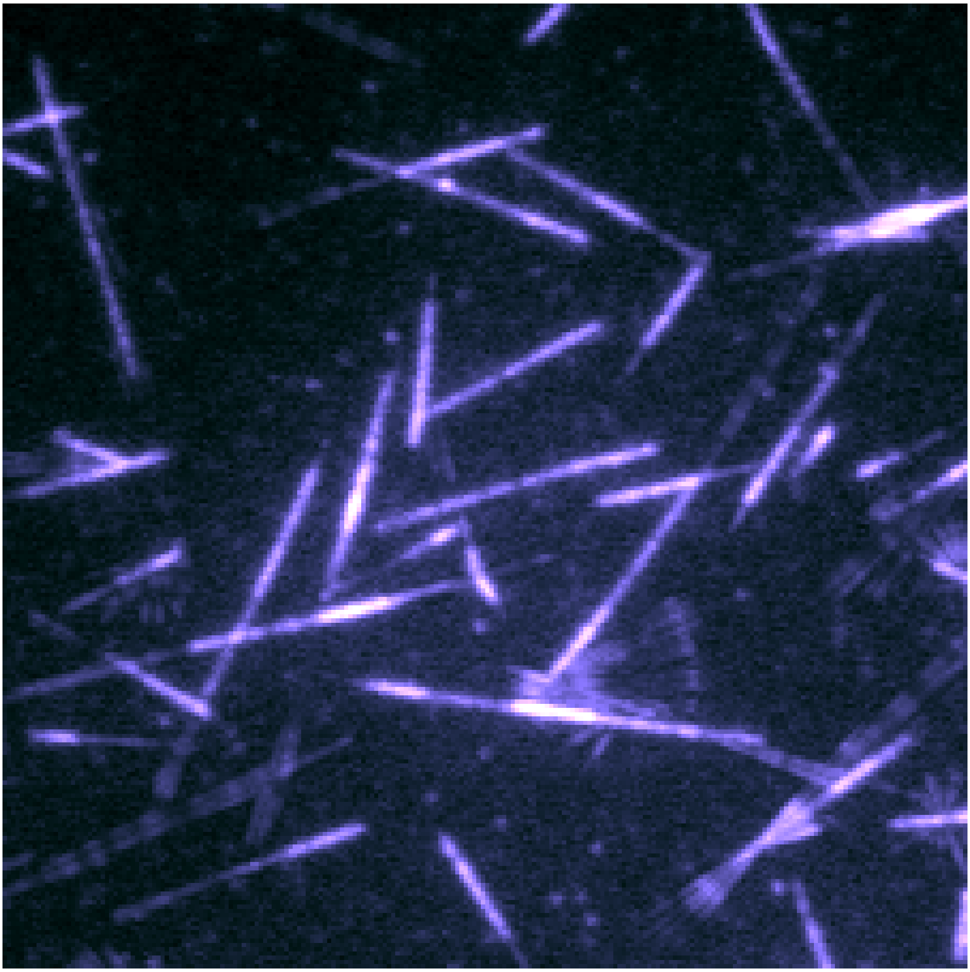

Cosmic roads

Gerard Castro-Linares

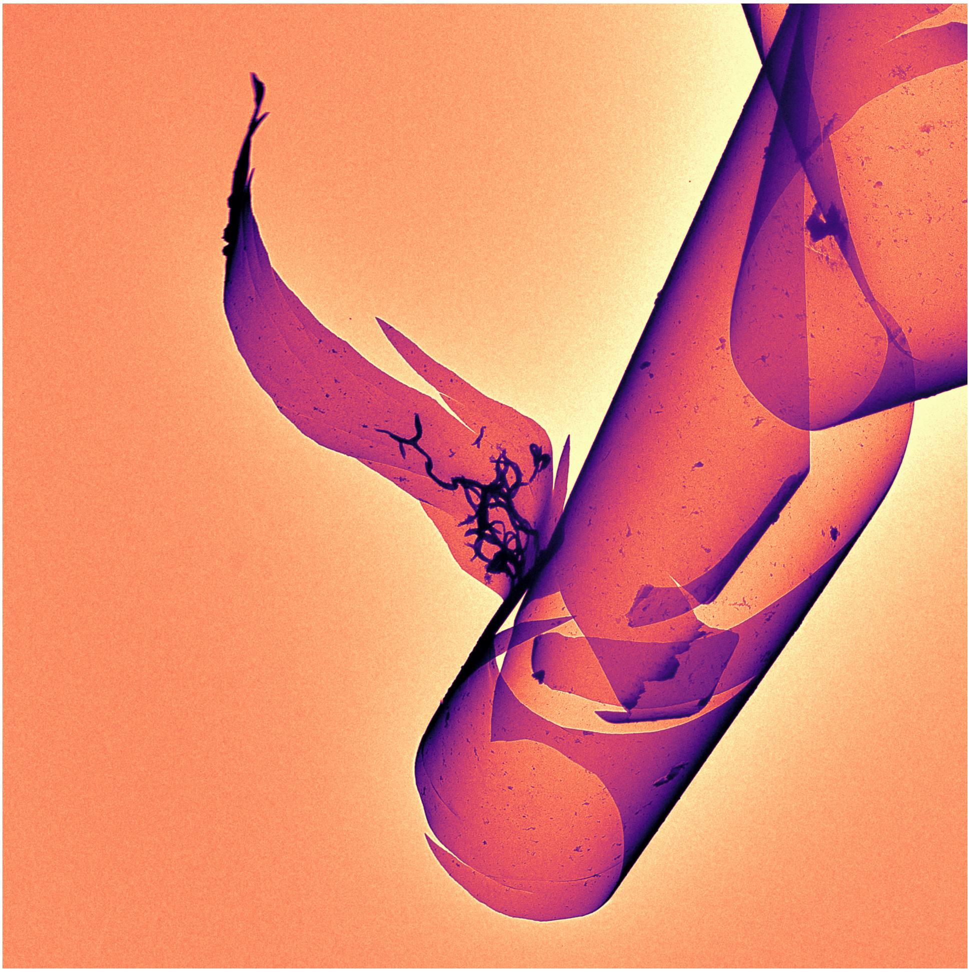

Successful disaster

Gerard Castro-Linares

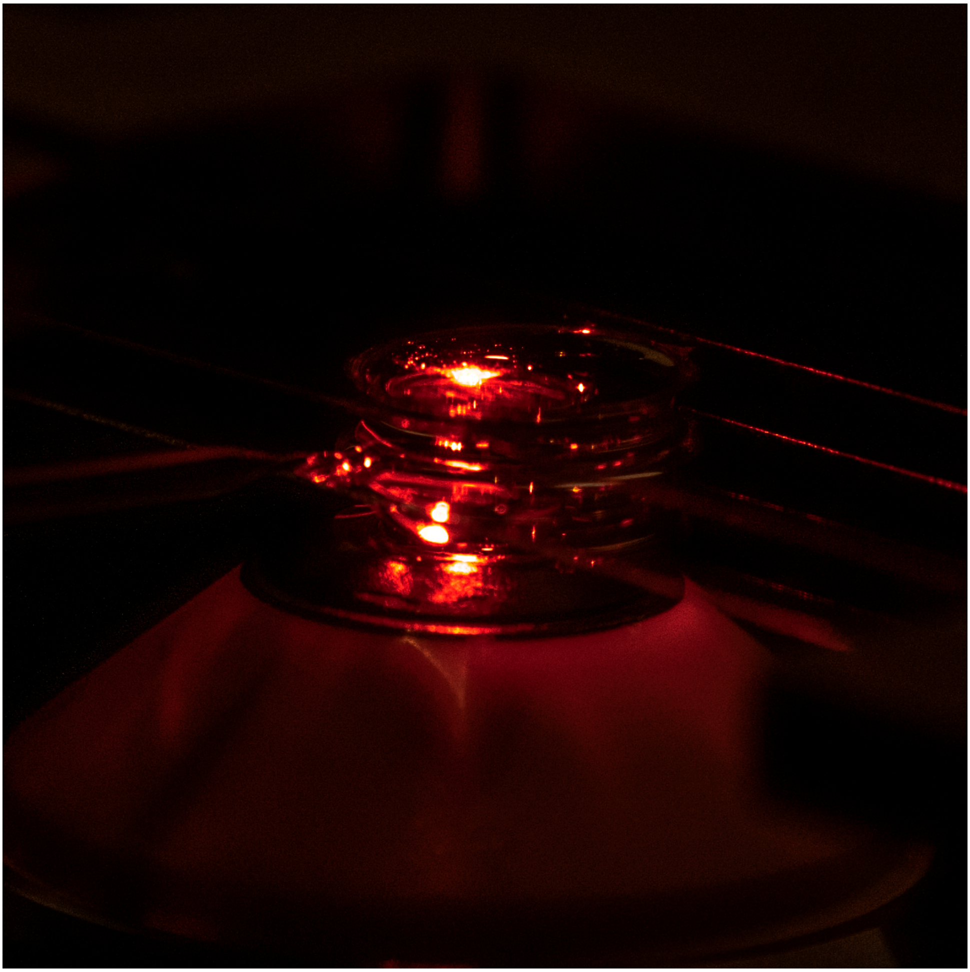

Glow

Gerard Castro-Linares and Nikki Nafar

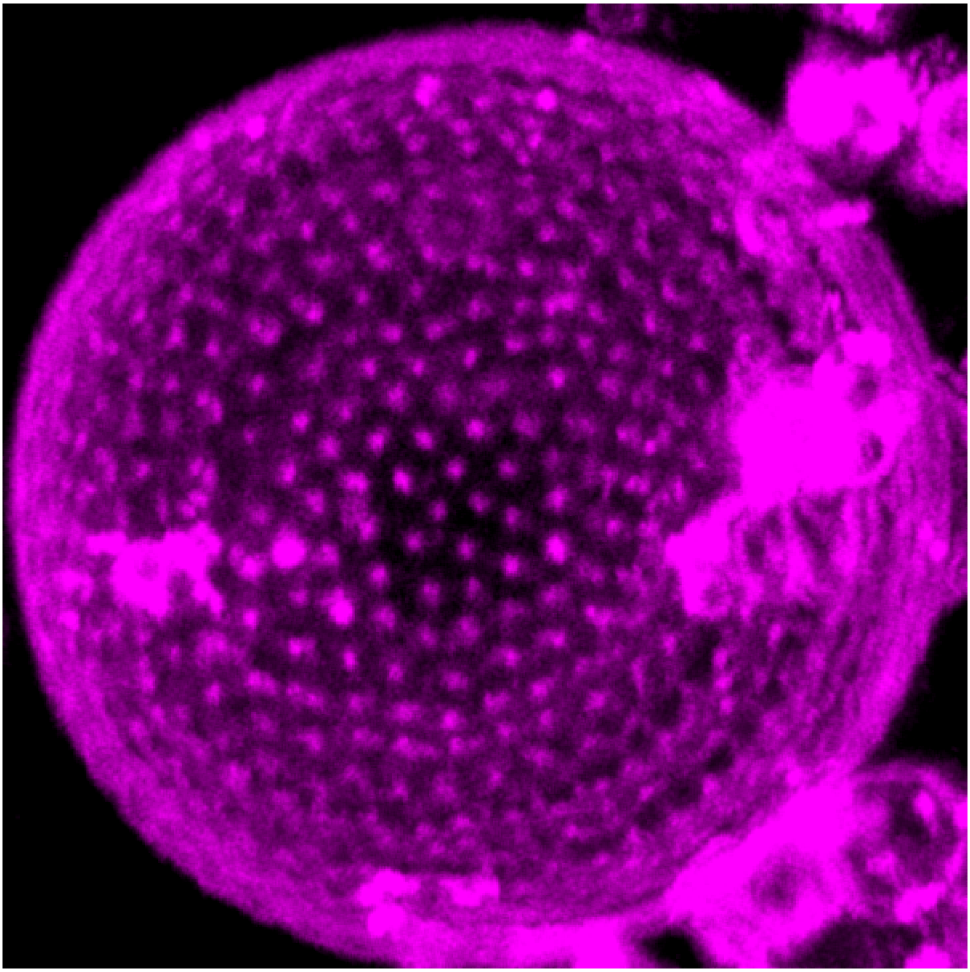

The lord's bottom

Gerard Castro-Linares

Bibliography

References

[1] Robert Hooke. *Micrographia: or, Some physiological descriptions of minute bodies made by magnifying glasses. With observations and inquiries thereupon.* The Royal Society, London, 1665.

[2] Bruce Alberts, Alexander Johnson, Julian Lewi, David Morgan, MArtin Raff, Keith Roberts, and Peter Walter. *Molecular Biology of the Cell.* Garland Science, 6th editio edition, 2014.

[3] Walther Flemming. *Zellsubstanz, Kern und Zelltheilung.* Vogel, F.C.W., Leipzig, 1882.

[4] Kurt Thorn. A quick guide to light microscopy in cell biology. *Molecular Biology of the Cell*, 27(2):219–222, 2016.

[5] Takahiro Deguchi, Malina K. Iwanski, Eva Maria Schentarra, Christopher Heidebrecht, Lisa Schmidt, Jennifer Heck, Tobias Weihs, Sebastian Schnorrenberg, Philipp Hoess, Sheng Liu, Veronika Chevyreva, Kyung Min Noh, Lukas C. Kapitein, and Jonas Ries. Direct observation of motor protein stepping in living cells using MINFLUX. *Science*, 379(6636):1010–1015, 2023.

[6] Hiroaki Kitano. Systems biology: A brief overview. *Science*, 295(5560):1662–1664, 2002.

[7] Kristina A. Ganzinger and Petra Schwille. More from less – Bottom-up reconstitution of cell biology. *Journal of Cell Science*, 132(4):jcs227488, 2019.

[8] Beáta Bugyi and Miklós Kellermayer. The discovery of actin: "to see what everyone else has seen, and to think what nobody has thought". *Journal of Muscle Research and Cell Motility*, 41(1):3–9, 2019.

[9] D. Ewen Cameron, Caleb J. Bashor, and James J. Collins. A brief history of synthetic biology. *Nature Reviews Microbiology*, 12(5):381–390, 2014.

[10] Bryan A. Bartley, Kyung Kim, J. Kyle Medley, and Herbert M. Sauro. Synthetic Biology: Engineering Living Systems from Biophysical Principles. *Biophysical Journal*, 112(6):1050–1058, 2017.

[11] Sandra Fernau, Matthias Braun, and Peter Dabrock. What is (synthetic) life? Basic concepts of life in synthetic biology. *PLoS ONE*, 15(7 July):e0235808, 2020.

[12] Olivia Gallup, Hia Ming, and Tom Ellis. Ten future challenges for synthetic biology. *Engineering Biology*, 5(3):51–59, 2021.

[13] Ivan Ivanov, Sebastiaacuten Loacutepez Castellanos, Severo Balasbas, Lado Otrin, Nika Maruscaroniccaron, Tanja Vidakovicacute-Koch, and Kai Sundmacher. Bottom-Up Synthesis of Artificial Cells: Recent Highlights and Future Challenges. *Annual Review of Chemical and Biomolecular Engineering*, 12(1):287–308, 2021.

[14] Jeong Wook Lee, Dokyun Na, Jong Myoung Park, Joungmin Lee, Sol Choi, and Sang Yup Lee. Systems metabolic engineering of microorganisms for natural and non-natural chemicals. *Nature Chemical Biology 2012 8:6*, 8(6):536–546, may 2012.

[15] Ahmad S. Khalil and James J. Collins. Synthetic biology: Applications come of age. *Nature Reviews Genetics*, 11(5):367–379, 2010.

[16] Tzu Chieh Tang, Bolin An, Yuanyuan Huang, Sangita Vasikaran, Yanyi Wang, Xiaoyu Jiang, Timothy K. Lu, and Chao Zhong. Materials design by synthetic biology. *Nature Reviews Materials*, 6(4):332–350, 2021.

[17] BaSyC - Building a Synthetic Cell, 2017.

[18] Baocai Zhang, Yihong Gao, Lanjun Zhang, and Yihua Zhou. The plant cell wall: Biosynthesis, construction, and functions. *Journal of Integrative Plant Biology*, 63(1):251–272, 2021.

[19] L. Pasquina-Lemonche, J. Burns, R. D. Turner, S. Kumar, R. Tank, N. Mullin, J. S. Wilson, B. Chakrabarti, P. A. Bullough, S. J. Foster, and J. K. Hobbs. The architecture of the Gram-positive bacterial cell wall. *Nature*, 582(7811):294–297, 2020.

[20] Matthew T. Cabeen and Christine Jacobs-Wagner. Bacterial cell shape. *Nature Reviews Microbiology*, 3(8):601–610, 2005.

[21] Atsushi Taguchi, Julia E. Page, Ho Ching Tiffany Tsui, Malcolm E. Winkler, and Suzanne Walker. Biochemical reconstitution defines new functions for membrane-bound glycosidases in assembly of the bacterial cell wall. *Proceedings of the National Academy of Sciences of the United States of America*, 118(36):e2103740118, 2021.

[22] Daniel A. Fletcher and R. Dyche Mullins. Cell mechanics and the cytoskeleton. *Nature*, 463(7280):485–492, 2010.

[23] Yuval Mulla, Anders Aufderhorst-Roberts, and Gijsje H Koenderink. Shaping up synthetic cells. *Physical Biology*, 15(4):041001, 2018.

[24] Philippe F. Devaux. Static and Dynamic Lipid Asymmetry in Cell Membranes. *Biochemistry*, 30(5):1163–1173, 1991.

[25] Gerrit Van Meer, Dennis R. Voelker, and Gerald W. Feigenson. Membrane lipids: Where they are and how they behave. *Nature Reviews Molecular Cell Biology*, 9(2):112–124, 2008.

[26] Mark S. Bretscher. Asymmetrical lipid bilayer structure for biological membranes. *Nature New Biology*, 236(61):11–12, 1972.

[27] A. J. Verkleij and J. A. Post. Membrane phospholipid asymmetry and signal transduction. *Journal of Membrane Biology*, 178(1):1–10, 2000.

[28] Peter A. Leventis and Sergio Grinstein. The distribution and function of phosphatidylserine in cellular membranes. *Annual Review of Biophysics*, 39(1):407–427, 2010.

[29] B. Tu-Sekine and D. M. Raben. Lipid Signaling. In *Encyclopedia of Cell Biology*, volume 1, pages 194–200. Academic Press, jan 2016.

[30] Jorge Bernardino de la Serna, Gerhard J. Schütz, Christian Eggeling, and Marek Cebecauer. There is no simple model of the plasma membrane organization. *Frontiers in Cell and Developmental Biology*, 4(SEP):106, 2016.

[31] Erdinc Sezgin, Ilya Levental, Satyajit Mayor, and Christian Eggeling. The mystery of membrane organization: Composition, regulation and roles of lipid rafts. *Nature Reviews Molecular Cell Biology*, 18(6):361–374, 2017.

[32] Thomas Lecuit and Pierre François Lenne. Cell surface mechanics and the control of cell shape, tissue patterns and morphogenesis. *Nature Reviews Molecular Cell Biology*, 8(8):633–644, aug 2007.

[33] Shang You Tee, Jianping Fu, Christopher S. Chen, and Paul A. Janmey. Cell shape and substrate rigidity both regulate cell stiffness. *Biophysical Journal*, 100(5):L25–L27, 2011.

[34] Julia Gilden and Matthew F. Krummel. Control of cortical rigidity by the cytoskeleton: Emerging roles for septins. *Cytoskeleton*, 67(8):477–486, 2010.

[35] Edward H. Egelman. The structure of F-actin. *Journal of Muscle Research and Cell Motility*, 6(2):129–151, 1985.

[36] Roberto Dominguez and Kenneth C. Holmes. Actin structure and function. *Annual Review of Biophysics*, 40(1):169–186, may 2011.

[37] Pekka Lappalainen, Tommi Kotila, Antoine Jégou, and Guillaume Romet-Lemonne. Biochemical and mechanical regulation of actin dynamics. *Nature Reviews Molecular Cell Biology*, 23(12):836–852, aug 2022.

[38] David Sept and J. Andrew McCammon. Thermodynamics and kinetics of actin filament nucleation. *Biophysical Journal*, 81(2):667–674, 2001.

[39] Thomas D. Pollard and Susan W. Craig. Mechanism of actin polymerization. *Trends in Biochemical Sciences*, 7(2):55–58, 1982.

[40] Elena G. Yarmola and Michael R. Bubb. Profilin: emerging concepts and lingering misconceptions. *Trends in Biochemical Sciences*, 31(4):197–205, 2006.

[41] Miia Bovellan, Yves Romeo, Maté Biro, Annett Boden, Priyamvada Chugh, Amina Yonis, Malti Vaghela, Marco Fritzsche, Dale Moulding, Richard Thorogate, Antoine Jégou, Adrian J. Thrasher, Guillaume Romet-Lemonne, Philippe P. Roux, Ewa K. Paluch, and Guillaume Charras. Cellular control of cortical actin nucleation. *Current Biology*, 24(14):1628–1635, 2014.

[42] David S. Courson and Ronald S. Rock. Actin cross-link assembly and disassembly mechanics for α-actinin and fascin. *Journal of Biological Chemistry*, 285(34):26350–26357, 2010.

[43] Laurent Blanchoin, Rajaa Boujemaa-Paterski, Cécile Sykes, and Julie Plastino. Actin dynamics, architecture, and mechanics in cell motility. *Physiological Reviews*, 94(1):235–263, 2014.

[44] Saravanan Palani, Sayantika Ghosh, Esther Ivorra-Molla, Scott Clarke, Andrejus Suchenko, Mohan K. Balasubramanian, and Darius Vasco Köster. Calponin-homology domain mediated bending of membrane-associated actin filaments. *eLife*, 10:e61078, jul 2021.

[45] Ondřej Kučera, Valerie Siahaan, Daniel Janda, Sietske H. Dijkstra, Eliška Pilátová, Eva Zatecka, Stefan Diez, Marcus Braun, and Zdenek Lansky. Anillin propels myosin-independent constriction of actin rings. *Nature Communications*, 12(1):1–12, 2021.

[46] Sari Tojkander, Gergana Gateva, and Pekka Lappalainen. Actin stress fibers - Assembly, dynamics and biological roles. *Journal of Cell Science*, 125(8):1855–1864, 2012.

[47] Priyamvada Chugh and Ewa K. Paluch. The actin cortex at a glance. *Journal of Cell Science*, 131(14):jcs186254, 2018.

[48] Anne J. Ridley. Life at the leading edge. *Cell*, 145(7):1012–1022, 2011.

[49] R. Rappaport. Cytokinesis in Animal Cells. *International Review of Cytology*, 31(C):169–214, 2015.

[50] Richard H. Wade. On and around microtubules: An overview. *Molecular Biotechnology*, 43(2):177–191, 2009.

[51] Jesús Avila. Microtubule functions. *Life Sciences*, 50(5):327–334, 1992.

[52] Nikita B. Gudimchuk and J. Richard McIntosh. Regulation of microtubule dynamics, mechanics and function through the growing tip. *Nature Reviews Molecular Cell Biology*, 22(12):777–795, 2021.

[53] Johanna Roostalu and Thomas Surrey. Microtubule nucleation: Beyond the template. *Nature Reviews Molecular Cell Biology*, 18(11):702–710, 2017.

[54] Holly V. Goodson and Erin M. Jonasson. Microtubules and microtubule-associated proteins. *Cold Spring Harbor Perspectives in Biology*, 10(6):a022608, 2018.

[55] Anna Akhmanova and Michel O. Steinmetz. Control of microtubule organization and dynamics: Two ends in the limelight. *Nature Reviews Molecular Cell Biology*, 16(12):711–726, 2015.

[56] Arshad Desai and Timothy J. Mitchison. Microtubule polymerization dynamics. *Annual Review of Cell and Developmental Biology*, 13:83–117, 1997.

[57] Tetsuya Horio, Takashi Murata, and Takashi Murata. The role of dynamic instability in microtubule organization. *Frontiers in Plant Science*, 5(OCT):511, 2014.

[58] Gary J. Brouhard. Dynamic instability 30 years later: Complexities in microtubule growth and catastrophe. *Molecular Biology of the Cell*, 26(7):1207–1210, 2015.

[59] Gabriella Li and Jeffrey K. Moore. Microtubule dynamics at low temperature: Evidence that tubulin recycling limits assembly. *Molecular Biology of the Cell*, 31(11):1154–1166, 2020.

[60] Eva Nogales, Francisco J. Medrano, Greg P. Diakun, Geoff R. Mant, Elizabeth Towns-Andrews, and Joan Bordas. The effect of temperature on the structure of vinblastine-induced polymers of purified tubulin: Detection of a reversible conformational change. *Journal of Molecular Biology*, 254(3):416–430, 1995.

[61] Elif Eren, Norman R. Watts, Dan L. Sackett, and Paul T. Wingfield. Conformational changes in tubulin upon binding cryptophycin-52 reveal its mechanism of action. *Journal of Biological Chemistry*, 297(4):101138, 2021.

[62] William Graham Hirst, Christine Kiefer, Mohammad Kazem Abdosamadi, Erik Schäffer, and Simone Reber. In Vitro Reconstitution and Imaging of Microtubule Dynamics by Fluorescence and Label-free Microscopy. *STAR Protocols*, 1(3):100177, 2020.

[63] C. S. Regula, J. R. Pfeiffer, and R. D. Berlin. Microtubule assembly and disassembly at alkaline pH. *Journal of Cell Biology*, 89(1):45–53, 1981.

[64] M. J. Schilstra, P. M. Bayley, and S. R. Martin. The effect of solution composition on microtubule dynamic instability. *Biochemical Journal*, 277(3):839–847, 1991.

[65] Vladimir Rodionov, Elena Nadezhdina, and Gary Borisy. Centrosomal control of microtubule dynamics. *Proceedings of the National Academy of Sciences of the United States of America*, 96(1):115–120, 1999.

[66] Carsten Janke and Maria M. Magiera. The tubulin code and its role in controlling microtubule properties and functions. *Nature Reviews Molecular Cell Biology*, 21(6):307–326, 2020.

[67] Clifford P. Brangwynne, Frederick C. MacKintosh, Sanjay Kumar, Nicholas A. Geisse, Jennifer Talbot, L. Mahadevan, Kevin K. Parker, Donald E. Ingber, and David A. Weitz. Microtubules can bear enhanced compressive loads in living cells because of lateral reinforcement. *Journal of Cell Biology*, 173(5):733–741, 2006.

[68] Yuhui Li, Ondřej Kučera, Damien Cuvelier, David M. Rutkowski, Mathieu Deygas, Dipti Rai, Tonja Pavlovič, Filipe Nunes Vicente, Matthieu Piel, Gregory Giannone, Dimitrios Vavylonis, Anna Akhmanova, Laurent Blanchoin, and Manuel Théry. Compressive forces stabilise microtubules in living cells. *bioRxiv*, feb 2022.

[69] Marileen Dogterom and Gijsje H. Koenderink. Actin–microtubule crosstalk in cell biology. *Nature Reviews Molecular Cell Biology*, 20(1):38–54, 2019.

[70] Ian A. Kent and Tanmay P. Lele. Microtubule-based force generation. *Wiley Interdisciplinary Reviews: Nanomedicine and Nanobiotechnology*, 9(3):e1428, 2017.

[71] Nikita B. Gudimchuk, Evgeni V. Ulyanov, Eileen O'Toole, Cynthia L. Page, Dmitrii S. Vinogradov, Garry Morgan, Gabriella Li, Jeffrey K. Moore, Ewa Szczesna, Antonina Roll-Mecak, Fazoil I. Ataullakhanov, and J. Richard McIntosh. Mechanisms of microtubule dynamics and force generation examined with computational modeling and electron cryotomography. *Nature Communications*, 11(1):1–15, 2020.

[72] R. M. Robson. Intermediate filaments. *Current Opinion in Cell Biology*, 1(1):36–43, 1989.

[73] Harald Herrmann and Ueli Aebi. Intermediate filaments: Structure and assembly. *Cold Spring Harbor Perspectives in Biology*, 8(11):a018242, 2016.

[74] Wolfgang H. Goldmann. Intermediate filaments and cellular mechanics. *Cell Biology International*, 42(2):132–138, 2018.

[75] Brent Shuman and Michelle Momany. Septins From Protists to People. *Frontiers in Cell and Developmental Biology*, 9:3802, 2022.

[76] Serge Mostowy and Pascale Cossart. Septins: The fourth component of the cytoskeleton. *Nature Reviews Molecular Cell Biology*, 13(3):183–194, mar 2012.

[77] Hoan Van Ngo and Serge Mostowy. Role of septins in microbial infection. *Journal of Cell Science*, 132(9):jcs226266, 2019.

[78] M. A. McIlhatton, J. F. Burrows, P. G. Donaghy, S. Chanduloy, P. G. Johnston, and S. E.H. Russell. Genomic organization, complex splicing pattern and expression of a human septin gene on chromosome 17q25.3. *Oncogene*, 20(41):5930–5939, 2001.

[79] Minhajuddin Sirajuddin, Marian Farkasovsky, Eldar Zent, and Alfred Wittinghofer. GTP-induced conformational changes in septins and implications for function. *Proceedings of the National Academy of Sciences of the United States of America*, 106(39):16592–16597, 2009.

[80] Corinne M John, Richard K Hite, Christine S Weirich, Daniel J Fitzgerald, Hatim Jawhari, Mahamadou Faty, Dominik Schläpfer, Ruth Kroschewski, Fritz K Winkler, Tom Walz, Yves Barral, and Michel O Steinmetz. The Caenorhabditis elegans septin complex is nonpolar. *EMBO Journal*, 26(14):3296–3307, 2007.

[81] Christine M. Field, Omayma Al-Awar, Jody Rosenblatt, Mei Lie Wong, Bruce Alberts, and Timothy J. Mitchison. A purified Drosophila septin complex forms filaments and exhibits GTPase activity. *Journal of Cell Biology*, 133(3):605–616, 1996.

[82] Aurelie Bertin, Michael A McMurray, Patricia Grob, Sang Shin Park, Galo Garcia, Insiyyah Patanwala, Ho Leung Ng, Tom Alber, Jeremy Thorner, and Eva Nogales. Saccharomyces cerevisiae septins: Supramolecular organization of heterooligomers and the mechanism of filament assembly. *Proceedings of the National Academy of Sciences of the United States of America*, 105(24):8274–8279, 2008.

[83] Minhajuddin Sirajuddin, Marian Farkasovsky, Florian Hauer, Dorothee Kühlmann, Ian G. Macara, Michael Weyand, Holger Stark, and Alfred Wittinghofer. Structural insight into filament formation by mammalian septins. *Nature*, 449(7160):311–315, 2007.

[84] Moshe S Kim, Carol D Froese, Mathew P Estey, and William S Trimble. SEPT9 occupies the terminal positions in septin octamers and mediates polymerization-dependent functions in abscission. *Journal of Cell Biology*, 195(5):815–826, 2011.

[85] Mikael E. Sellin, Linda Sandblad, Sonja Stenmark, and Martin Gullberg. Deciphering the rules governing assembly order of mammalian septin complexes. *Molecular Biology of the Cell*, 22(17):3152–3164, 2011.

[86] Makoto Kinoshita. Assembly of Mammalian Septins. *Journal of Biochemistry*, 134(4):491–496, 2003.

[87] Forooz Soroor, Moshe S. Kim, Oliva Palander, Yadu Balachandran, Richard F. Collins, Samir Benlekbir, John L. Rubinstein, and William S. Trimble. Revised subunit order of mammalian septin complexes explains their in vitro polymerization properties. *Molecular Biology of the Cell*, 32(3):289–300, 2021.

[88] Deborah C. Mendonça, Joci N. Macedo, Samuel L. Guimaraes, Fernando L. Barroso da Silva, Alexandre Cassago, Richard C. Garratt, Rodrigo V. Portugal, and Ana P. U. Araujo. A revised order of subunits in mammalian septin complexes. *Cytoskeleton*, 76(9-10):457–466, 2019.

[89] Danielle K.S.V. Castro, Higor V.D. Rosa, Deborah C. Mendonça, Italo A. Cavini, Ana P.U. Araujo, and Richard C. Garratt. Dissecting the Binding Interface of the Septin Polymerization Enhancer Borg BD3. *Journal of Molecular Biology*, 435(13):168132, 2023.

[90] Manuel Mendoza, Anthony A. Hyman, and Michael Glotzer. GTP binding induces filament assembly of a recombinant septin. *Current Biology*, 12(21):1858–1863, 2002.

[91] Khushboo Sharma and Manoj B Menon. Decoding post-translational modifications of mammalian septins. *Cytoskeleton*, pages 1–13, 2023.

[92] Carol S.L. Tang and Steven I. Reed. Phosphorylation of the septin cdc3 in g1 by the cdc28 kinase is essential for efficient septin ring disassembly. *Cell cycle (Georgetown, Tex.)*, 1(1):42–49, 2002.

[93] Yainitza Hernández-Rodríguez and Michelle Momany. Posttranslational modifications and assembly of septin heteropolymers and higher-order structures. *Current Opinion in Microbiology*, 15(6):660–668, 2012.

[94] David Ribet, Serena Boscaini, Clothilde Cauvin, Martin Siguier, Serge Mostowy, Arnaud Echard, and Pascale Cossart. SUMOylation of human septins is critical for septin filament bundling and cytokinesis. *Journal of Cell Biology*, 216(12):4041–4052, 2017.

[95] Andrew A Bridges, Maximilian S Jentzsch, Patrick W Oakes, Patricia Occhipinti, and Amy S Gladfelter. Micron-scale plasma membrane curvature is recognized by the septin cytoskeleton. *Journal of Cell Biology*, 213(1):23–32, 2016.

[96] Agata Szuba, Fouzia Bano, Gerard Castro-Linares, Francois Iv, Manos Mavrakis, Ralf P. Richter, Aurélie Bertin, and Gijsje H. Koenderink. Membrane binding controls ordered self-assembly of animal septins. *eLife*, 10:e63349, 2021.

[97] Koyomi Nakazawa, Gaurav Kumar, Brieuc Chauvin, Aurélie Di Cicco, Luca Pellegrino, Michael Trichet, Bassam Hajj, João Cabral, Anirban Sain, Stéphanie Mangenot, and Aurélie Bertin. A specific mesh-like organization of human septin octameric complex drives membrane reshaping and curvature sensitivity. *bioRxiv*, nov 2022.

[98] Alexandre Beber, Cyntia Taveneau, Manuela Nania, Feng Ching Tsai, Aurelie Di Cicco, Patricia Bassereau, Daniel Lévy, João T. Cabral, Hervé Isambert, Stéphanie Mangenot, and Aurélie Bertin. Membrane reshaping by micrometric curvature sensitive septin filaments. *Nature Communications*, 10(1):420, 2019.

[99] Yohko Tanaka-Takiguchi, Makato Kinoshita, and Kingo Takiguchi. Septin-Mediated Uniform Bracing of Phospholipid Membranes. *Current Biology*, 19(2):140–145, jan 2009.

[100] Alexandre Beber, Maryam Alqabandi, Coline Prévost, Fanny Viars, Daniel Lévy, Patricia Bassereau, Aurélie Bertin, and Stéphanie Mangenot. Septin-based readout of PI(4,5)P2 incorporation into membranes of giant unilamellar vesicles. *Cytoskeleton*, 76(1):92–103, 2018.

[101] Manos Mavrakis, Yannick Azou-Gros, Feng Ching Tsai, José Alvarado, Aurélie Bertin, Francois Iv, Alla Kress, Sophie Brasselet, Gijsje H. Koenderink, and Thomas Lecuit. Septins promote F-actin ring formation by crosslinking actin filaments into curved bundles. *Nature Cell Biology*, 16(4):322–334, 2014.

[102] Francois Iv, Carla Silva Martins, Gerard Castro-Linares, Cyntia Taveneau, Pascale Barbier, Pascal Verdier-Pinard, Luc Camoin, Stéphane Audebert, Feng-Ching Tsai, Laurie Ramond, Alex Llewellyn, Mayssa Belhabib, Koyomi Nakazawa, Aurélie Di Cicco, Renaud Vincentelli, Jerome Wenger, Stéphanie Cabantous, Gijsje H. Koenderink, Aurélie Bertin, and Manos Mavrakis. Insights into animal septins using recombinant human septin octamers with distinct SEPT9 isoforms. *Journal of Cell Science*, 134(15):jcs258484, 2021.

[103] Mira Kuzmić, Gerard Castro Linares, Jindřiška Leischner Fialová, François Iv, Danièle Salaün, Alex Llewellyn, Maxime Gomes, Mayssa Belhabib, Yuxiang Liu, Keisuke Asano, Magda Rodrigues, Daniel Isnardon, Taro Tachibana, Gijsje H. Koenderink, Ali Badache, Manos Mavrakis, and Pascal Verdier-Pinard. Septin-microtubule association via a motif unique to isoform 1 of septin 9 tunes stress fibers. *Journal of Cell Science*, 135(1):jcs258850, jan 2022.

[104] Peter J. Sheffield, Carey J. Oliver, Brandon E. Kremer, Sitong Sheng, Zhifeng Shao, and Ian G. Macara. Borg/Septin interactions and the assembly of mammalian septin heterodimers, trimers, and filaments. *Journal of Biological Chemistry*, 278(5):3483–3488, 2003.

[105] Elias T. Spiliotis. Spatial effects – site-specific regulation of actin and microtubule organization by septin GTPases. *Journal of Cell Science*, 131(1):jcs207555, 2018.

[106] Andrew A Bridges and Amy S Gladfelter. Septin form and function at the cell cortex. *Journal of Biological Chemistry*, 290(28):17173–17180, 2015.

[107] Giulia Russo and Michael Krauss. Septin Remodeling During Mammalian Cytokinesis. *Frontiers in Cell and Developmental Biology*, 9:3141, 2021.

[108] Damián Lobato-Márquez and Serge Mostowy. Septins recognize micron-scale membrane curvature. *Journal of Cell Biology*, 213(1):5–6, 2016.

[109] Lee Dolat, John L. Hunyara, Jonathan R. Bowen, Eva Pauline Karasmanis, Maha Elgawly, Vitold E. Galkin, and Elias T. Spiliotis. Septins promote stress fiber-mediated maturation of focal adhesions and renal epithelial motility. *Journal of Cell Biology*, 207(2):225–235, 2014.

[110] Katharina Neubauer and Barbara Zieger. The Mammalian Septin Interactome. *Frontiers in Cell and Developmental Biology*, 5:3, 2017.

[111] Dimitrios Angelis and Elias T. Spiliotis. Septin mutations in human cancers. *Frontiers in Cell and Developmental Biology*, 4:122, 2016.

[112] Aminata Toure, Baptiste Rode, Gary R. Hunnicutt, Denise Escalier, and Gérard Gacon. Septins at the annulus of mammalian sperm. *Biological Chemistry*, 392(8-9):799–803, 2011.

[113] Qicong Hu, Ljiljana Milenkovic, Hua Jin, Matthew P. Scott, Maxence V. Nachury, Elias T. Spiliotis, and W. James Nelson. A Septin Diffusion Barrier at the Base of the Primary Cilium Maintains Ciliary Membrane Protein Distribution. *Science*, 329(5990):436–439, 2010.

[114] Béatrice Benoit, Christian Poüs, and Anita Baillet. Septins as membrane influencers: direct play or in association with other cytoskeleton partners. *Frontiers in Cell and Developmental Biology*, 11:99, 2023.

[115] Elias T. Spiliotis and Konstantinos Nakos. Cellular functions of actin- and microtubule-associated septins. *Current Biology*, 31(10):R651–R666, 2021.

[116] Ting Yu Chen, Tzu Chien Lin, Pao Lin Kuo, Zi Rong Chen, Hui ling Cheng, Yu Ying Chao, Jhih Siang Syu, Fu I. Lu, and Chia Yih Wang. Septin 7 is a centrosomal protein that ensures S phase entry and microtubule nucleation by maintaining the abundance of p150glued. *Journal of Cellular Physiology*, 236(4):2706–2724, 2021.

[117] Mei Zhu, Fengsong Wang, Feng Yan, Phil Y. Yao, Jian Du, Xinjiao Gao, Xiwei Wang, Quan Wu, Tarsha Ward, Jingjing Li, Steve Kioko, Renming Hu, Wei Xie, Xia Ding, and Xuebiao Yao. Septin 7 interacts with centromere-associated protein E and is required for its kinetochore localization. *Journal of Biological Chemistry*, 283(27):18916–18925, 2008.

[118] Elias T. Spiliotis, Makoto Kinoshita, and W. James Nelson. A mitotic septin scaffold required for mammalian chromosome congression and segregation. *Science*, 307(5716):1781–1785, 2005.

[119] Julia K. Gilden, Sebastian Peck, Yi-Chun M. Chen, and Matthew F. Krummel. The septin cytoskeleton facilitates membrane retraction during motility and blebbing. *Journal of Cell Biology*, 196(1):103–114, 2012.

[120] Neza Vadnjal, Sami Nourreddine, Geneviève Lavoie, Murielle Serres, Philippe P. Roux, and Ewa K. Paluch. Proteomic analysis of the actin cortex in interphase and mitosis. *Journal of Cell Science*, 135(16):jcs259993, aug 2022.

[121] Emily Joo, Mark C. Surka, and William S. Trimble. Mammalian SEPT2 Is Required for Scaffolding Nonmuscle Myosin II and Its Kinases. *Developmental Cell*, 13(5):677–690, 2007.

[122] Matthew J. Renshaw, Jinghe Liu, Brigitte D. Lavoie, and Andrew Wilde. Anillin-dependent organization of septin filaments promotes intercellular bridge elongation and Chmp4B targeting to the abscission site. *Open Biology*, 4(JAN):130190, 2014.

[123] John H. Henson, Casey E. Ditzler, Aphnie Germain, Patrick M. Irwin, Eric T. Vogt, Shucheng Yang, Xufeng Wu, and Charles B. Shuster. The ultrastructural organization of actin and myosin II filaments in the contractile ring: new support for an old model of cytokinesis. *Molecular Biology of the Cell*, 28(5):613–623, 2017.

[124] Sabrya C. Carim, Amel Kechad, and Gilles R.X. Hickson. Animal Cell Cytokinesis: The Rho-Dependent Actomyosin-Anilloseptin Contractile Ring as a Membrane Microdomain Gathering, Compressing, and Sorting Machine. *Frontiers in Cell and Developmental Biology*, 8:575226, 2020.

[125] Eva P. Karasmanis, Daniel Hwang, Konstantinos Nakos, Jonathan R. Bowen, Dimitrios Angelis, and Elias T. Spiliotis. A Septin Double Ring Controls the Spatiotemporal Organization of the ESCRT Machinery in Cytokinetic Abscission. *Current Biology*, 29(13):2174–2182, 2019.

[126] Cyril Addi, Jian Bai, and Arnaud Echard. Actin, microtubule, septin and ESCRT filament remodeling during late steps of cytokinesis. *Current Opinion in Cell Biology*, 50:27–34, 2018.

[127] Koh Ichi Nagata, Yoko Mizutani, Hiroyuki Kanoh, Mariko Seishima, Hidenori Ito, Ikuko Iwamoto, and Rika Morishita. Possible role of a septin, SEPT1, in spreading in squamous cell carcinoma DJM-1 cells. *Biological Chemistry*, 394(2):281–290, 2013.

[128] Yi Wei Huang, Ming Yan, Richard F. Collins, Jessica E. DiCiccio, Sergio Grinstein, and William S. Trimble. Mammalian septins are required for phagosome formation. *Molecular Biology of the Cell*, 19(4):1717–1726, 2008.

[129] Gerard Castro-linares, Jeffrey den Haan, Francois Iv, Carla Silva Martins, Aurélie Bertin, Manos Mavrakis, and Gijsje H Koenderink. Purification and Quality Control of Recombinant Septin Complexes for Cell-Free Reconstitution. *Journal of Visualized Experiments*, e63871(184):e63871, 2022.

[130] Clayton Smith, Lee Dolat, Dimitrios Angelis, Eva Forgacs, Elias T. Spiliotis, and Vitold E. Galkin. Septin 9 Exhibits Polymorphic Binding to F-Actin and Inhibits Myosin and Cofilin Activity. *Journal of Molecular Biology*, 427(20):3273–3284, oct 2015.

[131] Joseph Marquardt, Xi Chen, and Erfei Bi. Architecture, remodeling, and functions of the septin cytoskeleton. *Cytoskeleton*, 76(1):7–14, 2018.

[132] Karen Y.Y. Fung, Lu Dai, and William S. Trimble. Cell and molecular biology of septins. In *International Review of Cell and Molecular Biology*, volume 310, pages 289–339. Academic Press, jan 2014.

[133] Makoto Kinoshita, Christine M. Field, Margaret L. Coughlin, Aaron F. Straight, and Timothy J. Mitchison. Self- and actin-templated assembly of mammalian septins. *Developmental Cell*, 3(6):791–802, 2002.

[134] Amin Zehtabian, Paul Markus Müller, Maximilian Goisser, Leon Obendorf, Lea Jänisch, Nadja Hümpfer, Jakob Rentsch, and Helge Ewers. Precise measurement of nanoscopic septin ring structures with deep learning-assisted quantitative super-resolution microscopy. *Molecular Biology of the Cell*, 33(8):ar76, 2022.

[135] Diana Connolly, Zhixia Yang, Maria Castaldi, Nichelle Simmons, Maja H. Oktay, Salvatore Coniglio, Melissa J. Fazzari, Pascal Verdier-Pinard, and Cristina Montagna. Septin 9 isoform expression, localization and epigenetic changes during human and mouse breast cancer progression. *Breast Cancer Research*, 13(4):R76, 2011.

[136] Diana Connolly, Hien G. Hoang, Esther Adler, Cagdas Tazearslan, Nichelle Simmons, Vahni Vishala Bernard, Maria Castaldi, Maja H. Oktay, and Cristina Montagna. Septin 9 amplification and isoform-specific expression in peritumoral and tumor breast tissue. *Biological Chemistry*, 395(2):157–167, 2014.

[137] Mathew P. Estey, Caterina Di Ciano-Oliveira, Carol D. Froese, Margaret T. Bejide, and William S. Trimble. Distinct roles of septins in cytokinesis: SEPT9 mediates midbody abscission. *Journal of Cell Biology*, 191(4):741–749, 2010.

[138] Abdellah Akil, Juan Peng, Mohyeddine Omrane, Claire Gondeau, Christophe Desterke, Mickaël Marin, Hélène Tronchère, Cyntia Taveneau, Sokhavuth Sar, Philippe Briolotti, Soumaya Benjelloun, Abdelaziz Benjouad, Patrick Maurel, Valérie Thiers, Stéphane Bressanelli, Didier Samuel, Christian Bréchot, and Ama Gassama-Diagne. Septin 9 induces lipid droplets growth by a phosphatidylinositol-5-phosphate and microtubule-dependent mechanism hijacked by HCV. *Nature Communications*, 7(1):1–19, 2016.

[139] Mohyeddine Omrane, Amanda Souza Camara, Cyntia Taveneau, Nassima Benzoubir, Thibault Tubiana, Jinchao Yu, Raphaël Guérois, Didier Samuel, Bruno Goud, Christian Poüs, Stéphane Bressanelli, Richard Charles Garratt, Abdou Rachid Thiam, and Ama Gassama-Diagne. Septin 9 has two polybasic domains critical to septin filament assembly and Golgi integrity. *iScience*, 13:138–153, 2019.

[140] Nour El Amine, Amel Kechad, Silvana Jananji, and Gilles R.X. Hickson. Opposing actions of septins and Sticky on Anillin promote the transition from contractile to midbody ring. *Journal of Cell Biology*, 203(3):487–504, 2013.

[141] Joëlle Salameh, Isabelle Cantaloube, Béatrice Benoit, Christian Poüs, and Anita Baillet. Cdc42 and its BORG2 and BORG3 effectors control the subcellular localization of septins between actin stress fibers and microtubules. *Current Biology*, 31(18):4088–4103.e5, 2021.

[142] Akari Hagiwara, Yasuhiro Tanaka, Rie Hikawa, Nobuhiro Morone, Akihiro Kusumi, Hiroshi Kimura, and Makoto Kinoshita. Submembranous septins as relatively stable components of actin-based membrane skeleton. *Cytoskeleton*, 68(9):512–525, 2011.

[143] Fernando Calvo, Romana Ranftl, Steven Hooper, Aaron J. Farrugia, Emad Moeendarbary, Andreas Bruckbauer, Facundo Batista, Guillaume Charras, and Erik Sahai. Cdc42EP3/BORG2 and Septin Network Enables Mechano-transduction and the Emergence of Cancer-Associated Fibroblasts. *Cell Reports*, 13(12):2699–2714, 2015.

[144] Carla Silva Martins, Cyntia Taveneau, Gerard Castro-Linares, Mikhail Baibakov, Nicolas Buzhinsky, Mar Eroles, Violeta Milanović, Shizue Omi, Jean-Denis Pedelacq, Francois Iv, Léa Bouillard, Alexander Llewellyn, Maxime Gomes, Mayssa Belhabib, Mira Kuzmić, Pascal Verdier-Pinard, Stacey Lee, Ali Badache, Sanjay Kumar, Cristel Chandre, Sophie Brasselet, Felix Rico, Olivier Rossier, Gijsje H. Koenderink, Jerome Wenger, Stéphanie Cabantous, and Manos Mavrakis. Human septins organize as octamer-based filaments and mediate actin-membrane anchoring in cells. *Journal of Cell Biology*, 222(3):e202203016, 2023.

[145] Asako Shindo, Anastasia Audrey, Maki Takagishi, Masahide Takahashi, John B. Wallingford, and Makoto Kinoshita. Septin-dependent remodeling of cortical microtubule drives cell reshaping during epithelial wound healing. *Journal of Cell Science*, 131(12):jcs212647, 2018.

[146] Qicong Hu, W. James Nelson, and Elias T. Spiliotis. Forchlorfenuron alters mammalian septin assembly, organization, and dynamics. *Journal of Biological Chemistry*, 283(43):29563–29571, 2008.

[147] M. Mavrakis, F. C. Tsai, and G. H. Koenderink. Purification of recombinant human and Drosophila septin hexamers for TIRF assays of actin–septin filament assembly. In *Methods in Cell Biology*, volume 136, pages 199–220. Academic Press Inc., 2016.

[148] Konstantinos Nakos, Megan R. Radler, and Elias T. Spiliotis. Septin 2/6/7 complexes tune microtubule plus-end growth and EB1 binding in a concentration- and filament-dependent manner. *Molecular Biology of the Cell*, 30(23):2913–2928, 2019.

[149] Charlotte Kaplan, Bo Jing, Christian M. Winterflood, Andrew A. Bridges, Patricia Occhipinti, Jürgen Schmied, Sören Grinhagens, Thomas Gronemeyer, Philip Tinnefeld, Amy S. Gladfelter, Jonas Ries, and Helge Ewers. Absolute Arrangement of Subunits in Cytoskeletal Septin Filaments in Cells Measured by Fluorescence Microscopy. *Nano Letters*, 15(6):3859–3864, 2015.

[150] Danielle Karoline Silva Vale Castro, Sabrina Matos Oliveira Silva, Humberto Dmuniz Pereira, Joci Neuby Alves MacEdo, Diego Antonio Leonardo, Napoleao Fonseca Valadares, Patricia Suemy Kumagai, Jose Brandao-Neto, Ana Paula Ulian Araujoa, and Richard Charles Garratta. A complete compendium of crystal structures for the human SEPT3 subgroup reveals functional plasticity at a specific septin interface. *IUCrJ*, 7:462–479, 2020.

[151] Fang Jiao, Kevin S. Cannon, Yi-Chih Lin, Amy S. Gladfelter, and Simon Scheuring. The hierarchical assembly of septins revealed by high-speed AFM. *Nature Communications 2020*, 11(1):1–13, 2020.

[152] Aurélie Bertin, Michael A. McMurray, Luong Thai, Galo Garcia, Violet Votin, Patricia Grob, Theresa Allyn, Jeremy Thorner, and Eva Nogales. Phosphatidylinositol-4,5-bisphosphate Promotes Budding Yeast Septin Filament Assembly and Organization. *Journal of Molecular Biology*, 404(4):711–731, 2010.

[153] R. Zhou, Y. Shi, and G. Yang. Expression, Purification, and Enzymatic Characterization of Intramembrane Proteases. In *Methods in Enzymology*, volume 584, pages 127–155. Academic Press, jan 2017.

[154] Caroline A. Schneider, Wayne S. Rasband, and Kevin W. Eliceiri. NIH Image to ImageJ: 25 years of image analysis. *Nature Methods*, 9(7):671–675, 2012.

[155] Elisabeth Gasteiger, Christine Hoogland, Alexandre Gattiker, S'everine Duvaud, Marc R. Wilkins, Ron D. Appel, and Amos Bairoch. Protein Identification and Analysis Tools on the ExPASy Server. In *The Proteomics Protocols Handbook*, pages 571–607. Humana Press, 2005.

[156] Maria A Lebedeva, Elena Palmieri, Philipp Kukura, and Stephen P Fletcher. Emergence and Rearrangement of Dynamic Supramolecular Aggregates Visualized by Interferometric Scattering Microscopy. *ACS Nano*, 14(9):11160–11168, 2020.

[157] Steven J. Ludtke, Philip R. Baldwin, and Wah Chiu. EMAN: Semiautomated Software for High-Resolution Single-Particle Reconstructions. *Journal of Structural Biology*, 128(1):82–97, 1999.

[158] Joachim Frank, Michael Radermacher, Pawel Penczek, Jun Zhu, Yanhong Li, Mahieddine Ladjadj, and Ardean Leith. SPIDER and WEB: Processing and visualization of images in 3D electron microscopy and related fields. *Journal of Structural Biology*, 116(1):190–199, 1996.

[159] Jasenko Zivanov, Takanori Nakane, Björn O. Forsberg, Dari Kimanius, Wim J.H. Hagen, Erik Lindahl, and Sjors H.W. Scheres. New tools for automated high-resolution cryo-EM structure determination in RELION-3. *eLife*, 7:e42166, 2018.

[160] Gayan Senavirathne, Miguel A. Lopez, Ryan Messer, Richard Fishel, and Kristine E. Yoder. Expression and purification of nuclease-free protocatechuate 3,4-dioxygenase for prolonged single-molecule fluorescence imaging. *Analytical Biochemistry*, 556:78–84, 2018.

[161] F. Molina, A. Rueda, J. M. Bosque-Sendra, and L. Megías. Determination of proteins in the presence of imidazole buffers. *Journal of Pharmaceutical and Biomedical Analysis*, 14(3):273–280, 1996.

[162] Gavin Young and Philipp Kukura. Interferometric Scattering Microscopy. *Annual Review of Physical Chemistry*, 70(1):301–322, 2019.

[163] Gavin Young, Nikolas Hundt, Daniel Cole, Adam Fineberg, Joanna Andrecka, Andrew Tyler, Anna Olerinyova, Ayla Ansari, Erik G. Marklund, Miranda P. Collier, Shane A. Chandler, Olga Tkachenko, Joel Allen, Max Crispin, Neil Billington, Yasuharu Takagi, James R. Sellers, Cédric Eichmann, Philipp Selenko, Lukas Frey, Roland Riek, Martin R. Galpin, Weston B. Struwe, Justin L.P. Benesch, and Philipp Kukura. Quantitative mass imaging of single biological macromolecules. *Science*, 360(6387):423–427, 2018.

[164] Gérard Joberty, Richard R Perlungher, Peter J Sheffield, Makoto Kinoshita, Makoto Noda, Timothy Haystead, and Ian G Macara. Borg proteins control septin organization and are negatively regulated by Cdc42. *Nature Cell Biology*, 3(10):861–866, 2001.

[165] Xi Chen, Kangji Wang, Tatyana Svitkina, and Erfei Bi. Critical Roles of a RhoGEF-Anillin Module in Septin Architectural Remodeling during Cytokinesis. *Current Biology*, 30(8):1477–1490.e3, 2020.

[166] Shu Chan Hsu, Christopher D. Hazuka, Robyn Roth, Davide L. Foletti, John Heuser, and Richard H. Scheller. Subunit composition, protein interactions, and structures of the mammalian brain sec6/8 complex and septin filaments. *Neuron*, 20(6):1111–1122, 1998.

[167] Martin Fischer, Dominik Frank, Reinhild Rösler, Nils Johnsson, and Thomas Gronemeyer. Biochemical Characterization of a Human Septin Octamer. *Frontiers in Cell and Developmental Biology*, 10:447, 2022.

[168] William A. Wells. Microtubules get a name. *Journal of Cell Biology*, 168(6):852, 2005.

[169] William B.R. Brinkley. Microtubules: A brief historical perspective. *Journal of Structural Biology*, 118(2):84–86, 1997.

[170] Andrew Muroyama and Terry Lechler. Microtubule organization, dynamics and functions in differentiated cells. *Development*, 144(17):3012–3021, 2017.

[171] William A. Wells. The discovery of tubulin. *Journal of Cell Biology*, 169(4):552, 2005.

[172] William A. Wells. Microtubules get dynamic. *Journal of Cell Biology*, 172(5):643, 2006.

[173] Anna Akhmanova and Lukas C Kapitein. Mechanisms of microtubule organization in differentiated animal cells. *Nature Reviews Molecular Cell Biology*, 23(8):541–558, 2022.

[174] Shailaja Seetharaman and Sandrine Etienne-Manneville. Cytoskeletal Crosstalk in Cell Migration. *Trends in Cell Biology*, 30(9):720–735, sep 2020.

[175] Florian Huber, Adeline Boire, Magdalena Preciado López, and Gijsje H. Koenderink. Cytoskeletal crosstalk: When three different personalities team up. *Current Opinion in Cell Biology*, 32:39–47, 2015.

[176] Jonathan R. Bowen, Daniel Hwang, Xiaobo Bai, Dheeraj Roy, and Elias T. Spiliotis. Septin GTPases spatially guide microtubule organization and plus end dynamics in polarizing epithelia. *Journal of Cell Biology*, 194(2):187–197, 2011.

[177] Kyungyeun Song, Claudia Gras, Gabrielle Capin, Niclas Gimber, Martin Lehmann, Saif Mohd, Dmytro Puchkov, Maria Rödiger, Ilka Wilhelmi, Oliver Daumke, Jan Schmoranzer, Annette Schürmann, and Michael Krauss. A SEPT1-based scaffold is required for Golgi integrity and function. *Journal of Cell Science*, 132(3):jcs225557, 2019.

[178] Elias T. Spiliotis, Stephen J. Hunt, Qicong Hu, Makoto Kinoshita, and W. James Nelson. Epithelial polarity requires septin coupling of vesicle transport to polyglutamylated microtubules. *Journal of Cell Biology*, 180(2):295–303, 2008.

[179] Elias T. Spiliotis and Ilona A. Kesisova. Spatial regulation of microtubule-dependent transport by septin GTPases. *Trends in cell biology*, 31(12):979–993, 2021.

[180] C. Martínez, J. Corral, J. A. Dent, L. Sesma, V. Vicente, and Jerry Ware. Platelet septin complexes form rings and associate with the microtubular network. *Journal of Thrombosis and Haemostasis*, 4(6):1388–1395, 2006.

[181] Rania Ghossoub, Qicong Hu, Marion Failler, Marie Christine Rouyez, Benjamin Spitzbarth, Serge Mostowy, Uwe Wolfrum, Sophie Saunier, Pascale Cossart, W. James Nelson, and Alexandre Benmerah. Septins 2, 7 and 9 and MAP4 colocalize along the axoneme in the primary cilium and control ciliary length. *Journal of Cell Science*, 126(12):2583–2594, 2013.

[182] Mikael E. Sellin, Per Holmfeldt, Sonja Stenmark, and Martin Gullberg. Microtubules support a disk-like septin arrangement at the plasma membrane of mammalian cells. *Molecular Biology of the Cell*, 22(23):4588–4601, 2011.

[183] Oleg V. Kim, Rustem I. Litvinov, Elmira R. Mordakhanova, Erfei Bi, Olga Vagin, and John W. Weisel. Contribution of septins to human platelet structure and function. *iScience*, 25(7):104654, 2022.

[184] Konstantinos Nakos, Marshall Rosenberg, and Elias T. Spiliotis. Regulation of microtubule plus end dynamics by septin 9. *Cytoskeleton*, 76(1):83–91, 2018.

[185] Natsumi Ageta-Ishihara, Takaki Miyata, Chika Ohshima, Masahiko Watanabe, Yoshikatsu Sato, Yuki Hamamura, Tetsuya Higashiyama, Ralph Mazitschek, Haruhiko Bito, and Makoto Kinoshita. Septins promote dendrite and axon development by negatively regulating microtubule stability via HDAC6-mediated deacetylation. *Nature Communications*, 4(1):1–11, 2013.

[186] Anne Müsch. Microtubule organization and function in epithelial cells. *Traffic*, 5(1):1–9, 2004.

[187] Sam F.B. van Beuningen and Casper C. Hoogenraad. Neuronal polarity: remodeling microtubule organization. *Current Opinion in Neurobiology*, 39:1–7, 2016.

[188] Gregor Kuhlenbäumer, Mark C. Hannibal, Eva Nelis, Anja Schirmacher, Nathalie Verpoorten, Jan Meuleman, Giles D.J. Watts, Els De Vriendt, Peter Young, Florian Stögbauer, Hartmut Halfter, Joy Irobi, Dirk Goossens, Jurgen Del-Favero, Benjamin G. Betz, Hyun Hor, Gert Kurlemann, Thomas D. Bird, Eila Airaksinen, Tarja Mononen, Adolfo Pou Serradell, José M. Prats, Christine Van Broeckhoven, Peter De Jonghe, Vincent Timmerman, E. Bernd Ringelstein, and Phillip F. Chance. Mutations in SEPT9 cause hereditary neuralgic amyotrophy. *Nature Genetics*, 37(10):1044–1046, sep 2005.

[189] M. C. Hannibal, E. K. Ruzzo, L. R. Miller, B. Betz, J. G. Buchan, D. M. Knutzen, K. Barnett, M. L. Landsverk, A. Brice, E. LeGuern, H. M. Bedford, B. B. Worrall, S. Lovitc, S. H. Appel, E. Andermann, T. D. Bird, and P. F. Chance. SEPT9 gene sequencing analysis reveals recurrent mutations in hereditary neuralgic amyotrophy. *Neurology*, 72(20):1755–1759, 2009.

[190] Mikael E. Sellin, Sonja Stenmark, and Martin Gullberg. Mammalian SEPT9 isoforms direct microtubule dependent arrangements of septin core heteromers. *Molecular Biology of the Cell*, 23(21):4242–4255, 2012.

[191] Koh ichi Nagata, Aie Kawajiri, Seiya Matsui, Mihoko Takagishi, Takashi Shiromizu, Noriko Saitoh, Ichiro Izawa, Tohru Kiyono, Tomohiko J. Itoh, Hirokazu Hotani, and Masaki Inagaki. Filament formation of MSF-A, a mammalian septin, in human mammary epithelial cells depends on interactions with microtubules. *Journal of Biological Chemistry*, 278(20):18538–18543, 2003.

[192] P. Verdier-Pinard, D. Salaun, H. Bouguenina, S. Shimada, M. Pophillat, S. Audebert, E. Agavnian, S. Coslet, E. Charafe-Jauffret, T. Tachibana, and A. Badache. Septin 9-i2 is downregulated in tumors, impairs cancer cell migration and alters subnuclear actin filaments. *Scientific Reports*, 7(1):1–18, 2017.

[193] Xiaobo Bai, Jonathan R. Bowen, Tara K. Knox, Kaifeng Zhou, Manuela Pendziwiat, Gregor Kuhlenbäumer, Charles V. Sindelar, and Elias T. Spiliotis. Novel septin 9 repeat motifs altered in neuralgic amyotrophy bind and bundle microtubules. *Journal of Cell Biology*, 203(6):895–905, 2013.

[194] Henrik Buschmann, Jordi Chan, Luis Sanchez-Pulido, Miguel A. Andrade-Navarro, John H. Doonan, and Clive W. Lloyd. Microtubule-Associated AIR9 Recognizes the Cortical Division Site at Preprophase and Cell-Plate Insertion. *Current Biology*, 16(19):1938–1943, 2006.

[195] Moshe S. Kim, Carol D. Froese, Hong Xie, and William S. Trimble. Uncovering principles that control septin-septin interactions. *Journal of Biological Chemistry*, 287(36):30406–30413, 2012.

[196] Tim Mitchison and Marc Kirschner. Dynamic instability of microtubule growth. *Nature*, 312(5991):237–242, 1984.

[197] Yalei Chen and William O. Hancock. Kinesin-5 is a microtubule polymerase. *Nature Communications*, 6(1):1–10, 2015.

[198] Leif Dehmelt and Shelley Halpain. The MAP2/Tau family of microtubule-associated proteins. *Genome Biology*, 6(1):1–10, 2005.

[199] Konstantinos Nakos, Md Noor A. Alam, Megan R. Radler, Ilona A. Kesisova, Changsong Yang, Joshua Okletey, Meagan R. Tomasso, Shae B. Padrick, Tatyana M. Svitkina, and Elias T. Spiliotis. Septins mediate a microtubule–actin crosstalk that enables actin growth on microtubules. *Proceedings of the National Academy of Sciences of the United States of America*, 119(50):e2202803119, 2022.

[200] Benjamin Targa, Laurence Klipfel, Isabelle Cantaloube, Joëlle Salameh, Béatrice Benoit, Christian Poüs, and Anita Baillet. Septin filament coalignment with microtubules depends on SEPT9_i1 and tubulin polyglutamylation, and is an early feature of acquired cell resistance to paclitaxel. *Cell Death and Disease*, 10(2):54, 2019.

[201] Toshinobu Shida, Juan G. Cueva, Zhenjie Xu, Miriam B. Goodman, and Maxence V. Nachury. The major α-tubulin K40 acetyltransferase αTAT1 promotes rapid ciliogenesis and efficient mechanosensation. *Proceedings of the National Academy of Sciences of the United States of America*, 107(50):21517–21522, 2010.

[202] Christopher Gell, Volker Bormuth, Gary J. Brouhard, Daniel N. Cohen, Stefan Diez, Claire T. Friel, Jonne Helenius, Bert Nitzsche, Heike Petzold, Jan Ribbe, Erik Schäffer, Jeffrey H. Stear, Anastasiya Trushko, Vladimir Varga, Per O. Widlund, Marija Zanic, and Jonathon Howard. Microtubule dynamics reconstituted in vitro and imaged by single-molecule fluorescence microscopy. *Methods in Cell Biology*, 95(C):221–245, 2010.

[203] Peter Bieling, Liedewij Laan, Henry Schek, E. Laura Munteanu, Linda Sandblad, Marileen Dogterom, Damian Brunner, and Thomas Surrey. Reconstitution of a microtubule plus-end tracking system in vitro. *Nature*, 450(7172):1100–1105, 2007.

[204] Pierre Sens and Julie Plastino. Membrane tension and cytoskeleton organization in cell motility. *Journal of Physics Condensed Matter*, 27(27):273103, 2015.

[205] Andŕas Kapus and Paul Janmey. Plasma membrane-cortical cytoskeleton interactions: A cell biology approach with biophysical considerations. *Comprehensive Physiology*, 3(3):1231–1281, 2013.

[206] Andrea Ghisleni, Camilla Galli, Pascale Monzo, Flora Ascione, Marc Antoine Fardin, Giorgio Scita, Qingsen Li, Paolo Maiuri, and Nils C Gauthier. Complementary mesoscale dynamics of spectrin and acto-myosin shape membrane territories during mechanoresponse. *Nature Communications*, 11(1):5108, 2020.

[207] Benjamin L. Woods, Kevin S. Cannon, Ellysa J.D. Vogt, John M. Crutchley, and Amy S. Gladfelter. Interplay of septin amphipathic helices in sensing membrane-curvature and filament bundling. *Molecular Biology of the Cell*, 32(20):br5, 2021.

[208] Diego A. Leonardo, Italo A. Cavini, Fernanda A. Sala, Deborah C. Mendonça, Higor V.D. Rosa, Patricia S. Kumagai, Edson Crusca Jr, Napoleão F. Valadares, Ivo A. Marques, José Brandão-Neto, Claudia E. Munte, Hans R. Kalbitzer, Nicolas Soler, Isabel Usón, Ingemar André, Ana P.U. Araujo, Humberto D'Muniz Pereira, and Richard C. Garratt. Orientational Ambiguity in Septin Coiled Coils and its Structural Basis. *Journal of Molecular Biology*, 433(9):166889, 2021.

[209] Andrea Sirianni, Sina Krokowski, Damián Lobato-Márquez, Stephen Buranyi, Julia Pfanzelter, Dieter Galea, Alexandra Willis, Siân Culley, Ricardo Henriques, Gerald Larrouy-Maumus, Michael Hollinshead, Vanessa Sancho-Shimizu, Michael Way, and Serge Mostowy. Mitochondria mediate septin cage assembly to promote autophagy of Shigella. *EMBO reports*, 17(7):1029–1043, 2016.

[210] Ilona A Kesisova, Benjamin P Robinson, and Elias T Spiliotis. A septin GTPase scaffold of dynein–dynactin motors triggers retrograde lysosome transport. *Journal of Cell Biology*, 220(2), 2021.

[211] Lee Dolat and Elias T. Spiliotis. Septins promote macropinosome maturation and traffic to the lysosome by facilitating membrane fusion. *Journal of Cell Biology*, 214(5):517–527, 2016.

[212] Kyungyeun Song, Giulia Russo, and Michael Krauss. Septins as modulators of endo-lysosomal membrane traffic. *Frontiers in Cell and Developmental Biology*, 4(NOV):124, 2016.

[213] Su Kyoung Kim, Asako Shindo, Tae Joo Park, Edwin C. Oh, Srimoyee Ghosh, Ryan S. Gray, Richard A. Lewis, Colin A. Johnson, Tania Attie-Bittach, Nicholas Katsanis, and John B. Wallingford. Planar cell polarity acts through septins to control collective cell movement and ciliogenesis. *Science*, 329(5997):1337–1340, 2010.

[214] Adriana M Mujal, Julia K Gilden, Audrey Gérard, Makoto Kinoshita, and Matthew F Krummel. A septin requirement differentiates autonomous and contact-facilitated T cell proliferation. *Nature Immunology*, 17(3):315–322, 2016.

[215] Zhonghua Liu, Queenie P Vong, Chengyu Liu, and Yixian Zheng. Borg5 is required for angiogenesis by regulating persistent directional migration of the cardiac microvascular endothelial cells. *Molecular Biology of the Cell*, 25(6):841–851, 2014.

[216] Annette Füchtbauer, Louise B Lassen, Astrid B Jensen, Jennifer Howard, Adán De Salas Quiroga, Søren Warming, Annette B Sørensen, Finn S Pedersen, and Ernst Martin Füchtbauer. Septin9 is involved in septin filament formation and cellular stability. *Biological Chemistry*, 392(8-9):769–777, 2011.

[217] Shunsuke Yamada, Takumi Isogai, Ryugo Tero, Yohko Tanaka-Takiguchi, Toru Ujihara, Makoto Kinoshita, and Kingo Takiguchi. Septin Interferes with the Temperature-Dependent Domain Formation and Disappearance of Lipid Bilayer Membranes. *Langmuir*, 32(48):12823–12832, 2016.

[218] Aurélie Bertin, Michael A. McMurray, Jason Pierson, Luong Thai, Kent L. McDonald, Elena A. Zehr, Galo García, Peter Peters, Jeremy Thorner, and Eva Nogales. Three-dimensional ultrastructure of the septin filament network in Saccharomyces cerevisiae. *Molecular Biology of the Cell*, 23(3):423–432, 2012.

[219] Gilbert Di Paolo and Pietro De Camilli. Phosphoinositides in cell regulation and membrane dynamics. *Nature*, 443(7112):651–657, 2006.

[220] Julie A. Brill, Raymond Wong, and Andrew Wilde. Phosphoinositide function in cytokinesis. *Current Biology*, 21(22):R930–R934, 2011.

[221] Juha Saarikangas, Hongxia Zhao, and Pekka Lappalainen. Regulation of the actin cytoskeleton-plasma membrane interplay by phosphoinositides. *Physiological Reviews*, 90(1):259–289, 2010.

[222] Jianshe Zhang, Chen Kong, Hong Xie, Peter S. McPherson, Sergio Grinstein, and William S. Trimble. Phosphatidylinositol polyphosphate binding to the mammalian septin H5 is modulated by GTP. *Current Biology*, 9(24):1458–1467, 1999.

[223] Stuart McLaughlin, Jiyao Wang, Alok Gambhir, and Diana Murray. PIP2 and proteins: Interactions, organization, and information flow. *Annual Review of Biophysics and Biomolecular Structure*, 31:151–175, 2002.

[224] Cyntia Taveneau, Rémi Blanc, Gérard Péhau-Arnaudet, Aurélie Di Cicco, and Aurélie Bertin. Synergistic role of nucleotides and lipids for the self-assembly of Shs1 septin oligomers. *Biochemical Journal*, 477(14):2697–2714, 2020.

[225] Sina Krokowski, Damián Lobato-Márquez, Arnaud Chastanet, Pedro Matos Pereira, Dimitrios Angelis, Dieter Galea, Gerald Larrouy-Maumus, Ricardo Henriques, Elias T. Spiliotis, Rut Carballido-López, and Serge Mostowy. Septins Recognize and Entrap Dividing Bacterial Cells for Delivery to Lysosomes. *Cell Host and Microbe*, 24(6):866–874, 2018.

[226] Sahaja Aigal, Ramin Omidvar, Kai Stober, Jessica Ziegelbauer, Thorsten Eierhoff, Janik Niklas Schampera, Winfried Römer, and Carsten Schwan. Septin barriers protect mammalian host cells against Pseudomonas aeruginosa invasion. *Cell Reports*, 41(3):111510, 2022.

[227] Alexander Mela and Michelle Momany. Septins coordinate cell wall integrity and lipid metabolism in a sphingolipid-dependent process. *Journal of Cell Science*, 135(5):jcs258336, 2022.

[228] Antonio Casamayor and Michael Snyder. Molecular Dissection of a Yeast Septin: Distinct Domains Are Required for Septin Interaction, Localization, and Function. *Molecular and Cellular Biology*, 23(8):2762–2777, 2003.

[229] Italo A. Cavini, Diego A. Leonardo, Higor V.D. Rosa, Danielle K.S.V. Castro, Humberto D'Muniz Pereira, Napoleão F. Valadares, Ana P.U. Araujo, and Richard C. Garratt. The Structural Biology of Septins and Their Filaments: An Update. *Frontiers in Cell and Developmental Biology*, 9:3246, 2021.

[230] Kevin S. Cannon, Benjamin L. Woods, John M. Crutchley, and Amy S. Gladfelter. An amphipathic helix enables septins to sense micrometer-scale membrane curvature. *The Journal of Cell Biology*, 218(4):1128–1137, 2019.

[231] Ilya Reviakine, Diethelm Johannsmann, and Ralf P. Richter. Hearing what you cannot see and visualizing what you hear: Interpreting quartz crystal microbalance data from solvated interfaces. *Analytical Chemistry*, 83(23):8838–8848, 2011.

[232] Ralf P. Richter, Rémi Bérat, and Alain R. Brisson. Formation of solid-supported lipid bilayers: An integrated view. *Langmuir*, 22(8):3497–3505, 2006.

[233] Nam Joon Cho, Curtis W. Frank, Bengt Kasemo, and Fredrik Höök. Quartz crystal microbalance with dissipation monitoring of supported lipid bilayers on various substrates. *Nature Protocols*, 5(6):1096–1106, 2010.

[234] Noel F. Bonet, Daniel G. Cava, and Marisela Vélez. Quartz crystal microbalance and atomic force microscopy to characterize mimetic systems based on supported lipids bilayer. *Frontiers in Molecular Biosciences*, 9(August):1–17, 2022.

[235] G. Sauerbrey. Use of Quartz Crystal Vibrator for Weighting Thin Films on a Microbalance. *Zeitschrift für Physik*, 155(2):206–222, 1959.

[236] Agata Szuba. *Deconstruction of septin assembly*. PhD thesis, AMOLF, 2019.

[237] Diethelm Johannsmann, Ilya Reviakine, and Ralf P. Richter. Dissipation in films of adsorbed nanospheres studied by quartz crystal microbalance (QCM). *Analytical Chemistry*, 81(19):8167–8176, 2009.

[238] Pit Bingen, Guoliang Wang, Nicole F. Steinmetz, Michael Rodahl, and Ralf P. Richter. Solvation effects in the quartz crystal microbalance with dissipation monitoring response to biomolecular adsorption. A phenomenological approach. *Analytical Chemistry*, 80(23):8880–8890, 2008.

[239] Edurne Tellechea, Diethelm Johannsmann, Nicole F. Steinmetz, Ralf P. Richter, and Ilya Reviakine. Model-independent analysis of QCM data on colloidal particle adsorption. *Langmuir*, 25(9):5177–5184, 2009.

[240] Victoria Shabardina, Corinna Kramer, Benjamin Gerdes, Julia Braunger, Andrea Cordes, Jonas Schäfer, Ingo Mey, David Grill, Volker Gerke, and Claudia Steinem. Mode of Ezrin-Membrane Interaction as a Function of PIP2 Binding and Pseudophosphorylation. *Biophysical Journal*, 110(12):2710–2719, 2016.

[241] Ixaskun Carton, Alain R. Brisson, and Ralf P. Richter. Label-free detection of clustering of membrane-bound proteins. *Analytical Chemistry*, 82(22):9275–9281, 2010.

[242] Patrick Drücker, Milena Pejic, David Grill, Hans Joachim Galla, and Volker Gerke. Cooperative binding of annexin A2 to cholesterol- and phosphatidylinositol-4,5-bisphosphate-containing bilayers. *Biophysical Journal*, 107(9):2070–2081, 2014.

[243] Chirag Vasavda, Nicholas W. Zaccor, Paul C. Scherer, Charlotte J. Sumner, and Solomon H. Snyder. Measuring g-protein-coupled receptor signaling via radio-labeled GTP binding. *Journal of Visualized Experiments*, 2017(124):e55561, 2017.

[244] Keisuke Sawada, Noriko Echigo, Narinobu Juge, Takaaki Miyaji, Masato Otsuka, Hiroshi Omote, Akitsugu Yamamoto, and Yoshinori Moriyama. Identification of a vesicular nucleotide transporter. *Proceedings of the National Academy of Sciences of the United States of America*, 105(15):5683–5686, 2008.

[245] Julia A. Braunger, Corinna Kramer, Daniela Morick, and Claudia Steinem. Solid supported membranes doped with PIP2: Influence of ionic strength and pH on Bilayer formation and membrane organization. *Langmuir*, 29(46):14204–14213, 2013.

[246] Egidijus E. Uzgiris and Roger D. Kornberg. Two-dimensional crystallization technique for imaging macromolecules, with application to antigen-antibody-complement complexes. *Nature*, 301(5896):125–129, 1983.

[247] Deborah F. Kelly, Danijela Dukovski, and Thomas Walz. A practical guide to the use of monolayer purification and affinity grids. *Methods in Enzymology*, 481(C):83–107, 2010.

[248] David Nečas and Petr Klapetek. Gwyddion: An open-source software for SPM data analysis. *Central European Journal of Physics*, 10(1):181–188, 2012.

[249] Kevin S. Cannon, Jose M. Vargas-Muniz, Neil Billington, Ian Seim, Joanne Ekena, James R. Sellers, and Amy S. Gladfelter. A gene duplication of a septin reveals a developmentally regulated filament length control mechanism. *The Journal of cell biology*, 222(3):e202204063, 2023.

[250] Clifford P. Brangwynne, F. C. MacKintosh, and David A. Weitz. Force fluctuations and polymerization dynamics of intracellular microtubules. *Proceedings of the National Academy of Sciences of the United States of America*, 104(41):16128–16133, 2007.

[251] Daniel T. Gillespie. Exact stochastic simulation of coupled chemical reactions. *J. Phys. Chem.*, 81(25):2340–2361, 1977.

[252] Radek Erban, Jonathan Chapman, and Philip Maini. A practical guide to stochastic simulations of reaction-diffusion processes. *arXiv*, 2007.

[253] Priyamvada Chugh, Andrew G. Clark, Matthew B. Smith, Davide A.D. Cassani, Kai Dierkes, Anan Ragab, Philippe P. Roux, Guillaume Charras, Guillaume Salbreux, and Ewa K. Paluch. Actin cortex architecture regulates cell surface tension. *Nature Cell Biology*, 19(6):689–697, 2017.

[254] Serge Mostowy, Sébastien Janel, Claire Forestier, Charles Roduit, Sandor Kasas, Javier Pizarro-Cerdá, Pascale Cossart, and Frank Lafont. A Role for Septins in the Interaction between the Listeria monocytogenes Invasion Protein InlB and the Met Receptor. *Biophysical Journal*, 100(8):1949–1959, 2011.

[255] Julia Patzig, Michelle S. Erwig, Stefan Tenzer, Kathrin Kusch, Payam Dibaj, Wiebke Möbius, Sandra Goebbels, Nicole Schaeren-Wiemers, Klaus-Armin Nave, and Hauke B. Werner. Septin/anillin filaments scaffold central nervous system myelin to accelerate nerve conduction. *eLife*, 5(AUGUST):e17119, aug 2016.

[256] Tianhui Sun, Yuzhao Song, Dequn Teng, Yanan Chen, Jianli Dai, Mengqi Ma, Wei Zhang, and José C. Pastor-Pareja. Atypical laminin spots and pull-generated microtubule-actin projections mediate Drosophila wing adhesion. *Cell Reports*, 36(10):109667, 2021.

[257] Valentin Laplaud, Nicolas Levernier, Judith Pineau, Mabel San Roman, Lucie Barbier, Pablo J. S ez, Ana Maria Lennon-Dum nil, Pablo Vargas, Karsten Kruse, Olivia Du Roure, Matthieu Piel, and Julien Heuvingh. Pinching the cortex of live cells reveals thickness instabilities caused by myosin II motors. *Science Advances*, 7(27), jun 2021.

[258] Lucia Baldauf, Felix Frey, Marcos Arribas Perez, Timon Idema, and Gijsje H. Koenderink. Branched actin cortices reconstituted in vesicles sense membrane curvature. *Biophysical Journal*, 122(0):1–14, 2023.

[259] Lori Van De Cauter, Federico Fanalista, Lennard Van Buren, Nicola De Franceschi, Elisa Godino, Sharon Bouw, Christophe Danelon, Cees Dekker, Gijsje H. Koenderink, and Kristina A. Ganzinger. Optimized cDICE for Efficient Reconstitution of Biological Systems in Giant Unilamellar Vesicles. *ACS Synthetic Biology*, 10(7):1690–1702, 2021.

[260] Kandice R. Levental, Eric Malmberg, Jessica L. Symons, Yang Yi Fan, Robert S. Chapkin, Robert Ernst, and Ilya Levental. Lipidomic and biophysical homeostasis of mammalian membranes counteracts dietary lipid perturbations to maintain cellular fitness. *Nature Communications*, 11(1):1–13, 2020.

[261] Jessica L. Symons, Kwang Jin Cho, Jeffrey T. Chang, Guangwei Du, M. Neal Waxham, John F. Hancock, Ilya Levental, and Kandice R. Levental. Lipidomic atlas of mammalian cell membranes reveals hierarchical variation induced by culture conditions, subcellular membranes, and cell lineages. *Soft Matter*, 17(2):288–297, 2021.

[262] Lennard van Buren, Gijsje Hendrika Koenderink, and Cristina Martinez-Torres. DisGUVery: A Versatile Open-Source Software for High-Throughput Image Analysis of Giant Unilamellar Vesicles. *ACS Synthetic Biology*, 12(1):120–135, 2023.

[263] Michael Schaich, Diana Sobota, Hannah Sleath, Jehangir Cama, and Ulrich F. Keyser. Characterization of lipid composition and diffusivity in OLA generated vesicles. *Biochimica et Biophysica Acta - Biomembranes*, 1862(9):183359, 2020.

[264] Siddharth Deshpande, Yaron Caspi, Anna E.C. Meijering, and Cees Dekker. Octanol-assisted liposome assembly on chip. *Nature Communications*, 7(1):1–9, 2016.

[265] A. Sonnleitner, G. J. Schütz, and Thomas Schmidt. Free Brownian motion of individual lipid molecules in biomembranes. *Biophysical Journal*, 77(5):2638–2642, 1999.

[266] Ralf P Richter, Nicolas Maury, and Alain R Brisson. On the effect of the solid support on the interleaflet distribution of lipids in supported lipid bilayers. *Langmuir*, 21(1):299–304, 2005.

[267] Kalani J. Seu, Anjan P. Pandey, Farzin Haque, Elizabeth A. Proctor, Alexander E. Ribbe, and Jennifer S. Hovis. Effect of surface treatment on diffusion and domain formation in supported lipid bilayers. *Biophysical Journal*, 92(7):2445–2450, 2007.

[268] M. M.A.E. Claessens, F. A.M. Leermakers, F. A. Hoekstra, and M. A.Cohen Stuart. Osmotic shrinkage and reswelling of giant vesicles composed of dioleoylphosphatidylglycerol and cholesterol. *Biochimica et Biophysica Acta - Biomembranes*, 1778(4):890–895, 2008.

[269] Jonas Henriksen, Amy C. Rowat, and John H. Ipsen. Vesicle fluctuation analysis of the effects of sterols on membrane bending rigidity. *European Biophysics Journal*, 33(8):732–741, 2004.

[270] T. P.T. Dao, M. Fauquignon, F. Fernandes, E. Ibarboure, A. Vax, M. Prieto, and J. F. Le Meins. Membrane properties of giant polymer and lipid vesicles obtained by electroformation and pva gel-assisted hydration methods. *Colloids and Surfaces A: Physicochemical and Engineering Aspects*, 533:347–353, 2017.

[271] Ida Louise Jørgensen, Gerdi Christine Kemmer, and Thomas Günther Pomorski. Membrane protein reconstitution into giant unilamellar vesicles: a review on current techniques. *European Biophysics Journal*, 46(2):103–119, 2017.

[272] Joseph H. Lorent and Ilya Levental. Preparation and properties of giant plasma membrane vesicles and giant unilamellar vesicles from natural membranes. In Ruminana Dimova, Carlos Marques, Pasquale Stano, and Peter Walde, editors, *The Giant Vesicle Book*, pages 1–18. CRC PRess, 1st edition, 2019.

[273] Wenzheng Shi, Kevin S. Cannon, Brandy N. Curtis, Christopher Edelmaier, Amy S. Gladfelter, and Ehssan Nazockdast. Curvature sensing as an emergent property of multiscale assembly of septins. *Proceedings of the National Academy of Sciences of the United States of America*, 120(6):e2208253120, 2023.

[274] Kyu I. Lee, Wonpil Im, and Richard W. Pastor. Langevin dynamics simulations of charged model phosphatidylinositol lipids in the presence of diffusion barriers: Toward an atomic level understanding of corralling of PIP2 by protein fences in biological membranes. *BMC Biophysics*, 7(1):1–10, nov 2014.

[275] Carolyn Kimme, Dana Ballard, and Jack Sklansky. Finding Circles by an Array of Accumulators. *Communications of the ACM*, 18(2):120–122, 1975.

[276] C. H. Li and P. K.S. Tam. An iterative algorithm for minimum cross entropy thresholding. *Pattern Recognition Letters*, 19(8):771–776, 1998.

[277] Revathi Ananthakrishnan and Allen Ehrlicher. The forces behind cell movement. *International Journal of Biological Sciences*, 3(5):303–317, 2007.

[278] H. Lee Sweeney, Anne Houdusse, and Julien Robert-Paganin. Myosin Structures. In *Advances in Experimental Medicine and Biology*, volume 1239, pages 7–19. Springer, 2020.

[279] Piyali Guhathakurta, Ewa Prochniewicz, and David D. Thomas. Actin-myosin interaction: Structure, function and drug discovery. *International Journal of Molecular Sciences*, 19(9):2628, 2018.

[280] Anne Houdusse and H. Lee Sweeney. How Myosin Generates Force on Actin Filaments. *Trends in Biochemical Sciences*, 41(12):989–997, 2016.

[281] M Kinoshita, S Kumar, A Mizoguchi, C Ide, A Kinoshita, T Haraguchi, Y Hiraoka, and M Noda. Nedd5, a mammalian septin, is a novel cytoskeletal component interacting with actin-based structures. *Genes & Development*, 11(12):1535–1547, 1997.

[282] Manoj B Menon and Matthias Gaestel. Sep(t)arate or not – how some cells take septin-independent routes through cytokinesis. *Journal of Cell Science*, 128(10):1877–1886, 2015.

[283] Katja Schmidt and Benjamin J Nichols. Functional interdependence between septin and actin cytoskeleton. *BMC cell biology*, 5(1):43, 2004.

[284] Aaron J. Farrugia, Javier Rodríguez, Jose L. Orgaz, María Lucas, Victoria Sanz-Moreno, and Fernando Calvo. CDC42EP5/BORG3 modulates SEPT9 to promote actomyosin function, migration, and invasion. *Journal of Cell Biology*, 219(9):e201912159, 2020.

[285] Joanna Kim and John A Cooper. Junctional Localization of Septin 2 Is Required for Organization of Junctional Proteins in Static Endothelial Monolayers. *Arteriosclerosis, Thrombosis, and Vascular Biology*, 41(1):346–359, 2020.

[286] Joanna Kim, Olivia L Mooren, Michael D Onken, and John A Cooper. Septin and actin contributions to endothelial cell–cell junctions and monolayer integrity. *Cytoskeleton*, pages 1–14, 2022.

[287] Asako Shindo and John B Wallingford. PCP and Septins Compartmentalize Cortical Actomyosin to Direct Collective Cell Movement. *Science*, 343(6171):649–652, 2014.

[288] Tae Joo Park, Su Kyoung Kim, and John B Wallingford. The planar cell polarity effector protein Wdpcp (Fritz) controls epithelial cell cortex dynamics via septins and actomyosin. *Biochemical and Biophysical Research Communications*, 456(2):562–566, 2015.

[289] Thomas Lecuit and Eric Wieschaus. Polarized insertion of new membrane from a cytoplasmic reservoir during cleavage of the Drosophila embryo. *Journal of Cell Biology*, 150(4):849–860, aug 2000.

[290] Poul M. Bendix, Gijsje H. Koenderink, Damien Cuvelier, Zvonimir Dogic, Bernard N. Koeleman, William M. Brieher, Christine M. Field, L. Mahadevan, and David A. Weitz. A quantitative analysis of contractility in active cytoskeletal protein networks. *Biophysical Journal*, 94(8):3126–3136, 2008.

[291] Viktoria Wollrab, Julio M. Belmonte, Lucia Baldauf, Maria Leptin, François Nédeléc, and Gijsje H. Koenderink. Polarity sorting drives remodeling of actin-myosin networks. *Journal of Cell Science*, 132(4):jcs219717, 2019.

[292] Camelia G. Muresan, Zachary Gao Sun, Vikrant Yadav, A. Pasha Tabatabai, Laura Lanier, June Hyung Kim, Taeyoon Kim, and Michael P. Murrell. F-actin architecture determines constraints on myosin thick filament motion. *Nature Communications*, 13(1):1–16, 2022.

[293] Kimberly L. Weirich, Samantha Stam, Edwin Munro, and Margaret L. Gardel. Actin bundle architecture and mechanics regulate myosin II force generation. *Biophysical Journal*, 120(10):1957–1970, 2021.

[294] Simone Köhler, Kurt M. Schmoller, Alvaro H. Crevenna, and Andreas R. Bausch. Regulating Contractility of the Actomyosin Cytoskeleton by pH. *Cell Reports*, 2(3):433–439, 2012.

[295] Neil Billington, Aibing Wang, Jian Mao, Robert S. Adelstein, and James R. Sellers. Characterization of three full-length human nonmuscle myosin II paralogs. *Journal of Biological Chemistry*, 288(46):33398–33410, 2013.

[296] Péter Ecsédi, Neil Billington, Gyula Pálfy, Gergo Gógl, Bence Kiss, Éva Bulyáki, Andrea Bodor, James R. Sellers, and X. László Nyitray. Multiple S100 protein isoforms and C-terminal phosphorylation contribute to the paralog-selective regulation of nonmuscle myosin 2 filaments. *Journal of Biological Chemistry*, 293(38):14850–14867, 2018.

[297] Christopher B. O'Connell, Matthew J. Tyska, and Mark S. Mooseker. Myosin at work: Motor adaptations for a variety of cellular functions. *Biochimica et Biophysica Acta - Molecular Cell Research*, 1773(5):615–630, 2007.

[298] Michael P. Sheetz and James A. Spudich. Movement of myosin-coated structures on actin cables. *Cell Motility*, 303(5):485–489, 1983.

[299] Bipasha Barua, Attila Nagy, James R. Sellers, and Sarah E. Hitchcock-Degregori. Regulation of nonmuscle myosin II by tropomyosin. *Biochemistry*, 53(24):4015–4024, 2014.

[300] Enrico Grazi. What is the diameter of the actin filament? *FEBS Letters*, 405(3):249–252, 1997.

[301] Stanislav Nagy, Benjamin L. Ricca, Melanie F. Norstrom, David S. Courson, Crista M. Brawley, Philip A. Smithback, and Ronald S. Rock. A myosin motor that selects bundled actin for motility. *Proceedings of the National Academy of Sciences of the United States of America*, 105(28):9616–9620, 2008.

[302] F. Backouche, L. Haviv, D. Groswasser, and A. Bernheim-Groswasser. Active gels: Dynamics of patterning and self-organization. *Physical Biology*, 3(4):264–273, 2006.

[303] Darius Vasco Köster, Kabir Husain, Elda Iljazi, Abrar Bhat, Peter Bieling, R. Dyche Mullins, Madan Rao, and Satyajit Mayor. Actomyosin dynamics drive local membrane component organization in an in vitro active composite layer. *Proceedings of the National Academy of Sciences of the United States of America*, 113(12):E1645–E1654, 2016.

[304] Samantha Stam, Simon L. Freedman, Shiladitya Banerjee, Kimberly L. Weirich, Aaron R. Dinner, and Margaret L. Gardel. Filament rigidity and connectivity tune the deformation modes of active biopolymer networks. *Proceedings of the National Academy of Sciences of the United States of America*, 114(47):E10037–E10045, 2017.

[305] A. E. Carlsson. Contractile stress generation by actomyosin gels. *Physical Review E - Statistical, Nonlinear, and Soft Matter Physics*, 74(5):051912, 2006.

[306] Vitold E. Galkin, Albina Orlova, Matthijn R. Vos, Gunnar F. Schröder, and Edward H. Egelman. Near-Atomic Resolution for One State of F-Actin. *Structure*, 23(1):173–182, 2015.

[307] Michael Murrell, Patrick W. Oakes, Martin Lenz, and Margaret L. Gardel. Forcing cells into shape: The mechanics of actomyosin contractility. *Nature Reviews Molecular Cell Biology*, 16(8):486–498, 2015.

[308] Michael P Murrell and Margaret L Gardel. F-actin buckling coordinates contractility and severing in a biomimetic actomyosin cortex. *Proceedings of the National Academy of Sciences of the United States of America*, 109(51):20820–20825, 2012.

[309] José Alvarado, Michael Sheinman, Abhinav Sharma, Fred C. Mackintosh, and Gijsje H. Koenderink. Molecular motors robustly drive active gels to a critically connected state. *Nature Physics*, 9(9):591–597, 2013.

[310] Hajer Ennomani, Gaëlle Letort, Christophe Guérin, Jean Louis Martiel, Wenxiang Cao, François Nédélec, Enrique M. De La Cruz, Manuel Théry, and Laurent Blanchoin. Architecture and Connectivity Govern Actin Network Contractility. *Current Biology*, 26(5):616–626, 2016.

[311] Gijsje H. Koenderink, Zvonimir Dogic, Fumihiko Nakamura, Poul M. Bendix, Frederick C. MacKintosh, John H. Hartwig, Thomas P. Stossel, and David A. Weitz. An active biopolymer network controlled by molecular motors. *Proceedings of the National Academy of Sciences of the United States of America*, 106(36):15192–15197, 2009.

[312] Wei Yung Ding, Hui Ting Ong, Yusuke Hara, Jantana Wongsantichon, Yusuke Toyama, Robert C. Robinson, François Nédélec, and Ronen Zaidel-Bar. Plastin increases cortical connectivity to facilitate robust polarization and timely cytokinesis. *Journal of Cell Biology*, 216(5):1371–1386, 2017.

[313] Shashank Shekhar and Marie France Carlier. Enhanced Depolymerization of Actin Filaments by ADF/Cofilin and Monomer Funneling by Capping Protein Cooperate to Accelerate Barbed-End Growth. *Current Biology*, 27(13):1990–1998.e5, 2017.

[314] Jingyuan Xu, William H. Schwarz, Josef A. Käs, Thomas P. Stossel, Paul A. Janmey, and Thomas D. Pollard. Mechanical properties of actin filament networks depend on preparation, polymerization conditions, and storage of actin monomers. *Biophysical Journal*, 74(5):2731–2740, 1998.

[315] Sarkis S. Margossian and Susan Lowey. Preparation of Myosin and Its Subfragments from Rabbit Skeletal Muscle. In *Methods in Enzymology*, volume 85, pages 55–71. Academic Press Inc., jan 1982.

[316] Colin Echeverría Aitken, R. Andrew Marshall, and Joseph D. Puglisi. An oxygen scavenging system for improvement of dye stability in single-molecule fluorescence experiments. *Biophysical Journal*, 94(5):1826–1835, 2008.

[317] Pravin V. Patil and David P. Ballou. The use of protocatechuate dioxygenase for maintaining anaerobic conditions in biochemical experiments. *Analytical Biochemistry*, 286(2):187–192, 2000.

[318] Ivan Rasnik, Sean A. McKinney, and Taekjip Ha. Nonblinking and long-lasting single-molecule fluorescence imaging. *Nature Methods*, 3(11):891–893, 2006.

[319] Oskar Staufer, Jacqueline A. DE LORA, Eleonora Bailoni, Alisina Bazrafshan, Amelie S. Benk, Kevin Jahnke, Zachary A. Manzer, Lado Otrin, Telmo Díez Pérez, Judee Sharon, Jan Steinkühler, Katarzyna P. Adamala, Bruna Jacobson, Marileen Dogterom, Kerstin Göpfrich, Darko Stefanovic, Susan R. Atlas, Michael Grunze, Matthew R. Lakin, Andrew P. Shreve, Joachim P. Spatz, and Gabriel P. López. Building a community to engineer synthetic cells and organelles from the bottom-up. *eLife*, 10, 2021.

[320] Lorenzo Olivi, Mareike Berger, Ramon N.P. Creyghton, Nicola De Franceschi, Cees Dekker, Bela M. Mulder, Nico J. Claassens, Pieter Rein ten Wolde, and John van der Oost. Towards a synthetic cell cycle. *Nature Communications*, 12(1):1–11, 2021.

[321] Koen Schakenraad, Jeremy Ernst, Wim Pomp, Erik H.J. Danen, Roeland M.H. Merks, Thomas Schmidt, and Luca Giomi. Mechanical interplay between cell shape and actin cytoskeleton organization. *Soft Matter*, 16(27):6328–6343, 2020.

[322] Tim Hohmann and Faramarz Dehghani. The cytoskeleton—a complex interacting meshwork. *Cells*, 8(4):362, 2019.

[323] T. P. Stossel, C. Chaponnier, R. M. Ezzell, J. H. Hartwig, P. A. Janmey, D. J. Kwiatkowski, S. E. Lind, D. B. Smith, F. S. Southwick, and H. L. Yin. Nonmuscle actin-binding proteins. *Annual review of cell biology*, 1:353–402, 1985.

[324] John H. Hartwig and David J. Kwiatkowski. Actin-binding proteins. *Current Opinion in Cell Biology*, 3(1):87–97, 1991.

[325] C. G. Dos Remedios, D. Chhabra, M. Kekic, I. V. Dedova, M. Tsubakihara, D. A. Berry, and N. J. Nosworthy. Actin binding proteins: Regulation of cytoskeletal microfilaments. *Physiological Reviews*, 83(2):433–473, 2003.

[326] Jonathan Garamella, David Garenne, and Vincent Noireaux. *TXTL-based approach to synthetic cells*, volume 617. Elsevier Inc., 1 edition, 2019.

[327] Anne Doerr, David Foschepoth, Anthony C. Forster, and Christophe Danelon. In vitro synthesis of 32 translation-factor proteins from a single template reveals impaired ribosomal processivity. *Scientific Reports*, 11(1):1–12, 2021.

[328] Jonathan R. Terman and Anna Kashina. Post-translational modification and regulation of actin. *Current Opinion in Cell Biology*, 25(1):30–38, 2013.

[329] Boris Macek, Karl Forchhammer, Julie Hardouin, Eilika Weber-Ban, Christophe Grangeasse, and Ivan Mijakovic. Protein post-translational modifications in bacteria. *Nature Reviews Microbiology*, 17(11):651–664, 2019.

[330] Minoru Tamura. Production of Human β-Actin Using a Bacterial Expression System with a Cold Shock Vector. *Current protocols in protein science*, 93(1):e61, 2018.

[331] Takeshi Sakamoto, John Limouze, Christian A. Combs, Aaron F. Straight, and James R. Sellers. Blebbistatin, a myosin II inhibitor, is photoinactivated by blue light. *Biochemistry*, 44(2):584–588, 2005.

[332] Kim S. Horger, Daniel J. Estes, Ricardo Capone, and Michael Mayer. Films of agarose enable rapid formation of giant liposomes in solutions of physiologic ionic strength. *Journal of the American Chemical Society*, 131(5):1810–1819, 2009.

[333] Edith Schäfer, Marian Vache, Torben Tobias Kliesch, and Andreas Janshoff. Mechanical response of adherent giant liposomes to indentation with a conical AFM-tip. *Soft Matter*, 11(22):4487–4495, 2015.

[334] Etienne Loiseau, Jochen A.M. Schneider, Felix C. Keber, Carina Pelzl, Gladys Massiera, Guillaume Salbreux, and Andreas R. Bausch. Shape remodeling and blebbing of active cytoskeletal vesicles. *Science Advances*, 2(4), 2016.

[335] Ian Linsmeier, Shiladitya Banerjee, Patrick W. Oakes, Wonyeong Jung, Taeyoon Kim, and Michael P. Murrell. Disordered actomyosin networks are sufficient to produce cooperative and telescopic contractility. *Nature Communications*, 7(1):1–9, 2016.

[336] Katharina Dürre, Felix C. Keber, Philip Bleicher, Fridtjof Brauns, Christian J. Cyron, Jan Faix, and Andreas R. Bausch. Capping protein-controlled actin polymerization shapes lipid membranes. *Nature Communications*, 9(1):1630, 2018.

[337] Thomas Litschel, Charlotte F. Kelley, Danielle Holz, Maral Adeli Koudehi, Sven K. Vogel, Laura Burbaum, Naoko Mizuno, Dimitrios Vavylonis, and Petra Schwille. Reconstitution of contractile actomyosin rings in vesicles. *Nature Communications*, 12(1):1–10, 2021.

[338] Yashar Bashirzadeh, Hossein Moghimianavval, and Allen P. Liu. Encapsulated actomyosin patterns drive cell-like membrane shape changes. *iScience*, 25(5):104236, 2022.

[339] Laurent Limozin and Erich Sackmann. Polymorphism of Cross-Linked Actin Networks in Giant Vesicles. *Physical Review Letters*, 89(16):168103, 2002.

[340] Carsten F.E. Schroer, Lucia Baldauf, Lennard van Buren, Tsjerk A. Wassenaar, Manuel N. Melo, Gijsje H. Koenderink, and Siewert J. Marrink. Charge-dependent interactions of monomeric and filamentous actin with lipid bilayers. *Proceedings of the National Academy of Sciences of the United States of America*, 117(11):5861–5872, 2020.

[341] Feng Ching Tsai, Björn Stuhrmann, and Gijsje H. Koenderink. Encapsulation of active cytoskeletal protein networks in cell-sized liposomes. *Langmuir*, 27(16):10061–10071, 2011.

[342] Kevin Carvalho, Feng C. Tsai, Edouard Lees, Raphaël Voituriez, Gijsje H. Koenderink, and Cecile Sykes. Cell-sized liposomes reveal how actomyosin cortical tension drives shape change. *Proceedings of the National Academy of Sciences of the United States of America*, 110(41):16456–16461, 2013.

[343] Dennis Merkle, Nicoletta Kahya, and Petra Schwille. Reconstitution and anchoring of cytoskeleton inside giant unilamellar vesicles. *Chembiochem : a European journal of chemical biology*, 9(16):2673–2681, 2008.

[344] Lucia Baldauf, Felix Frey, Marcos Arribas Perez, Miroslav Mladenov, Michael Way, Timon Idema, and Gijsje Hendrika Koenderink. Biomimetic actin cortices shape cell-sized lipid vesicles. *bioRxiv*, 2023.

[345] Jeffrey A. Nye and Jay T. Groves. Kinetic control of histidine-tagged protein surface density on supported lipid bilayers. *Langmuir*, 24(8):4145–4149, 2008.

[346] Gokul Raghunath and R. Brian Dyer. Kinetics of Histidine-Tagged Protein Association to Nickel-Decorated Liposome Surfaces. *Langmuir*, 35(38):12550–12561, 2019.

[347] L. Limozin, M. Bärmann, and E. Sackmann. On the organization of self-assembled actin networks in giant vesicles. *European Physical Journal E*, 10(4):319–330, 2003.

[348] Feng Ching Tsai and Gijsje Hendrika Koenderink. Shape control of lipid bilayer membranes by confined actin bundles. *Soft Matter*, 11(45):8834–8847, 2015.

[349] Pattipong Wisanpitayakorn, Keith J. Mickolajczyk, William O. Hancock, Luis Vidali, and Erkan Tüzel. Measurement of the persistence length of cytoskeletal filaments using curvature distributions. *Biophysical Journal*, 121(10):1813–1822, 2022.

[350] Lior Haviv, Yifat Brill-Karniely, Rachel Mahaffy, Frederic Backouche, Avinoam Ben-Shaul, Thomas D. Pollard, and Anne Bernheim-Groswasser. Reconstitution of the transition from lamellipodium to filopodium in a membrane-free system. *Proceedings of the National Academy of Sciences of the United States of America*, 103(13):4906–4911, 2006.

[351] Moritz Schu, Emmanuel Terriac, Marcus Koch, Stephan Paschke, Franziska Lautenschläger, and Daniel A.D. Flormann. Scanning electron microscopy preparation of the cellular actin cortex: A quantitative comparison between critical point drying and hexamethyldisilazane drying. *PLoS ONE*, 16(7 July):e0254165, 2021.

[352] Avital A. Rodal, Lukasz Kozubowski, Bruce L. Goode, David G. Drubin, and John H. Hartwig. Actin and septin ultrastructures at the budding yeast cell cortex. *Molecular Biology of the Cell*, 16(1):372–384, 2005.

[353] Jianli Hu, Xiaobo Bai, Jonathan R. Bowen, Lee Dolat, Farida Korobova, Wenqian Yu, Peter W. Baas, Tatyana Svitkina, Gianluca Gallo, and Elias T. Spiliotis. Septin-driven coordination of actin and microtubule remodeling regulates the collateral branching of axons. *Current Biology*, 22(12):1109–1115, 2012.

[354] Sonal, Kristina A. Ganzinger, Sven K. Vogel, Jonas Mücksch, Philipp Blumhardt, and Petra Schwille. Myosin-II activity generates a dynamic steady state with continuous actin turnover in a minimal actin cortex. *Journal of Cell Science*, 132(4):jcs219899, 2019.

[355] Edwin Munro. Anillin Puts RhoA in Touch with PIP2. *Developmental Cell*, 49(6):819–820, 2019.

[356] Kenneth S Gerien and Jian Qiu Wu. Molecular mechanisms of contractile-ring constriction and membrane trafficking in cytokinesis. *Biophysical Reviews*, 10(6):1649–1666, 2018.

[357] Rebecca A. Green, Ewa Paluch, and Karen Oegema. Cytokinesis in Animal Cells. *Annual Review of Cell and Developmental Biology*, 28(1):29–58, 2012.

[358] Nadab H. Wubshet and Allen P. Liu. Methods to mechanically perturb and characterize GUV-based minimal cell models. *Computational and Structural Biotechnology Journal*, 21:550–562, 2023.

[359] W. Helfrich and R. M. Servuss. Undulations, steric interaction and cohesion of fluid membranes. *Il Nuovo Cimento D*, 3(1):137–151, 1984.

[360] Rumiana Dimova. Recent developments in the field of bending rigidity measurements on membranes. *Advances in Colloid and Interface Science*, 208:225–234, 2014.

[361] Rubèn Serral Gracià, Natalya Bezlyepkina, Roland L. Knorr, Reinhard Lipowsky, and Rumiana Dimova. Effect of cholesterol on the rigidity of saturated and unsaturated membranes: Fluctuation and electrodeformation analysis of giant vesicles. *Soft Matter*, 6(7):1472–1482, 2010.

[362] Emil Endress, Sybille Bayerl, Katrin Prechtel, Christian Maier, Rudolf Merkel, and Thomas M. Bayerl. The effect of cholesterol, lanosterol, and ergosterol on lecithin bilayer mechanical properties at molecular and microscopic dimensions: A solid-state NMR and micropipet study. *Langmuir*, 18(8):3293–3299, 2002.

[363] Vadim Bogatyr, Andreas S. Biebricher, Giulia Bergamaschi, Erwin J.G. Peterman, and Gijs J.L. Wuite. Quantitative Acoustophoresis. *ACS Nanoscience Au*, 2(4):341–354, 2022.

[364] Yoshihiro Shimizu, Akio Inoue, Yukihide Tomari, Tsutomu Suzuki, Takashi Yokogawa, Kazuya Nishikawa, and Takuya Ueda. Cell-free translation reconstituted with purified components. *Nature Biotechnology*, 19(8):751–755, 2001.

[365] Johannes Kattan, Anne Doerr, Marileen Dogterom, and Christophe Danelon. Shaping Liposomes by Cell-Free Expressed Bacterial Microtubules. *ACS Synthetic Biology*, 10(10):2447–2455, 2021.

[366] Elisa Godino and Christophe Danelon. Gene-Directed FtsZ Ring Assembly Generates Constricted Liposomes with Stable Membrane Necks. *Advanced Biology*, 7(3):2200172, 2023.

[367] L. van Buren. *Synthetic Cell Aspirations A Toolbox for Building a Membrane Container from the Bottom Up.* PhD thesis, Delft University of Technology, 2022.

[368] J. Pécréaux, H. G. Döbereiner, J. Prost, J. F. Joanny, and P. Bassereau. Refined contour analysis of giant unilamellar vesicles. *European Physical Journal E*, 13(3):277–290, 2004.

Curriculum Vitæ

Gerard Castro-Linares

1994/05/17	Born in Vilanova i la Geltrú, Spain

Education

2012	Selectivtitat Institut Joaquim Mir
2012-2016	Bachelor of Science in Genetics Universitat Autònoma de Barcelona
2016-2019	Pre-master and Master of Science in Molecular Life Sciences Radboud Universiteit Nijmegen
2019-2023	Ph.D. research AMOLF and Technische Universiteit Delft Promotor: Gijsje H. Koenderink

List of Publications

Included in this thesis:

7. F. Iv, C. Silva Martins, **G. Castro-Linares**, C. Taveneau, P. Barbier, P. Verdier-Pinard, L. Camoin, S. Audebert, F. Tsai, L. Ramond, A. Llewellyn, M. Belhabib, K. Nakazawa, A. Di Cicco, R. Vincentelli, J. Wenger, S. Cabantous, G.H. Koenderink, A. Bertin, and M. Mavrakis. Insights into animal septins using recombinant human septin octamers with 2 distinct SEPT9 isoforms. Journal of Cell Biology (2021). DOI: 10.1242/JCS.258484.

6. A. Szuba, F. Bano, **G. Castro-Linares**, F. Iv, M. Mavrakis, R.P. Richter, A. Bertin, and G.H. Koenderink. Membrane binding controls ordered self-assembly of animal septins. eLife (2021). DOI: 10.7554/ELIFE.63349.

5. M. Kuzmić, **G. Castro Linares**, J. Leischner Fialová, F. Iv, D. Salaün, A. Llewellyn, M. Gomes, M. Belhabib, Y. Liu, K. Asano, M. Rodrigues, D. Isnardon, T. Tachibana, G.H. Koenderink, A. Badache, M. Mavrakis, and P. Verdier-Pinard. Septin-microtubule association via a motif unique to isoform 1 of septin 9 tunes stress fibers. Journal of Cell Science (2022). DOI: 10.1242/jcs.258850.

4. **G. Castro-Linares**, J. den Haan, F. Iv, C. Silva Martins, A. Bertin, M. Mavrakis, and G.H. Koenderink. Purification and Quality Control of Recombinant Septin Complexes for Cell-Free Reconstitution. Journal of Visualized Experiments (2022). DOI: 10.3791/63871

3. M. Carla Silva, C. Taveneau, **G. Castro-Linares**, M. Baibakov, N. Buzhinsky, M. Eroles, V. Milanović, S. Omi, J. Pedelacq, F. Iv, L. Bouillard, A. Llewellyn, M. Gomes, M. Belhabib, M. Kuzmić, P. Verdier-Pinard, S. Lee, A. Badache, S. Kumar, C. Chandre, S. Brasselet, F. Rico, O. Rossier, G.H. Koenderink, J. Wenger, S. Cabantous, and M. Mavrakis. Human septins organize as octamer-based filaments and mediate actin-membrane anchoring in cells. Journal of Cell Biology (2023). DOI: 10.1083/jcb.202203016.

2. **G. Castro-Linares**, D. de Ridder, F. Felix, S. Reese, M. Mavrakis, R.P. Richter, T. Idema, and G.H. Koenderink. Septin complexes form two types of membrane bound layers depending on environmental conditions. Manuscript in preparation.

1. **G. Castro-Linares**, K. Kourkolou, E. Perton, M. Arribas Pérez, and G.H. Koenderink. Human septins exhibit lipid and curvature sensitivity in binding to cell-sized vesicles. Manuscript in preparation.

Not included in this thesis:

3. F. Bano, G. **Castro-Linares**, A. Szuba. Nanoscale imaging of proteins' filament assembly on membrane in rebuilt cell membrane. InFocus (2022).

2. S. El-Gebali, M. Donaldson, Ö. Özkan, **G. Castro-Linares**, E. Plomp, A. Sarre, Y. Turkyilmaz-van der Velden. ELNs and FAIR practises. Manuscript in preparation.

1. G. Giubertoni, L. Feng, K. Klein, G. Giannetti, Y. Choi, A. van der Net, **G. Castro-Linares**, F. Caporaletti, D. Micha, J. Hunger, A. Deblais, D. Bonn, A. Šaric, I.M. Iliea, G.H. Koenderink, and S. Woutersen. Elucidating the role of water in collagen self assembly by isotopically modulating collagen hydration. Manuscript submitted.

Epilogue - The circus

Come one, come all! To the smallest circus of all!

This sentence has been typically used to announce the performance of a circus but I have changed the word ”greatest” to ”smallest” to adapt it to the topic discussed in this thesis, the interaction of septins with the cell membrane or other cytoskeletal proteins. But, many could wonder why I did this? This is a dissertation describing the work done in scientific project during my PhD. It is common in scientific literature to use titles that very precisely describe, like I did for the titles of the chapters, the work done. In this epilogue I want to explain why I chose ”the circus” not only to be part of the title, but also a theme in my thesis. But before explaining these reasons, let's look at some relevant definitions of circus that I found on the collins dictionary (in British English):

1. a traveling company of entertainers such as acrobats, clowns, trapeze artistes, and trained animals
2. a public performance given by such a company
3. an oval or circular arena, usually tented and surrounded by tiers of seats, in which such a performance is held

8. (informal) a person or group of people whose behaviour is wild, disorganized, or (especially unintentionally) comic

The entries 1-3 obviously refer to the typical circus company that travels from town to town performing entertaining events with a vast array of seemingly unconnected activities. While entry 8 refers to the usage of the word circus as an adjective that usually gives a negative connotation of something wild an uncontrolled, done without much thought. Below I will give my reasons why I chose this theme for the thesis. While reading the following paragraphs, one should consider that both of these definitions or meanings of circus apply to each of the reasons.

The first comes from mixing proposition number 11 with my own personality. I personally feel that not only scientific writing, but scientific communication, is usually boring. The work that scientists do is very important and can contribute to many aspects of our life: curing or preventing diseases, developing new and useful technologies, help feeding the our growing population with limited space and resources, solving the increasingly worrying climate crisis, etc. Therefore, we have the duty to work seriously and objectively. However, do we have to do the same when we communicate? Despite scientific writing does not reach the dullness level of legal writing, sometimes scientific writing reminds me of it. And that also happens during scientific talks. In my opinion, scientific communication should include a comical and/or personal touch. I really think this would make reading papers or listening to talks related to topics that we do not directly work with more engaging and attractive. Sadly, I did not have the time to practice it, and I could not incorporate this ”personal scientific writing” into the writing of my scientific chapters (1-8). However, due to my clownish personalty I wanted to have a different, more comical, and entertaining theme for the rest of the thesis, what led me to this theme and to include a Gallery.

”But why a circus?” you could ask. There are 4 reasons that made me resonate with that idea. The first reason originates from the beginning of my PhD, when our lab technician, Jeff, and I were trying to purify the human septin complexes from the plasmids that our collaborator Manos sent. But it did not work, we had strangely massive yields that gave septins that did not polymerize into needle-like bundles and could not bind DOPS-containing SLBs, like the fly septins did. We spent months doing purification after purification with rounds of functional testing to check where the issue was coming from. In short, we were trying to make the septins work. At some point it felt like I was doing random things, like preparing the flow channels in an excessively clean way for no obvious reason. During that time, I had to present in group meeting and I titled it ”Taming septins”. The next time I had to present, we were still having issues and I changed the title to ”Taming septins (again...)”. Because of the word ”taming” I added an image of me taming a lion, the septins, as in a circus. This idea of adding an image that represents the results and my feelings towards the subproject kept growing and I added one as the first slide of each group meeting presentation, which I have included at the end of each chapter. This word ”taming” led me to use animals to represent each protein and even gave me the title of ”septin tamer”. And that is the first reason for choosing a circus as a theme. Oh, in case you were wondering, the purification was not working because we did not read ”50% buffer B” in the protocol, so we were adding much more imidazole than needed.

The second reason comes from the nature of my project: septin, microtubules, lipid bilayers, actin, myosin, TIRF, confocal, QCM-D, iSCAT, TEM, AFM... That is similar to a circus: clowns, animal acts (tamers), acrobats, jugglers, tigthrope walkers, magicians, contortionists, aerial performances, fire-eaters... I have had many different subprojects where I had to apply many different techniques. One day I could do QCM-D of septins binding lipids bilayers and the next I could go to the TEM to image septin-actin bundles. And this is without counting group meetings, conferences, seminars, BaSyC meetings, discussions with collaborators, supervising students, meeting with Gijsje. Organizing these array of activities within days, weeks and months made me feel like the ringmaster of a circus: it was quite hectic, but honestly quite fun (most of the times).

The third and fourth reasons are a bit more delicate: the BaSyC consortium and academia. They both include a lot of variety of activities, and sometimes feel wild and disorganized. However, the reasons why I think BaSyC and academia are circus-like have been thoroughly discussed with whoever I think should know or written in my propositions. In here, I would like to focus on the positives: I see that BaSyC is slowly starting to change with the future spring meeting of 2023 avoiding presentations and focusing on discussions, which can help boost natural collaboration - the only way in which science will be able to build a synthetic cell. I hope these and more changes are applied for the future of BaSyC and for any other project like this. On the side of academia, I am happy to see a focus on increasing diversity, to stimulate open science, and avoid predatory journals. I think there are still many things to change (see my propositions), but I think it will slowly improve.

In sum, 'the circus' metaphor, with its variety of performers, unpredictable twists, and lively spirit, mirrors the essence of my PhD journey. I chose these theme to try to inject some humor and personality into my work, aiming to make "my" science more engaging and entertaining. As I wrap up this journey, I look to the future, where I hope science will continue to evolve - much like a circus - adapting to changing times.